Single-Molecule Spectroscopy on Pigment-Protein Complexes

Im Fachbereich Physik
der Freien Universität Berlin
eingereichte Dissertation von

Jana Berit Nieder

Berlin, 2011

Die vorgestellten Arbeiten wurden hauptsächlich in der Arbeitsgruppe von Prof. Dr. Robert Bittl am Institut für Experimentalphysik am Fachbereich Physik der Freien Universität Berlin durchgeführt.

Das Forschungsprojekt lcvu_1512: "Fluorescence line narrowing on phytochromes"wurde in Kooperation mit Dr. John T.M. Kennis am LaserLaB Europe Vrije Universiteit Amsterdam durchgeführt und gefördert durch: European Community – Access to Research Infrastructures action of the Improving Human Potential Program, Contract no. RII-CT-2003-506350.

1. Gutachter: Prof. Dr. Robert Bittl
2. Gutachter: Prof. Dr. Karsten Heyne

Tag der Disputation: 29. Juni 2011

PUBLICATIONS

Parts of this thesis are already published and can be found in:

Jana B. Nieder, Marc Brecht, Robert Bittl. *Fluorescence Studies into the Effect of Plasmonic Interactions on Protein Function.* Angewandte Chemie International Edition, **49**(52):10217–10220, 2010. http://dx.doi.org/10.1002/anie.201002172
This article also appeared in german: *Fluoreszenzstudien zum Einfluss plasmonischer Wechselwirkungen auf die Funktion eines Proteins.* Angewandte Chemie, **122** (52):10415–10418, 2010. http://dx.doi.org/10.1002/ange.201002172

Marc Brecht, Volker Radics, **Jana B. Nieder**, Robert Bittl. *Protein dynamics-induced variation of excitation energy transfer pathways.* Proceedings of the National Academy of Science (USA), **106**(29):11857-11861, 2009. http://dx.doi.org/10.1073/pnas.0903586106

Jana B. Nieder, Marc Brecht, Robert Bittl. *Dynamic Intracomplex Heterogeneity of Phytochrome.* Journal of the American Chemical Society, **131**(1):69-71, 2009. http://dx.doi.org/10.1021/ja8058292

Marc Brecht, Hauke Studier, Volker Radics, **Jana B. Nieder**, Robert Bittl. *Spectral Diffusion Induced by Proton Dynamics in Pigment-Protein Complexes.* Journal of the American Chemical Society, **130**(51):17487-17493, 2008. http://dx.doi.org/10.1021/ja806216p

Marc Brecht, Volker Radics, **Jana B. Nieder**, Hauke Studier, Robert Bittl. *Red Antenna States of Photosystem I from Synechocystis PCC 6803.* Biochemistry, **47**(20):5536-5543, 2008. http://dx.doi.org/10.1021/bi800121t

Marc Brecht, **Jana B. Nieder**, Hauke Studier, Eberhard Schlodder, Robert Bittl. *Red Antenna States of Photosystem I from Synechococcus sp. PCC 7002.* Photosynthesis Research, **95**(2-3):155-165, 2008. http://dx.doi.org/10.1007/s11120-007-9241-6

Several results were furthermore presented in form of poster presentations and talks at the following conferences and seminars:

1. Jana B. Nieder, Robert Bittl, Marc Brecht, *Plasmonic Interaction Affects Protein Function*, " Annual Meeting of the German Biophysical Society ", Bochum, Germany, Okt. 2010, poster.
2. Jana B. Nieder, Robert Bittl, Marc Brecht *Plasmonic interaction Affects Protein Function*, ISACS2 "Challenges in Physical Chemistry and Nanoscience ", Budapest, Hungaria, Jul. 2010, poster.
3. Jana B. Nieder, *Single-Molecule Spectroscopy on Photosystem I Complexes Coupled to Metal Nanostructures*, CECP " Central European Conference on Photochemistry ", Bad Hofgastein, Austria, Feb. 2010, talk.
4. Jana B. Nieder, *Low-Temperature Single-Molecule Spectroscopy - Analysis of the Light-Harvesting System of Photosystem I*, " Marie Curie ITN: HARVEST Network-Meeting ", Naantali, Finland, Nov./Dez. 2009, talk.
5. Jana B. Nieder, *Low-temperature single-molecule spectroscopy on pigment-protein-complexes*, seminar of the group Prof. Dr. Rienk van Grondelle / PD Dr. John Kennis, Vrije Universiteit Amsterdam, Netherlands, Okt. 2009, talk.
6. Jana B. Nieder, Tim Heinemann, Marc Brecht, and Robert Bittl, *Phytochrome: High-resolution single-molecule spectroscopy*," Annual Dutch meeting on Molecular and Cellular Biophysics ", Veldhoven, Netherlands, Sept. 2009, poster.
7. Jana B. Nieder, *Single-Molecule Spectroscopy on Photosystem I Complexes Coupled to Metal Nanostructures*," 15th Single molecule Workshop "PicoQuant, Berlin, Germany, Sept 2009, talk.
8. Jana B. Nieder, *Tuning light-harvesting: Photosystem I in hybrid metal nanostructure assemblies*, seminar of the group Prof. Dr. Fumagalli, Freie Universität Berlin, Germany, Juli 2009, talk.
9. Jana B. Nieder, Tim Heinemann, Marc Brecht, and Robert Bittl, *Catalytic specificity of proteins: high-resolution single-molecule spectroscopy*, Cluster of Excellence, Unicat: " Unifying Concepts in Catalysis: Meeting of scientific advisory board ", Berlin, Germany, Mai 2009, poster.
10. Jana B. Nieder, Robert Bittl and Marc Brecht, *Fluorescence spectroscopy of single photosystem I complexes coupled to metal nanostructures*, " Light Har-

vesting Processes – LHP 2009 “, Kloster Banz, Germany, March 2009, poster.

11. Jana B. Nieder, Tim Heinemann, Marc Brecht, and Robert Bittl, *Phytochrome: High-resolution single-molecule spectroscopy*, “ German Biophysical Society Meeting 2008 “, Berlin, Germany, Sept. 2008, poster.

12. Jana B. Nieder, *Single-Molecule Spectroscopy on Pigment-Protein-complexes*, seminar of the group Prof. Dr. Röder, Humboldt Universität Berlin, Germany, Jun. 2008, talk.

13. Jana B. Nieder, Marc Brecht, and Robert Bittl, *Single-Molecule Spectroscopy on Phytochromes*,“ Frühjahrstagung der Deutschen Physikalischen Gesellschaft “, Biological Physics Division, Berlin, Germany, Feb. 2008, poster.

14. Jana B. Nieder, Marc Brecht, and Robert Bittl, *Single-Molecule Spectroscopy on Phytochromes*, CECP “ Central European Conference on Photochemistry “, Bad Hofgastein, Austria, Feb. 2008, poster.

15. Jana B. Nieder, Marc Brecht, and Robert Bittl, *Single-Molecule Spectroscopy on Phytochromes*, “ 10th Annual Linz Winter Workshop on Advances in Single-Molecule Research for Biology & Nanoscience “, Linz, Austria, Feb. 2008, poster.

16. Jana B. Nieder, *Single-Molecule Spectroscopy on Phytochromes*,“ 5th Course in Advanced Optical Spectroscopic Methods “, Forschungszentrum Jülich, Germany, Okt. 2007, talk.

17. Jana B. Nieder, Marc Brecht, and Robert Bittl, *Single-Molecule Spectroscopy on Phytochromes*, ECSBM: “ 12th European Conference on the Spectroscopy of Biological Molecules “, Paris, France, Sept. 2007, poster.

ABSTRACT

Single-molecule spectroscopy is used to study pigment-protein interactions relevant in photoreceptor proteins as well as in photosynthetic light-harvesting antennas.
The photoreceptor protein studied is phytochrome; a light-sensitive molecular switch which is reversibly triggered by red and far-red light, respectively. A photo-induced conformational change of the protein-bound pigment initiates a signal cascade, thereby controlling growth and other developmental processes in plants, bacteria and fungi.
For phytochromes an intrinsic heterogeneity was proposed based on ensemble spectroscopy as well as computational analysis. Single-molecule spectroscopy is applied to directly characterize the phytochrome heterogeneity. An intermolecular heterogeneity is confirmed, and moreover, a dynamic intra-complex heterogeneity is revealed. The high-resolution spectra obtained at the low-temperature conditions of 1.4 K contain vibrational information of individual chromophores. The narrow line structures from different molecules were analyzed by a pattern recognition technique, developed for single-molecule spectra. Additionally, fluorescence line narrowing spectroscopy is applied on phytochromes. Strong heterogeneity between different bacterial phytochrome species is observed.
Photosystem I (PSI) is a large pigment-protein complex essential in photosynthesis. It harbors a large light-harvesting system composed of about 300 chlorophyll molecules. A small number of low energy chlorophyll states contribute to the fluorescence emission of PSI. These states are characterized by single-molecule spectroscopy at 1.4 K. Single-emitter profiles are resolved. State-specific spectral dynamics are observed, and an additional yet unknown fluorescent state is found.
In the further parts of this thesis, PSI is employed as a model system to study excitation energy transfer characteristics between pigments in photosynthetic light-harvesting systems, as well as to analyze the source for spectral diffusion and in the last part to characterize plasmonic effects on multi-FRET coupled systems.

KURZFASSUNG

Tieftemperatur-Einzelmolekülspektrosokpie wurde zur Analyse des Ein-Chromophor-Systems Phytochrom sowie des Multi-Chromophor-Systems Photosystem I (PSI) angewendet. Phytochrome sind Photorezeptoren, die an der Steuerung verschiedener lichtabhängiger Prozesse in Pflanzen, Bakterien und Pilzen beteiligt sind. Mittels zeitaufgelöster Einzelmolekülspektroskopie konnte neben der bereits vermuteten Heterogenität zwischen verschiedenen einzelnen Phytochrom-Molekülen gezeigt werden, dass sich die spektralen Eigenschaften eines einzelnen Phytochrom-Moleküls auch dynamisch ändern. Für einige Phytochrome konnten Ein-Chromophor-spezifische schwingungsaufgelöste Fluoreszenzspektren mi bislang unerreichter Sensitivität aufgenommen werden. Die Schwingungsspektren wurden mit einem Mustererkennungs-Algorithmus analysiert, der speziell hierfür entwickelt wurde. Eine weitere Methode, die in der Schwingungspektroskopie etabliert ist, bisher aber noch nicht zur Analyse von Phytochromen herangezogen wurde, ist die Fluoreszenzlinien-Verschmälerungs-Spektroskopie. Diese wurde zusätzlich auf Phytochrome angewandt und mit Bezug auf die Ergebnisse der einzelmolekülspektroskopischen Untersuchungen diskutiert.
PSI ist ein essentieller Proteinkomplex der Photosynthese. Dieser bindet rund 300 Chlorophyll-Moleküle, die als Lichtsammelsystem dienen. Nur eine geringe Anzahl von niederenergetischen Chlorophyll-Molekülen ist an der Fluoreszenz-Emission von PSI beteiligt. Diese Beiträge wurden mit Hilfe der Tieftemperatur-Einzelmolkülspektroskopie spektral getrennt. Es konnte eine weitere spektrale Komponente der PSI-Fluoreszenz nachgewiesen werden.
Nach einer detaillierten Analyse der Einzelemitter-Beiträge wird in den darauffolgenden Teilen der Arbeit PSI als Modellsystem verwendet, um verschiedene generellere Fragestellungen zu beleuchten. Diese beschäftigen sich mit der Natur der Fluktuationen, die bei 1.4 K in Proteinen vorkommen, mit Eigenschaften des Anregungs-Energie-Transfers, sowie mit plasmonischen Wechselwirkungseffekten zwischen einem multi-FRET-gekoppelten System und Metall-Nanostrukturen. Die Ergebnisse werden in Hinblick auf durch plasmonische Nanostrukturen veränderte Proteinfunktion diskutiert.

CONTENTS

1

INTRODUCTION

Many aspects of life are connected to the interaction of molecules with sunlight. Plants and some bacteria are able to use sunlight as an energy source for their nutrition during photosynthesis and light-sensing allows for vision and light-dependent developmental processes. Not only do humans and animals use photoreceptors in their eyes for color vision, but most organisms make use of photoreceptor molecules which allow for light-sensing. Thereby, light-dependent developmental processes such as seedling, growth and flowering could have been evolved.

The functional units for light-sensing and energy conversion in biological organisms are pigment-protein complexes. Pigments are the part of the macromolecular structures which absorb light most often in the visible region of the spectrum. The interaction of the excited pigments with the protein surroundings allow for signal or excitation energy transmission. The details of excitation energy transfer mechanisms as well as molecular signaling are the subjects of much current research.

The macromolecular protein structures are connected to complex energetics of the molecules which are qualitatively described in the energy landscape model of proteins [1]. Instead of a single ground state, distributions of nearly isoenergetic, so called conformational substates, form the ground states of proteins. These protein specific energy landscapes make proteins fluctuating systems. The protein intrinsic static and dynamic disorder makes the analysis of their molecular characteristics often difficult as signals from standard ensemble techniques get averaged over different protein conformations.

After the first pioneering works of Moerner and Kador in 1989 [2] and Orrit and Bernard in 1990 [3] single-molecule spectroscopy has developed into a fascinating tool that can observe optical signals from individual molecules. The optical signals of protein-embedded pigments can be used to study the specific

pigment-protein interactions. The optical properties of pigments can be tuned in various ways by interaction with protein surroundings. Absorption color ranges can be increased, shifted or even become photo-switchable.

Photo-induced switching occurs for example in the photoreceptor protein phytochrome. After excitation of the red absorbing ground state of phytochromes, a far red light absorbing state is formed. Phytochrome photoreceptor proteins control various aspects of growth in dependence of the light conditions. In plants, phytochromes control flowering, seedling and shade avoidance. The control of these fundamental development processes led to an early discovery of this photoreceptor protein in the 1950s. In bacteria and fungi, phytochrome-like proteins trigger for example protein synthesis, however, the specific functions of many of the more recently identified bacterio-phytochromes are in parts yet unknown. The photoactive part of the protein is a single pigment, a linear tetrapyrrole. The protein is able to stabilize two different conformers of the linear tetrapyrrole. Switching between these isomeric states is reversibly triggered by red and far red light, respectively and involves supposedly a rotation of the D-ring of the chromophore [4]. This conformational change induces a cascade of conformational rearrangements of the protein allowing for signal transduction. Results from various experimental methods performed on phytochrome ensembles indicate the functional heterogeneity of phytochromes [5–9]. By performing spectroscopy on the single phytochrome molecule level, the putative intrinsic heterogeneity can directly be determined. Single-molecule experiments are conducted at low temperature conditions of 1.4 K. On the one hand these temperatures stabilize the protein in the red absorbing P_r-ground state, and on the other hand the thermal broadening of spectroscopic lines gets reduced.

Apart from the characterization of the fluorescence emission of individual phytochrome molecules, an alternate low temperature fluorescence emission technique, fluorescence line narrowing spectroscopy (FLN), is chosen to investigate sub-ensembles of phytochrome molecules. The name of the method refers to the ability to obtain vibrational fine structure in the fluorescence emission signal. For pigment-protein complexes the vibrational information in fluorescence emission spectrum is chromophore specific. Chromophores are the color giving part of the protein, composed of the pigment itself and the pigment binding pocket constituents which directly influence the pigment's optical properties. Phytochromes from different bacteria are analyzed. To obtain further detailed insights into the interaction between the switchable tetrapyrrole pigments and their specific binding pockets, selected phytochrome mutants with alterations either in the pigment itself or in the amino acid composition of the phytochrome binding pocket are investigated.

In Figure 1.1 a part of the work on phytochromes on the single-molecule level is visualized on the left. Fluorescence emission spectra from an individual phytochrome molecule are shown together with the molecular structure, which is still incomplete of phytochromes. However, the full photo-sensory part of the protein from different bacterial species has recently been resolved allowing for a detailed comparative analysis with respect to the spectroscopic information. In anticipation of the detailed description of the outcomes, heterogeneities within a single phytochrome molecule are observable by time-dependent single-molecule spectroscopy, as illustrated by the spectra shown in Figure 1.1 a).

The interactions of the proteins that lead to increased or shifted absorption ranges of pigments seem to be essential for photosynthetic light-harvesting antennas. Photosynthetic light harvesting systems are composed of multiple pigments which are able to funnel absorbed light energy towards a photochemical active site, the reaction center. The increased absorption range is in parts due to electron-phonon coupling, which describes the coupling of the electronic transitions to delocalized vibrations of the protein, referred to as phonons. And absorption wavelength shifts of electronic energies are due to interactions with specific binding pockets, leading to various site-energies of the different pigments. Due to dense packing of chlorophyll pigments inside the protein complex (see **Figure 1.1**), some pigments couple excitonically, forming dimers or trimers with strongly red-shifted absorption.

In the second part of this thesis, individual photosystem I (PSI) complexes are first analyzed by low temperature fluorescence emission spectroscopy and then taken as a model system to study general aspects of pigment-protein interactions. The transmembrane pigment-protein complex PSI is essential in oxygenic photosynthesis. The protein complex harbors a light-harvesting system composed of hundreds of chlorophyll *a* (Chla) molecules. In PSI, the absorbed light energy is converted into electrical energy. The light-harvesting system is used to efficiently absorb and transfer the energy to the reaction center whereupon its excitation, a charge separation and subsequent electron transfer takes place. The reaction center is composed of a special pair chlorophyll absorbing at 700 nm and is therefore called P700. The subjected electron is transferred across the membrane and catalyzes chemical reactions on the protein surface which are needed to produce the redox equivalent NADPH and ATP which is referred to as the energy currency of cells. Most chlorophylls of the light-harvesting system have higher electronic excitation energies compared to the reaction center and are optimized for fast and efficient downhill excitation energy transfer towards P700. Interestingly there are further Chla states with lower electronic excitation energies falling below that of the reaction center and thus require additional

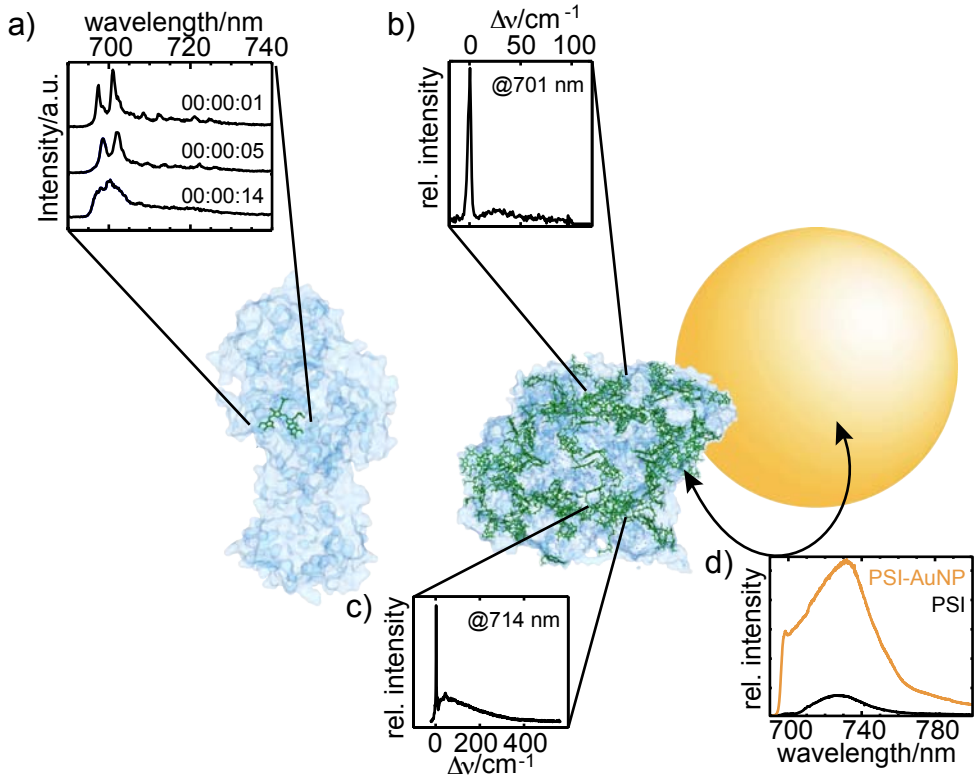

Figure 1.1: This figure gives an overview of the systems studied and a selection of the spectroscopic strategies applied. The molecular structure of phytochrome is shown on the left. The protein-bound pigment is shown in green and the protein surrounding in transparent light blue. Heterogeneity between individual phytochromes as well as from single phytochrome molecules in time (a) becomes observable by means of low temperature single-molecule spectroscopy. On the right the structure of photosystem I (PSI) is visualized. Coloring is as for phytochrome. PSI is a many chlorophyll molecules binding protein complex. A number of chlorophyll states emit fluorescence at low temperatures. Highly resolved single-emitter profiles as obtained by low temperature single-molecule spectroscopy (LT-SMS) (b) and (c) can be used to determine the pigment-protein coupling strengths. The analysis of plasmonic effects is illustrated the golden sphere on the right representing a gold nanoparticle and average spectra (d) taken over many individual PSI complexes in pure and hybrid configuration with gold nanoparticles. From these studies effects of plasmonic interaction on protein function can be analyzed. Illustration of the pigment-protein complexes are based on the PDB entries 3C3W [10] and 1JB0 [11] and visualized by using DS Visualizer [12].

thermal energy to be involved in the excitation transport towards P700. These low energy chlorophylls are ubiquitous for all light-harvesting systems of PSI from different plants and cyanobacteria. The number of Chla contributing to these low energy chlorophylls as well as their mean electronic energy positions vary for PSI of different species. The low energy Chlas are referred to as the 'long-wavelength', or 'red' Chlas. These red Chla have substantial influence on the excitation energy transfer dynamics and on the integral absorption range of PSI. Putatively, the red Chlas are connected to robustness and efficiency of the light-harvesting antenna of PSI. Nevertheless, their exact role is still puzzling.

At low temperature conditions the red Chlas act as deep traps for excitation energy and partially release energy in the form of fluorescence emission detectable on the single PSI complex level [13–15]. In ensemble spectroscopy the contributions of the red Chla cannot be discerned unambiguously due to overlapping signals of the emitters. At the single-molecule level, the spectral characteristics of the different red state Chl can be distinguished [13–15]. In this work, the fluorescence emission from the red Chla of PSI from the cyanobacteria *Synechococcus* PCC7002, *Thermosynechococcus elongatus* (*T. elongatus*) and from *Synechocystis* PCC6803 are analyzed by static and time-dependent single-molecule fluorescence emission spectroscopy. The specific pigment-protein interactions of the different Chla molecules contributing to the PSI spectrum are investigated. Time-dependent single-molecule spectroscopy is used to determine the time scales as well as the spectral ranges in which the protein surroundings are able to tune the electronic transition of the red Chla states. Furthermore, resolved low temperature single-emitter profiles are used to determine the electron-phonon coupling strengths described by the Huang-Rhys factor. The spectral characteristics of the single emitters should be used for a tentative assignment of the emitting Chla states to specific chlorophyll molecules inside the pigment-protein complex of PSI. For an assignment the inspection of the chromophore surroundings are inspected on the basis of the high-resolution structure available for PSI with 2.5 Å resolution. After the spectroscopic characterization of the red Cha states in the natural system, PSI is used as a model system to specify the nature of conformational changes occurring inside proteins at low temperatures of T = 1.4 K. For this purpose solvent water isotope exchange experiments are performed. Furthermore, time-dependent low temperature single-molecule spectroscopy (LT-SMS) is used in conjunction with a 2D correlation analysis to unravel details of excitation energy transfer in light-harvesting antennas. The multiple emitting states of PSI being part of a large light-harvesting antenna make PSI ideally suited to follow excitation energy transfer interplays between them.

In the middle part of Figure 1.1 the molecular structure of PSI is illustrated.

Again the photoactive chlorophyll pigments are shown in green while the protein backbone is shown in light blue. In anticipation of the detailed presentation of the spectroscopic results, highly resolved single-emitter profiles were indeed resolved for red Chla states. The spectra shown indicate rather weak (Figure 1.1b) and strong (Figure 1.1c) electron-phonon couplings, respectively.

An additional topic in this thesis is plasmonic interaction between metal nanoparticles and pigment-protein complexes. Plasmonic metal-nanostructures are an emerging tool for manipulating the optical properties of fluorophores. The quickly evolving range of plasmonic nanoparticle applications includes *in vivo* imaging techniques. These imaging techniques highlight in particular the need for a deeper understanding of the interaction effects of plasmonic nanostructures with biological matter. Concerning the interaction with pigment-protein complexes detailed investigation into the interaction effects were reported for one- and two-chromophore FRET-coupled systems[1] and studies on multi-chromophore FRET-coupled systems are lacking. In this work, PSI will serve as a model system for the study of plasmonic interaction effects on a multi-FRET-coupled system. Again single-molecule spectroscopy at low temperatures is used because with this technique nanostructure-intrinsic luminescence and fluorescence emission of the pigment-protein complexes can be discerned.

This part of the work is visualized on the right in Figure 1.1. The golden sphere represents a plasmonic nanoparticle. From the comparison of fluorescence emission characteristics between uncoupled and coupled PSI the plasmonic effects are observable (Figure 1.1d). Furthermore, the single-molecule fluorescence emission signals can be used to analyze metal nanoparticle influences on protein function.

[1] FRET stands for Förster resonance energy transfer.

2

PHOTOPHYSICS OF PIGMENTS

In this chapter, the fundamentals describing the optical properties of pigments as well as the effects of interactions with different coupling partners including solvents, other pigments, plasmonic nanostructures, co-solvent molecules and protein moieties are described.

2.1 Optical Properties of Pigments

Optical transitions in a pigment
To a first approximation the electronic transition energy of an organic pigment molecule with alternating single and double bonds can be estimated from the length of its delocalized π-electron system. This is why the Hückel method, which implies a reduction of the linear combination of atomic orbitals (LCAO) calculation to the calculation of the interaction energies of the p_z-orbitals of the conjugated C atoms, gives comparatively good quantitative results. Larger conjugation length hereby correlates with lower transition energy and vice versa. This is in accordance with the 'particle in the box model'. The electronic transitions typically are in the optical range, while transitions between the vibrational states are in the infrared region of the electromagnetic spectrum. In a first step the influence of solvent, pigment-pigment or pigment-protein interactions on the molecular energy levels are neglected and a simplified three state model is employed to summarize the relevant processes which follow upon molecular absorption of photon.

The different relaxation mechanisms occurring after electronic excitation of the first electronic excited state manifold S_1 can be summarized in a Jablonski diagram (see Figure 2.1a). For simplicity, the rotational levels as well as excitations to higher excited states are not included in the scheme. According to Kasha's rule, relaxation towards the vibrational ground state v = 0 of the exited

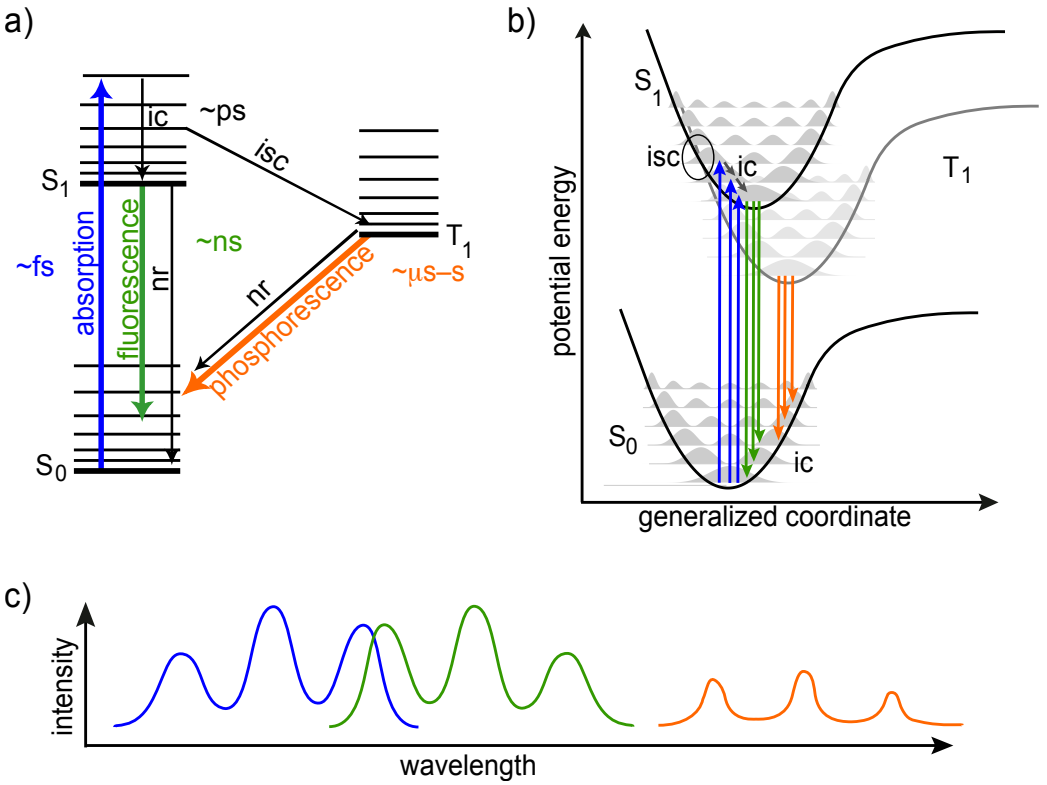

Figure 2.1: a) Simplified Jablonski scheme including the relaxation processes occurring within a molecule after resonant absorption of a photon. The absorption involves an electronic transition from the vibrational ground state of the electronic ground state S_0 towards a higher vibrational level of the first excited state S_1. The processes absorption, fluorescence and phosphorescence are indicated together with their typical lifetimes. Non-radiative (nr) transitions including internal conversion (ic) and intersystem crossing (isc) are indicated by black arrows. b) The electronic potentials of a molecule are visualized by schematic Morse potentials and the vibrational levels include the square of the associated wavefunctions. The Franck-Condon principle implies that only vertical transitions occur with probabilities described by the overlap integrals of the wavefunctions. c) Relative wavelength positions of absorption, emission, and phosphorescence. The approximate mirror symmetry between absorption and emission including the Stokes shift leading to a shift of the fluorescence emission as well as differences in spectroscopic line widths for fluorescence emission and phosphorescence are schematically taken into account.

state manifold S_1 happens prior to fluorescence emission on a picosecond time scale without emission of a photon [16]. This process is called internal conversion. Fluorescence emission is the radiative process from the vibrational ground state of S_1 to the S_0 electronic ground state manifold and has typical lifetimes of nanoseconds. A competing process to fluorescence emission is intersystem

crossing, the transition from a singlet to a triplet state of the molecular system. Due to the optical selection rules the transition between triplet and singlet states are forbidden. This restriction is partially lifted by spin-orbit couplings in the molecular system. The forbidden nature of the T_1 to S_0 transition results in reduced transition probabilities and therefore in relatively long triplet state lifetimes. In comparison to the typical fluorescence lifetimes in the range of nanoseconds, triplet lifetimes vary between microseconds to seconds for different pigments.

Rate equations of the different competing deactivation processes can be used to calculate the fluorescence quantum yield Φ_f:

$$\Phi_f = \frac{k_f}{k_f + k_{isc} + k_{nr}} \tag{2.1}$$

where k_f is the rate for fluorescence, k_{isc} the intersystem crossing rate and k_{nr} the rate of non-radiating deactivation processes. In Figure 2.1 interactions involving additional pigment or solvent molecules as well as protein matrices were neglected. Thereby, several non-radiative processes competing with fluorescence deactivation such as excitation energy transfer (EET) were not explicitly included. These processes are implicitly summarized in the rate constant for non-radiative processes k_{nr}.

Absorption and fluorescence emission

Absorption of light by a molecule only occurs in resonance condition, i.e. when the energy of the incident photon $h\nu$ matches the energy difference between an occupied initial state with energy E_i and an unoccupied state of the molecular system with the energy E_f ($h\nu = E_f - E_i = \Delta E$). In thermal equilibrium the relative populations N_1 and N_2 of the molecular states follow the Boltzmann distribution: $\frac{N_2}{N_1} = e^{\frac{-\Delta E}{k_B T}}$, with k_B the Boltzmann constant and thus depend on their energy difference and on temperature. The electronic energy level differences are in the range of 10000 cm^{-1}, vibrational level differences between $\sim$ 10 – 2000 cm^{-1} and rotational levels between $\sim$1 – 100 cm^{-1}. At room temperature $k_B T$ is of the order of $\sim$ 200 cm^{-1} and molecules are largely found in the vibrational and rotational levels of the electronic ground states. In this work, spectroscopic investigations were mainly performed at temperatures of T = 1.4 K, where $k_B T$ gets in the range of 1 cm^{-1}. Rotational levels are not activated in a frozen sample and the thermal occupation of the vibrational and electronic levels is mainly restricted to the vibrational and electronic ground state. Spectroscopically, this is observed by narrowing of the optical lines.

According to the Born-Oppenheimer approximation, electronic transitions occur much faster than any nuclear rearrangements. In the context of optical tran-

sitions, this approximation is often referred to as the Franck-Condon principle [17]. In Figure 2.1b the electronic potentials of a molecule are visualized by schematic Morse potentials. Following the Franck-Condon principle, only vertical transitions between S_0 and S_1 are included. The electron density according to the square of the wavefunctions associated with the vibrational levels are illustrated. The probabilities for transitions into the (S_1, v_i) states via absorption are proportional to the overlap integrals of their associated vibrational wavefunctions with the wavefunction of the electronic ground state. The square of the respective overlap integrals are called the Franck-Condon factors of the transition. The probability for fluorescence emission towards the different vibrational levels of the S_0 electronic ground state manifold scales with the respective Franck-Condon factors connected to the (S_1, v_0) to (S_0, v_i) transitions.

Prerequisite for an optical transition is the interaction of the pigment with the electromagnetic field. This is possible if the molecule at least temporally has a dipole which can oscillate with the frequency of the incident light. A measure for the strength of the coupling of electromagnetic field and electronic transition of a molecule is the transition dipole moment, which is determined by molecular structure and symmetry. The quantum mechanical expression of the transition dipole moment of a molecule is [17]:

$$\vec{\mu}_{f\leftarrow i} \;=\; -e \int \Psi_f^* \, \vec{r} \, \Psi_i d\tau \tag{2.2}$$

here e is the elementary electron charge, Ψ_i the initial ground state associated wavefunction and Ψ_f the final excited state wavefunction of the molecule. For an allowed transition, the transition dipole moment $\vec{\mu}_{f\leftarrow i}$ must have a non-vanishing value, and the intensity of a spectral line is proportional to its squared:

$$I \propto |\vec{\mu}_{f\leftarrow i}|^2. \tag{2.3}$$

Often the oscillator strength f is used to describe the intensity of an optical transition:

$$f \;=\; \frac{8\pi^2}{3} \frac{m_e \nu}{he^2} |\vec{\mu}_{f\leftarrow i}|^2. \tag{2.4}$$

The wavefunctions Ψ_i and Ψ_f in equation 2.2 can be split into electronic and vibrational parts, which depend on the electronic ($\vec{r}$) and nuclear coordinates ($\vec{R}$): $\psi_\epsilon(\vec{r})$ and $\psi_v(\vec{R})$, respectively. Then the transition dipole moment of transitions $\epsilon', v' \leftarrow \epsilon, v$ can be written as [17]:

$$\vec{\mu}_{f\leftarrow i} \;=\; -e \int \psi_{\epsilon'}^*(\vec{r}) \psi_{v'}^*(\vec{R}) \, \vec{r} \, \psi_\epsilon(\vec{r}) \psi_v(\vec{R}) d\tau_{elec} d\tau_{nuc} \tag{2.5}$$

$$\;=\; -e \int \psi_{\epsilon'}^*(\vec{r}) \, \vec{r} \, \psi_\epsilon(\vec{r}) d\tau_{elec} \int \psi_{v'}^*(\vec{R}) \psi_v(\vec{R}) d\tau_{nuc} \tag{2.6}$$

The first term is also referred to as the electronic transition matrix element:

$$M_{\epsilon' \leftarrow \epsilon} \;=\; -e \int \psi^*_{\epsilon'}(\vec{r})\; \vec{r}\; \psi_{\epsilon}(\vec{r}) d\tau_{elec} \tag{2.7}$$

and the second term is the overlap integral S of the vibrational wavefunctions:

$$S_{v' \leftarrow v} \;=\; \int \psi_{v'}(\vec{R})^* \psi_v(\vec{R}) d\tau_{nuc} \tag{2.8}$$

The square of the nuclear overlap integral $S^2_{v' \leftarrow v}$ is known as the Franck-Condon factor (FC). This factor scales the intensity of vibrational lines. The generalized transition rate $\Gamma_{f \leftarrow i}$ per time interval for a system with states Φ_i and Φ_j can be expressed by:

$$\Gamma_{f \leftarrow i} \propto E_0^2 \, |M_{f \leftarrow i}|^2 \; FC \; \delta(\nu, \nu_{f \leftarrow i}), \tag{2.9}$$

where E_0 is the amplitude of the oscillating electromagnetic wave coupling to the electronic transition of the molecule and $\delta(\nu, \nu_{f \leftarrow i})$ the delta function enforcing the resonance condition, known as 'Fermi's golden rule'. The delta function in general has to be replaced by an appropriate line shape function which accounts for the different line-broadening processes which are described in the following paragraph.

The electronic transition energies of molecules in solutions are distributed due to their limited state life times and due to molecule-specific interactions with the surroundings, referred to as homogenous and inhomogenous line broadening processes, respectively. According to Heisenberg's uncertainty principle the energy of a state with lifetime τ is only determinable to an uncertainty $\Delta E \approx \hbar/\tau$. For the frequency uncertainty it follows:

$$\delta\nu \approx \frac{\Delta E}{h} \approx \frac{1}{2\pi\tau} \tag{2.10}$$

The value $\delta\nu \;:=\; \gamma$ is referred to as the homogeneous line width. For fluorescence and phosphorescence deactivation processes being related to excited state lifetimes of the order of nanoseconds and microseconds, the homogenous broadening are $\approx\; 1 \cdot 10^{-3}\,\mathrm{cm}^{-1}$ and $\approx 1 \cdot 10^{-5}\,\mathrm{cm}^{-1}$, respectively. These values are much smaller than typical spectral resolutions, which for the setups used in this work are $\sim 1 - 3\,\mathrm{cm}^{-1}$ in the considered wavelength ranges.

Besides homogeneous line broadening, which is the same for all molecules in an ensemble, there are many different processes causing inhomogeneous line broadening. While for molecules in the gas phase different relative velocities of molecules lead to Doppler-broadened spectral lines, for molecules in solution line broadenings are due to specific interactions of each pigment with slightly different local surroundings. Optical spectra of an ensemble of pigments in solution typically show substantial line broadenings on the order of $100\,\mathrm{cm}^{-1}$. In

pigment-protein complexes, pigments have their specific binding sites. Each binding site (or binding pocket) leads to a characteristic pigment-protein interaction modifying inhomogenously the energy levels of the protein-embedded pigments. In addition to the different specific protein environments of pigments causing static disorder, also dynamic disorder is observed. This will be explained in the context of the energy landscape model (see below). The interaction with the surroundings leads to an overall red-shifted fluorescence emission in comparison to the absorption spectrum, referred to as Stokes shift. Excitation energy on the pigment can be transferred to the pigment's direct surroundings where it is converted to heat in the form of phonons. In the case of proteins the delocalized vibrational phonon modes typically have energies between 20 – 30 cm^{-1} and have a width of $\sim$ 30 cm^{-1} [18]. For light-harvesting and excitation energy transfer in photosynthetic antenna complexes coupling to phonon modes is of particular relevance. The simultaneous creation or annihilation of a phonon during an electronic transition of a pigment permits the absorption of photons that do not match its electronic 0-0 transition. Thereby, a considerable increase of the spectral absorption cross section of a single pigment is achieved [19]. In Section 5.3, the electron-phonon coupling strengths for single emitters from PSI are determined. The needed spectroscopic parameters as well as the relation used to calculate the Huang-Rhys factor are given in the following.

The Huang-Rhys factor

Figure 2.2a shows the calculated line profiles of a single emitter at different temperatures as taken from Ref.: [20]. At ambient conditions the thermally activated degrees of freedom lead to strongly increased inhomogenous line width, such that for a single emitter a broadened band is expected. When lowering the thermal energy available, specific substructures can arise. Beside a an intense and narrow zero phonon line (ZPL), a red-shifted phonon wing (PW) is part of a single-emitter spectrum at low temperatures (see Figure 2.2b). These spectroscopic contributions are due to the purely electronic transition and to the coupling of the electronic transition to phonon modes of the pigment surrounding.

From a single-emitter profile composed of a ZPL and a red-shifted PW, the Huang-Rhys factor S which is closely related to the Debye-Waller factor α_{DW} can be determined from their relative intensities I_{ZPL} and I_{PW}. In the low temperature limit the relation is as follows:

$$\alpha_{DW} = \frac{I_{\mathrm{ZPL}}}{I_{\mathrm{ZPL}} + I_{\mathrm{PW}}} = \exp(-S). \tag{2.11}$$

In contrast to the need of a line shape model to determine the Huang-Rhys

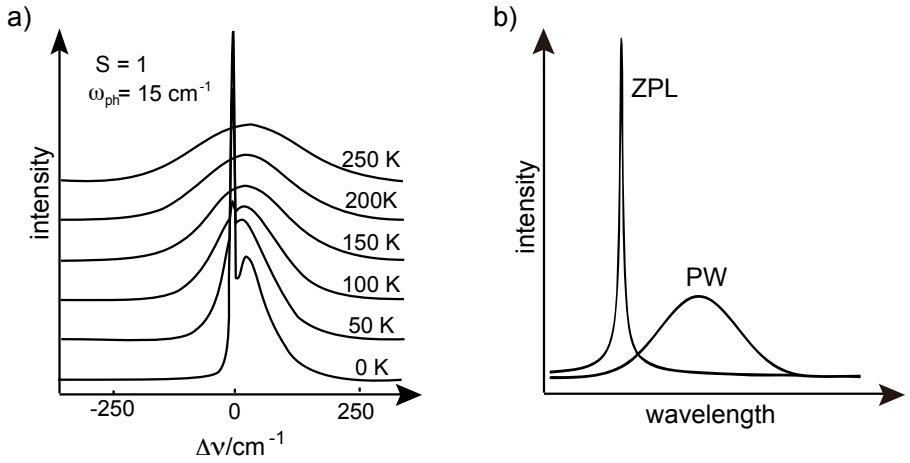

Figure 2.2: a) Temperature-dependence of the emission profile of a single emitter with a constant Huang-Rhys factor (taken from [20]). Parameters used for calculations were: Huang-Rhys factor of $S = 1$ and energy of the phonon mode ω_{ph} = 15 cm^{-1}. The zero phonon line (ZPL) of the 0 K spectrum is cut off. b) Schematic contributions to a low temperature fluorescence emission spectrum of a protein-bound pigment. Beside the pure electronic transition leading to the ZPL contribution a red-shifted phonon wing (PW) appears when coupling to phonon modes of the proteins is part of the fluorescence emission spectrum of a protein-bound pigment. Coupling of the electronic transition to vibrational modes of the pigment are not included in this scheme.

factor from site-selective spectra obtained by hole-burning or fluorescence line narrowing spectroscopy [21], the Huang-Rhys factor can directly be determined from the intensities in the specific wavelength ranges of the ZPL and PW parts of the single-emitter profile. Uncertainties in the determination of the Huang-Rhys factor S as derived from single-emitter profiles are therefore only due to the spectral resolution and signal-to-noise and not to uncertainties in empirically derived line shapes.

Fluorescence emission spectroscopy and vibrational spectroscopy methods
Figure 2.3 shows schematic electronic potential curves with vibrational levels, and the transitions relevant in a) fluorescence emission-, b) Raman- and c) IR spectroscopy are illustrated. Fluorescence emission spectra show a higher number of vibrational contributions the more the potential energy curves of ground and excited state are displaced on the generalized conformation coordinate. Then vibrational levels of the excited and ground state have overlapping vibrational wavefunctions and thus contribute to a non-vanishing FC factor. Therefore, the number of vibrational modes coupling to the electronic transition is a measure of excited-state geometry variation.

The photoswitchable tetrapyrrole pigment in phytochromes and the more rigid

chlorophyll pigments in PSI complexes represent systems with strong and weak geometric excited state variation. Vibrationally resolved spectra of individual phytochrome molecules are obtained on the one hand side and on the other, single-emitter contributions without vibrational band mixing for PSI. Thereby highlighting particularly well this relation (see results presented in Chapter 4 and 5, respectively).

In Section 4.3, the vibrational information obtained from individual phytochrome molecules is compared to published vibrational data on phytochrome ensembles as analyzed by Fourier-Transform Infrared (FT-IR) difference- and Pre-Resonance Raman (Pre-RR) spectroscopy. Different selection rules apply to these methods. Infrared absorption occurs if the dipole momentum $\vec{\mu}$ of the molecule changes during the associated vibration. The intensity of an infrared absorption band I_{IR} depends on the change of the dipole moment $\vec{\mu}$ during the vibration: $I_{\mathrm{IR}} \propto \frac{\delta\vec{\mu}}{\delta q}$, where q is the normal coordinate of the vibration. A Raman-active vibration requires changed polarizability α of the molecule during its vibration. The intensity I_{Raman} of a Raman-active band is proportional to the change in polarizability: $I_{\mathrm{Raman}} \propto \frac{\delta\alpha}{\delta q}$. Due to these selection rules, molecular symmetric vibrations are forbidden in the infrared spectrum, whereas antisymmetric vibrations are forbidden in the Raman spectrum. This is known as the rule of mutual exclusion relevant when studying small molecules. For larger molecules with multiple symmetry axes usually IR- or Raman-specific intensities are observed rather than exclusive occurrence of modes in either of the spectra. Infrared spectroscopy particularly is useful for the analysis of side groups and Raman spectroscopy for the carbon backbone of organic molecules.

Interpretation of vibrational spectra

Often density functional theory (DFT) calculations are used to assign the spectral lines observed by FT-IR or Pre-RR spectroscopy to the vibrational modes of a molecule. A recent review on the present state of DFT can be found in Ref.: [22]. In-vacuo calculations of protein-bound pigments are often taken as a first approximation to assign the measured vibrational peaks to vibrational modes of a protein-bound pigment. This approach, though, can lead to erroneous results since interactions with the protein environment might strongly modify the pigment conformation [23]. This is the case for the phytochrome bound linear tetrapyrroles. Strong pigment-protein interactions elongate and bend the rather flexible pigment molecule. Quantum mechanical calculations combined with molecular dynamics simulations take the protein surrounding into account and allow for more reliable determination of chromophore conformations from vibrational spectroscopic data [23]. An experimental approach for the assignment of vibrational peaks to molecular vibrations includes isotopic labeling of the chromophore or solvent isotope exchange experiments. By

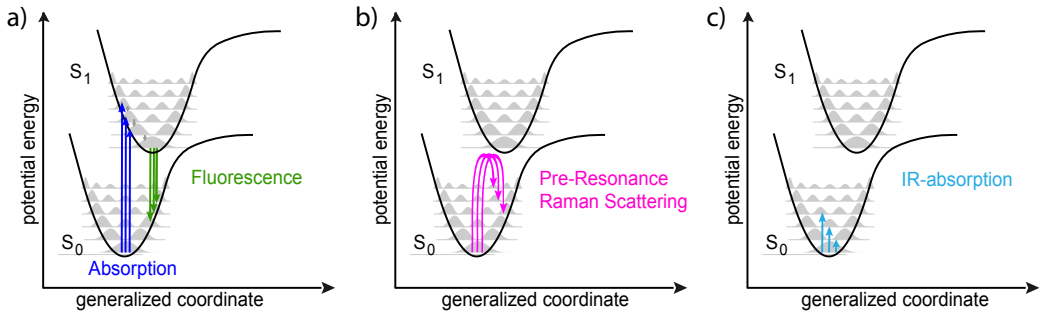

Figure 2.3: Visualization of the transitions of a molecule probed by different spectroscopic techniques. The electronic energy levels S_0 and S_1 are visualized by schematic Morse potentials and the vibrational levels by their squared wavefunctions. The electronic potentials are slightly shifted along the generalized coordinate to account for a molecule whose electronic transition is coupled to vibrational modes. All techniques can be used to probe the vibrational levels of the electronic ground state. a) After electronic excitation from S_0 to S_1 and internal conversion, the fluorescence emission occurs between $S_{1,v=0}$ and the ground state level manifold S_{0,v_i}. b) Pre-Resonance Raman spectroscopy involves an excitation with energy smaller but close to the electronic transition of the molecule to make use of the resonance enhancement of the Raman effect. The scattering process involves virtual energy levels. c) Infrared spectroscopy does not involve the excited state S_1 but the vibrational levels of the S_{0,v_i} ground state manifold are directly excited.

this approach, e.g. the vibrational modes containing exchangeable proton sites can be identified. The frequency ν of a vibrational mode with spring constant k is related by $\nu = \frac{1}{2\pi}\sqrt{\frac{k}{\mu}}$ to the reduced mass $\mu = \frac{m_1 \cdot m_2}{m_1 + m_2}$ of the vibrating atoms. Therefore, deuteration induces a downshift of the associated bands.

2.2 Pigment – Pigment Interaction

Pigments can be so densely packed in proteins that they interact with each other either in weak coupling conditions, where the electronic energy levels are approximated as being independent from each other, or in strong coupling conditions, where the energetic levels split and form degenerate dimer energy levels. In the studied multiple chlorophyll binding pigment-protein complex PSI both interaction conditions are relevant.

Weak excitonic coupling regime
In the weak coupling regime excitation energy is transferable between pigments which are described as being independent. The excitation energy transfer between two pigments either occurs via Förster transfer [24] or Dexter transfer [25]. The respective transitions causing excitation energy transfer from an excited donor D^* to an acceptor A in its ground state are visualized in Figure 2.4. During the excitation energy transfer via the Förster-type process, the exciton is delivered from the excited donor molecule to the acceptor molecule by a virtual photon. The donor relaxes back to its ground state transmitting simultaneously the excess energy by a virtual photon to the acceptor molecule which is promoted to its excited state. Dexter-type excitation energy transfer describes the direct transfer of the excited electron to the excited state orbital of the acceptor molecule with simultaneous exchange of electrons between the ground state orbitals of D and A.

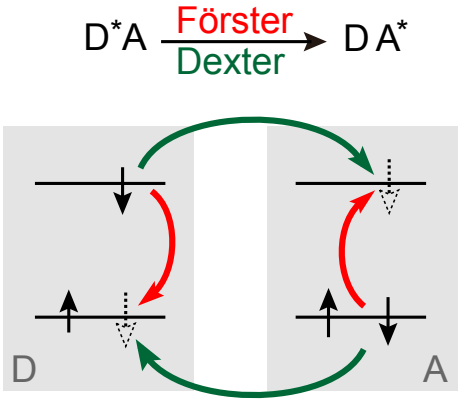

Figure 2.4: Illustration of different mechanisms to transfer an excitation from an excited donor molecule D^* to an acceptor molecule A. During the Förster type energy transfer, the excitation energy is transferred without exchanging electrons between the molecules. The Dexter transfer considers a simultaneous exchange of two electrons.

Förster-type excitation energy transfer between two given pigments depends

on their spectral overlap, their inter-pigment distance and their relative orientation. The rate k_{DA} of excitation energy transfer by Förster-type excitation energy transfer is given by [26]:

$$k_{DA} = \frac{9000\, ln10\, \Phi_D\, \kappa^2}{128\, \pi^5\, n^4\, N_A\, \tau_D\, R_{DA}^6} \int f(\tilde{\nu})\, \epsilon(\tilde{\nu})\, \frac{d\tilde{\nu}}{\tilde{\nu}^4} \tag{2.12}$$

with Φ_D, and τ_D the fluorescence quantum yield and fluorescence lifetime of the donor, $\epsilon(\tilde{\nu})$ the absorption spectrum of the acceptor, $f(\tilde{\nu})$ the fluorescence spectrum of the donor, R_{DA} the distance between donor and acceptor, and n the refractive index of the medium. κ is an orientation factor suited to describe the relative orientation of two dipoles [27]:

$$\kappa = \cos\theta - 3\, \cos\alpha \cos\beta. \tag{2.13}$$

the geometric definition of the three angles α, β and θ with respect to the orientation of two dipoles $\vec{\mu}_a$ and $\vec{\mu}_b$ can be found in Figure 2.5a.

Often the above parameters are included in the Förster radius R_0 which is a measure of the Förster critical distance [28]:

$$k_{DA} = \Phi_D \frac{R_0}{R_{DA}^6}. \tag{2.14}$$

Due to the distance dependence for Förster resonance energy transfer (FRET) proportional to R_{DA}^{-6} typical critical FRET distances R_0 for spectrally overlapping pigments are $\sim$ 10 nm [28]. Dexter transfer on the other hand involves electron exchange between the pigment molecules. This only occurs when the orbitals of the participating pigments overlap [25]. Limiting distances between pigment molecules for Dexter transfer are as small as $\sim$ 5 Å [28]. While Förster-type energy transfer can only occur between singlet states of D and A , Dexter transfer can also occur between triplet states of the molecules.

Arrangements of pigments thus can be used as antenna systems. Depending on inter-pigment distance, orientation and spectral overlap excitation energy can be transferred from one pigment to another. Nature has developed various different antenna systems which are used for light-harvesting purposes. The use of multiple pigments within one molecular complex has advantages in terms of broader absorption ranges and multiple excitation energy pathways, which enhances the robustness of these systems.

Modulated optical properties of FRET-interacting pigments, either spectral or in fluorescence lifetime, are associated with a changed FRET rate (see equation

2.12). This relation is relevant for the interpretation of spectroscopic data on PSI, as described in Chapter 5, Section 5.6 and in Chapter 6, Section 6.2.

Strong excitonic coupling regime

When two pigments are brought to close proximity, the energy levels of the individual pigments E_a and E_b split into new states with energies E_+ and E_- (see energy level splitting scheme in Figure 2.5b. Depending on the relative orientations of the transition dipole moments of the pigments, the occupation of the energy levels E_+ and E_- varies.

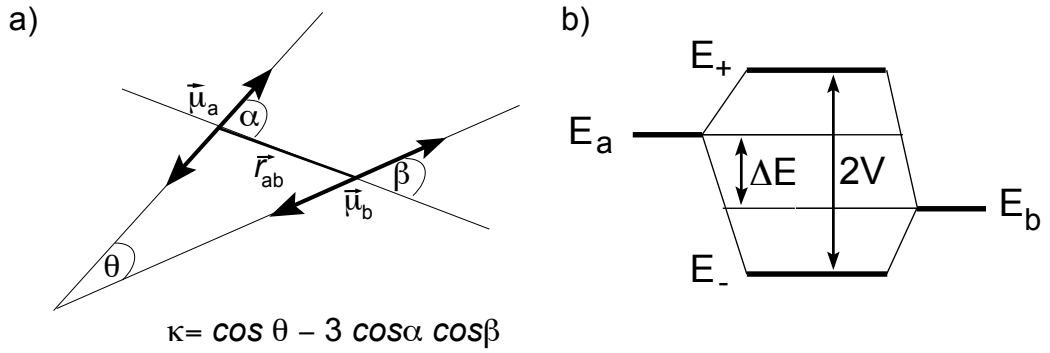

Figure 2.5: a) Illustration of the parameters used to describe the relative geometries of interacting dipoles. The orientation factor κ depends on the angles α, β, and θ describing the relative orientations of the interacting dipoles $\vec{\mu}_a$ and $\vec{\mu}_b$ with intermolecular distance $\vec{r}_{ab}$. b) Energy level splitting of pigments in strong coupling conditions. The splitting is dependent on the energy level difference Δ E while the occupancy of the E_+ and E_- states depends on the mutual orientation of the transition dipole moments which are included in the expression of the interaction energy V (see text).

In the point-dipole approximation, the interaction energy between two dipoles, $\vec{\mu}_a$ and $\vec{\mu}_b$, separated by distance $\vec{r}_{ab}$ is given by [27]:

$$V_{ab} = \frac{\vec{\mu}_a \cdot \vec{\mu}_b}{\vec{r}_{ab}{}^3} - 3\frac{(\vec{\mu}_a \cdot \vec{r}_{ab}) \cdot (\vec{\mu}_a \cdot \vec{r}_{ab})}{\vec{r}_{ab}{}^5} \tag{2.15}$$

leading to the energy levels of a coupled pigment dimer of [27]:

$$E_\pm = \frac{E_a + E_b}{2} \pm \frac{1}{2}\sqrt{\Delta E^2 + 4V_{ab}{}^2}, \tag{2.16}$$

where $\Delta E = |E_a - E_b|$ is the energy difference between the ground states of the uncoupled pigments. The interaction energy V between two molecules with dipole moments $\vec{\mu}_a$ and $\vec{\mu}_b$ depends on their relative orientation described by κ.

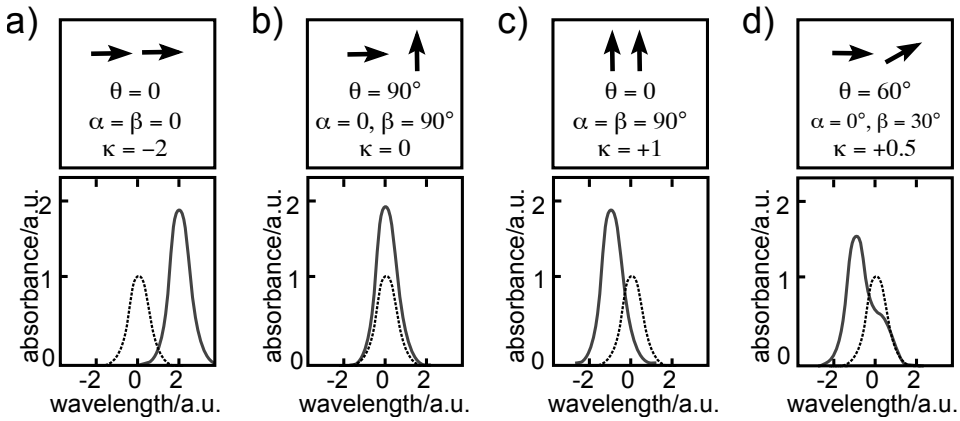

Figure 2.6: Schematic spectra with dipole strength for different dimer configurations. The relative orientations of the dipole moments are indicated by arrows on top of the spectra and the geometrical factor κ is given. The relative dipole strength of the two bands Ψ_+ and Ψ_- are a) 0:2, b) 1:1, c) 0:2 and d) 0.5:1,5. Picture was taken with modifications from Ref.: [27].

For a dimer of identical molecules $\vec{\mu} = \vec{\mu}_a = \vec{\mu}_b$ the interaction energy is [27]:

$$V \approx |\vec{\mu}|^2 \frac{\kappa}{\vec{r}_{ab}{}^3} n^2. \tag{2.17}$$

This relation shows the fast decrease of the interaction energy dependent on the molecular distance by $\vec{r}_{ab}{}^{-3}$. Since $|\vec{\mu}|^2$ and $|\vec{r}_{ab}|$ are positive quantities, the sign of V only depends on κ. In Figure 2.6 the qualitative spectral shift and dipole strength variation due to strong excitonic coupling between two identical pigments is illustrated for four different coupling geometries. The orientation factor κ can vary between -2 and $+1$ for the head-to-tail – and face-to-face – orientation of the dipoles, respectively (Figure 2.6a,c). Thus the red-shift for the head-to-tail orientation is twice that of the blue-shift for the parallel arrangement.

2.3 Pigment – Surface Plasmon Interaction

In the last part of this thesis, the pigment-protein complex PSI is studied in coupling conditions with plasmonic metal nanostructures (see Chapter 6). The optical properties of metal nanostructures as well as interaction effects with pigments are described in this section.

Optical properties of metal nanostructures
Nanometer-sized metal structures have material and shape-dependent optical properties [29]. Illumination with wavelengths longer than the dimension of

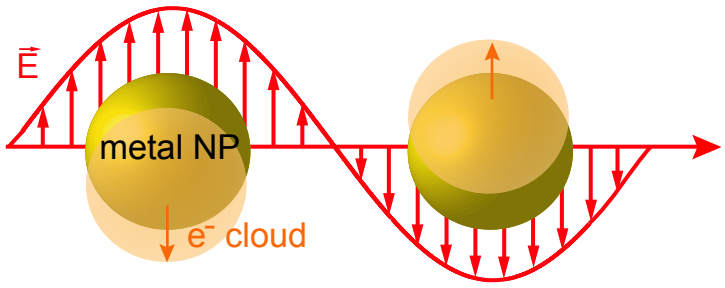

Figure 2.7: Interaction of a nanostructure with light (after Kelly et al. [29]).

the metallic nanoparticle leads to the excitation of so-called surface plasmons. Surface plasmons are the oscillations of conduction band electrons which are accelerated by the oscillating electric field vector of the incident electromagnetic wave, as illustrated in Figure 2.7. The frequency of the surface plasmons depends on the dielectric function $\epsilon(\lambda)$ of the material together with the dimensions of the metal nanostructure [29]. Beside the absorption at the surface plasmon frequency also scattering is relevant for the optical properties of metal nanostructures.

In the limit of sub-wavelength-sized spherical particles, Mie theory can be used to calculate the cross sections of the extinction σ_E [30]:

$$\sigma_E = \sigma_A + \sigma_S = k_1 Im(\alpha) + \frac{k_1^4}{6\pi}|\alpha|^2, \tag{2.18}$$

with σ_A the absorption cross section and σ_S the scattering cross section, $k_1 = 2\pi n/\lambda$ is the wave vector of the incident light in the surrounding medium 1, and α the polarizability of the metal sphere with radius r. The polarizability depends on the complex dielectric functions ϵ_m of the metal and ϵ_i of the surrounding medium and can be expressed as [30]:

$$\alpha = 4\pi r^3 \left(\frac{\epsilon_m - \epsilon - 1}{\epsilon_m + 2\epsilon_1} \right), \tag{2.19}$$

Figure 2.8 shows results of a Mie theory based calculation of the wavelength-dependent absorption, extinction and scattering cross sections calculated for spherical particles of gold and silver of different sizes. The respective surface plasmon peaks as determined by the absorption contribution in the calculated spectra for 20 nm diameter spheres are positioned at $\sim$ 520 nm for gold and at $\sim$ 400 nm for silver. The absorption contribution shows minor shifts upon particle increase. The scattering contributions are stronger affected by the particle size variation. The scattering cross section predominate the extinction of the spherical particles when exceeding diameters of 20 nm in diameter. This is

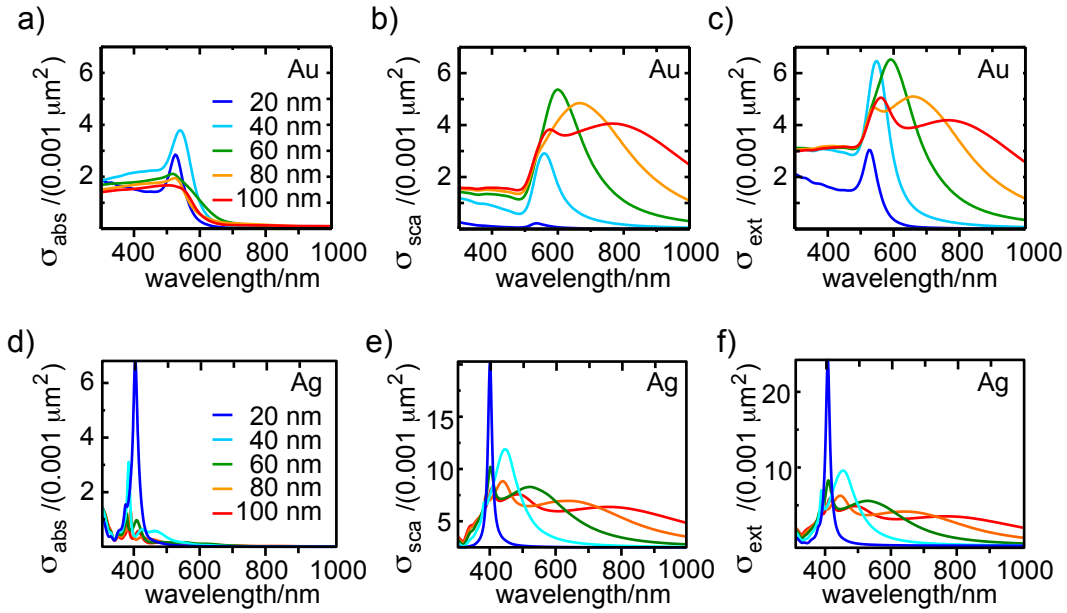

Figure 2.8: Calculated absorption, scattering and extinction cross sections of spherical gold a)-c) and silver d)-f) nanoparticles. The diameter of the spherical particles was increased from 20 nm to 100 nm in 20 nm steps. For the Mie theory based calculations the program in Ref.: [31] was used. Besides selection of the metal and the associated dielectric function, $n_{H_2O} = 1.33$ was chosen for the refractive index of the surrounding medium.

due to the absorption being proportional to r^3 while the scattering component is proportional to r^6 (see equations 2.18) and 2.19).

Interaction of plasmonic particles with fluorophores

First experimental evidence for interactions between metals and fluorophores was reported by Drexhage in 1970 [32]. The observations were interpreted as influence of the plasmonic interactions on the radiative decay time of fluorophores. The term radiative decay engineering (RDE) was introduced. In 2002, RDE was renamed metal-enhanced fluorescence (MEF) [33] to also take enhanced absorption into account. More recently, a new explanation of plasmonic nanoparticle-fluorophore interactions was described by the radiating plasmon (RP) model [34]. According to this model, optically excited fluorophores induce surface plasmons (mirror dipoles) in metal nanoparticles, which in turn radiate the spectral properties of the excited state [34]. It was furthermore observed that larger silver nanostructures are more efficient for MEF than smaller ones indicating that the scattering contribution is important for the interaction between fluorophore and metal nanoparticles [35].

The energy level scheme in Figure 2.9 visualizes the effect of plasmonic interaction. The transition rates which are modified by plasmonic interaction are

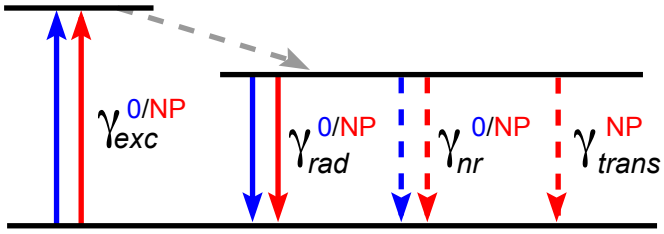

Figure 2.9: Optical transitions of a fluorophore in the presence of metal nanostructures. Rates with superscript 0 indicate the optical rates without plasmonic interaction and the superscript NP refers to the rates in coupling conditions with a metal nanoparticle (NP). Beside an altered excitation rate γ_{exc} the radiative rate γ_{rad} as well as non-radiative decay rate γ_{nr} can be altered by the interaction of a fluorophore with a NP with resonant optical characteristics. An additional decay channel of the excited state of the fluorophore is opened by FRET-like transitions towards the NP which is included in γ_{trans} (after: Ref. [36]).

the extinction and the relaxations rates of a fluorophore as indicated by the respective rates γ_0^{exc} and $\gamma_{\mathrm{NP}}^{\mathrm{exc}}$ as well as γ_0^{rad} and $\gamma_{\mathrm{NP}}^{\mathrm{rad}}$ for radiative relaxations, and furthermore γ_0^{nr} and $\gamma_{\mathrm{NP}}^{\mathrm{nr}}$ for nonradiative relaxations of the molecular system in the absence of metal NP, as well as in coupling conditions where an additional relaxation process in form of Förster-type excitation energy transfer towards the metal NP can occur as indicated by the rate γ_{trans}.

The interaction between a plasmonic nanostructure and a fluorophore is highly distance dependent. In Figure 2.10 the theoretical enhancement curve for a resonant pigment with a gold nanosphere of 100 nm in diameter is shown. The calculations were performed by Anger et al. [37], who additionally performed distance dependent fluorescence intensity measurements on an individual fluorophore interacting with a single gold nanosphere attached to an optical fiber. The enhancement curve shows quenching at distances shorter than approximately 2 nm, maximum enhancement at approximately 13 nm, and an exponential decay to longer distances indicating absence of interactions at around 80 nm.

Surface plasmon interactions not only enhance or quench fluorescence emission but increase drastically by factors of 10^{10} – 10^{14} the cross section for Resonance Raman (RR) and non-resonant Raman (R) scattering, thereby allowing for the detection of RR and putatively also of R on the single-molecule level [38–40]. This is used in surface-enhanced spectroscopy, referred to as SERRS and SERS, respectively. During the analysis of phytochromes coupled to nanostructures, highly resolved spectra showing indications for SERRS were obtained (not reported here).

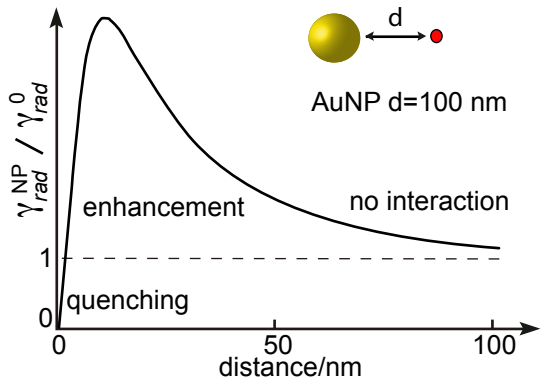

Figure 2.10: Enhancement curve for a resonant fluorophore near a nanostructure. The ratio of radiation from the fluorophore alone, $\gamma_{\mathrm{rad}}^{0}$, and when coupled to a nanoparticle, $\gamma_{\mathrm{rad}}^{\mathrm{NP}}$, is given in dependence of the inter-particle distance d. On the top right, the golden sphere represents the gold nanoparticle (AuNP) and the red circle represents the fluorophore. The calculated curve of an AuNP sphere of 100 nm diameter and a resonant fluorophore, as taken from Ref.: [37], is shown. Depending on the inter-particle distance the fluorescence is either quenched or enhanced. At longer distances no interaction takes place.

2.4 Pigment – Protein Interaction

The fluorescence emission signals analyzed in this study stem from pigments buried inside protein binding pockets. Highly specific interactions with the constituents of the binding pocked as well as protein dynamics influence the optical properties of the pigments.

Static interactions inside chromophore binding pockets
Interaction of the pigment with the direct protein environment includes steric interactions as well as electrostatic interactions. Steric effects are due to the relatively high densities within the protein affecting the conformation of the pigment. For example, the geometry of the rather flexible linear tetrapyrrole pigment as a chromophore of phytochromes is strongly bent and elongated in comparison to its structure in solution [41]. Another example for protein-induced change of symmetry of a pigment is asymmetric ligation. A chlorophyll *a* molecule for example can be asymmetrically ligated at the center magnesium atom, affecting the symmetry of the π-conjugated system of the chlorin ring. Electrostatic interactions include interactions of the pigment with charged amino acid residues. These can lead to large alterations of the electronic energies of a pigment. In the case of chlorophylls the associated spectral shifts can be of the order of tens of nanometers when the charge is positioned in direction of the dipole moment Q_y of the transition [42].

Dynamic interactions inside chromophore binding pockets
In the last decade, low temperature single-molecule spectroscopic studies were applied on various pigment-protein complexes [13, 43–49]. These studies show as a common feature that the spectral contributions in the optical spectra of protein-bound pigments largely exceed the homogenous line width of a single emitter by several orders of magnitude. By time-dependent spectroscopy on protein-embedded pigments, dynamic emission wavelength changes even at low temperature conditions are observed. These spectral dynamics are related to conformational dynamics of the protein surroundings. The high degree of flexibility is qualitatively described by the energy landscape model, which was first proposed by Frauenfelder et al. [1].

2.4.1 The Energy Landscape Model of Proteins

Proteins are the molecular machines accomplishing most reactions in cells. For their functioning, a subtle balance between structural rigidity and flexibility is needed. The energy landscape model of proteins accounts for the fast folding mechanisms of proteins into functional structures as well as for structural flexibility, which is present to a certain degree even at low temperatures.

In the energy landscape model the folded protein state is not described by a singular global minimum but instead is described by distributions of so-called conformational substates [50]. These are found with different magnitude of energy barrier heights and thus are hierarchically ordered. A cartoon of a protein energy hypersurface is shown in Figure 2.11. To visualize a potential energy hypersurface of a many-atom protein, a generalized conformation coordinate is used such that the potential-energy hypersurface is projected from the high-dimensional space into a two dimensional coordinate system. Due to the influence of solvent molecules on the dynamics of a protein, description of the potential energy surface of a protein must include the hydration shell and bulk solvent [51] (illustrated in Figure 2.12). The overall energy surface of proteins is funnel-shaped, showing a steep decline between the coordinates describing unfolded protein conformations and those describing the folded protein conformation(s).

Folded structures in comparison to unfolded structures have a reduced Gibbs free energy. The change can be due to enthalpic or entropic effects: $\Delta G = \Delta H - T\Delta S$ [54]. Beside the enthalpic effects which are caused by electrostatic interactions like ionic, dipole, van der Waals interactions, and hydrogen bonding, the hydrophobic effect lowers the Gibbs free energy of proteins by an entropic effect. The hydrophobic effect is based on the large entropy of H_2O molecules

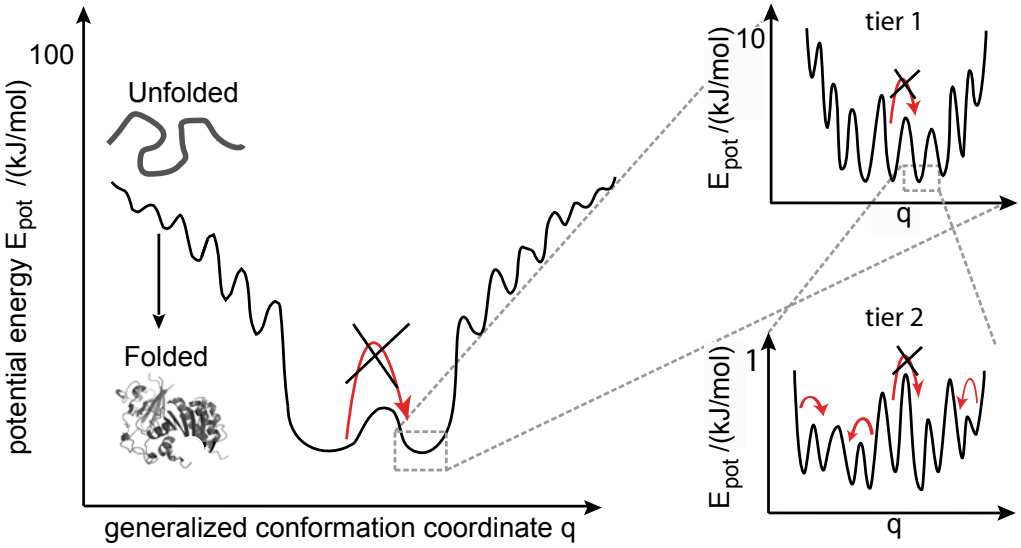

Figure 2.11: Illustration of a hierarchically ordered energy landscape of a protein. The global potential form of proteins is funnel-shaped, here, illustrated for a protein with two functional or taxonomic states. A zoom into a minimum representing a functional state shows a number of so-called conformational substates, with relatively lower energy barriers whose heights are characteristic for this first tier of the hierarchic energy landscape. A further zoom into one of the conformational substates of the first tier reveals a further set of conformational substates with again lower energy barriers characteristic for the second tier. The potential energy ranges are taken from Ref.: [52]. The effect of the low temperature conditions used in this work is highlighted by red arrows indicating possible and blocked transitions between substates (crossed out arrows). At T = 1.4 K large conformational changes as well as transitions between the substates of the first tier are frozen. Conformational changes of the protein are restricted to transitions between conformational substates of the second tier [53].

showing H-bond formation dynamics with time constants of 10^{11} s^{-1} in solution and its strong decrease when being exposed to non-polar molecules, or non-polar side chains of amino acid residues. The lack of hydrogen bond interaction partners at protein surfaces containing non-polar amino acid residues subsequently lowers the entropy of the system. Therefore, the hydrophobic effect forces non-polar residues to cluster to the inner part of the protein making the hydrophobic effect a driving force for protein folding. The overall reduction of the Gibbs free energy of the folded vs. the unfolded state of proteins is of the order of 100 kJ/mol [55]. Local minima on the way to a degenerate global minimum can be assigned to folding intermediates. Multiple degenerate global minima in the overall potential energy curve represent multiple functional conformers of a protein, called taxonomic states. Figure 2.11 represents a protein with two taxonomic states.

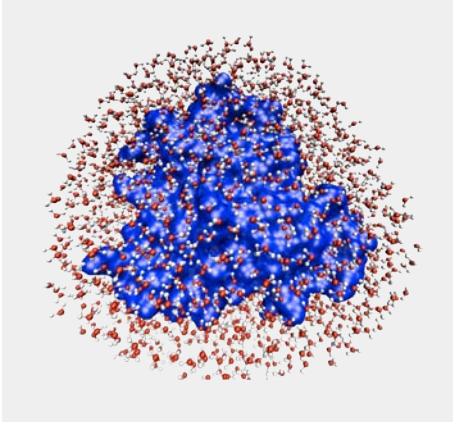

Figure 2.12: The protein dynamics are related to the dynamics in the solvation shell and vice versa. The hydration shell around myoglobin is illustrated, as taken with modifications from [55].

A zoom into one of the taxonomic ground states of the energy landscape is given. This first tier of the energy landscape of a protein has conformational substates with energy barriers of the order of 10 kJ/mol. The conformational changes associated with transitions on this level of the energy landscape typically involve intra-protein domain rearrangements. A further zoom in a local minimum of the energy landscape of the first tier of a protein is given. The second tier of the energy landscape has local minima with energy barriers of the order of 1 kJ/mol. Transitions between these conformational substates are associated with subtle conformational changes of the protein, including for example proton dynamics.

The hierarchic order is specific for proteins [56]. Other complex systems for example glasses don't show hierarchic order but have barriers of random heights [57]. The hierarchical order of protein energy landscapes was first observed for myoglobin, the "H-atom of biophysics" [50]. The large number of nearly isoenergetic states create dynamic protein structures which fluctuate between different conformations. Thus, representations of static protein structures as commonly used to visualize proteins only give a reduced picture. Recently, the hypothesis of direct translation of amino acid sequences into protein structure was further questioned by statistical analysis of redundant models in the protein data base (PDB) [58]. Deciphering the details of the energy landscape of proteins and the protein dynamics is a field of ongoing research. The ambitious scientific goal is the formulation of a predictive model for the protein state of matter.

The energy landscape of proteins and spectral diffusion analysis
Protein dynamics induce changes of electronic energies of a protein-embedded pigment, referred to as spectral diffusion. By the analysis of solvent- and pressure-induced effects on the spectral diffusion characteristics it was inferred that the spectral dynamics of protein-embedded pigments are due to conformational changes in spatial-restricted protein surroundings, and more specifically within the first coordination sphere of the pigments [59]. Therefore, protein-embedded pigments can be used to map the energy landscapes associated with specific protein moieties. At temperatures below 2–3 K tunneling dynamics become dominant compared to Arrhenius-activated transitions [60], therefore optical spectra of chromophore molecules yield representative information on the intrinsic protein dynamics. Spectral diffusion is connected to the tunneling parameter λ of an interacting two level system (TLS), with $\lambda = d\,(2mV)^{1/2}\,/\hbar$, where d is the displacement along a generalized coordinate, m is the effective mass of the entity rearranging during the conformational change, and V is the energy barrier height [61], as indicated in Figure 2.13. In addition to tunneling in the ground state TLS α, photo-induced transitions occur as considered in the model by a smaller energy barrier height in the excited state TLS β compared to the ground state-coupled TLS α. The smaller energy barrier raises the probability for tunneling and Arrhenius-activated transitions [61].

In time-dependent single-molecule spectroscopy at low temperatures, interactions with TLSs become visible in the form of spectral line hopping. If only two spectral positions occur interaction with one TLS is probable while multiple spectral positions are interpreted as resulting from interaction with multiple TLS, referred to as nTLS [43]. Recently, the 'TLS kernel' for protein-bound pigments in the light-harvesting system 2 (LH2) [43] as well as in conjugated polymers [62] was deduced by low temperature single-molecule spectroscopy. The size of frequency shifts of the electronic transitions is related to the distance between the chromophore and an interacting TLS [43]. Shifts of 7 – 10 cm^{-1} of the optical transition of a chlorophyll pigment in LH2 were associated with an interacting TLS with distances of $\sim$ 0.4 nm from the chromophore. Larger spectral shifts in this model are due to closer located TLS [43].

In addition to the protein-induced broadening of spectral lines of chromophores, charge transfer character of electronic transition in strongly coupled pigments can also lead to line broadenings. The dynamic and static broadening effect can be discerned by time-dependent analysis of single-emitter contributions. Simulations are performed to highlight the effect either of strong electron-phonon couplings or of spectral diffusion on the broadening of single-emitter profiles as observable in an experimental setup at low temperature conditions.

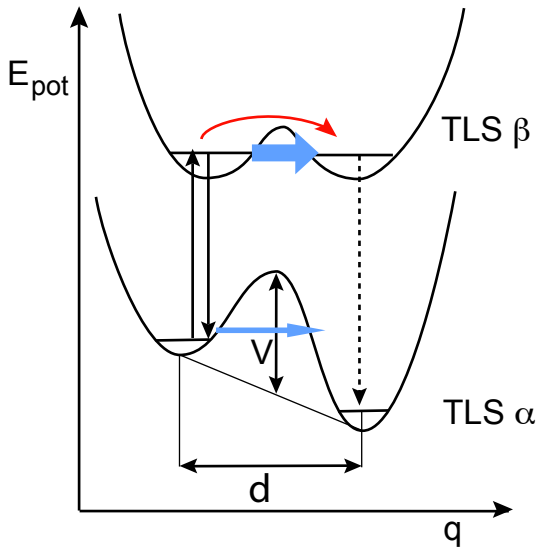

Figure 2.13: Illustration of a two-level system (TLS) (after [18]). The TLS model was developed to account for the observation that spectral diffusion often is a photoinduced effect. The TLS β connected to the excited state of the chromophore has a reduced energy barrier height compared to the ground state coupled TLS α. This leads to enhanced probability for tunneling (blue filled arrows) and might additionally be suited for Arrhenius-activated transitions (red arrow). Transitions between the local minima of the TLS in the excited state can be associated with large spectral shifts (dashed arrow). The parameters relevant for the calculation of tunneling probability are given: the displacement coordinate d, and the energy barrier height V.

Simulation of single-emitter profiles of protein-bound pigments

Simulations using the line shape model for single emitters in the low temperature limit were performed with (black curves) and without adding appropriate noise (red curves in Figure 2.14), accounting for the detection efficiency and the dark counts in the experimental low temperature single-molecule setup.

The empirically derived formula for the line shape of a single-emitter in the low temperature limit is [63]:

$$L(\omega) = \underbrace{e^{-S} l_0(\omega - \Omega)}_{\text{ZPL}} + \underbrace{\sum_{R=1}^{\infty} S^R \frac{e^{-S}}{R!} l_R(\omega - \Omega + R\omega_m)}_{\text{PW}}$$

with Ω the energy of the zero-phonon transition (0-0 transition), ω_m the phonon energy, S the Huang-Rhys factor $e^{-S} = I_{ZPL}/(I_{ZPL} + I_{PW})$, l_0 a Lorentzian line shape and l_R a line profile with asymmetric Lorentzian and Gaussian line shape contribution.

The resulting theoretical line shapes in dependence of the Huang-Rhys factor S

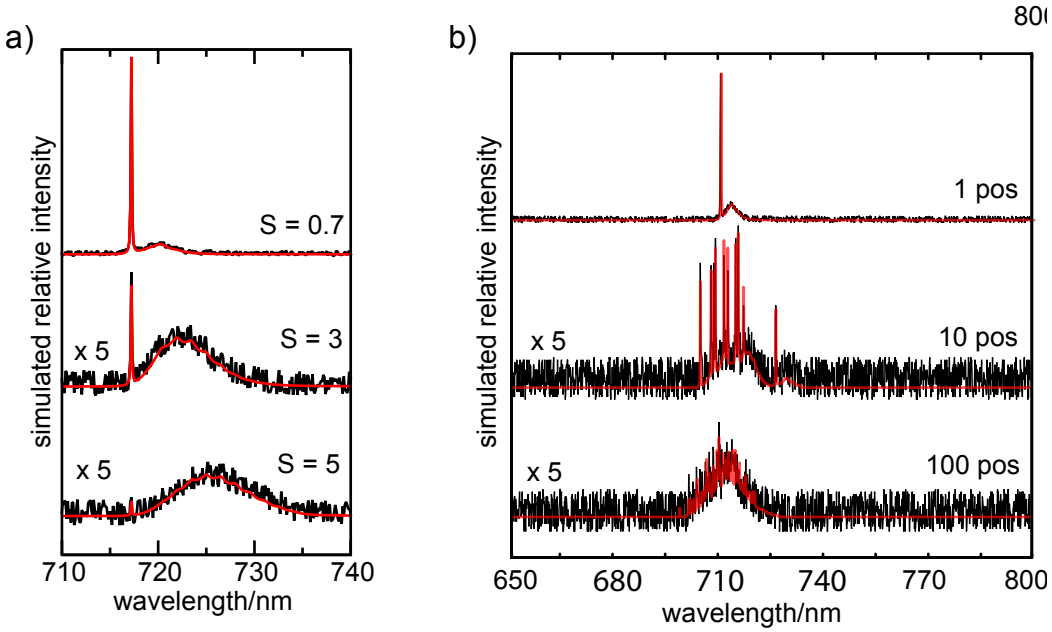

Figure 2.14: Simulation of single-emitter line shapes: a) Dependency on Huang-Rhys factors S. The S values as well as scaling factors are indicated. Besides the theoretical line shape (red), line shapes under simulated experimental conditions are shown (black) (as published in [64]). b) Effect of random spectral diffusion, here modeled by a Gaussian distribution of states with a variance of 7 nm. The numbers of spectral positions (pos) occupied within the modeled integration time of 1 s under typical experimental conditions are given. The Huang-Rhys factor was kept constant with S = 1 (details see text).

are shown in Figure 2.14a (red curves). Beside the theoretical line shapes, simulated line shapes are shown with a noise level comparable to the experimental situation. For each line profile, the integrated intensity of the line profile composed of the ZPL and PW contributions were kept constant at a value of 5000 counts, which is the approximate intensity measured for a single emitter of PSI within a 1s detection time interval. For the simulation of the experimental conditions, dark counts with random distribution were added, by using 10 ± 2.5 random counts per pixel (black curves). For better visibility the simulated spectra associated with large Huang-Rhys factors are scaled by a factor of 5.

The Huang-Rhys factor S was varied from 0.5 to 5, as indicated in the plots. All other parameters: Width of the ZPL, γ_{ZPL} = 2 cm^{-1}; mean frequency for the phonon-distribution, ω = 30 cm^{-1}; width of the phonon-distribution, $\Delta\omega$ = 30 cm^{-1} were kept constant. While for a rather small Huang-Rhys factor of S = 0.5 the ZPL is clearly identified in the simulated noise affected spectrum, an unambiguous identification of a ZPL becomes difficult at a Huang-Rhys factor of S = 3 and is impossible under the assumed signal-to-noise ratio at an

Huang-Rhys factor of S = 5. As a result of the simulations, ZPLs from single-emitters with Huang-Rhys factors of $S \leq 5$ are not observable in 1 s spectra as the ZPL contribution relative to the PW contribution approaches noise level.

To visualize the effect of spectral diffusion, single-emitter lines shapes normally distributed with a variance of 7 nm along the wavelength axis, which is a typical wavelength range accessible for a single emitter from PSI. The number of wavelength positions occupied during the simulated 1 s spectra was varied from 100, to 10 and to 1, the Huang-Rhys factor was kept constant at a value of S = 1 and all parameters as before. The simulated spectra are shown in Figure 2.14b. ZPL contributions are only discernible in the 1 and 10 position averages. Already the average over 100 single-emitter profiles generates a strongly broadened distribution. As a result, only second scale dynamics of spectral diffusion occurring in in a few nanometer range lead to resolved single-emitter line shapes in our setup while faster spectral diffusion leads to broadened bands without ZPL indications. In conclusion, two scenarios make the direct detection of single-emitter line shapes for protein-bound pigments difficult, firstly large electron-phonon couplings and secondly spectral diffusion dynamics.

3

MATERIAL AND METHODS

3.1 Site-Selective and Single-Molecule Spectroscopic Methods

Confocal low temperature single-molecule spectroscopy (LT-SMS) and fluorescence line narrowing (FLN) spectroscopy are employed to study the fluorescence emission of pigment-protein complexes. These methods as well as the related hole burning spectroscopy method are described in the first part of this section.

Historic development
The spectroscopic precursors of single-molecule spectroscopy are fluorescence line narrowing and hole burning spectroscopy. In 1972, Personov and coworkers discovered that under selective excitation with a narrow bandwidth laser for many organic solutions a fine structure can be resolved in their fluorescence emission spectra [65]. Shortly after the detection of line-narrowed fluorescence emission spectra, in 1974 the first observations of persistent spectral holes in the absorption band after site-selective excitation were reported by the groups of Personov and Rebane [66, 67]. Initially applied to crystals and glasses doped with organic molecules, site-selective techniques have been extended from small molecules to large biological systems. Reviews on the site-selective methods including their application to pigment-protein complexes can be found in Refs.: [18, 19, 68–70].

Both low temperature site-selective spectroscopic methods rely on the spectral selection of sub-ensembles of molecules. A laser with a narrow bandwidth is used to excite a sub-ensemble out of the inhomogeneously broadened band from an ensemble of molecules.

Fluorescence line narrowing spectroscopy
For the observation of line-narrowed fluorescence emission spectra, the narrow band excitation laser has to be tuned to the red edge of the inhomogenously broadened absorption profile of the sample. In this way, efficient excitation of the electronic 0-0 transition of a subset of resonant molecules takes place without overlapping fluorescence emission rising from vibrationally excited molecules. This implies a limitation of FLN to the analysis of molecules with extraordinarily red-shifted transition energies compared to the average electronic transition energies of the sample molecules. Figure 3.1 illustrates the typical spectral information obtainable by FLN on pigments in amorphous matrices or pigment-proteins solutions. The illustration contains an inhomogenous broadened room temperature absorption spectrum together with a low temperature FLN spectrum. The different contributing features are schematically shown. The zero-phonon line (ZPL) is typically associated with a phonon wing (PW) in sample solutions. Due to scattering light from laser excitation, often the pure electronic ZPL is not included in the detection range.[1] Red-shifted compared to the pure electronic transition, the vibrational lines referred to as vZPLs appear in the FLN spectrum. The vZPLs can similarly be accompanied by PWs due to respective couplings of the vibrational modes to the low-frequency phonon modes of the protein [72].

Hole burning spectroscopy
Hole burning spectroscopy relies on the use of a narrow wavelength band excitation laser, called hole burning laser, which excites a subset of molecules whose electronic 0-0 transition is in resonance with the excitation wavelength. Subsequent absorption spectra of the inhomogenous band show specific dip-profiles at the burning frequency. The loss of absorption is either due to a photochemical reaction of the excited pigments or to spectral diffusion of the excited molecules, referred to as photochemical- and non-photochemical hole-burning. At low temperatures, mostly non-photochemical hole-burning occurs, which was derived from the analysis of the broadening process of hole profiles in dependency of illumination duration and fluence rate of the hole burning laser [73]. For pigment-protein complexes the dip profile after hole burning is composed of a sharp dip at the burning frequency and broader spectral side holes due to electron-phonon coupling. Hayes and Small developed a line shape model which is widely used to estimate the electron-phonon couplings of chromophores [74].

[1] A technique referred to as ΔFLN was recently developed to lift this drawback in FLN [71]. The scattering component is eliminated by taking difference spectra of two FLN spectra, one taken before and the other taken after intermediate hole burning excitation at the 0-0 transition of the pigment.

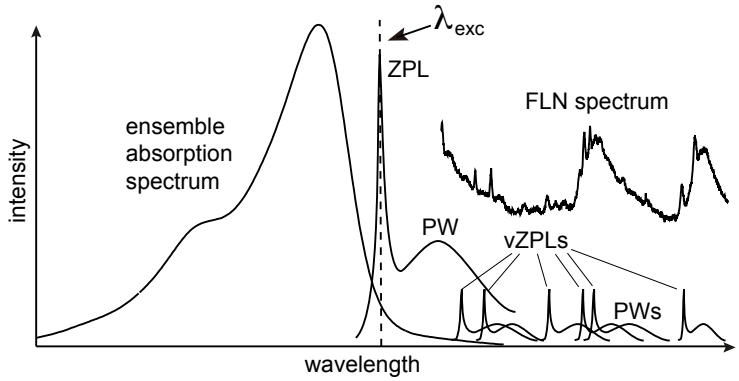

Figure 3.1: The spectral composition of a fluorescence line narrowing (FLN) spectrum of a pigment-protein complex is illustrated. Excitation in FLN condition implies excitation with a narrow band laser on the long wavelength edge of the absorption spectrum at low temperatures. Only molecules with their 0-0 transition at the laser wavelength position λ_{exc} get efficiently excited. The fluorescence emission of such spectrally selected sub-ensemble of molecules typically contains an intense zero-phonon line (ZPL) contribution and a phonon wing (PW) due to electron-phonon coupling. Often the ZPL is not included in the detection window as it is obscured by scattered laser light. Vibrational fine structure can be observable upon site-selective excitation. The vibrational contributions are referred to as vZPLs which can have red-shifted PWs due to coupling of the vibrational transition to delocalized phonon modes of the protein. Broad contributions in FLN spectra are mainly due to spectral diffusion which for some pigment-proteins is too large for evolution of narrow lines to be observed (for details see text).

Single-molecule spectroscopy (SMS)

The first spectroscopic measurements with single-molecule sensitivity were achieved by Moerner and Kador [2] in 1989 and Orrit and Bernard [3] in 1990. Both groups conducted their single-molecule experiments on pentacene in para-terphenyl crystals and at liquid helium temperatures. At that time, pentacene in para-terphenyl crystals had already been extensively studied by hole burning spectroscopy.

To gain single-molecule sensitivity, Moerner and Kador applied two different double modulation techniques combined with optical hole burning applied to the far red absorption wing of pentacene [2]. Orrit and Bernard, on the other hand, measured fluorescence excitation spectra of pentacene in para-terphenyl from crystals with strongly reduced pentacene concentrations as probed in spatially confined volumes. This was achieved in two ways: one experiment was performed with a focussed laser beam produced by a plancovex lens and the other was performed by using cleaved crystals attached to the end of a single-mode fibre with a core diameter of 4 μm. For reaching appropriate collection

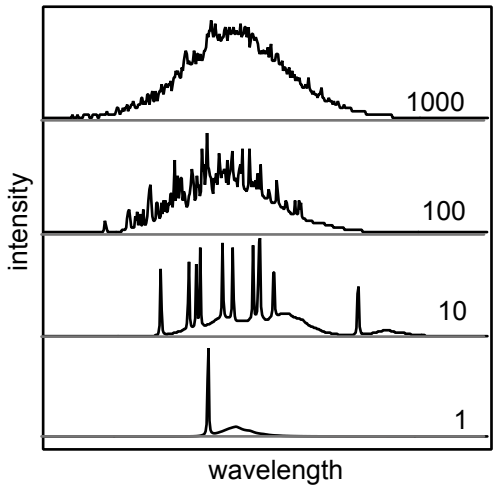

Figure 3.2: Illustration of the transition from an inhomogenously broadened band of an ensemble of molecules to the detection of a single-emitter profile. The simulated line profiles rely on the line shape model from Ref.: [63]. From top to bottom the number of normally distributed single-emitter profiles is decreased from 1000 to 100 to 10 and finally to a single-emitter profile.

efficiency for fluorescence emission detection a parabolic mirror with high numerical aperture (NA) was used [3]. The evolution from site-selective to single-molecule spectroscopic techniques are discussed and reviewed in Ref.: [75].

Figure 3.2 illustrates the spectral features observable upon the transition from an ensemble of 1000 molecules contributing to an fluorescence emission spectrum towards a single emitter. The simulated line profile relies on the single-emitter line shape model and contains a ZPL and a PW [63]. While the summation over 100 Gaussian-distributed single-emitter profiles adds up to an unstructured inhomogenously broadened band, a small number of contributing profiles allows for the observation of the single-emitter contributions, the ZPL and the PW. Thus, at the single-molecule level the inhomogenous broadening due to different site energies of a pigment can be lifted.

Recent approaches in single-molecule techniques

Today, most single-molecule techniques rely on the detection of fluorescence emission. In low temperature single-molecule spectroscopy (LT-SMS) spectral information is either obtained by tuning the laser across the absorption profile of the sample molecule and detecting the associated fluorescence emission intensity, called fluorescence excitation spectroscopy, or by using a fixed laser wavelength for excitation and detecting spectrally resolved fluorescence emission (as used in this thesis). For the spectroscopy of one-chromophore-systems vibronic excitation was shown to be advantageous [76]. By vibronic excitation

the full red-shifted fluorescence emission spectrum of a single chromophore can be detected, in contrast to an excitation scheme involving the excitation of the 0-0 transition, whereupon the usage of cut-off filters needed to suppress scattering light from the excitation laser cuts parts of the spectrum on the short wavelength side. Since the first pioneering experiments, different optical devices were applied and developed to achieve single-molecule sensitivity. For collecting maximum proportions of the isotropic fluorescence radiation, besides parabolic mirrors [77] and simple lenses [78], microscope objectives [79] are widely used. With the high quantum efficiencies of today's optical detectors it became comparatively easy to detect the fluorescence signals of single molecules.

More recently, different strategies were developed to achieve single-molecule sensitivity in biological tissues and cells at ambient conditions. The excitation volume can be decreased below the diffraction-limited volume by using tiny apertures as in scanning near-field optical microscopy (SNOM) experiments [80], stimulated emission depletion technique (STED) [81], by using single emitters as light sources [82], or by taking advantage of local electromagnetic fields near plasmonic nanostructures [83]. The tip-enhancement can be used to detect metal-enhanced fluorescence but also allows for the detection of single-molecule tip-enhanced Resonance Raman spectra (TERRS) [83]. Excited state dynamics have recently been followed by fs-spectroscopy on the single-molecule level [84].

As stated above, single-molecules are typically detected by their fluorescence characteristics. This implies applicability to molecules with appropriate fluorescence emission quantum yields only. Recently, three groups have independently achieved single-molecule sensitivity at room temperature by optical absorption. Each group used a different technique. Either the absorption of a single-molecule was measured directly, by detecting the minute intensity change of a laser beam passing through the sample [85], or by the photothermal effect [86], or by a ground-state depletion technique [87].

3.1.1 Confocal Single-Molecule Spectroscopy

The combination of spacial and spectral selectivity allows for the detection of single-molecules [88]. This can be achieved by using a confocal setup together with highly diluted samples [89]. An illustration of the confocal principle can be found in Figure 3.3 and is described in this section.

The confocal principle

The basis of the confocal principle is dual focussing. Firstly, the excitation beam

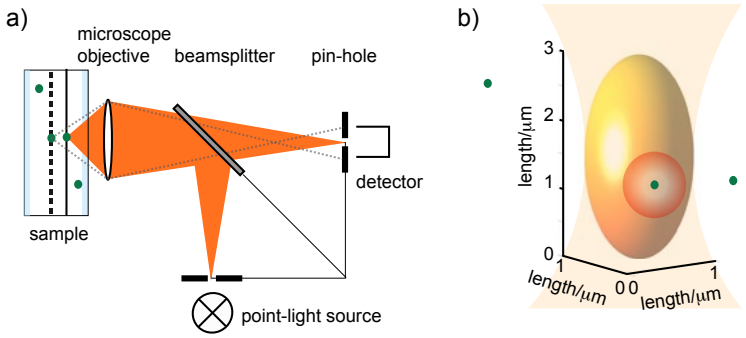

Figure 3.3: Illustration of the confocal principle and focal volume. a) In confocal configuration excitation light is focussed onto the sample by a lens which is also used for detecting the emission from the focal volume. A pin-hole is positioned confocal with the excitation volume such that radiation from outside the focal volume is efficiently blocked from reaching the detector. b) The concentration of the sample for single-molecule sensitivity has to be such that statistically less than one molecule resides within the focal volume. When a laser with Gaussian beam profile is used, the focal volume has approximately ellipsoidal form and dimensions in the range of μm, corresponding to femtoliter excitation volumes.

is focussed onto a diffraction limited volume and secondly the same volume is probed by another objective or, in epifluorescence configuration, by the same objective lens. To increase lateral resolution a pinhole can be placed in front of the detector such that radiation with origin in the confocal volume can efficiently pass and contribution from scattering, or from fluorescence emission outside the focal volume are hindered to reach the detection path. In Figure 3.3a this is visualized by an additional optical pathway (dashed lines) which has its origin in a plane (black dashed line) other than the focal plane (black line). Since in confocal configuration fluorescence emission is only collected from tiny volumes of the sample, for obtaining a spatially resolved fluorescence image, scanning of the sample, or alternatively of the excitation/detection volume is needed. The latter is referred to as laser scanning. Laser scanning can be realized by using a scanner module and a telecentric lens system [88] (implemented in the LT-SMS setup used). By the telecentric arrangement of two lenses the scanned excitation beam enters the main axis of the objective under different angles, such that the confocal volume is formed at different lateral positions in the focal plane.

Optical resolution in confocal configuration

A confocal scanning microscope has higher contrast and resolution in comparison to a conventional microscope. The point spread function (PSF) of a point light source in confocal configuration is the square PSF of a conventional microscope, which is described by the intensity pattern known as the Airy disc. This

is due to the double-focusing; the PSF of the incoming light is multiplied by the PSF of detection pathway. Following the Abbé-Rayleigh criterion, in conventional microscopy two point light sources can be resolved when having a minimal distance of [88]:

$$\Delta s_{min} = 0.61\frac{\lambda}{NA} \tag{3.1}$$

where λ is the wavelength of light and NA is the numerical aperture $NA = n \cdot \sin\alpha$, with the refractive index of the medium n and α being half the collection angle of the objective.

For the optical resolution in confocal configuration the minimal distance reduces by a factor of $\frac{1}{\sqrt{2}}$ to:

$$\Delta x_{min} = 0.44\frac{\lambda}{NA} \tag{3.2}$$

in axial direction and to:

$$\Delta z_{min} = 1.5\frac{n\lambda}{NA^2} \tag{3.3}$$

in lateral direction [88]. The high resolution in lateral direction allows for three dimensional imaging with confocal microscopes.

Sample requirements for single-molecule detection

The concentration of sample molecules has to be reduced to match the condition that statistically less than one fluorescent molecule resides within the diffraction limited excitation/detection volume. The focal volume produced by a Gaussian beam has approximately ellipsoidal form. At a wavelength of $\lambda\sim$ 700 nm and with $NA = 0.85$, as used in the described LT-SMS experiments, the focal volume measures approximately 1 μm in axial direction and approximately 3μm in lateral direction. An illustration of the focal volume for a Gaussian beam is given in Figure 3.3b. Therefore, single-molecule spectroscopy on fluorophores in solution requires pico-molar concentrations of sample molecules to match the condition that less than one molecule is found per voxel. Other preparation techniques for single-molecule spectroscopy include nanometer-sized thin film preparations with spatially distributed active molecules. For room temperature single-molecule spectroscopy immobilization techniques are required, which is not needed in low temperature spectroscopy.

The sample requirements for fluorescence emission detection on the single-molecule level include a sufficiently high fluorescence quantum yield and photostability of the molecules, as these are the factors limiting the number of emitted photons arriving at the detectors. Generally it is found that photo-stability of pigments increases drastically at low temperatures compared to room temperatures.

3.2 Experimental Setups

3.2.1 Low-Temperature Confocal Single-Molecule Spectrometer

The experimental setup used here for low temperature single-molecule fluorescence emission spectroscopy (LT-SMS) is a home-built confocal spectrometer designed for measurements at cryogenic temperatures (T = 1.4 K). A detailed description can be found in the Ph.D thesis of Hauke Studier [90] who built the first version of the spectrometer, which since then has been optimized and further equipped for time-correlated single-photon counting (TCSPC), for fluorescence lifetime imaging and for spectrally resolved fluorescence lifetime determination. Optimization of the LT-SMS setup included implementation of a reservoir bath-cryostat (Janis Research Company, Wilmington, USA), a scanning module based on a two-axis pivotable mirror (Physik Instrumente (PI) GmbH & Co. KG, Karlsruhe, Germany), a motorized sample positioning system and a rotatable mirror allowing for multiple detection paths for the fluorescence lifetime detectors (miCos GmbH, Eschbach, Germany). A scheme of the setup used for the LT-SMS measurements described in this work is given in Fig. 3.4.

Description of the setup
The spectrometer is set up on an optical table (OPTA GmbH, Bensheim, Germany), which is vibrationally decoupled by pneumatic isolators (Newport Corporation, Irvine, USA). The laser excitation source is a λ = 680 nm continuous-wave (cw) diode laser (57FCM-A-680-28-M02-TO-2-28-150; Schäfter+Kirchhoff GmbH, Hamburg, Germany). The laser beam is coupled into a single-mode polarization maintaining fiber (PMC-630-4.4-NA010-3-APC-150-P; Schäfter+Kirchhoff GmbH, Hamburg, Germany). At the fiber exit the beam is collimated with an output coupler (Newport Corporation, Irvine, USA). The collimated beam passes a band pass filter ($\Delta\Gamma$ = 5 nm, T = 88%, OD 6 else; AHF Analysentechnik AG, Tübingen, Germany) removing luminescence background from the semiconductor material of the laser. A dichroic beam splitter (T = 90% for λ >690 nm, R > 90% else; AHF Analysentechnik AG, Tübingen, Germany) reflects the excitation beam into the optical path of the spectrometer. As laser scanning module a piezo driven tip/tilt mirror (S-334; Physik Instrumente (PI) GmbH & Co. KG, Karlsruhe, Germany) is used. On this piezo device a silver-coated mirror is pivotable around two coplanar axes with a fixed pivot point. By a telecentric lens system composed of two lenses with focal length of f = 250 mm the excitation beam is focussed into the main plane of the microscope objective (60x, Plan APO, infinity-corrected NA = 0.85,

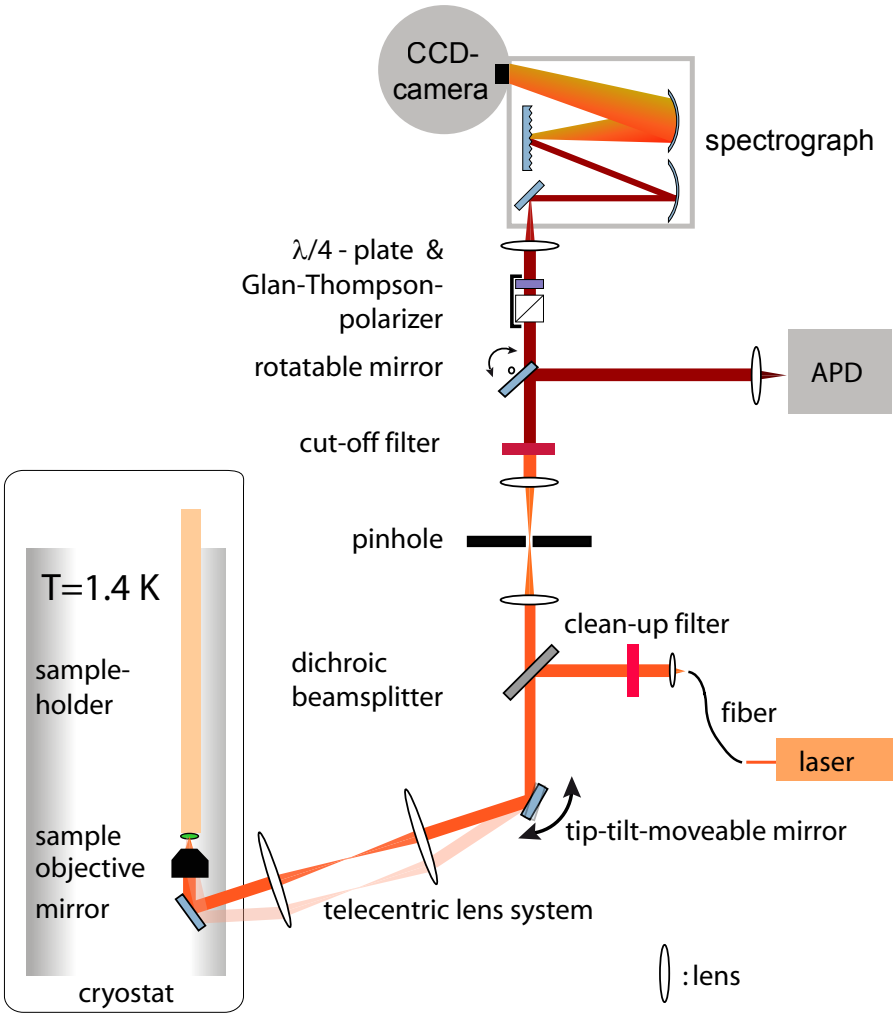

Figure 3.4: Scheme of the home-built confocal spectrometer designed for fluorescence emission measurements at temperatures of T = 1.4 K. The laser beam is collimated behind the exit of a single-mode polarization-maintaining fiber and passes a laser clean-up filter before being deflected into the excitation pathway of the spectrometer. The excitation volume is scanned by using a laser scanning device comprising a pivotable tip-tilt moveable mirror and a telecentric lens system. The microscope objective is located together with the sample inside the cryostat. The fluorescence emission signal is detected in epifluorescence configuration. The signal passes the dichroic beam splitter and is focussed onto a pin-hole followed by a re-collimating lens. A fluorescence cut-off filter is positioned behind the lens and only allows the red-shifted fluorescence emission light to either be detected by an APD or by a LN_2-cooled CCD camera mounted on the exit slit of a grating spectrograph. A rotatable Glan-Thompson broadband polarizer combined with a quarter-wave plate can optionally be placed into the detection pathway in front of the spectrograph (see text for details).

f = 0.1 mm; Microthek GmbH, Hamburg, Germany) which is located inside the cryostat. A 45° inclined mirror inside the cryostat is needed to reflect the beam upwards into the vertically mounted objective. The fluorescence emission is collected in epifluorescence configuration. After passing the dichroic beam splitter the signal is focussed (lens with f = 60 mm) onto the pin-hole (d = 50 μm; Newport Corporation, Irvine, USA). Approximately only the first order of the Airy-disc diffraction pattern can pass. It is then collimated again by a lens (f = 60mm). Longer wavelength fluorescence emission signals pass the cut-off filter (OD 6 for λ $<$ 695 nm, T = 95$\pm$3 % for λ $>$695 nm; AHF analysentechnik AG, Tübingen, Germany). A computer-controlled rotatable mirror is used to reflect the signal onto a lens focussing on the detection surface of an avalanche photo diode (APD) (SPCM-ARQ-15; Perkin-Elmer, Waltham, USA). When the mirror is retracted from the beam path the signal passes to a lens focussing the light onto the entrance slit of a spectrograph (Acton Spectra Pro 300i; Princeton Instruments, Trenton, USA). Three exchangeable gratings with 300, 600 or 1200 lines per mm are available. At the output slit of the spectrograph a nitrogen-cooled CCD camera (SPEC-10 LN, back illuminated, deep depleted, 1340x100 pixels; Princeton Instruments, Trenton, USA) is mounted, which is used for spectral data acquisition. For spectral measurements 7 to 10 out of 100 row pixels containing the signal were binned. Readout time was between 0.1 and 0.2 seconds. The different gratings correspond to wavelength intervals of 0.21 nm, 0.10 nm and 0.04 nm per pixel, respectively. The detection efficiency of collecting fluorescence emission with the setup is approximately 1%. Largest losses are due to the relatively small NA of the microscope objective. For polarization-dependent measurements a broad-band Glan-Thompson polarizer can be positioned in front of the spectrograph. To circumvent artifacts due to polarization-dependent reflectivity of the grating, the linear polarized light after the Glan-Thompson polarizer is transformed into circular polarized light by a quarter-wave plate.

Generation of low temperature conditions of T = 1.4 K

The low temperature conditions of T = 1.4 K, which were used for all single-molecule experiments described in in this work, are generated by pressure reduction to $\sim$ 2 mbar in the ^{4}He-filled cryostat. At these temperatures, ^{4}He is in the suprafluid phase. The pump system used, consists of a roots pump and an upstream vane pump (EH250 and El/2M40; BOC Edwards, West Sussex, GB). The temperature is measured by a temperature sensor which has a precision of $\pm$ 12 mK in the temperature range from 1.4 to 10 K (DT-670-SD; Lake Shore Cryotronics Inc., Westerville, USA). During the studies presented here, the cryostat was exchanged from a home-built version, to a commercial available cryostat (Janis Research Company, Wilmington, USA). Both cryostats are

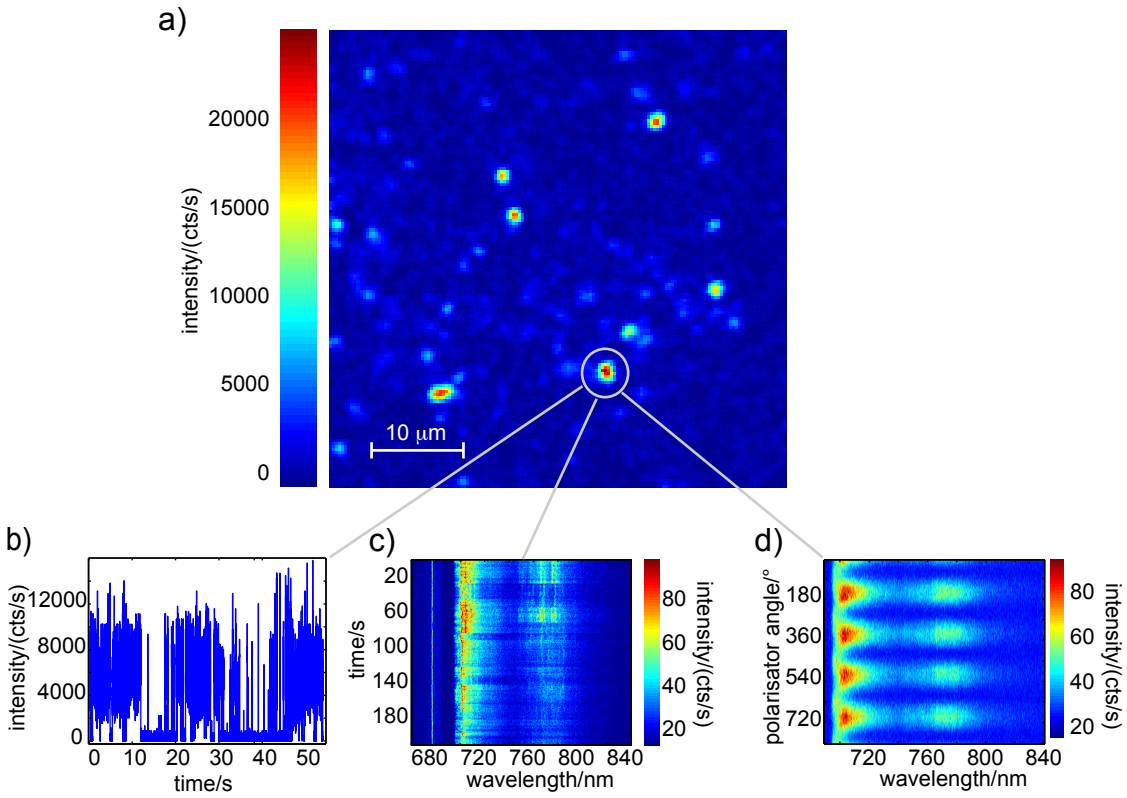

Figure 3.5: Examples of fluorescence emission data obtained in the different measurement modes of the spectrometer. a) Fluorescence intensity image as taken while laser scanning the sample in a 50 μm $\times$ 50 μm large area. b) Fluorescence intensity time trace (here the typical single-molecule blinking behaviour is shown). c) Time-dependent fluorescence emission spectra series as measured with the CCD camera. d) Polarization-dependent fluorescence emission spectral sequence as measured with the CCD camera in configuration with an computer-controlled rotating Glan-Thompson and quarter-wave plate combination positioned in front of the spectrograph.

helium bath cryostats, the cryostat from Janis Research, however, has an additional helium reservoir from which helium can continuously be transferred into the main chamber by a capillary. This configuration removes the temporal limitation for maintaining measurement conditions, which was restricted to $\sim$ 4 h in the home-built helium bath cryostat.

Computer-controlled data acquisition

To localize the sample molecules, the laser beam is scanned over the focal plane under continuos APD detection. The sample holder can linearly be moved in lateral direction in computer-controlled fashion. The positioning of the sample into the focal plane is performed by optimizing signal intensity. For each scan-

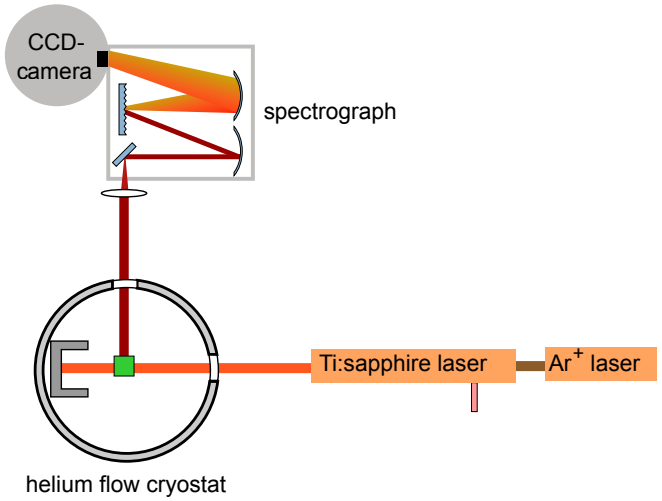

Figure 3.6: Schematic fluorescence line narrowing setup. Detection of the fluorescence light happens under 90 degree with respect to the incident beam.

ner position the associated signal intensity is detected by the APD. From this information an intensity image is created (example data in Figure 3.5a). Single scanner positions can be selected and the signal associated with the focal volume can either be detected by the APD or by the CCD on which the radiation is dispersed by the grating spectrograph. By APD detection, fluorescence time traces can be recorded (example data in Figure 3.5b). The CCD detection allows for recording single spectra or time-dependent spectral sequences (example data in Figure 3.5c). When the computer-controlled rotatable broad band polarizer combined with a quarter-wave plate is positioned in front of the spectrograph, polarization-dependent spectral sequences can be recorded (example data in Figure 3.5d).

3.2.2 Fluorescence Line Narrowing Spectrometer

A scheme of the setup for fluorescence line narrowing spectroscopy can be found in Figure 3.6. A tunable continuous wave Titan:Sapphire laser pumped by an Argon ion laser (Coherent Inc., Santa Clara, USA) was used as source providing variable excitation wavelengths between 700 nm to 1030 nm with a narrow bandwidth of ~ 0.1 cm^{-1}. A standard fluorescence detection setup working in 90° geometry is used. The sample is placed inside the helium flow cryostat, providing temperature conditions between 4.2 and 300 K (UTRECS; Cryogenic Technologies Laboratory, Kiev, Ukraine). For spectral analysis a spectrograph (500is; Chromex, Albuquerque, USA) with a 600 lines per mm grating and a CCD camera (ST-6, Santa Barbara Instrument Group, Santa Bar-

bara, USA) was used. The resolution of the setup was 0.2 nm.

3.3 List of Samples: Nomenclature and Preparation

All pigment-protein complexes studied in this thesis are listed in Table 3.2 together with the names of our cooperation partners who provided the respective proteins in highest purification grade. For details of protein expression, extraction and purification of the phytochrome Agp1 from *Agrobacterium tumefaciens* see Ref.: [91]. The synthesis and assembly of the chromophore BV15Za with Agp1 is described in Ref.: [92]. Purification of the phytochromes from *Rhodopseudomonas palustris* is described in Refs.: [93, 94]. Details on the phytochrome *Dr*BphP from *Deinococcus radiodurans* can be found in Ref.: [95]. PSI complexes from *T. elongatus*, *Synechocystis* PCC6803 and *Synechococcus* PCC7002 were isolated as described in Refs: [96], [97] and [98], respectively.

Preparation of the samples for single-molecule spectroscopy
About 1 μl of the respective sample solutions (as described below) were squeezed between two cover slips assuring spatial separation of individual pigment-protein complexes and mounted on a sample holder made of epoxy glass fibre and partly titan (see Figure 3.7).

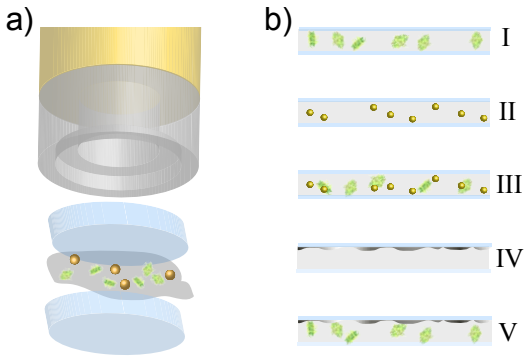

Figure 3.7: a) Sample configuration. Droplets of $\sim$ 1 μl of diluted sample solutions were squeezed between two cover slips and mounted on the metallic part of the sample holder. b) Sketches of the sample configuration for the analysis of single pigment-protein complexes (I), analysis of gold nanoparticles (AuNP) (II), hybrid samples composed out of pigment-protein complexes and AuNP (III) as well as for characterization of silverisland films (SIF) (IV). The SIF-coated cover slip is brought to the backside of the sample with respect to the incident beam. For hybrids composed of pigment-protein complexes and SIF a drop of the diluted sample solution was put between a SIF-coated and a normal cover slip (V).

Phytochrome samples and measurement conditions for LT-SMS
Agp1-BV solutions were highly diluted in a Tris-HCl buffer (50 mM Tris, 5 mM EDTA, 150 mM NaCl, pH 7.8) containing 50% (w/w) glycerol to a concentration of 5 pM, thereby, yielding primarily monomeric phytochrome [99] and conditions suitable for single-molecule detection. Agp1-PCD-BV15Za were diluted to a 500 pM concentration in a Tris-HCl buffer (50 mM Tris, 5 mM EDTA, 150 mM NaCl, pH 7.8).

The dilution procedure was accomplished under safe green light conditions for all phytochrome samples to prevent the phytochrome photoreceptor from its red-light inducible photoconversion, thereby, preserving the phytochromes in their P_r ground state. The sample was transferred into the pre-cooled cryostat ($T \sim 100K$). Measurement temperature for all samples was T = 1.4 K. This temperature leads to efficient trapping of the phytochromes in their P_r state even upon photoactivation. The excitation source for fluorescence investigation with LT-SMS was a $\lambda = 680$ nm diode laser (Schäfter-Kirchhoff, 57FCM) attenuated to 100 – 600 μW, which was measured behind the laser scanning module.

Phytochrome samples for FLN and measurement conditions
For the low temperature FLN measurements, the same buffer solutions as for LT-SMS were used for the agrobacterial phytochrome and variants. For the phytochromes and variants from *Rhodopseudomonas palustris* and *Deinococcus radiodurans* a Tris-buffer (30 mM Tris, pH 8.0) was used. A content of 60% glycerol (w/w) was chosen to allow for glass-formation at low temperature conditions. In the case of deuterated samples, the buffer was exchanged to D_2O-based buffer solutions. This was done by centrifuging the sample in a $>$ 30 kDa microfilter at a speed of 9000 rpm for 15 minutes. The concentrated protein then was diluted in a D_2O-based buffer. This procedure was repeated three times. Then deuterated glycerol was added to a concentration of 60% (w/w). An UV/Vis spectrum was measured for all samples used for FLN measurements. The extinction at 280 nm is indicative for the sample concentration and is listed together with the absorption maxima and the experimental parameters used for FLN measurements comprising the excitation wavelength and acquisition times in Tab. 3.1. By the chosen glycerol content, the glass forming solution remained transparent upon freezing. An exchange chamber allowed for sample exchange at low temperatures. In addition to each FLN spectrum a spectrum of the laser line was taken with short accumulation time, to prevent saturation of the CCD. The laser spectrum was used to transform the wavelength scale into the relative wavenumber scale with respect to the laser wavelength. For all FLN measurements the excitation power was measured in front of the cryostat.

Phytochrome sample	solvent	λ_{abs}	λ_{exc}	P_L	t_{acq}	$E_{280}/E_{\lambda_{max}}$
Agp1-PCD-BV	H_2O	702 nm	714 nm	200 μW	100 s	1.9/2.2
Agp1-PCD-Y166H-BV	H_2O	703 nm	718 nm	100 μW	379 s	1.9/2.2
Agp1-PCD-BV15Za	H_2O	714 nm	726 nm	100 μW	32 s	>3/>3
RpBphP2-BV	H_2O	710 nm	720 nm	100 μW	240 s	0.3 /0.6
RpBphP3-BV	H_2O	704 nm	708 nm	100 μW	30 s	1.3/0.6
RpBphP3-CBD-BV	H_2O	703 nm	711 nm	100 μW	30 s	2.3/1.1
RpBphP3-D216A-BV	H_2O	704 nm	710 nm	100 μW	180 s	1.0/0.7
RpBphP2-BV	D_2O	709 nm	720 nm	100 μW	100 s	0.5/1.1
RpBphP3-BV	D_2O	704 nm	712 nm	100 μW	85 s	1.0/0.3
RpBphP3-CBD-BV	D_2O	703 nm	710 nm	100 μW	96 s	>3/2.2
RpBphP3-D216A-BV	D_2O	703 nm	712 nm	100 μW	28 s	1.3/0.8
DrBphP-BV	H_2O	703 nm	715 nm	100 μW	120 s	1.9/1.9
DrBphP-CBD-Y307S-BV	H_2O	702 nm	718 nm	100 μW	46 s	1.2/1.5

Table 3.1: Absorption maxima of the phytochrome variants as measured by UV/Vis spectroscopy and measurement parameters used for FLN spectroscopy.

PSI samples and measurement conditions

Identical sample preparation was chosen for all PSI from different species (unless explicitly indicated, e.g. PSI samples coupled to nanostructures). In a first step purified PSI trimers were diluted in a pH 7.5 Tricine buffer solution, containing 20 μmM Tricine, 25 mM $MgCl_2$, and 0.4 mM (0.02 % w/v) detergent (β-DM), to reach a concentration of about 20 μM Chla. This amount of detergent is adequate for the critical solubilization concentration for a PSI trimer concentration of 0.5 μM, avoiding PSI aggregation [100]. For pre-reduction of P700, a final concentration of 5 mM Na-ascorbate was added. In further steps, this PSI containing solution was diluted to a PSI trimer concentration of 3 pM. Sample preparation and mounting were accomplished under indirect daylight. The PSI samples were rapidly frozen by putting the sample directly into the pre-cooled (T = 4.2 K) cryostat.

PSI in D_2O or $H_2{}^{18}O$

Purified PSI trimers were at first diluted either in a D_2O-based or $H_2{}^{18}O$-based Tricine buffer, containing 20 μmM Tricine, 25 mM $MgCl_2$, and 0.4 mM (0.02 % w/v) detergent (β-DM), to a PSI trimer concentration of 3 pM. In the case of H/D exchange, pD was equilibrated with deuterated NaOD and DCl to a value

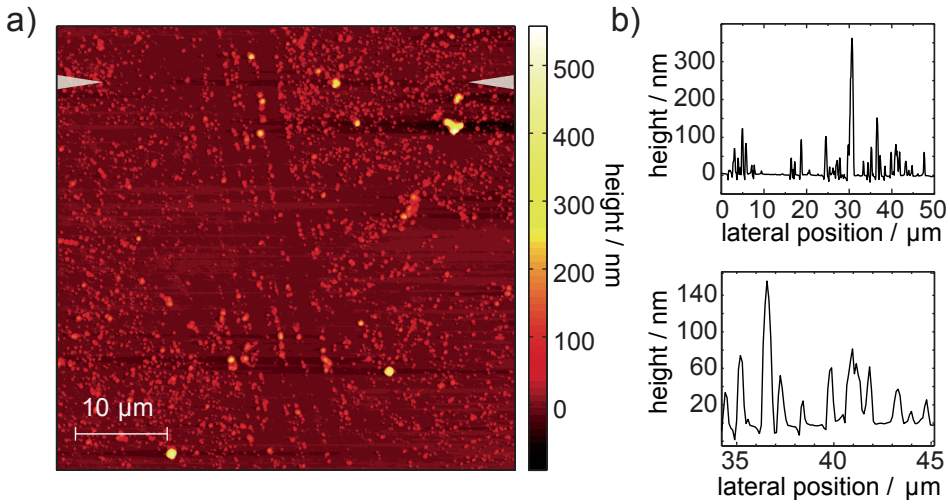

Figure 3.8: 50x 50 μm AFM scan of the silver island film obtained in tapping mode (AFM: XE-150, Park Systems, Suwon, South Korea). b) Cross section taken along the horizontal line indicated by gray arrow heads in the scan image on the left.

of 7.66 and in the case of $H_2{}^{18}O$-based buffer the pH was 7.5. Before freezing, the samples were stored for at least 3 h at ambient temperatures to allow for isotope exchange. For pre-reduction of P700, a final concentration of 5 mM Na-ascorbate was added. In further steps, the PSI containing solution was diluted with the respective buffer to a PSI trimer concentration of 3 pM.

Preparation of the silverisland film (SIF)
The preparation of the SIF consists of reducing silver nitrate with D-glucose under controlled conditions, following the description in Ref.: [101].

Suprasil cover slips used as SiF coating substrate were first cleaned by soaking them in a 10:1 (v/v) mixture of H_2SO_4 (95-98%) and H_2O_2 (30%) (piranha solution) and stored in MilliQ deionized water. About 1.5 ml of 5% NaOH solution was added to a stirring aqueous silver nitrate solution (0.375 g in 45 ml of water) in a glass beaker. Subsequently, the resulting dark-brown precipitate was redissolved by slowly adding 1 ml of NH_4OH. The solution was cooled to 5°C in an ice bath and a fresh solution of D-glucose (0.540 g in 11 ml of water) was added. Then six pairs of sandwiched suprasil coverslips were placed into this solution. The mixture was stirred for 2 min in an ice bath and then allowed to warm to 30°C for the next 5 min. As the color of the mixture turned from yellow-greenish to yellow-brown, the color of the slides became greenish. The slides were removed from the beaker and rinsed with Milli-Q water. To remove excess and nonadhesive silver particles on the suprasil surface, mild sonication was applied for 1 min. The SiF slides were stored in Milli-Q water until

they were used. The resulting SIF-coated suprasil coverslips were examined using atomic force microscopy in tapping mode (AFM:XE-150, Park Systems). AFM characterization of the SIF shows size distributions of silverislands ranging from 200 – 400 nm in width and 20 – 550 nm in height (see Figure 3.8).

PSI-SIF samples
The PSI-SIF sample was prepared by placing 1 μl of the diluted 30 pM PSI from *T. elongatus* sample (see PSI samples) between an untreated and one SIF-coated coverslip, such that the SIF coated side is in contact with the sample solution. The SIF-coated coverslip was placed on the back side of the sample with respect to the incident beam.

PSI-AuNP samples
To couple PSI to gold nanoparticles (PSI-AuNP) an excess of colloidal gold nanospheres of approximately 100 nm diameter [2] was added to pre-diluted PSI from *T. elongatus* such that final PSI concentration was 3 pM and ratio of AuNP: PSI was ca. 12:1.

[2] According to the product analysis report of BBInternational provided for the 100 nm AuNP spheres, the size distribution was: mean diameter: 97.1 nm; Coefficient of Variation $< 8\%$.

Protein sample	**Cooperation partner**
Phytochrome	
Phytochrome from *Agrobacterium tumefaciens*	
Agp1–BV	T. Lamparter, U Karlsruhe
Agp1-PCD-BV	T. Lamparter, U Karlsruhe
Agp1-PCD-BV15Za	T. Lamparter, U Karlsruhe
Agp1-PCD-Y166H-BV	T. Lamparter, U Karlsruhe
Phytochrome from *Rhodopseudomonas palustris*	
*Rp*BphP2-BV	A. Verméglio, IRD Montpellier
*Rp*BphP3-BV	K. Moffat, U Chicago
*Rp*BphP3-PCD-BV	K. Moffat, U Chicago
*Rp*BphP3-PCD-D216A-BV	K. Moffat,, U Chicago
Phytochrome from *Deinococcus radiodurans*	
*Dr*BphP-BV	K. T. Forest, U Wisconsin-Madison
*Dr*BphP-CBD-Y307S-BV	K. T. Forest, U Wisconsin-Madison
Photosystem I	
PSI from *T. elongatus*	E. Schlodder, TU Berlin
PSI from *Synechocystis* PCC6803	B. A. Diner, Wilmington
PSI from *Synechococcus* PCC7002	J. H. Golbeck, U Pennsylvania state

Table 3.2: List of the protein samples analyzed in this thesis, together with the names of the cooperation partners who kindly provided the proteins.

Chemicals	**used for/as**
Ammonium hydroxide	SIF preparation
β-DM (n-dodecyl-β-D-maltoside)	buffer solution
D_2O (deuterated water)	solvent
DCl (deuterochloric acid	buffer solution
Diethyl ether	cleaning
EDTA (Ethylene diamine tetra acetic acid)	buffer solution
Ethanol	cleaning
FluoroSpheres® Beads 715/755	alignment
Glucose	SIF preparation
Glycerol	cryoprotectant
Glycer(ol-d3) $(DOH_2)_2CHOD$	cryo-protectant
Gold nanospheres (d = 100 nm)	plasmonic interaction
H_2O (Milli-Q grade)	solvent/cleaning
H_2O^{18} (heavy-oxygen water)	solvent
Magnesium chloride	buffer solution
NaOH/NaOD	buffer solution
Piranha solution (10:1 H_2SO_4:H_2O_2)	cleaning
Silver nitrate	SIF preparation
Sodium ascorbate	buffer solution
Tricine N-(Tri(hydroxymethyl)methyl)glycine	buffer solution
Tris (Tris(hydroxymethyl)-aminomethan)	buffer solution

Table 3.3: List of the chemicals used. The chemicals were purchased from Sigma-Aldrich with the highest purity grade available, only the FluoroSpheres ® Beads were purchased from Invitrogen and the gold nanospheres from BBInternational. Besides the buffer solutions for the different phytochromes and PSI samples, co-solvents were used. SIF were prepared, following the procedure described in Ref.: [101]. The coverslips were either unused or cleaned three times for at least half an hour in 'Piranha solution' and polished with a ($\sim$80%/$\sim$20%) ethanol/ether solution before adding the sample.

4

SINGLE-MOLECULE AND FLUORESCENCE LINE NARROWING SPECTROSCOPY ON PHYTOCHROME

The following section contains an introduction to the current knowledge on the photoreceptor protein phytochrome concerning its function, molecular structure as well as the spectroscopic characteristics. Additionally, putative applications of phytochromes are considered. In the last part of this section, open questions on phytochrome function and characteristics are presented. Different experimental approaches are discussed with respect to their suitability to gain further insights.

4.1 The Photoreceptor Phytochrome

A light-sensitive molecular switch

Phytochromes are photosensory proteins controlling various aspects of growth and development of plants, fungi and bacteria in dependence of the light condition. For plants phytochrome are involved in the regulation of germination, seedling de-etiolation (see Figure 4.1) and induction of flowering. Plant phytochromes were already discovered in the mid-20th century in the course of agricultural research. Butler et al. [102] discovered a reversibly acting pigment and already described an assay for its purification and spectral analysis. Since then phytochromes were continuously studied due to their relevant influences in plant development and morphogenesis. Thus, phytochromes are one of the most intensely studied photoreceptor families. Five different phytochrome types were discovered in plants which were denoted PhyA–E. Shortly after publication of the genomes of different bacteria, various phytochrome-

like proteins were discovered, in certain cases with so far unknown function. After the identification of characteristic amino acid sequences of high homology to those of the known plant phytochromes, bacterio-phytochromes were expressed and purified [91, 103–105].

Figure 4.1: The growth of *Arabidopsis* seedlings differs when they lack phytochromes. The wild type (WT) is compared to several mutants lacking one or more of the different phytochromes Phy A–E . The seedlings lacking specific phytochrome types show the typical growth characteristics of plants grown in the dark, characterized by long, weak stems and smaller, sparser leaves. Etiolation is a mechanism for shade avoidance. In the case of low-light conditions due to competing plants, the increased growth of seedlings increases the likelihood for reaching heights with direct sunlight irradiation. The figure was taken with modifications from [106].

Phytochromes are single pigment binding proteins. They covalently bind a linear open-chain tetrapyrrole pigment from the bilin family. In comparison to pigments with closed ring structures such as porphyrins, these pigments are rather flexible and can adopt various conformations. For example, in solution they occupy a nearly cyclic conformation with the first and last ring in close contact (Figure 4.2a), while in the phytochrome chromophore binding pocket they adopt elongated forms (Figure 4.2b). The protein backbone is involved in the stabilization of two isomeric forms of the chromophore, the P_r form absorbing in the red and the P_{fr} form absorbing in the far-red spectral range (Figure 4.2 c). Beside the phytochrome spectra taken before and after irradiation with red light, a spectrum of biliverdin (BV) in water is given in Figure 4.2c. Binding of BV to the phytochrome apo-protein leads to a strong increase in the absorption cross section in the red spectral region.

The interconversion between the isomeric forms P_r and P_{fr} is reversible and triggered by red and far-red light, respectively. In most phytochromes the P_r state is the ground state and the P_{fr} form is the metastable excited state. Only a few bacterio-phytochromes, called bathy-phytochromes, have a reverse pho-

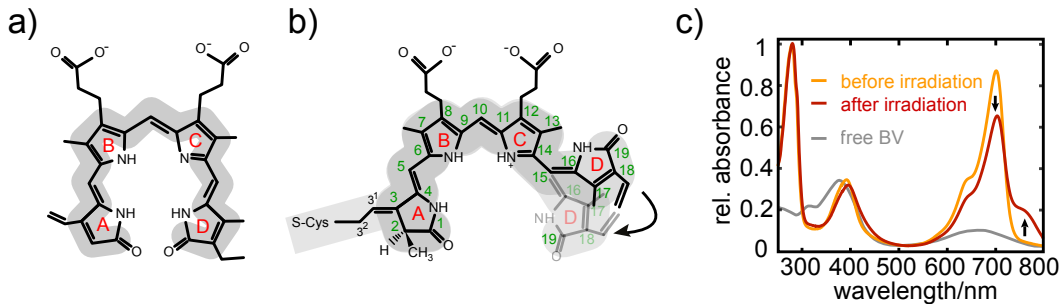

Figure 4.2: Biliverdin (BV) in solution and as cofactor of bacterio-phytochromes. a) Structure of the BV in solution, as presented in Ref.:[107]. The nomenclature of the pyrrole rings, which are denoted A to D is given in red. The gray band visualizes the spread of the π-conjugated system. b) Structure of the phytochrome-bound BV in the stable P_r and metastable P_{fr} form. The putative isomerization along the C_{15} $=C_{16}$ double bond causing a rotation of pyrrole ring D is visualized. The numbering of the C atoms [108] is shown in green. The double bond between C_3 and $C_3{}^1$ as in Ref.:[107] possibly leads to an extended π-conjugation system in the direction of the covalent cysteine binding site as indicated by the gray rectangle. c) Absorption spectra of BV in solution (free BV) from Ref.:[92] and of Agp1 phytochrome in its P_r ground state, and after illumination with red light of λ_{exc} = 705 $\pm$ 5 nm. The resulting spectrum indicates a mixture of P_r and P_{fr} with decreased absorption at 701 nm and increased absorption at 755 nm.

tochemistry with the red-shifted state P_{fr} state as their ground state. Bathy-phytochromes for example are Agp2, a phytochrome from *Agrobacterium tumefaciens* [91], *Rp*BphP1 and *Rp*BphP5 from *Rhodopseudomonas palustris*,[109] and *Pa*BphP from *Pseudomonas aeruginosa* [110]. For all phytochromes rapid conformational changes of the pigment are induced by the absorption of a photon within picoseconds and are followed by a signal cascade with time constants of micro- to milliseconds [41]. The isomerization of the chromophore results in conformational changes in its direct surrounding but most probably also leads to conformational changes in remote protein parts [111], affecting the tertiary and quaternary structure of the protein. At typical concentrations within the cell, phytochrome molecules form dimers [112]. The dimerization interfaces subsequently change due to the large conformational changes of the protein after light-activation [112]. In plants, photo-activation can lead to a translocation of phytochromes within the cell [113]. While in the dark state phytochromes are located in the cytosol they move into the cell nucleus after light activation. This process occurs within minutes [113, 114]. Inside the nucleus, the activated phytochrome initializes a cascade of changes in gene expression [113]. Bacterio-phytochromes are light-regulated kinases that transphosphorylate enzymes, so-called Phytochrome Interacting Factors (PIFs) [115]. Whether the kinase activity

of phytochromes is needed for their biological function in plants is unclear yet [116]. The reversible phytochrome photoreaction after activation with red and far-red light respectively was mainly studied by spectroscopic methods. The states of the photoreceptor that can be discerned spectroscopically are summarized in an interaction scheme referred to as the photocycle of phytochromes.

The phytochrome photocycle

The phytochrome photocycle summarizes the photo-induced changes observed by various spectroscopic techniques after activation with red and far-red light, respectively (see Fig. 4.3). After excitation of the ground state by light, relaxation processes take place which can be blocked by lowering temperature. A number of different intermediates in the course of the forward and backward reaction $P_r \rightleftarrows P_{fr}$ were trapped in this way and spectrally analyzed [117] for example by UV/Vis optical spectroscopy, flash photolysis, CD-, Pre-Resonance Raman- (Pre-RR-) and Fourier transform infrared (FTIR) spectroscopy [41]. As the photoinduced dynamics in phytochromes happen on various timescales covering 12 orders of magnitude spreading from sub-picoseconds to seconds, various time-resolved spectroscopic methods are needed to follow the respective state transitions [118]. From FTIR and RR spectroscopic investigations into the photodynamics it was inferred that the first light-induced step in most phytochromes involves a conformational change of the tetrapyrrole, more specifically a rotation of the pyrrole ring D around the connecting C_{15}=C_{16} double bond [4, 119, 120]. Within picoseconds a short-lived photoproduct is created which decays within typically 20 – 100 ps to the Lumi-R (Lumi-F) state, which decays non-radiatively via the metastable intermediates Meta-R_A and Meta-R_C (Meta-F) to the final state P_{fr} (P_r). The tetrapyrrole chromophore in the P_r ground- and metastable P_{fr}-state was found to be fully protonated, while during the photoreaction a de- and re-protonation step was discovered [121, 122]. Interestingly, the photodynamics are similar between the phytochromes from different species, even though the chromophores, chromophore attachment sites and protein backbones show differences. The characteristic time constants for the state transitions at room temperature are indicated in Fig. 4.3 as well as the temperatures required to trap the following intermediate state. In contrast to the photoisomerization found for most phytochromes, recent NMR structural analysis on a cyanobacterial phytochrome fragment revealed a C_4=C_5 bond rotation as the first photo-induced conformational change [123], which seems to be specific for this cyanobacterial phytochrome [124].

Potential applications of phytochromes

Phytochromes are attracting an increasing amount of attention as targets for protein engineering due to their potential use as gene photoswitches, as fluorescent reporters, and in agricultural biotechnology [125–128]. Biologically

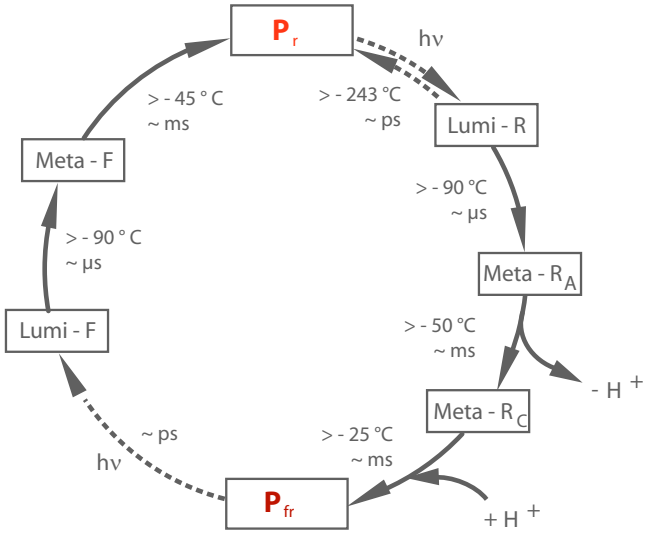

Figure 4.3: The phytochrome photocycle. After photoactivation, phytochrome undergoes conformational changes, which can be followed by spectroscopic techniques. Different intermediates in the course of the forward and backward reaction $P_r \rightleftarrows P_{fr}$ were identified. Thermal transitions can be blocked by using low temperature conditions. The required temperatures to block the transition to the subsequent intermediate states as well as the typical time constants of the respective transitions at room temperature are indicated and taken from Refs.: [6, 117, 119].

compatible fluorescent protein probes, particularly the self-assembling green fluorescent protein (GFP) from the jellyfish *Aequorea victoria*, have revolutionized research in cell, molecular and developmental biology because they allow visualization of biochemical events in living cells. A drawback of GFP is its absorption and emission characteristic in the green spectral range, which overlaps with high absorption cross sections of organic tissues. Therefore, GFP-based imaging is prohibited in intact animals. A spectral window of low tissue absorbance is found in the red to infra-red wavelength region. Therefore, the red-absorbing phytochromes are excellent candidates for increasing the range of imaging applications towards deeper-lying organic materials. For this purpose, however, the fluorescence quantum yield of the natural phytochrome complex needs to be artificially increased. Different strategies including insertion of fluorescent dyes [129] or especially synthesized pigments into the phytochrome apo-protein [130], or modifications of the chromophore binding pocket [122, 125, 127] were already addressed and show high potentials. Shu et al. [127] have shown a genetically modified variant of the *Deinococcus radiodurans* phytochrome that can be used for imaging purposes in mammals.

An advantage of bacterio-phytochrome-based implementations is the natural abundance of the BV chromophore in all aerobic organisms, including animals. Nevertheless, in this work additional BV was needed for obtaining a sufficient signal-to-noise ratio, since the fluorescence quantum yield of the engineered phytochrome variant does not exceed $\Phi_{FL} = 0.07$ [127]. Recent advances in the understanding of competing deactivation processes [122], however, opened the road for further fluorescence quantum yield engineering protocols. Another proposed application of phytochromes relies on the PIF interaction which can be used to reversibly translocate proteins to the plasma membrane in a light-controlled fashion [131]. In the following paragraph, the current state of knowledge on the molecular structure of phytochromes is presented.

Molecular structure of phytochromes
In Figure 4.4 the domain structure of different phytochromes is illustrated. The N-terminal part contains the photosensory module while the C-terminal part is the output- or regulatory part of the phytochrome photoreceptor. The N-terminal photosensory core domain (PCD) of phytochromes from different species is of high sequence homology and contains three different protein domains, a PAS (Per/Arnd/Sim) [95] domain, a GAF (cGMP phosphodiesterase/adenyl cyclase/FhlA) [95] domain forming most of the bilin-binding pocket, and a PHY domain which is needed to stabilize the P_{fr} form of most phytochromes. Depending on the organism, the chromophore binding cystein is located in the PAS or in the GAF domain as indicated in Figure 4.4. An output (or effector) module that transduces the light signal to appropriate sensory responses is C-terminal to the PCD. That part of the phytochrome protein is more diverse than the PCD. The domain composition is depending on the host organism. While bacterio-phytochromes have a histidine kinase domain (HKD), in all five classes of plant phytochromes the output module contains a histidine kinase-related domain (HKRD) and two additional PAS domains between the photosensory core domain (PCD) and the HKRD, while in fungi a response regulator (R) domain is an additional part of the full length phytochrome protein [41]. While phytochromes from bacteria bind biliverdin (BV) [132], which is synthesized by oxidative cleavage of heme, phytochromes from plants and cyanobacteria bind phytochromobilin (PΦB) [133] and phycocyanobilin (PCB) [134], respectively, which are generated from BV by enzymatic reduction [41].

For the full length protein only lower resolution structures are available as obtained by small angle X-ray scattering (SAXS) [135] and recently by cryo-electron microscopy [136]. The first high-resolution X-ray structure was resolved in 2005, on a protein-fraction of *Dr*BphP containing the chromophore binding domain (CBD), which comprises the PAS-GAF domains but lacks the PHY domain (*Dr*BphP-CBD-BV), with a resolution of 2.5 Å [95]. Later on, ad-

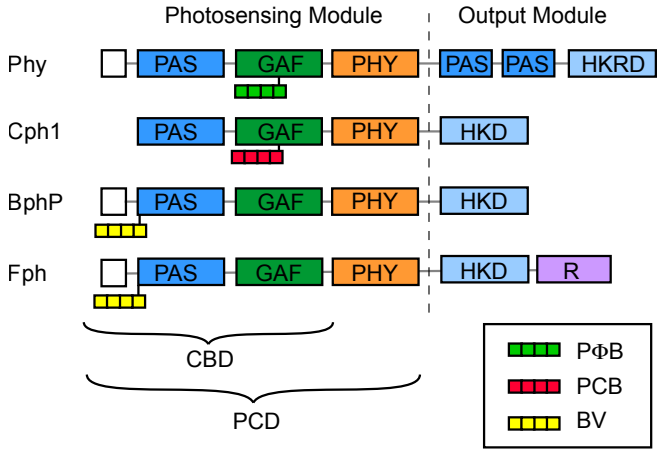

Figure 4.4: Domain architecture of phytochromes from different organisms including plant phytochromes (Phy), a cyanobacterial phytochrome (Cph1), bacterio-phytochromes (BphP) and fungal phytochromes (Fph). The N-terminal part of the photoreceptor protein is the photosensory part of the protein. The chromophore binding module (CBM) and the photosensory core domain (PCD) are differentiated. The different linear tetrapyrroles used as photoactive pigment in plant-, cyanobacterial- and bacterio-phytochromes are given in the legend and their respective binding positions are indicated in the domain structure. The C-terminal part of phytochromes is the output module which is highly diverse between the phytochromes from different organisms; comprising two PAS domains in the case of Phys, histidine kinase (related) domains (HK(R)D), as well as a response regulator domain (R) in the case of Fphs [41].

ditional high-resolution X-ray structures became available. Improved crystallization of the point-mutated variant *Dr*BphP-CBD-Y307S-BV with a mutation at the crystal contact yielded resolution-enhanced structures with resolutions of 2.15 Å and 1.45 Å [107]. A 2.2 Å resolution crystal structure of the *Rp*BphP3-CBD-BV [94], which is a member of another group of unusual phytochromes having a regular UV/Vis absorption spectrum in the P_r state, but producing a blue-shifted P_{nr} ('near-red absorbing') state after photoactivation with red light was resolved [93, 94]. The first structure published for a complete PCD was obtained on Cph1-PCD-PCB [137] with a resolution of 2.21 Å. Shortly afterwards, a 2.85 Å resolution crystal structure of the entire PCD of the bathy-phytochrome from *Pa*BphP-PCD-BV *Pseudomonas aeruginosa* in its P_{fr} ground state was published [111] (see Figure 4.5a). A variant with the point mutation Q188L, suited to reveal P_r to P_{fr} conformational changes, was resolved by the same authors [111]. By implementing a sterically locked chromophore (see Figure 4.7) structural information with 3.1 to 3.4 Å resolution were obtained for the PCD of Agp1 [138]. While the PCD of has full photo-activity compared to the full-length protein for most phytochromes, the CBD has restricted photo-activity because stabilization

of the P_{fr} state requires the PHY domain. An exception is the phytochrome-like protein SyB-Cph1 from *Synechococcus* OSB where the GAF domain alone shows full $P_r \rightleftarrows P_{fr}$ photoconversion [123]. This fragment was structurally solved by NMR [123].

The particularities of the molecular structure of phytochromes are discussed in the following. The secondary structure of phytochromes contains an unusual knot Fig. 4.5b) [95] discussed as a putative protein structure stabilizing feature [139]. The structural models reveal that phytochromes enclose bulk water around their linear tetrapyrrole chromophore, forming a so-called pyrrol-water network via hydrogen bridges (see Fig. 4.5c). The structure of the photoactive pigment is resolved in the high-resolution structures and provides insights into the chromophore isomerization process. The crystal structure of *Dr*BphP with highest resolution shows a P_r state conformation of the linear tetrapyrrole chromophore BV. In the crystallized conformation the open-chain linear tetrapyrrole chromophore has an elongated conformation (see Figure 4.5c). The rings B and C are coplanar while ring A and ring D are tilted by $\sim 15^\circ$ and 44° with respect to the plane formed by ring B and C [107]. It is common to describe the geometry of linear tetrapyrroles by the stereo descriptors indicating the relative positioning of chemical groups with respect to a plane passing through double bonds. The stereo descriptors are Z (”zusammen”, *engl.*:together) indicating a positioning of the groups on the same side of the plane and E (”entgegen”, *engl.*: opposite) referring to a positioning on opposite sides. For the methine bridges a similar description with s/a denoting syn/anti is used [140]. Using these descriptors the crystal structure of *Dr*BphP in the P_r form shows the BV chromophore in ZZZssa geometry [95]. Electron density calculations based on the high-resolution structure at 1.45 Å resolution suggest furthermore that the π-conjugation system of BV extends to the cysteine binding site (see Figure 4.2) and gets similarly extended as in the PΦB and PCB chromophores of plant and cyanobacterial phytochromes [107]. Thereby, a reason for the similar optical properties of plant, cyanobacterial and bacterio-phytochromes was identified. The P_{fr} state as resolved in the crystal structure of *Pa*BphP shows a ZZEssa configuration [111]. These findings corroborate the results from vibrational spectroscopic analysis which indicate a Z/E isomerization at the C_{15}=C_{16} double bond as being part of the conformational change during the P_r to P_{fr} photo-reaction.

The crystal structures of the phytochrome fragments containing the full PCD, Cph1-PCD-PCB and *Pa*BphP-PCD-BV show an extended helix bundle connecting the chromophore binding site with the distant PHY domain. This structural feature might be relevant for signal transduction to remote parts of the protein [141].

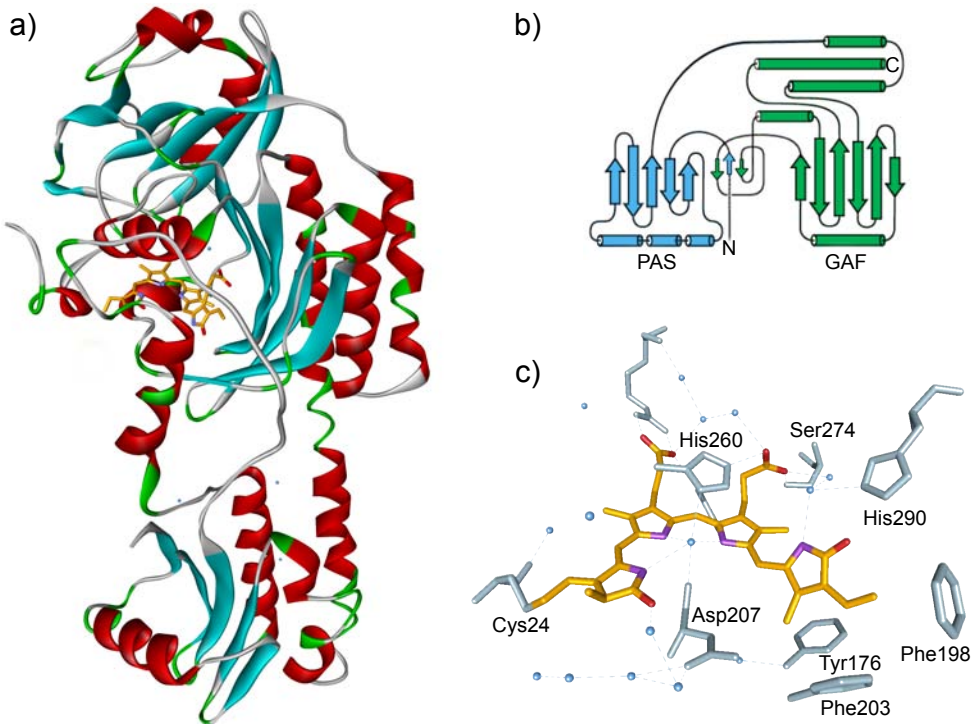

Figure 4.5: The molecular structure of phytochromes. a) Structure of *Pa*BphP-PCD-BV with the pigment in its unusual P_{fr} ground state at a resolution of 2.9 Å (PDB entry: 3C2W) [111]. Color indicates secondary structure, and the colors of the BV constituting atoms are: orange (carbons), violet (nitrogens) and red (oxygens). The oxygens from internal water molecules are shown in blue. b) Scheme of the knot ubiquitous in phytochromes and first discovered in the structure of *Dr*BphP [95]. c) Zoom into the binding pocket of *Dr*BphP-CBM-BV at a resolution of 1.45 Å (PDB entry: 2O9C) in the P_r form [107]. BV coloring as in a). Selected conserved amino acids (gray) and internal water molecules (blue) are shown. Structure visualization was performed with Discovery Studio Visualizer [12].

Structure analysis vs. optical spectroscopy

From the discovery of the red/far-red light photoreceptor phytochrome by Butler et al. in the early 1950s until today, a detailed molecular view has been obtained of the phytochrome photoreceptor. Until 2005 the molecular information on phytochromes were mainly gained by the use of spectroscopic techniques. With the spectral absorption of phytochromes in the red to far-red wavelength range most optical spectroscopy methods can be used. Advantages of the spectroscopic methods in contrast to the structure analysis methods include their applicability to the natural phytochrome system. In contrast, crystallization of the phytochrome molecules was so far only successful on phytochrome fragments possessing modifications in the amino acid sequence or in the chromophore

[10, 94, 95, 107]. Crystallization of phytochromes often modifies the conformational dynamics of the natural protein due to the dense packing. The remaining dynamics are related to losses in scattering properties or crystal stability. Instead, time-resolved spectroscopic methods can be used to follow the conformational dynamics which are crucial to conceive the molecular phytochrome function.

Spectroscopic approaches using phytochrome variants
By comparison of spectroscopic information from the natural phytochrome system and specifically modified phytochromes, the functional influence of specific phytochrome parts or phytochrome surroundings on the photophysical and photochemical processes can be analyzed [122, 125, 142–148].

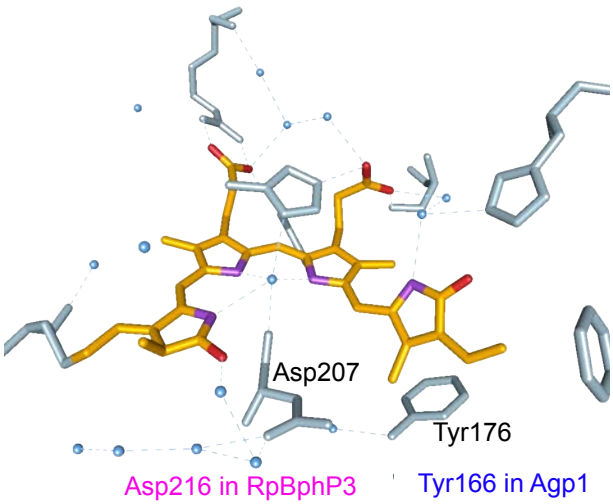

Figure 4.6: Locations of the amino acid residues aspartate and tyrosine inside the chromophore binding pocket of *Dr*BphP. A zoom into the binding pocket is given showing BV in the P_r form at a resolution of 1.45 Å (PDB entry: 2O9C) [107]. In this work, the point mutants *Rp*BphP3-PCD-D216A-BV with an aspartate-to-alanine mutation and Agp1-PCD-Y166H-BV with a thyrosine-to-histidine mutation are studied by fluorescence line-narrowing spectroscopy. Coloring as in Figure 4.5. Structure visualization was performed with Discovery Studio Visualizer[12].

This strategy of parameter variation within the sample can be applied for phytochromes in a particularly diverse way. Firstly, biochemical methods have rapidly evolved providing protein engineering techniques allowing targeted point mutations in phytochromes (see Figure 4.6). In combination with spectroscopic investigation site-specific mutants already allowed the identification of the function of specific amino acid residues within the chromophore binding pocket [122, 143, 145]. Secondly, advances in pigment synthesis made modi-

fied tetrapyrroles with reduced conformational flexibility available, which bind to the apo-protein [92]. In Figure 4.7 a structure of one of these synthesized pigments is presented. These can be used to identify the natural pigment conformations by spectroscopic techniques [118].

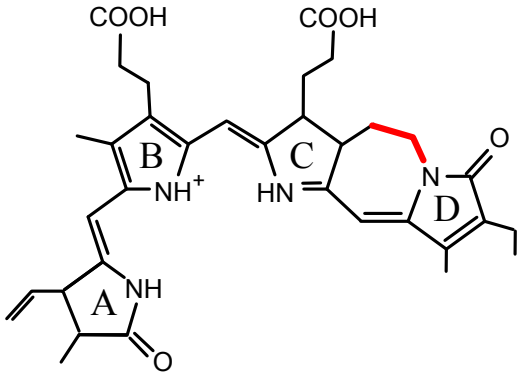

Figure 4.7: The biliverdin derivative BV15Za is a synthetic sterically locked chromophore [92]. Ring C and D are fixed by an additional carbon chain (red). Thereby, a P_r-like conformation is stabilized [41]. The chromophore BV15Za is used in the present work as bound to the PCD fragment of agrobacterial phytochrome Agp1-PCB-BV15Za.

Furthermore, isotopically labelled pigments are available and can be used to study local flexibilities of the chromophore [124, 149]. A simpler approach with respect to sample preparation but with high potential to identify photophysical and photochemical mechanisms including intramolecular dynamics are solvent exchange experiments [142].

Intrinsic heterogeneity of phytochromes

Interestingly, the spectroscopic observations of phytochromes are marked by a high degree of variance [5]. The P_r excited state exhibits multiexponential fluorescence decay dynamics with at least two lifetime components [150], thereby implying the presence of at least two forms of the excited state. The model of heterogenous phytochrome states has been corroborated by results from ultrafast transient absorption measurements on plant phytochrome phyA [151], on cyanobacterial phytochrome Cph1 [6], and on the bacterio-phytochrome Agp1 [152], all of which exhibit two excited-state lifetimes characterized by a smaller (5 – 16 ps) and a larger (25 – 40 ps) time constant. To explain these observations excited-state as well as ground state heterogeneity are discussed [6, 153]. The phytochrome heterogeneity might be due to the high chromophore flexibility as observed for various phytochromes by NMR techniques [124, 149, 154]. Accordingly, the mobility of the chromophore seems to be different for the individual phytochrome states within the photocycle [155]. Resonance Raman

spectroscopic studies on *Dr*BphP-CBD crystals [8] suggest the coexistence of two or more PΦB conformers. The same phenomenon has been detected for the *Agrobacterium tumefaciens* phytochrome Agp1 crystals [8], plant phytochrome Phy A [156], and cyanobacterial phytochrome in solution (Cph1) [9]. Recently, combined QM/MM calculations gave additional insight into phytochrome heterogeneity by revealing the existence of two stable conformational states of the chromophore in the P_r state [157]. These studies suggest that structural heterogeneity of the tetrapyrrole chromophore is an intrinsic property of phytochromes in general. Various methods applied so far to unravel molecular structure and function of phytochromes are discussed with respect to substate sensitivity.

Advantages and limitations of analytical methods with respect to heterogeneous systems

Crystals with high scattering cross sections are needed for X-ray diffraction. This implies homogeneous ordering of structures. The crystallization process promotes the selection of one singular conformer or, if the structural variance of a heterogeneous system is only subtle, the crystal may comprise multiple conformers, but accordingly low diffraction cross sections will occur in the region of structural variance. The identification of multiple conformers becomes either challenging or even impossible by X-ray diffraction. Therefore, X-ray diffraction is not the method of choice for identification or characterization of heterogeneity. Taking into account the insights from spectroscopic and computational methods on heterogeneity of the phytochrome system, it becomes clear that the results from substate-insensitive methods, such as X-ray diffraction, must be interpreted with care.

While spectroscopic methods on phytochromes may encounter all naturally occurring phytochrome states, the signal averaging over multiple sub-conformers render the spectra complex and disentangling the underlying sub-species becomes extremely difficult or even impossible, especially when dealing with vibrational data. Therefore, ensemble spectroscopic methods are hardly suited for the discrimination between different functional substates of phytochromes.

Instead, subspecies-sensitive methods are needed to investigate the characteristics of the different contributing phytochrome states. One sub-state specific method is fluorescence line narrowing (FLN) spectroscopy. The FLN method implies that only molecules with relatively low electronic transition energies are selected. Due to this selection, however, only one substate species is accessible. Far more efficient for the analysis of heterogenous systems is the single-molecule approach. Single-molecule sensitive methods, in principle, allow for the identification of all contributing states of a heterogenous sys-

tem. Since in single-molecule spectroscopic experiments no signal averaging over molecules with different spectral characteristics takes place, the molecule- and more specifically the chromophore-specific fingerprints are directly accessible. In this work, both fluorescence emission techniques LT-SMS and FLN are applied to analyze the P_r phytochrome ground state. Besides natural phytochromes also variants with specific point mutations, protein fragments as well as with a sterically locked chromophore are analyzed to further investigate into the chromophore-specific interactions inside the protein binding pocket in phytochromes.

4.2 Dynamic Intracomplex Heterogeneity of Phytochrome

To directly investigate the presumed phytochrome heterogeneity, the single-molecule approach is chosen. Besides the direct observation of the proposed phytochrome heterogeneity of the P_r state heterogeneities for single phytochrome molecules occurring in the time domain were observed. The results indicate dynamic variability of pigment-protein interactions and are discussed with respect to the influence of the pyrrole water network, which provides a de- and reprotonation coordinate needed for phytochrome function.

This section is basically a reproduction of the work published in *Journal of the American Chemical Society* (2009), **131**(1):69-71 (see publication list on page i).

Results

Low temperature fluorescence emission spectra from 80 individual Agp1-BV phytochrome complexes from *Agrobacterium tumefaciens* in the P_r state were investigated.[1] A selection of representative spectra with an acquisition time of t_{acq} = 40 s is depicted in Figure 4.8. Beside broad fluorescence bands with linewidth of $\Gamma_{FWHM} \sim 30$ nm (~ 500 cm^{-1}; spectrum I), narrow emission lines are detected in the spectra of individual phytochromes, with linewidth of $\Gamma_{FWHM} \sim 1$ nm (~ 15 cm^{-1}; spectrum V) which is close to the spectral resolution limit of the setup used. The selection of spectra visualizes the observed continuous transition from the broad fluorescence bands to the narrow emission lines dependent on the individual molecule. Most spectra show fluorescence intensity within two broad wavelength intervals, one centered at ~ 710 nm and the second at ~ 770 nm. Interestingly, the energy difference between these two prominent bands lies within the vibrational fingerprint region of the phytochrome chromophore ($\sim 1100 - 1700$ cm^{-1}), where C=C stretching and N–H bending modes are observed in FT-IR [158] and RR [8] spectroscopy.

Beside the differences in line widths also differences occur for the exact peak positions and intensity distributions. Thus, spectrum I shows broad emission bands, spectrum II is marked by a double peak structure in both emission bands and additionally shows contributions at 730 and 750 nm. Spectrum III shows similar broad emission bands as spectrum I, but additional narrow line features (~ 5 nm) lie on top of these broad fluorescence contributions. These additional lines have very similar line widths and unequal distances between each other.

[1] For details on the sample preparation see Chapter 3, page 43.

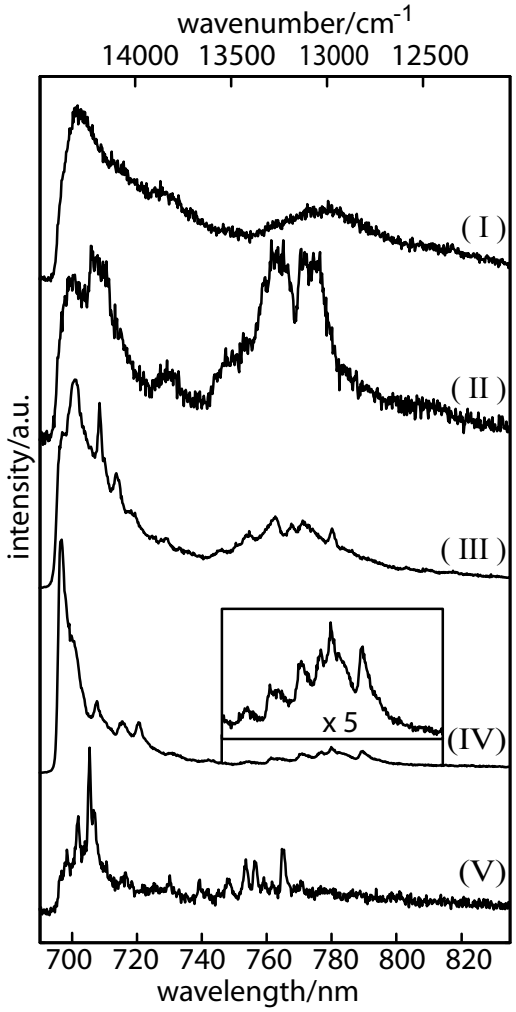

Figure 4.8: Low temperature fluorescence emission spectra of individual phytochromes (λ_{exc} = 680 nm, t_{acq} = 40 s, T = 1.4 K).

In spectrum IV the relative intensity between the broad band at 770 nm and the superimposed narrow lines is strongly shifted toward the narrow lines (see inset at IV). In spectrum V even narrower lines ($\sim$ 1 nm) are detected but with the longer wavelength spectral center shifted toward 760 nm. The partially resolved lines in the 740 to 780 nm region, with a distance of $\sim$ 1100 – 1700 cm^{-1} from the emission maxima, are similar to narrow fluorescence line structures detected from conjugated polymers [159–161, 161–165] and dendrimeric structures [166, 167] which were assigned to vibrational modes. Further heterogeneity is observed in the intensity distribution. Whereas mostly the shorter wavelength contribution clearly dominates, exceptions are observed, e.g., in spectrum II. The observation of drastically different emission spectra confirms on the single-molecule level the idea of a strong heterogeneity of phytochrome. To gain a deeper insight into the characteristics of the fluorescence fingerprints of single

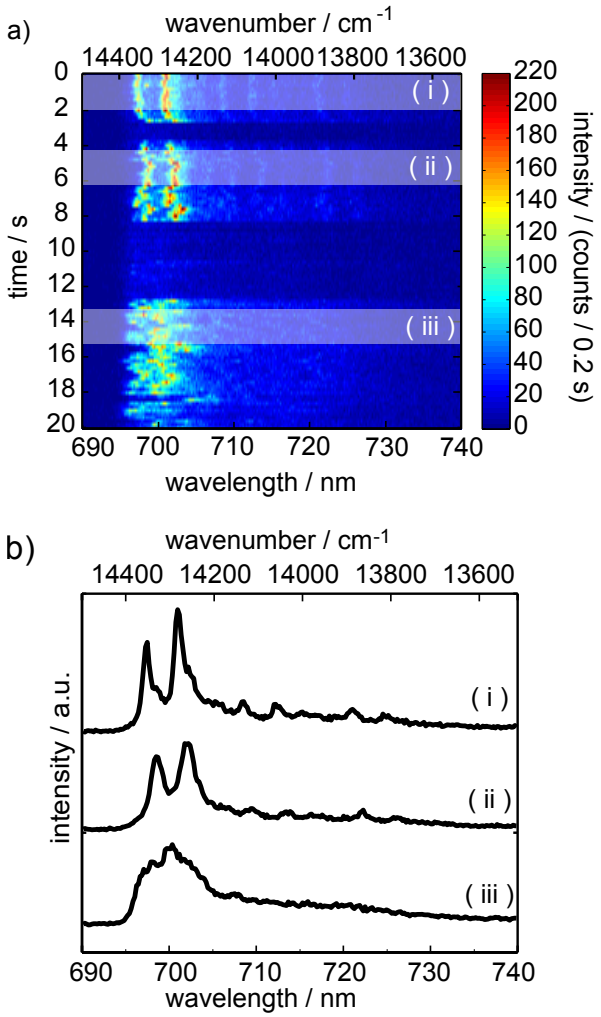

Figure 4.9: (a) 2D representation of a series of time-dependent spectra taken from one single phytochrome molecule (λ_{exc} = 680 nm, t_{acq} = 0.2 s per spectrum, T = 1.4 K). (b) Spectra obtained by averaging over the highlighted 2 s intervals in (a).

phytochrome molecules their time-dependence on the second time scale was observed.

Figure 4.9a shows a series of spectra from an individual Agp1-BV phytochrome molecule. These spectra were collected with the minimum acquisition time t_{acq} = 0.2 s providing a sufficient signal-to- noise ratio for the fluorescence detection of single Agp1-BV in our setup. The fluorescence intensity is color-coded. At the beginning of the observation the two dominant fluorescence lines show a rather stable emission wavelength. After a transition to a dark state, the fluorescence reappears. However, the emission wavelength now undergoes changes in the range of a few nanometers with a rate similar to the time resolution of the

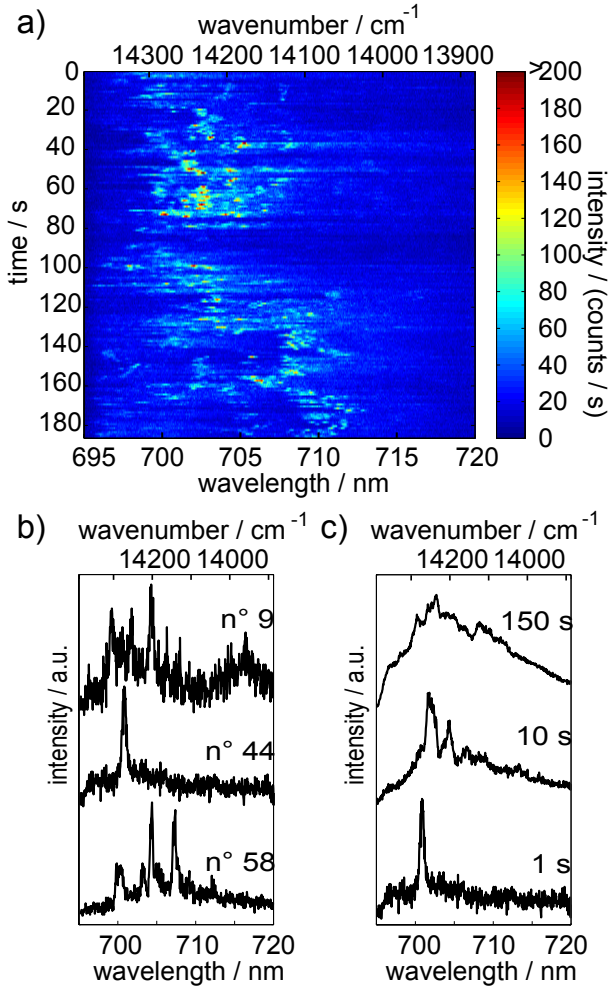

Figure 4.10: (a) 2D representation of a series of time-dependent spectra (λ_{exc} = 680 nm, t_{acq} = 1 s per spectrum, T = 1.4 K). (b) Selected 1 s spectra from the series and (c) spectra averaged over different indicated time intervals.

experiment. This jump rate on the sub-second time scale and the jump width of the order of 100 cm^{-1} are comparable to those of a dye in an amorphous polymer matrix [76]. In the third interval, again after a transition to a dark state, the spectral changes are accelerated further, such that the underlying spectral lines cannot be observed individually anymore. In Fig. 4.9b the spectra averaged over 2 s within these three different emission periods are presented. They show that an individual phytochrome molecule undergoes dynamic changes between states characterized by the different fluorescence emission properties seen in Figure 4.8, namely from type V in period (i) to type IV in period (ii) and then to the broadened type I in period (iii). Thus, fluorescence single-molecule spectroscopy not only confirms intercomplex heterogeneity but also shows a dynamic intracomplex heterogeneity of phytochromes.

Another example of strong time-dependent intracomplex heterogeneity is shown in Figure 4.10a. The sequence of spectra has a time resolution of 1 s. Instead of observing stable fluorescence fingerprints, again strong spectral dynamics occur. Selected spectra from the time-dependent series are depicted in Figure 4.10b. Here the spectral changes, often designated spectral diffusion, occur rather frequently. Therefore, intense narrow sharp lines, similar to the fluorescence signal in spectrum 44, are rarely detected. Mainly multiple lines like those in spectrum 58 are observed, where several changes of the emission wavelength occurred within the acquisition period. Broadened features like those in spectrum 9 are observed if the spectral diffusion rate is even higher. As a consequence, the observed line width increases with increasing accumulation times. This is exemplified in Figure 4.10c. Thus, the time-dependent spectrally resolved single-molecule data show spectral diffusion as the origin of line broadening and the similarity of time-averaged single-molecule spectra of type I with ensemble fluorescence spectra.

Discussion

Phytochromes are natural one-chromophore binding molecules. They are an excellent choice for the analysis of interactions between a pigment and its protein surrounding. The static single-molecule fluorescence spectra revealed different spectral types with a high diversity of emission fingerprints from the P_r state. Most striking is the variation in the observed line widths, differing by more than one order of magnitude. This observation corroborates the ensemble data from various spectroscopic techniques concerning the heterogeneity of phytochromes.

Moreover, time-resolved single-molecule spectroscopy showed that this heterogeneity is observable within one single phytochrome molecule as a time-dependent phenomenon even at very low temperatures. The dynamic changes lead to different spectral forms varying in their line widths, fluorescence peak positions, and intensity distributions. Thereby, these time-dependent measurements revealed the source of line broadening in time-averaged spectra. The characteristics of spectral diffusion are not statically associated with the individual molecules but also vary in time for each molecule.

Under the employed low temperature conditions, where conformational changes are largely frozen out, only minor conformational alterations have to be taken into account to explain the spectral dynamics. The switching of phytochromes between the different spectral forms at these extremely low temperatures requires rather low barriers between the conformational states or tunnel-

ing processes as a source of the different emission properties. The pyrrole-water network in the direct chromophore environment is a likely candidate for a structure with such shallow potential energy minima or for tunneling processes since hydrogen movement remains possible at T = 1.4 K (see Chapter 5 and Ref. [64]). Significant shifts in the emission wavelength might be induced by small-scale proton movements along the deprotonation/reprotonation coordinate followed later in the photocycle [121]. A direct comparison of the dynamic processes observed here at low temperatures on the second time scale with conformational exchange monitored on the micro- to millisecond time scale in NMR experiments [9] at ambient temperatures is impossible at present.

Broadened spectral shapes are observed in the limit of fast spectral diffusion compared to the experimental time resolution. In this case, the intrinsic line shape is no longer detectable. The occurrence of this fast spectral diffusion is a likely reason for the lack of results from site-selective ensemble techniques, e.g., spectral hole-burning and fluorescence line narrowing spectroscopy, on phytochrome.

During periods of slow spectral diffusion with respect to the time resolution of the setup, the underlying spectral information of the pigment in its natural protein environment becomes accessible. In this case highly resolved spectra with a multitude of narrow lines were detected. Their distances from the main emission are compatible with an assignment to vibrational modes. Vibrational data from an individual pigment in its natural protein environment have, to our knowledge, not been reported before.

4.3 Analysis of Highly Resolved Fluorescence Emission Spectra of Individual Phytochrome Molecules

Low-temperature fluorescence emission spectra of single phytochrome molecules in the P_r-state were presented in the preceding section of this chapter. Several of the spectra show narrow line features on top of broad fluorescence bands which are in the vibrational energy range with respect to the purely electronic transition. These lines are analyzed in more detail here. We present the design and application of a pattern recognition technique as well as the analysis of the line positions and compare them to published vibrational data.

Results

Narrow peak structures are observed either exclusively or on top of broadened spectral bands in some of the low temperature fluorescence emission spectra of individual phytochrome molecules (see Figure 4.8). The time-dependent spectral data sets reveal that the line broadening is due to spectral dynamics (see Figure 4.10) and that for some molecules intra-complex heterogeneity leads to the observation of narrow line structures in restricted time intervals only (see Figure 4.9). As the focus is put on the narrow peak contributions, for each molecule only these time intervals are taken into account which show reduced spectral diffusion dynamics, and thus, contain narrow fluorescence emission contributions. In this way, narrow line-structured spectra were obtained from 32 of the 80 overall analyzed Agp1 molecules. Interestingly, the peak positions of narrow line-structured spectra show synchronous wavelength shifts such that the respective distances between the narrow peaks are preserved during the wavelength jumps (see example in Figure 4.11a). Such spectra series can be used to generate spectra with increased signal-to-noise ratio and spectral resolution by shifting the spectra from a time-series according to best spectral overlap along the wavelength axis, as can be seen from the example given in Figure 4.11. Single spectra from a time-dependent spectral sequence can have high resolution but low signal-to-noise ratio compared to spectra taken at longer accumulation times, as can be seen for the spectra presented in Figure 4.11b taken with accumulation times of 1 s and 120 s, respectively. By shifting the single spectra such that the spectral diffusion dynamics occurring on the second time scale are removed, high-resolution and signal-to noise ratio can be obtained, as can be seen from the shown average spectrum (Figure 4.11d) as calculated over the

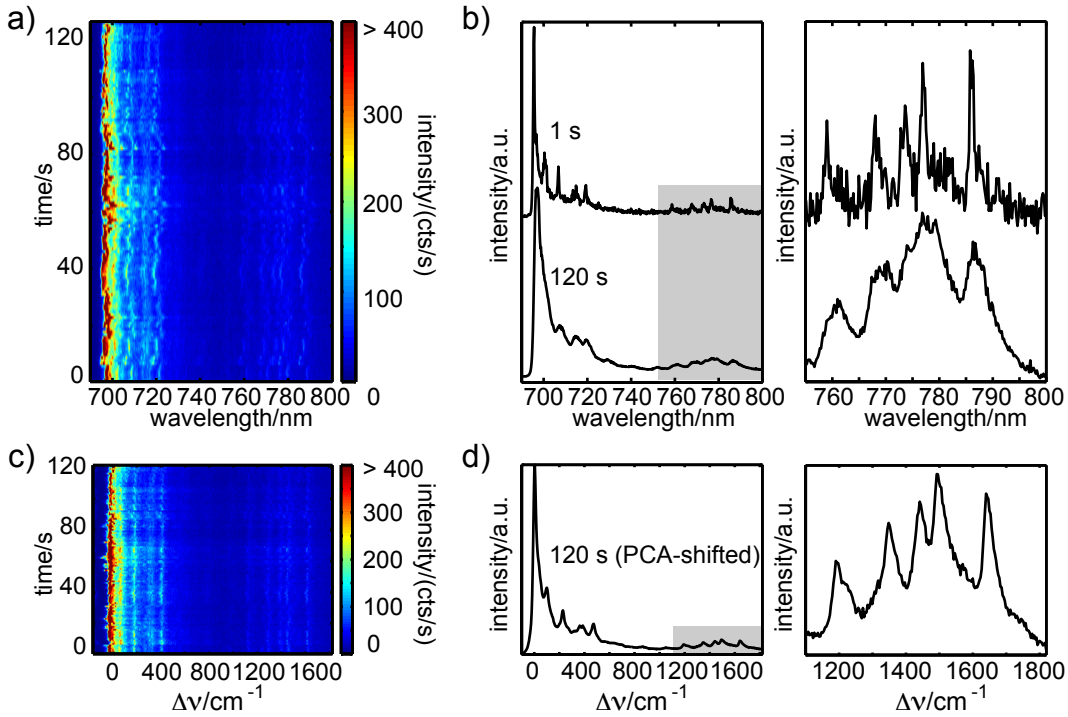

Figure 4.11: Spectral data of an individual phytochrome molecule before and after application of a PCA-based shifting algorithm. a) Time-dependent spectral series of an individual phytochrome molecule (T = 1.4 K, λ_{exc} = 680 nm, t_{acq} = 1 s per spectrum). b) Fluorescence emission spectrum with t_{acq} = 1 s as taken from the time-dependent series and a spectrum with t_{acq} = 120 s, as obtained by calculation of the average spectrum over the entire time-dependent data set displayed in a); on the right a zoom into the vibrational fingerprint region is given. The line width is broadened in the 120 s spectrum compared to the 1 s spectrum, whereas the signal-to-noise ratio is increased. c) PCA-shifted spectra series of the time series shown in a). For the PCA-shifted data a wavenumber axis normalized to the ZPL is given. d) Average spectrum as obtained by the calculation of the average spectrum over the PCA-shifted spectra series displayed in c) and a zoom into the vibrational fingerprint region. Compared to the 120 s spectrum in b) the signal-to-noise ratio and the spectral resolution is increased. (for details on the PCA-based shifting see text).

shifted time series displayed in Figure 4.11c. After shifting the spectra from the time-series along the wavelength scale the ZPL contribution on the short wavelength side of the spectrum was taken as the origin of a relative wavenumber scale. The shifting for resolution-enhancement is performed for all narrow line containing time-dependent spectra from single phytochromes by an automatic procedure, which is described in the following.

The simplest algorithm for shifting is the search of the peak maximum in a given

wavelength interval and subsequent alignment of all spectra in the way that their maxima overlay. This simple maximum search algorithm, however, has drawbacks when dealing with low signal-to-noise spectra where the maximum position of peaks can be obscured by noise. Therefore, a shifting algorithm with stronger robustness against noise was developed. The shifting algorithm relies on the standard multivariate statistical method Principal Component Analysis (PCA) [168]. A PCA algorithm implemented in MATLAB® [169] is used for the design of a shifting procedure applicable to single-molecule data. The principle of PCA is shortly presented.

The PCA method is widely used in pattern recognition and information reduction, e.g.when reducing file sizes of images. PCA implies a projection **P** of the data matrix **X** into a new vector space **Y** with orthogonal eigenvectors matching the directions of maximal variances of the data points. These new eigenvectors are called the principal components (PCs). Figure 4.12 shows a 2D example, of a data point cloud spread in a 2D coordinate system with arbitrary axis x_i and x_j which are independent with respect to the data values. The new coordinate system with orthogonal PCs oriented with respect to largest variance such that the first PC(PC_1) is oriented along the direction of largest spread of the point cloud, and the PC_2 is orthogonal to PC_1 and goes through the center position of the point cloud. In higher dimensional spaces, the following PCs all have the same constraints, being orthogonal and oriented in the direction of maximal variance and going through the center of the higher dimensional point cloud. Information reduction in the 2D example would lead to the description of the data cloud by a single linear curve along PC_1. A general projection into a new

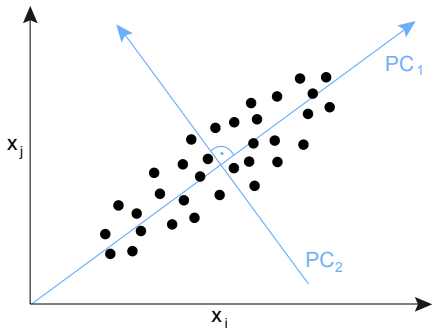

Figure 4.12: Illustration of the PCA coordinate transformation in a 2D example. The directions of extreme variances of data points define the orthogonal eigenvectors of the new vector space. The direction of maximal variance, is defined as the first principal component (PC). The second PC per definition is orthogonal to the first PC and matches the direction of the second largest variance in the case of Gaussian distributed data points.

vector space is of the form:

$$\begin{pmatrix} y_{11} & \cdots & y_{1n} \\ \vdots & \ddots & \vdots \\ y_{m1} & \cdots & y_{mn} \end{pmatrix} = \begin{pmatrix} p_{11} & \cdots & p_{1m} \\ \vdots & \ddots & \vdots \\ p_{m1} & \cdots & p_{mm} \end{pmatrix} \begin{pmatrix} x_{11} & \cdots & x_{1n} \\ \vdots & \ddots & \vdots \\ x_{m1} & \cdots & x_{mn} \end{pmatrix} \tag{4.1}$$

It can be shown that the new eigenvectors following the directions of maximal variances can be found by solving the eigenvalue problem of the covariance matrix $\mathbf{C_X}$ of the data matrix $\mathbf{X}$. The covariance matrix of a $m \times n$ data matrix $\mathbf{X}$, scaled by $\frac{1}{n-1}$ to account for the number of measurements, is given by [168]:

$$\mathbf{C_X} = \frac{1}{n-1}\mathbf{X}\mathbf{X^T}. \tag{4.2}$$

This matrix contains the variances $\sigma^2_{x_i x_i} = \langle \mathbf{x_i} \mathbf{x_i} \rangle$ along the diagonal and the covariances $\sigma^2_{x_i x_j} = \langle \mathbf{x_i} \mathbf{x_j} \rangle$ on the off-diagonal positions.

Due to the symmetry of $\mathbf{C_X}$ the matrix can be diagonalized:

$$\mathbf{C_X} = \mathbf{E} \begin{pmatrix} \lambda_1 & & \\ & \ddots & \\ & & \lambda_n \end{pmatrix} \mathbf{E^T}, \tag{4.3}$$

where λ_i are the eigenvalues and $\mathbf{E}$ is the eigenvector matrix of $\mathbf{C_X}$.

The magnitude of the eigenvalues corresponds to the variance of the data along the eigenvector directions. An ordering following the decreasing magnitude of eigenvalues $\lambda_1 \geqslant \lambda_2 \geqslant \ldots \geqslant \lambda_n$ can be used to order the eigenvectors which are then called the PCs.

To describe the effect of PCA for resolution enhancement the application of PCA on a $2xn$ data matrix $\mathbf{X}$ containing two identical spectra with n data points is considered. The resulting PC-matrix $\mathbf{Y}$ is of the order $2xn$ and has two associated eigenvalues with $\lambda_1 \geqslant \lambda_2$. In the case of two identical spectra, only one PC is needed to describe both spectra and the eigenvalues are $\lambda_1 = 1$ and $\lambda_2 = 0$. The more the spectra differ, for example by shifting these against each other, the more the first eigenvalue λ_1 decreases and the second eigenvalue λ_2 increases. Hence, the ratio of first and second eigenvalue decreases with vanishing similarity. This relation can be used to identify the best spectral overlap of two spectra within a time-dependent spectral series.

In a first step, the spectra from a time-dependent spectral series are padded with buffer regions on both wavelength interval borders composed out of random

noise by using in MATLAB® [169] implemented noise function: 'randn' which is scaled to the noise level in the respective experimental spectrum. Secondly, the spectra are shifted pairwise step by step against each other within a predefined wavelength range. For each relative position PCA application on the $2 \times n$ matrix is followed by the calculation of the ratio of first and second eigenvalues. This ratio is stored together with the corresponding shift. The maximum of the eigenvalue ratio is used to identify the shifting width needed to obtain the best matching spectral overlap.The pairwise comparison of the spectra reduces the computational cost to the order of $\mathcal{O}(i \cdot j!)$, where i denoted the maximum shift width which is associated with the selected shifting wavelength interval and j denotes the number of spectra in the spectral series. Thus, the algorithm is substantially less demanding than evaluated on each relative positioning of all spectra within the time-dependent spectral series which would require $\mathcal{O}(i^j)$ calculations. The quality of the shifting results justifies the reduced pairwise application of the PCA-based shifting method as being suited to identify spectral patterns along entire spectra series taken in a time-dependent measurement (see example in Figure 4.11). In the case of intra-complex heterogeneity, where the spectral shape varies in time, a threshold defining a minimum first eigenvalue is used ensuring that only spectra with a certain degree of similarity are considered and others are excluded from the PCA-shifted data set.

A physically meaningful abscissa after the shifting process is a relative scale taking the purely electronic transition as origin. The 0-0 transition is spectroscopically identifiable as a ZPL contribution, which can be identified by a narrow peak located at the short wavelength side of a high-resolved fluorescence emission spectrum. Furthermore the purely electronic transition is expected to have high-most intensity in high resolution fluorescence emission spectra. For a number of spectra from individual phytochromes a ZPL can be identified in the fluorescence emission spectra, as is the case for the spectrum (I) shown in Figure 4.13. For other phytochrome molecules a ZPL is not identified. Either the spectral shape at the short wavelength side of the fluorescence emission spectrum indicates a truncation by the fluorescence cut off filter, as in spectrum (II) in Figure 4.13 or the blue-most line does not show maximum intensity, as for spectrum (III) in Figure 4.13. This observation can be understood by considering the excitation scheme used for the LT-SMS measurements. The excitation wavelength was 680 nm on the short wavelength side of the main absorption peak at 701 nm of Agp1-BV in the P_r-state. The effect of the so-called vibronic excitation scheme can be visualized by a simulation as shown in Figure 4.14.

In this calculation the excitable molecules in a phytochrome sample are simulated, based on a recorded fluorescence emission spectrum of Agp1-BV in the $P_r$state (Figure 4.14b, which was mirrored with respect to its 0-0 transition (see

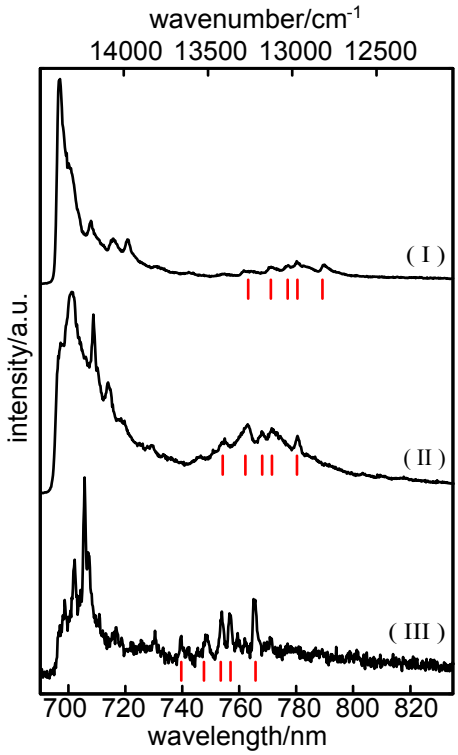

Figure 4.13: LT-SM spectra (I)-(II) from different individual phytochrome molecules (T = 1.4 K, λ_{exc} = 680 nm, t_{acq} was between 1 and 120 s per spectrum). While in spectrum (I) a ZPL contribution is identified at 699 nm, for the spectra (II) and (III) no high-most narrow line is detected in the short wavelength side of the spectrum. A five lines comprising line pattern with preserved distances but appearance at different wavelength positions is highlighted by red lines (for details see text).

Figure 4.14a) and normally distributed along the wavelength scale, accounting for the inhomogenous broadening in an ensemble of molecules. The sum over 1000 single-molecule absorption spectra distributed with a variance of 16 nm was found to resemble the experimental ensemble UV/Vis spectrum of phytochromes in the P_r-state (Figure 4.14c and for comparison see Figure 4.2). On this set of single-molecule absorption spectra the excitation at 680 nm is simulated. Some spectra contributing to the modeled ensemble spectrum have their 0-0 transition at 680 nm and other contribute by vibrational bands to the extinction at 680 nm (see the four example spectra in Figure 4.14c). The higher the energy of the vibrational band contribution to the absorption at 680, the more red-shifted is the associated 0-0 transition of the specific molecule. The simulated fluorescence emission spectra of single molecules excited vibronically were scaled with respect to the extinction at the excitation wavelength. Simulated fluorescence emission spectra from 200 molecules are shown in in Fig-

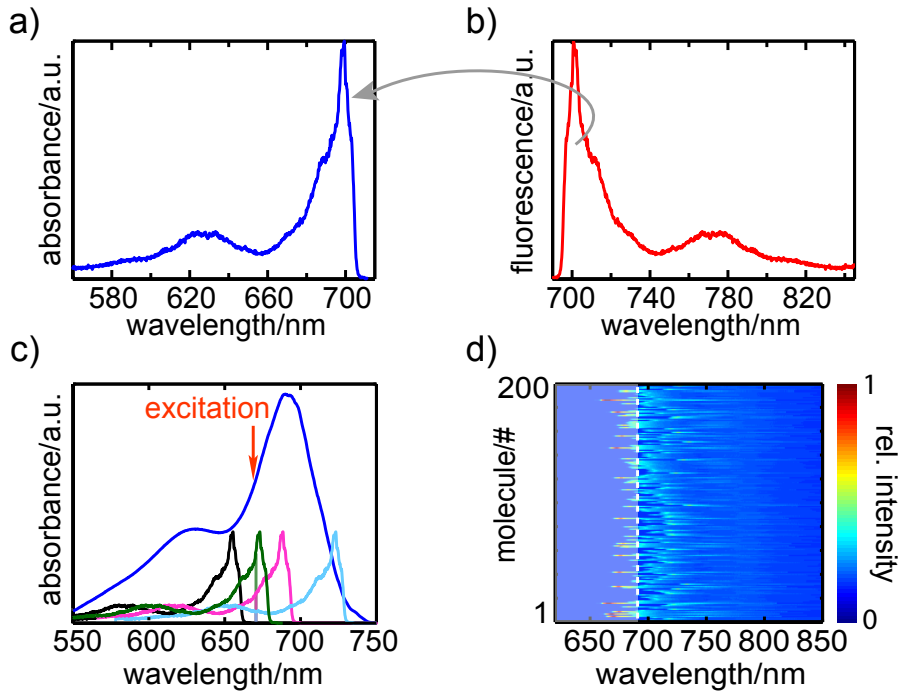

Figure 4.14: Simulation on vibronic excitation. a) Generated absorption spectrum of a single phytochrome based on b) a fluorescence emission spectrum of an individual Agp1 in the P_r-state. c) Generated ensemble absorption spectrum (blue) and four underlying single-molecule absorption spectra are shown in arbitrary intensity. Three of the four example spectra show oscillator strength at the excitation wavelength (highlighted by vertical lines). d) The set of spectra shows simulated single-molecule fluorescence emission spectra from 200 different individual molecules as obtained when modeling excitation at 680 nm (attention here the 2D contour presentation does not show time-dependent but spectra from different individual molecules!). Depending on the excitation into the 0-0 transition or into vibrational bands the respective fluorescence emission appears at different wavelength positions. In the experiment some of the spectra are cut by the fluorescence cut-off filter as indicated by the white dashed line (for details see text).

ure 4.14d in a 2D contour representation. The spectra with high-most intensity are those which have a ZPL transition at 680 nm. Other spectra appear shifted to longer wavelength. The variance of electronic energies accessible by vibronic excitation is visualized by this set of spectra. The red-most ZPL position observed between the 200 simulated spectra is located at 730 nm. With regard to the simulated ensemble absorption spectrum for phytochromes in the P_r-state it turns out that in principle ZPL positions of up to 750 nm are possible, however occurring with minor probability. The simulated single molecule absorption spectrum shown in Figure 4.14c) in black, indicates the other extreme. As the

ZPL position is at λ <680 nm the molecule cannot be exited. For the detection of fluorescence emission typically a cut off filter is needed. In the experiments on single phytochrome molecules the cut-off filter used opens at 695 nm. This situation is visualized by a dashed line at 695 nm in Figure 4.14d. Only phytochrome molecules which have the ZPL at >695 nm and thus are excited via vibronic modes with energies of > 320 cm^{-1} show a ZPL within the detection range. Only the long wavelength part of the spectrum is detected for other other molecules, which are excited via their 0-0 transition or vibronically into modes with energies< 320 cm^{-1}. For molecules which show only a partial fluorescence emission in the detection window the origin of a relative wavenumber scale after shifting was chosen at a middle position between laser wavelength and filter opening. Thus the maximal shift to a physical meaningful scale can be as large as ca. 8 nm or 170 cm^{-1}, respectively.

Many spectra from different individual phytochrome molecules show a recurring narrow line pattern. In Figure 4.13 a line patterns comprising five narrow spectral lines is highlighted by red lines. This line pattern appears at different wavelength positions. While the blue-most line of the pattern appears at 763 nm in spectrum (I) it is found at 754 nm in spectrum (II) and at 739 nm in spectrum (III). The use of a reference spectrum containing a ZPL contribution possibly is the only way to obtain a meaningful energy scale for spectra lacking a ZPL contribution in the recorded wavelength range. From comparison with a ZPL-containing reference spectrum, the wavelength position of the 0-0 transition between laser excitation and filter opening can be inferred. The observation of similar line patterns in the long wavelength part of the fluorescence emission spectra from different individual phytochrome molecules renders the search for a reference spectrum within the set of single-molecule spectra promising.

The PCA-based shifting algorithm proved to be efficient to identify similarities between spectra from one time-dependent spectra series of an individual phytochrome molecule. In the following, the same PCA-based pattern recognition technique is used to identify spectral similarities in spectra from different molecules. The spectra in Figure 4.13 show a similar narrow peak patterns on heterogenous broad fluorescence emission backgrounds. They appear either exclusively (III) or on top of broadened fluorescence bands of low (I) and high (II) relative intensity. To render the PCA-based pattern recognition technique sensitive for the narrow peak structures in the fluorescence emission spectra from different single phytochrome molecules the broad fluorescence emission bands have to be removed as the broad contributions would obscure similarities in the fine structure. The information contained in broad unstructured fluorescence emission bands can be used to analyze the degree of spectral diffusion which is indicative for pigment-protein interaction, while the narrow peaks

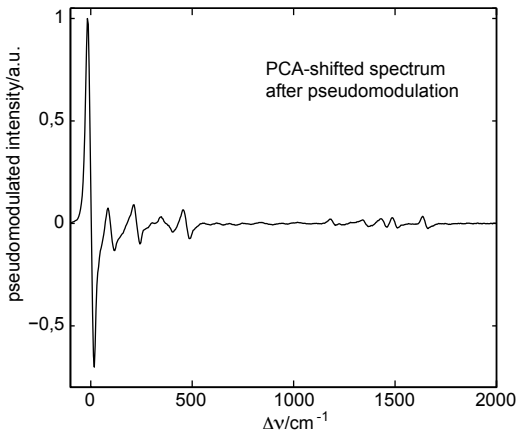

Figure 4.15: After application of the pseudomodulation technique the broad fluorescence emission contributions are removed from the single-phytochrome molecule spectra.

possibly contain vibrational information which can e.g. be used to determine chromophore conformations. By a separation of the spectral components by a convolution technique these spectral components can be analyzed exclusively. Here a pseudomodulation technique is applied to solely focus on the narrow line information.

The pseudomodulation technique was developed in the frame of EPR spectroscopy [170]. Pseudomodulation simulates the effect of a sinusoidal field modulation on a magnetic resonance spectrum. However, pseudomodulation turned out to be a versatile filter function for resolution-enhancement of more general spectroscopic data. In the limit of vanishing modulation amplitude the pseudomodulated spectrum is the derivative of the spectrum. However, pseudomodulation circumvents the numerically dangerous calculation of a derivative. The result of the "modulation" instead is calculated by folding the spectrum with a modulation function and subsequent filtering of a specific component. Thereby, low frequencies associated with broad unstructured fluorescence emission and high frequencies from noise can be suppressed. Figure 4.15 shows the pseudomodulated spectrum of the PCA-shifted average spectrum depicted in Figure 4.11d.

Results from Pattern Recognition Analysis

The resolution-enhanced and pseudomodulated spectra of 32 individual phytochrome molecules were collected in one data matrix. Then, a pairwise application of the PCA-based shifting algorithm was performed within the wavenumber range from $\sim 960 - 2500\ \mathrm{cm}^{-1}$ covering the above-mentioned five lines comprising pattern. This range contains the vibrational fingerprint region where N-H in plane bending and C=C stretching modes of tetrapyrroles occur

[171]. An appropriate minimal eigenvalue ratio is used as a threshold for sorting out dissimilar spectra. A group of 20 molecules was identified with a similar overall fluorescence line pattern in the considered wavenumber range, referred to as group I. The resolution-enhanced and pseudomodulated spectra after relative shifting are shown in Figure 4.16a. Due to the identification of a similar pattern an assignment of the origin of an relative wavenumber scale even for the ZPL-lacking spectra becomes possible. In Figure 4.16b the associated resolution-enhanced fluorescence emission spectra are shown plotted against a relative wavenumber scale which was taken from the reference spectrum shown on top. The in parts by pattern recognition inferred ZPL positions vary between 680 nm and 702 nm for these spectra. The ZPL positions determined by a reference spectrum are estimated to have an error of ± 15 cm^{-1}. This error was estimated on the basis of the observed variance of ZPL-positioning upon PCA-based pattern identification in the fingerprint region and relative shifting of the 8 spectra from group I which contain a ZPL.

The narrow peak structures are observed at distances from the 0-0 transition which are characteristic for vibrational energies of tetrapyrroles [171]. This observation let us conclude that the narrow line structures are due to couplings of the electronic transition from S_0 to S_1 to vibrational modes of the chromophore. According to Kasha's rule [16] the transitions observed in fluorescence emission occur from the vibrationally relaxed electronic excited $S_{1,v=0}$ state to the vibrational levels of the ground state S_{0,v_i}. Thus, vibrational information contained in the recorded fluorescence emission spectra of individual phytochromes report on the vibrational modes of the P_r ground state which couple to the electronic transition of the chromophore.

By zooming into the high energy region of the vibrationally-resolved spectra associated with the spectral group I, it can be observed that the peak positions are heterogenous for the individual molecules (see Figure 4.17). The typical wavenumber ranges which are associated with C-C and C-N vibrations (1000 – 1300 cm^{-1}), as well as the range of N-H in-plane and out-of-plane modes ($\sim$ 1300 – 1580 cm^{-1}), the C=C stretching modes (1580 – 1700 cm^{-1}) as well as the range of C=O vibrational modes (1700 – 1800 cm^{-1}) [172] are highlighted in different colors. Beside these vibrations other more complicated modes with contributions from multiple atoms of the chromophore can occur. Per definition the chromophore is not only the tetrapyrrole pigment but the tetrapyrrole and all protein parts which have a direct influence on the electronic and vibronic characteristics of the protein-bound tetrapyrrole pigment. The interaction with the binding pocket include steric effects, electrostatic and H-bonding as well as π-stacking with aromatic amino acid residues or elongation of the π conjugation system of the tetrapyrrole by an electron accepting bond formation. All

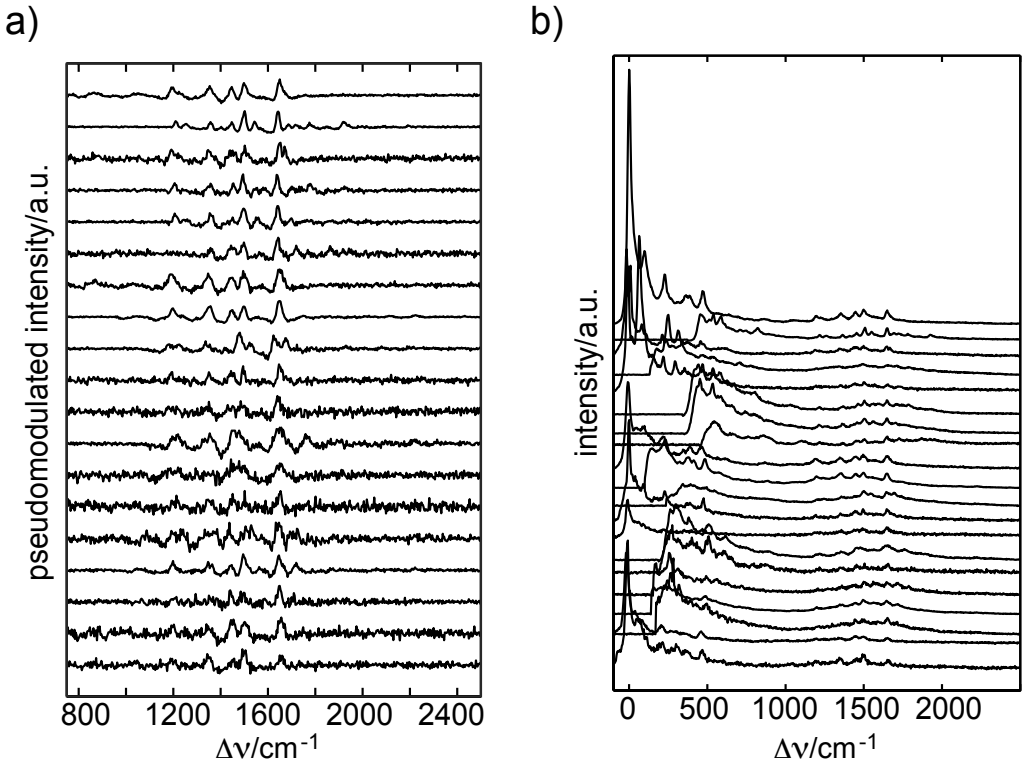

Figure 4.16: Spectra of the subgroup of 20 phytochrome molecules with similar overall line pattern in the vibrational fingerprint region as identified by pattern recognition. a) Pseudomodulated and resolution-enhanced spectra in the spectral range used for pattern recognition comprising the vibrational fingerprint region (details see text). b) The associated resolution-enhanced spectra in the full spectral range. The spectra were scaled to a peak maximum within the fingerprint region. Differences in the low frequency region are due to experimental constraints implying the use of a fluorescence cut-off filter (details in the text.)

these interactions seem to be important in phytochromes.

Determination of Vibrational Peak Positions

The peak positions for the group I spectra are separately analyzed for ZPL- and no ZPL-containing spectra. In the spectra where a ZPL is present the estimated error for manually selecting the peak positions is $\pm$ 8 cm^{-1}, while for spectra containing no ZPL the peak positions are determined to $\pm$ 17 cm^{-1}.

Table 4.1 contains the peak positions of the narrow line structures for the ZPL containing spectra. The numbering follows the ordering of the spectra from Figure 4.16 from top to bottom. The frequencies are arranged graphically for the different molecules, such that with respect to the error similar peak positions from different molecules can be found in a row. The peaks with high occurrence are highlighted by color and a numbering of the peaks associated with the five

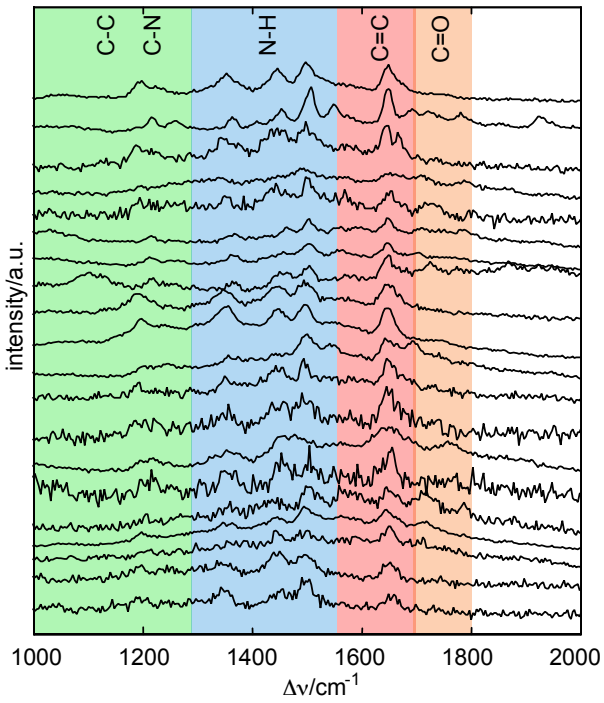

Figure 4.17: Fingerprint region of the resolution-enhanced fluorescence emission spectra associated with the subgroup of 20 phytochrome molecules with overall similar line pattern as identified by pattern recognition. The typical wavenumber ranges which are associated with C-C and C-N vibrations, as well as the range of N-H in plane and out of plane modes, the C=C stretching modes as well as the range of C=O vibrational modes [172] are indicated by underlaid colored boxes. It is to mention, that e. g. coupled modes comprising several pyrrole ring atoms or the propionate side chains can similarly occur in these wavenumber ranges [145] (for details see text).

lines comprising patterns is given on the left. Beside the peak positions of the fingerprint region the lower frequency modes are additionally given. Published data on the vibrational modes below 600 $^{-1}$ are scarce, thus peak assignments to vibrational modes are only discussed for the higher frequency modes. The number of vibrational peaks observable in this subset of spectra from individual phytochrome molecules varies between 10 and 13. Low frequency modes with wavenumbers between 23 and 55 cm^{-1} are observed in 5 of 8 spectra and a minor fraction of two molecules show a peak at 77 and 71 cm^{-1}. Except of one spectrum all other 7 spectra show a peak in the wavenumber range 92 – 101 cm^{-1}, which are the same frequencies with respect to the experimental error. In the range 115 – 165 cm^{-1} 50% of the spectra show a contribution. All spectra have a peak at 220 – 231 cm^{-1}. For five molecules bands in the wavenumber interval 257 – 302 cm^{-1} as well as in the range of 372 – 390 cm^{-1} are found. Another mode which occurs in all 8 spectra is located at 470 – 481 cm^{-1} and is

	SM1	SM3	SM5	SM9	SM12	SM13	SM19	SM20
	0	0	0	0	0	0	0	0
		23		46	37		50	55
			77			71		
	92	95		92	94	101	94	99
			159		165	126		115
	225	229	231	222	227	229	224	220
		257	302		328		286	314
	353	357	369	352		362		
	383			398	390		380	372
	470	472	476	467	477	470	481	475
			553					
				623				
				874				
(1)	1191	1208		1194	1197	1197	1217	1201
					1291			
(2)	1345	1362	1361	1352	1353	1359	1361	1350
(3)	1442	1457	1448	1452	1447	1458	1467	1463
(4)	1498	1516	1509	1503	1497	1504	1520	1513
			1586					
(5)	1646	1660	1662	1656	1653	1664	1673	1669
		1685						
			1739					

Table 4.1: Vibrational data obtained from individual phytochrome by LT-SMS. The frequencies are given in wavenumbers. The peak positions were determined from the resolution-enhanced spectra for which the ZPL position contained in the spectrum was taken as the origin of an relative wavenumber scale (as shown in Figure 4.16b). The numbering follows the ordering of the spectra as shown in Figure 4.16b from top to bottom. The error is $\pm$ 8 cm^{-1} for each value.

again the same for all molecules with respect to the experimental error. Single spectra show a contribution at 553 cm^{-1}, 623 cm^{-1} and 827 cm^{-1}, whereby the latter lies in the range of C-H out-of-plane modes [4, 146]. All but one spectrum show a contribution at 1191 – 1208 cm^{-1} (1). This spectral band is neither present in FTIR- [145] nor in Pre-RR spectra [121] of Agp1-BV, but falls in the vibrational range of C-N and C-C vibrational modes [172]. Only one spectrum of these selected 8 phytochrome spectra shows a contribution at 1291 cm^{-1}, while for the spectral regions 1345 – 1361 cm^{-1} (2), 1442 – 1467 cm^{-1} (3) and 1498 – 1520 cm^{-1} (5) all spectra from this subset show one peak. These modes fall into the range of N-H vibrations [172]. These bands are not observed by FTIR difference spectroscopy which shows an unstructured P_r - P_{fr} spectrum in the wavenumber range at 1250 – 1480 cm^{-1} [145] but show up in the Pre-RR spectrum of Agp1-BV in the P_r state. Due to strongly overlapping bands in this region which also are attributed to vibrational modes of the apo-protein, these were not assigned to specific modes of the chromophore [121]. One spectrum of a single phytochrome molecule has a peak at 1586 cm^{-1} which is at a frequency

	SM2	SM4	SM6	SM7	SM8	SM10	SM11	SM14	SM15	SM16	SM17	SM18
		174				144				169	155	
						229					199	
		246						263	270	258	245	265
		313				318	339	300	311	306	290	284
											334	318
						372	392	384		382	368	389
						410			400		419	
	457	469	443	454						442	437	430
	510		469			484	490	510	506	494	488	501
	539	528	535	533	546	564	546			556		
			579	563			587					
	585	593	622	587				618	602	623		
			671	656	653				643			
	708	708								717	705	
	746	775		742	758	761		747			758	
	823		804	796					781			
					863	883		884	859			
			1034									
					1108							
(1)	1216	1193	1215	1210	1218	1195	1208	1205	1210	1203	1201	1203
	1262						1251					
(2)	1365	1339	1366	1364	1366	1354	1356	1354	1354		1345	
											1361	
	1406											
(3)	1457		1461		1451	1443	1446	1462	1450		1437	1441
(4)	1508	1498	1504	1507	1504	1499	1500		1503	1501	1496	1499
	1547	1567	1561	1563			1546			1560	1560	
			1596									1593
(5)	1649	1647	1653	1650	1653	1650	1645	1645	1654	1648	1645	1654
	1690	1706		1704			1699			1709		
	1716		1712		1719						1719	
	1783	1788	1781					1760		1785		
		1860			1867							
	1926											

Table 4.2: Vibrational data obtained from individual phytochrome by LT-SMS. The frequencies are given in wavenumbers. The peak positions were determined from the resolution-enhanced spectra (as shown in Figure 4.16b) after an assignment of the origin of an relative wavenumber scale from a reference spectrum (details see text). The numbering follows the ordering of the spectra as shown in Figure 4.16b from top to bottom. The error is estimated to be $\pm$ 17 cm^{-1} for the peak positions.

position typically assigned to a N-H in plane mode of ring B or C of the tetrapyrrole chromophore [121]. The same molecule has a further narrow spectral line at 1739 cm^{-1}. This mode was observed also by FTIR-difference spectroscopy on Agp1-BV and was attributed to a C_1=O stretching mode [145]. A further peak is observed in all spectra at wavenumbers between 1646 and 1673 cm^{-1}. The chromophore-specific vibrations found in this region are attributed to C=C stretching vibrations [121].

Table 4.2 compiles the vibrational energies for the 12 remaining phytochrome spectra of group I, which do not contain a ZPL. Again, the numbering follows the ordering of the spectra from Figure 4.16 from top to bottom. The number of vibrational peaks observable varies between 11 and 19. In the following, only the vibrational lines with major occurrence are described in the text and for single events the reader should consult the table. The vibrational modes with high-most occurrence in the fluorescence emission spectra of these 12 individual phytochromes lie in the range of 1193 – 1218 cm^{-1}, and 1645 – 1654 cm^{-1}. In these ranges all analyzed molecules show one contribution in the fluorescence emission spectrum. 11 of 12 molecules show a vibrational band at 1496 – 1508 cm^{-1}. In the range 1339 – 1366 cm^{-1} 10 of 12 molecules show one or two spectral peaks. The fifth range of the fingerprint region with relative high signal occurrence is found at 1431 – 1450 cm^{-1}, where 9 of the 12 molecules show a narrow spectral component. These wavenumber bands strongly overlap with the ranges found for the molecules which contain a ZPL in their spectra and thus were the bands relevant in the pattern recognition analysis (1) – (5). A number of modes fall in the range of C=O vibrational bands, at wavenumbers between 1690 and 1788 cm^{-1} [145]. For two molecules from this subset of resolution enhanced spectra, extremely high energy modes are observed at 1860, 1867 and 1926 cm^{-1}, which do not have a counterpart in Pre-RR and FTIR difference spectra of phytochromes.

For the 13 remaining spectra which were not attributed to the spectral group I and which show narrow line contributions in the vibrational energy range, pattern recognition did not reveal a further spectral subgroup (spectra not shown). For the spectra which were not assigned to the group I and which contain a ZPL the peak positions are given in Table 4.3. This was the case for 8 of these 13 spectra. The number of observed vibrational peaks for these spectra shows a large variance from 6 to 22. Again only the peak positions with major occurrence are discussed. The fluorescence emission spectra of 8 individual phytochrome molecules show all a narrow peak in the wavenumber ranges at 198 – 230 cm^{-1} and 467 – 486 cm^{-1}, which are the same with respect to the error. In 7 spectra of the 8 phytochrome spectra one peak is found between 361 – 400 cm^{-1}. Thus, a high similarity between the spectra is observed on the low frequency range. In

SM21	SM22	SM23	SM24	SM25	SM26	SM28	SM32
0	0	0	0	0	0	0	0
	29		23	31			
	60	78				75	66
87	92		92				
	115					123	130
	156		144	164			
205	216	222	230	227	234	198	226
	268					259	
389		363	366	363	361	361	
	400						
	435						
467	467	467	472	475	475	476	486
	510						
893							
	959						
	1002						
	1040						
	1112					1103	
	1158						
1205		1199					
	1262	1233	1230			1251	1249
	1305	1311					1332
1383						1362	
1449	1463	1444	1440				
	1489	1470	1466				
						1508	
				1558		1562	
1660	1651	1657				1666	
	1682						

Table 4.3: Peak positions as determined from resolution enhanced LT-SMS spectra, which contain a ZPL. Pattern recognition applied on the fingerprint region did not reveal overall similarity to the group I spectra nor an additional group with characteristic features was found in the fingerprint region. The error for each value is ± 8 cm^{-1}.

the vibrational fingerprint region, peaks are found at 1230 – 1262 cm^{-1} for 5 of 8 molecules. And for 4 of 8 molecules a narrow line is found in the wavenumber ranges 1305 – 1332 cm^{-1}, 1466 – 1508 cm^{-1} and 1651 – 1666 cm^{-1}. Other peak positions occur with minor probability. For the remaining vibrationally-resolved fluorescence emission spectra of individual Agp1-BV molecules no reference spectrum could be assigned and thus were not suited for a vibrational peak analysis.

Discussion

Highly resolved fluorescence emission spectra from individual phytochrome molecules in the P_r-state taken at T = 1.4 K were analyzed. It was found that the narrow peak contributions occur at energy differences with respect to the 0-0 transition of the chromophore which are typical for vibrational modes of tetrapyrroles. Thus, the narrow peaks were identified as vibrational contri-

butions. In fluorescence emission spectroscopy only vibrational modes coupling to the electronic transition of the chromophore from the relaxed excited state S_1 to the different vibrational modes of the S_0 ground state manifold contribute to the spectrum and thus the vibrational information is not obscured by apoprotein bands, as is the case for other vibrational spectroscopic methods as FTIR and Raman spectroscopy. Most probable the vibrational modes involved in isomerization are apparent in the fluorescence emission spectrum, as these are excited in the first picoseconds of the photocycle [173] directly after photo-activation. Thus, low temperature fluorescence emission spectra contain valuable information with respect to the phytochrome function which relies on the photo-induced conformational changes of the chromophore. Therefore, the spectra were investigated to a greater detail here. In the first part of this study, a pattern recognition algorithm was developed for i) resolution enhancement and for ii) pattern recognition in the long wavelength range of the spectra to obtain reference spectra for partially detected spectra lacking a ZPL contribution.

Synchronous wavelength changes of the narrow peaks as observed in time-dependent spectra series became efficiently removable by PCA-based pattern recognition between the different spectra from such series. As a result resolution-enhanced spectra were obtained which were used for vibrational peak analysis. To reach sensitivity of the pattern recognition technique to the vibrational information contained in the spectra from different individual phytochrome molecules, the broad fluorescence emission bands occurring with variable intensity were removed by a pseudomodulation technique.

Pattern recognition was applied on 32 resolution-enhanced and pseudomodulated spectra from different individual phytochrome molecules. As a result of the pattern recognition analysis a subgroup of 20 spectra were identified to show an overall similar vibrational line pattern in the fingerprint region of the chromophore (group I). For 12 partially detected fluorescence emission spectra, thereby, a reference spectrum was identified, which was used to obtain a relative wavenumber scale with respect to the 0-0 transition of the molecule.

The vibrational peak positions were determined for all spectra containing a ZPL or having a reference ZPL. The analysis of the vibrational peaks reveals heterogeneity concerning the number of peaks present in the spectra and in the peak positions in the spectra from individual phytochrome molecules also between the spectra which appear to have an overall similar line pattern. The spectra associated with the group I show at least 10 narrow line contributions. The wavelength ranges associated with a recurring line pattern are located at 1191 – 1218 cm^{-1} (C-C/C-N stretching range), 1339 – 1366 cm^{-1} (N-H in plane ring A and D, also C-C and C-N stretch [174]), 1431 – 1467 cm^{-1} (N-H in plane), 1496 –

1520 cm^{-1} (N-H in plane range) and at 1646 – 1673 cm^{-1} (C=C range) [172]. The 8 spectra containing a ZPL and minor similarity in the long wavelength part of the spectrum with the spectra from group I, show large similarities in the low energy modes were three modes occur with high probability. Interestingly the band at 1450 cm^{-1} as found in Pre-RR data was assigned to apo-protein modes [121]. The single-molecule spectra taken in fluorescence emission show that this assignment is likely erroneous, as only chromophore specific bands contribute to the spectrum. While FTIR-difference spectra of P_r - P_{fr} states of Agp1-BV are spectroscopically silent within the broad wavenumber range 1250 – 1480 cm^{-1} [145], in Pre-RR the chromophore specific bands in this spectral region are obscured by overlapping vibrational modes of the apo-protein (amide I bands). The fluorescence emission spectra also contain vibrational information in this wavenumber region and, as only chromophore-specific bands contribute to the fluorescence emission spectrum, they provide a clear gain in information on the chromophore states present in the P_r-ground state of phytochromes.

Not all spectra connected to the spectral group I show contributions in all five wavenumber intervals. For two phytochrome molecules the spectra do not show a resolved peak at $\sim$ 1450 cm^{-1}, one molecule lacks a peak at $\sim$ 1200 cm^{-1} and a fourth molecule does not show peaks at $\sim$ 1350 cm^{-1} and at $\sim$ 1450 cm^{-1}. Beside the N-H modes reported for these wavenumber ranges also C-H rocking modes were calculated to fall into these wavenumber ranges [4]. If these bands would be, however, indicative for the different N-H in plane vibrations, the protonation state of the different nitrogen sites of the individual BV chromophores would directly be derivable from the LT-SMS spectra. If so, the data suggest fully protonated chromophores for most of the phytochrome molecules and and only minor fractions would indicate one or two deprotonated nitrogen sites and more specifically the molecule which is lacking the 1450 cm^{-1} vibration putatively lacks a proton at the ring A or D nitrogen. The fully protonated form of the chromophore is consistent with the findings from flash light photolysis and Pre-RR spectroscopy [121].

At $\sim$1650 cm^{-1} highest intensity is observed in FTIR and Pre-RR spectra of phytochromes. Most intensity is assigned to amide I bands and only minor contribution to chromophore-specific bands, which are attributed to C=C stretching vibrations including the stretching of the C_{15}=C_{16} bond. In the fluorescence emission of several phytochrome molecules a peak in the wavenumber range of 1646 – 1673 cm^{-1} is found for all molecules from group I and for 4 of the 8 spectra which were not included in group I. Their high occurrence corroborates their involvement in the photoinduced isomerization of the tetrapyrrole chromophore.

The associated 0-0 transitions for the analyzed phytochrome molecules lie between 680 nm and 702 nm. This large variance in electronic energies indicates strong pigment-protein interactions between BV and the chromophore binding pocket in phytochromes. This assignment is supported by the observation of strongly broadened fluorescence emission bands from individual phytochrome molecules at 1.4.K. By time-dependent measurements it was found that the line-broadening is due to fast spectral diffusion over large wavelength ranges (see Section 4.2, Figure 4.10). The spectral diffusion leads to line widths which are in parts as large as the inhomogenously broadened bands found in ensemble fluorescence emission spectroscopy (see spectrum II in Figure 4.13 and Section 4.2, Figure 4.8). Taken that conformational changes are highly restricted at low temperatures of T = 1.4 K, it turns out that similar conformations can relate to strongly varying electronic energies of the chromophore. The time-dependent spectra sequences of vibrational resolved spectra indicate the same, as they reveal synchronous wavelength changes of the vibrational peaks. Thus, during variations in electronic energy the vibrational fingerprint remains largely the same. One could expect that individual modes are affected by the spectral diffusion-inducing conformational change but this was not observed. The observation of a high degree of spectral diffusion reports on a strong coupling of the electronic transition of the pigment to conformational dynamics of the protein. Beside proton dynamics which are shown to cause strong spectral diffusion effects at T = 1.4 K (see Section 5.3), also other conformational changes occurring in the first coordination sphere of the tetrapyrrole can influence the site energy of the chromophore. When aiming at an assignment of the vibrational modes detected in the phytochrome fluorescence emission spectra the interaction partners of the tetrapyrrole have to be considered. Vibrational peaks in the fluorescence emission spectra may arise from the tetrapyrrole pigment itself but also from vibrational modes comprising atoms from strongly coupled amino acid residues inside the chromophore binding pocket.

Interaction partners from the protein binding pocket which contribute to the tuning of the electronic energy will shortly be discussed. Considering the π-conjugated system of the phytochrome chromophore it was found that the length which it adopts inside the protein as derived from the 2.5 Å crystal structure data is not sufficient to explain the large red-shifted electronic energy, neither for the P_r- nor for the P_{fr}-state [175]. This is different compared to a number of other bilin-binding proteins where a linear relationship between the conjugation length of their chromophores and their absorption maximum is found [175]. Electron density calculations based on the high-resolution structure at 1.45 Å resolution suggest that the π-conjugation system of BV extends to the cysteine binding site (as indicated in Figure 4.2). It is assumed that the electronic

energy is furthermore tuned by highly interacting aromatic amino acids [175]. In the direct chromophore binding pocket phenylalanine, tyrosine and histidine residues [107, 111, 138] are found. A highly conserved tyrosine residue near ring D (Y166 in Agp1) was for example found to influence the photo-reaction of Cph1 [125] and NMR data indicate that strong hydrogen bonds connect the ring D carbonyl to adjacent amino acid residues leading to a furthermore increased π-conjugation of the chromophore [124]. A highly conserved histidine residue is interacting with ring B and C (His250 in Agp1) and possibly leads to electronic energy variation by π-stacking. Additionally van der Waals interactions between the C_2 methyl group and the carbons from the C_3 side chain and the hydrophobic methionine residue located nearby in *Dr*BphP) [107] which is replaced in Agp1 to a hydrophobic valine (Val259 in Agp1). This methionine residue together with covalent binding was found to be needed for P_{fr} formation in *Dr*BphP. These strongly interacting amino acid residues supposedly contribute to the fluorescence emission spectrum as nearby amino acid rearrangements are expected after photoactivation of phytochromes. A way to identify the modes corresponding to conformational changes in the binding pocket would be a high-resolution LT-SMS analysis applied on phytochrome variants with point mutations in the chromophore binding pocket.

Typically, a restricted 1500 – 1700 cm^{-1} wavenumber range is sufficient for deducing the tetrapyrrole chromophore conformation from vibrational resolved Pre-RR spectra [144, 176]. The small number of four to five spectral bands typically resolved by Pre-RR spectroscopy in that spectral range was shown to be suited to determine the phytochrome chromophore structure by combined QM/MM analysis of the spectra [23]. The number of resolved peaks in the fluorescence spectra of individual phytochrome molecules in this wavenumber range is similar. Thus, it can be suspected that the spectral information is sufficient to derive the specific tetrapyrrole geometries for the individual phytochrome chromophores. However, the calculation of fluorescence emission intensities, in contrast to the calculation of RR intensities, are demanding in DFT due to the need of calculating the excited state characteristics and are not reported yet for tetrapyrroles.

4.4 Fluorescence Line Narrowing on Phytochromes

Fluorescence line narrowing (FLN) was used as an alternate low temperature fluorescence emission technique to study pigment-protein interactions. Phytochromes from different bacteria were investigated including Agp1 from *Agrobacterium tumefaciens*, *Dr*BphP from *Deinococcus radiodurans* and *Rp*BphP2 as well as *Rp*BphP3 from *Rhodopseudomonas palustris*. A phytochrome species-dependent fluorescence line narrowing accessibility is found. The results indicate largely different pigment-protein interactions, possibly connected to differently extended water pyrrole networks inside the binding pockets. *Dr*BphP and Agp1 do not, and *Rp*BphP2 and *Rp*BphP3 show fluorescence line narrowing. The results corroborate the findings for Agp1 on the single-molecule level concerning its in average high degree of spectral diffusion. By solvent isotope exchange vibrational modes involving exchangeable proton sites were identified to contribute to the FLN spectrum and allow for peak assignments. Proton dynamics inside the protein binding pocket are a source for spectral diffusion at low temperatures (see Section 5.3). This is corroborated by the observation of significantly increased line narrowing for phytochromes in deuterated compared to protonated solvents. By specific alterations inside the binding pocket, as by an aspartate-to-alanine point mutation or by the implementation of a sterically locked tetrapyrrole, the pigment-protein interactions in phytochromes were further specified. Strong alterations concerning the strength of pigment-protein interactions are observed for these phytochrome variants indicating a less extended pyrrole water network and, at the same time, highlighting aspartate 216 in *Rp*BphP3 to be involved in an H-bond network around the chromophore. This finding corroborates results from X-ray structure analysis and time-resolved spectroscopic methods. High resolution structural data for *Rp*BphP2 is not available. On the basis of similar fluorescence line narrowing accessibility for *Rp*BphP2 and *Rp*BphP3 a similar extended H-bond network around the chromophores is expected despite the different photo-reactions of these phytochromes at later stages of the photocycle.

Introduction

FLN is used to study the pigment-protein interactions of the phytochrome chromophores in their P_r state. The FLN spectrum solely contains chromophore-specific information as fluorescence emission implies an electronic transition at energies where the protein surrounding is transparent. FLN is a site-selective method by which only a sub-ensemble of molecules with low excitation ener-

gies compared to the overall ensemble are investigated.

The following phytochromes and phytochrome variants were studied: Three variants of Agp1 are analyzed: i) Agp1-PCD-BV: this wild type PCD fragment shows full phytochrome photochromicity [177]; ii) Agp1-PCD-Y166H-BV: a mutant with a tyrosine-to-histidine mutation at position 166 of the amino acid sequence which is located near the chromophore binding site (see Figure 4.6). For the cyanobacterial phytochrome Cph1 an analogous tyrosine-to-histidine mutation leads to the formation of a phytochrome strongly fluorescent at ambient conditions [125]. iii) Agp1-PCD-BV15Za: a variant where the natural BV is exchanged to the synthetic chromophore BV15Za with an additional bond between ring C and D (see Figure 4.7). This bond locks the chromophore in a P_r-like conformation [92]. Two phytochrome samples are studied from the bacterium *Deinococcus radiodurans*: iv) *Dr*BphP: the wild type full length protein, and v) *Dr*BphP-CBD-Y305S-BV: a mutant with a serine-to-tyrosine mutation located far from the chromophore site at the protein dimerization interface. This variant shows improved crystallization characteristics compared to the wild type fragment [107]. This mutated protein fully photo-converts from P_r to P_{fr} but lacks stabilization of the P_{fr} state.

Additionally, two different phytochromes and variants from *Rhodopseudomonas palustris* are characterized: vi) *Rp*BphP2-BV: the full length proteins and vii) *Rp*BphP3-BV: showing an unusual phytochrome photocycle [93]. Upon photoexcitation of the P_r state peaking at 705 nm for this phytochrome not a red-shifted P_{fr} state is formed but a minor increase in absorption occurs at 650 nm. This spectral form is referred to as the P_{nr} (near red) state. viii) *Rp*BphP3-PCD-BV: displaying photoconversion efficiency comparable to that of the full length protein [94] and ix) *Rp*BphP3-PCD-D216A-BV: a variant with an aspartate-to-alanine mutation near the chromophore binding site at position 216 of the amino acid sequence (see Figure 4.6). This mutation influences the photochemistry of phytochromes by changing the hydrogen bonding and proton transfer characteristics [122]. The samples from the phytochromes from *Rhodopseudomonas palustris* vi) – ix) were additionally analyzed in deuterated buffer x) – xiv).

Results

Figure 4.18 shows temperature-dependent fluorescence emission spectra taken from Agp1-PCD-BV15Za[2]. The temperature conditions were varied between

[2]For details on the sample preparations see Chapter 3, page 44.

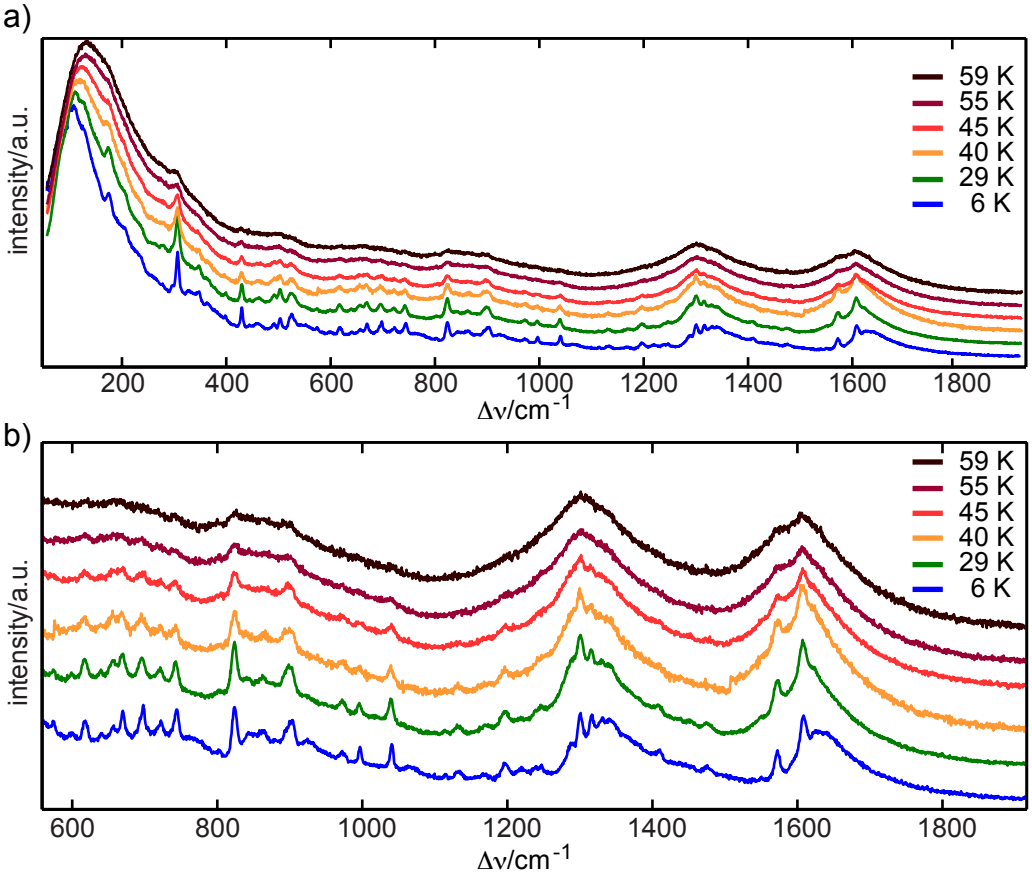

Figure 4.18: Temperature-dependent fluorescence emission spectra of Agp1-PCD-BV15Za taken under FLN excitation with λ_{exc} = 723 nm, P_L = 100μW, acquisition times were 4 s at T = 6 K and 1 s otherwise.

59 K and 6 K. For Agp1-PCD-BV15Za having its maximum absorption in the red at 714 nm the excitation wavelength for FLN spectroscopy was adjusted to 723 nm. Thereby only a sub-ensemble of molecules with extreme red-shifted electronic energies gets excited via their 0-0 transition. The FLN spectra are all given in a relative wavenumber scale with respect to the excitation wavelength. In Figure 4.18a the entire measured wavenumber range and in Figure 4.18b a zoom into the higher wavenumber range is given. For the spectrum taken at 59 K a maximum is found at 144 cm^{-1}. This maximum shifts to lower frequencies upon decreasing temperature and is found at 120 cm^{-1} in the spectrum taken at T = 6 K. This temperature-dependent spectral contribution can be identified as the PW corresponding to the 0-0 transition which was not included in the detection range. At 59 K the fluorescence emission spectrum is broad and relatively unstructured. To higher wavenumbers from the peak found at 144 cm^{-1} a shoulder is found at $\sim$ 300 cm^{-1} and two peaks are found at 1300 cm^{-1} and 1600 cm^{-1}, respectively. The broad fluorescence emission

extends to about 1820 cm^{-1} where noise level is reached. At lower temperatures the line width decreases and vibrational fine structure arises on top of the broader fluorescence bands. The line width of the vibrational fine structure is of the order $\lesssim$ 10 cm^{-1}. These narrow peaks do not show a temperature-dependent wavenumber shift. About 40 narrow peaks can be identified in the spectrum taken at 6 K. The spectral diffusion as detected for Agp1-BV on the single-molecule levels seems to be minor for the variant with sterically locked chromophore, ss strong spectral diffusion would hinder the detection of vibrational fine structure from a sub-ensemble of molecules.

The narrow lines are attributed to the ground state vibrational modes of the chromophore coupling to the electronic transition from $S_{1,v=0}$ to S_{0,v_i} (see Chapter 2, Figure 2.3). The spectral features are commonly referred to as vZPLs. These vibrational transitions can couple to delocalized phonon modes leading to red-shifted PWs associated with the vZPLs. In the 6 K spectrum PWs are observed red-shifted to the vZPL located at $\sim$ 300 cm^{-1}, 820 cm^{-1}, 1300 cm^{-1} and 1610 cm^{-1}. For other vZPLs the PW is not clearly observed. This might either be due to the high density of narrow peaks in several ranges of the spectrum or to less coupling strength of the associated vibrational transitions to phonon modes.

FLN spectra were taken for all phytochrome samples at T = 6 K. The excitation wavelength was selected for each sample individually, balancing between signal intensity and evolution of narrow lines. The particular excitation wavelengths can be found in Table 3.1. In the following, the wavenumber range from 800 to 1800 cm^{-1} is inspected for all phytochrome samples. This range contains the vibrational fingerprint region of tetrapyrroles which are indicative for the chromophore conformation (1500 – 1700 cm^{-1}) [144, 176]. Peak positions are determined for the various phytochrome variants by applying the 'max' function in MATLAB® [169] in selected wavenumber ranges around the peaks. The values are given in wavenumbers and the estimated error is $\pm$ 6 cm^{-1}, mainly due to the spectral resolution of 0.2 nm. Fig.s 4.19 – 4.22 show the 6 K FLN spectra in the considered energy range. The determined peak positions are included in the charts and given in wavenumbers.

Figure 4.19 shows the FLN spectra of the agrobacterial phytochrome variants. The FLN spectra taken from Agp1-PCD-BV and Agp1-PCD-Y166H-BV do not show substantial narrow peaks in the spectral range of 800 – 1800 cm^{-1}. For these phytochrome variants the spectral diffusion seems to prevent the evolution of narrow line structures under FLN excitation. For Agp1-PCD-BV which has full photochromicity compared to the full length protein this is in line with the observation of strongly spectral diffusion affected fluorescence emission sig-

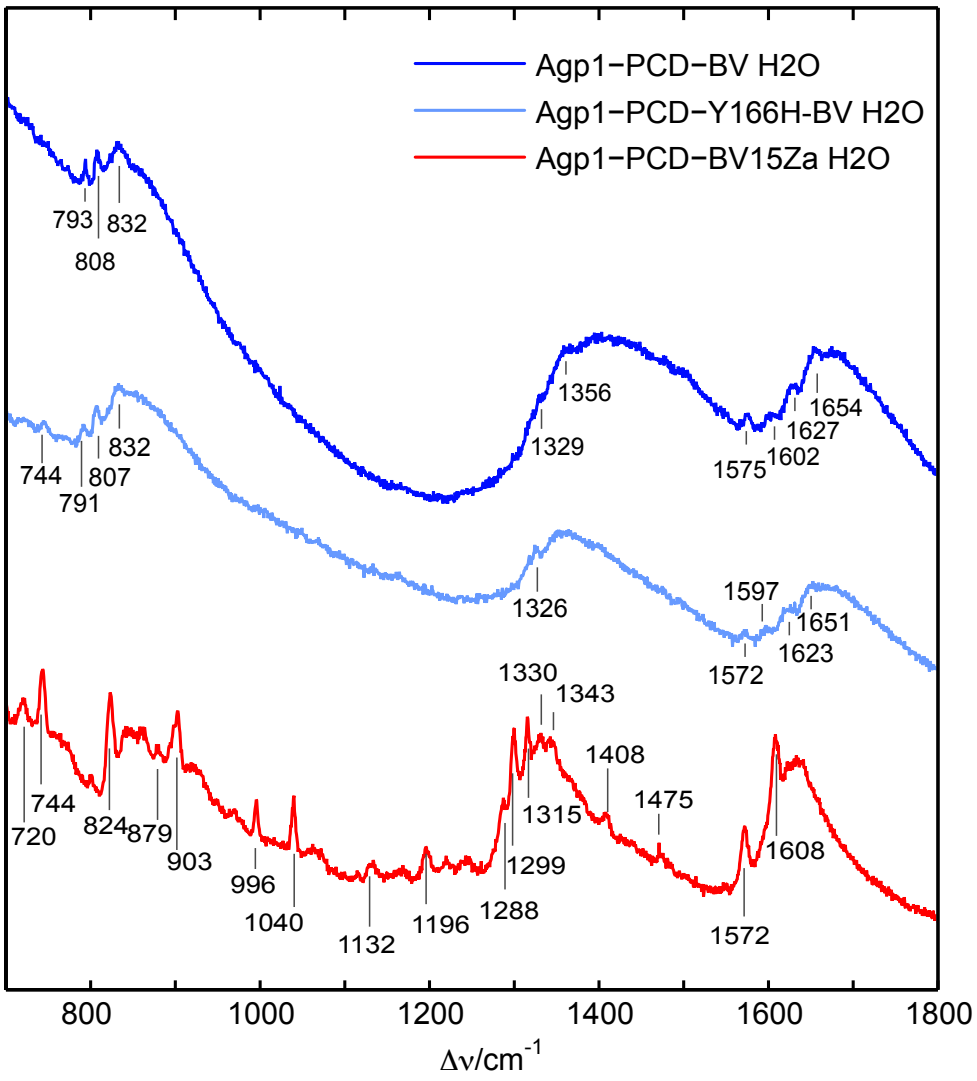

Figure 4.19: FLN spectra in the extended fingerprint region taken from Agp1-PCD-BV, Agp1-PCD-Y166H-BV and Agp1-PCD-BV15Za at 6 K. The further experimental parameters can be found in Table 3.1. The peak positions are given in wavenumbers with an estimated error of $\pm$ 6 cm^{-1}.

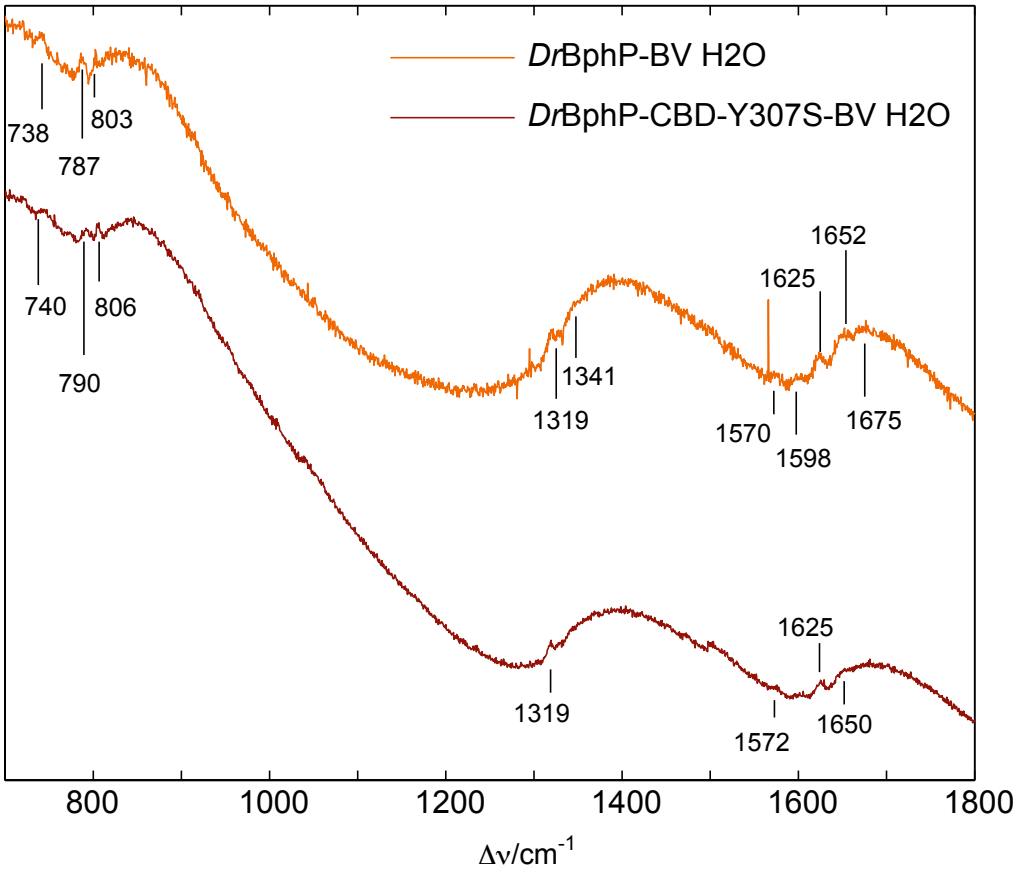

Figure 4.20: FLN spectra in the extended fingerprint region as taken from *Dr*BphP-BV and *Dr*BphP-CBD-Y307S-BV at 6 K. The further experimental parameters can be found in Table 3.1. The peak positions are given in wavenumbers with an estimated error of $\pm$ 6 cm^{-1}.

nals detected on the single-molecule level on Agp1-BV. Only 9 narrow substructures with low relative intensity are found on the high energy side of the broadened bands with widths in the order of 100 cm^{-1}. The broad fluorescence emission bands are observed at $\sim$ 830 cm^{-1}, 1400 cm^{-1} and 1670 cm^{-1} for Agp1-PCD-BV, while the band at the middle position is found shifted to 1350 cm^{-1} for Agp1-PCD-Y166H-BV.

In contrary, the variant with the synthetic chromophore Agp1-PCD-BV15Za shows a highly structured FLN spectrum (as already presented in the temperature-dependent series). In the extended fingerprint region 18 vZPLs and fine structures were determined. The most prominent peaks are found at 744 cm^{-1}, 824 cm^{-1}, 903 cm^{-1}, 996 cm^{-1}, 1040 cm^{-1}, 1299 cm^{-1}, 1315 cm^{-1}, 1572 cm^{-1} and 1608 cm^{-1}.

Figure 4.20 shows the fingerprint region of the FLN spectra taken for the full

length protein *Dr*BphP-BV from *Deinococcus radiodurans* and the point mutated variant *Dr*BphP-CBD-Y305S-BV. Shifting the laser excitation wavelength to the red edge of the absorption spectrum again did not lead to the observation of vibrational resolved vZPLs. The degree of spectral diffusion seems to be similar as for Agp1-PCD-BV and Agp1-PCD-Y166H-BV. Broad fluorescence bands with widths in the order of 100 cm^{-1} are found for both phytochrome samples at similar positions as for Agp1-PCB-BV at $\sim$ 820 cm^{-1}, $\sim$1400 cm^{-1} and $\sim$ 1670 cm^{-1}. In the considered energy interval 10 peak positions were determined for *Dr*BphP-BV and 7 for *Dr*BphP-Y305S-BV. Again the subtle fine structure is mostly observed on the high energy side of the broadened bands.

Figure 4.21 shows the fingerprint region of the FLN spectra taken from the *Rhodopseudomonas palustris* phytochromes and phytochrome variants. The spectra show high vZPL occurrence compared with the spectra from the wild type fragment and point mutated Agp1 and *Dr*BphP-BV samples. For all variants from *Rhodopseudomonas palustris* additionally similar broad fluorescence emission bands as observed for Agp1 and *Dr*BphP-BV phytochromes are observed located at similar positions around 830 cm^{-1}, 1360 cm^{-1} and 1650 cm^{-1}. Thus the spectra seem to be the result of averaging spectral diffusion-affected as well as less spectral diffusion-affected fluorescence emission spectra. The FLN spectra are scaled to similar intensity in the broad band around 1650 cm^{-1}. While for the PCD-containing *Rp*BphP3-BV mutants the intensity decreases approximately linearly from $\sim$ 840 to 1220 cm^{-1} in the wild type *Rp*BphP3-BV a signal increase is found from 1150 cm^{-1} to 1290 cm^{-1}. Minor differences in the overall spectral shape are observed between the wild type *Rp*BphP2-BV and *Rp*BphP3-BV. In the considered energy interval 11 vZPLs and vibrational substructures were identified in the spectrum from *Rp*BphP2-BV, 7 peak positions for *Rp*BphP3-BV and 9 peak positions for *Rp*BphP3-PCD-BV. The vZPL with highest relative intensity is found at 805 cm^{-1} for *Rp*BphP2-BV. This mode seems to be shifted slightly for the *Rp*BphP3 and its variants as a similar intense peak is present at 816 cm^{-1} for *Rp*BphP3-BV, at 820 cm^{-1} for *Rp*BphP3-PCD-BV and at 823 cm^{-1} for *Rp*BphP3-PCD-D216A-BV, respectively. The wavenumber range around 800 cm^{-1} is indicative e.g. for C-H out-of-plane (HOOP) modes of the tetrapyrrole chromophore [178]. The highest occurrence of well resolved vZPLs from this series on phytochromes and variants from *Rhodopseudomonas palustris* is observed for *Rp*BphP3-PCD-D216A-BV with 20 vZPLs and vibrational substructures in the considered spectral range.

The major difference upon introducing the point mutation D216A inside the chromophore binding pocket is observed on the higher wavenumber side of the peak located at 820 nm. A broadened band is observed for the wild type and fragment of *Rp*BphP3-BV and for the D216A point mutant a substructure

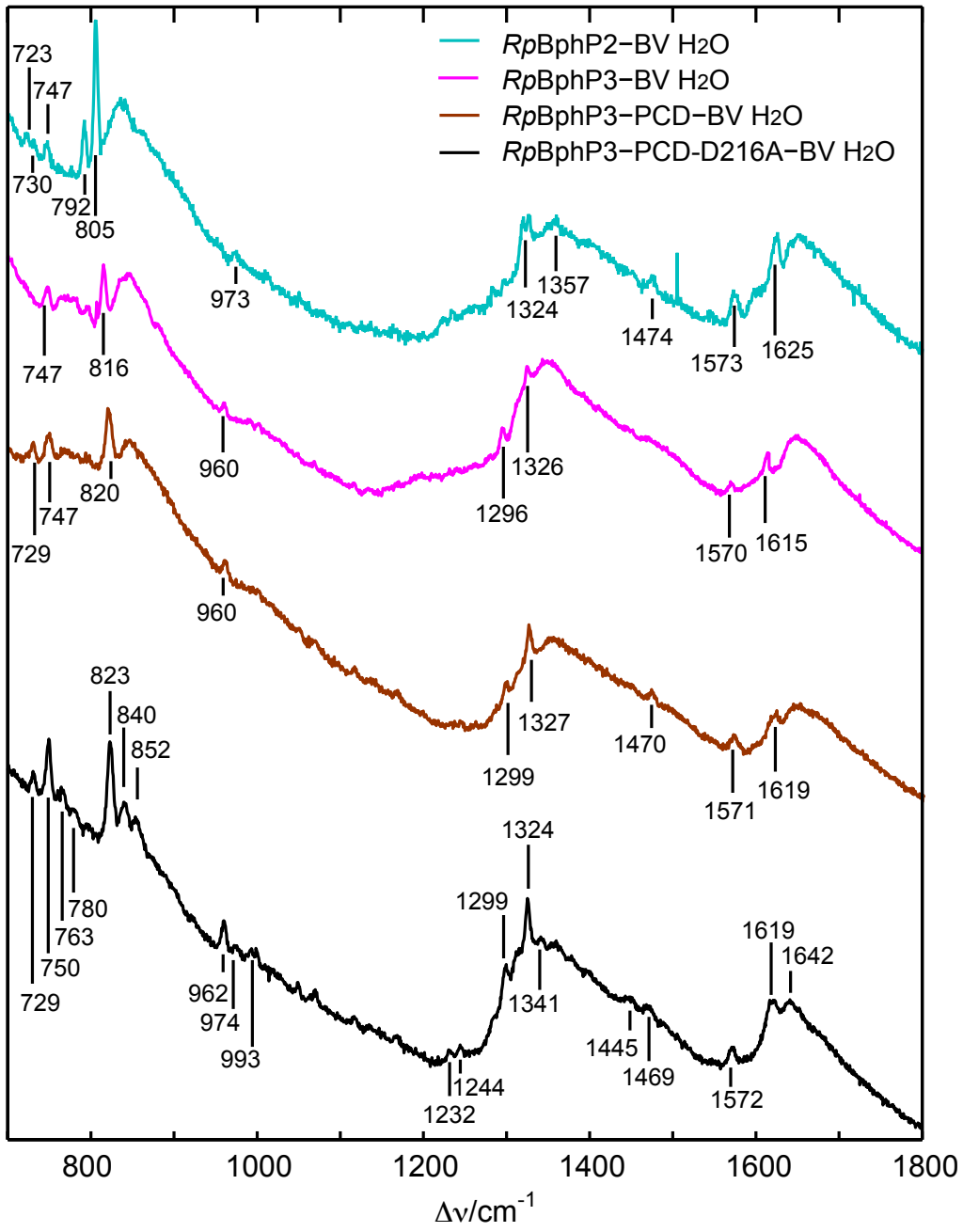

Figure 4.21: FLN spectra in the extended fingerprint region as taken from *Rp*BphP2-BV, *Rp*BphP3-BV as well as from the variants *Rp*BphP3-PCD-BV and *Rp*BphP3-PCD-D216A-BV in protonated buffer solutions at 6 K. The further experimental parameters can be found in Table 3.1. The peak positions are given in wavenumbers with an estimated error of $\pm$ 6 cm^{-1}.

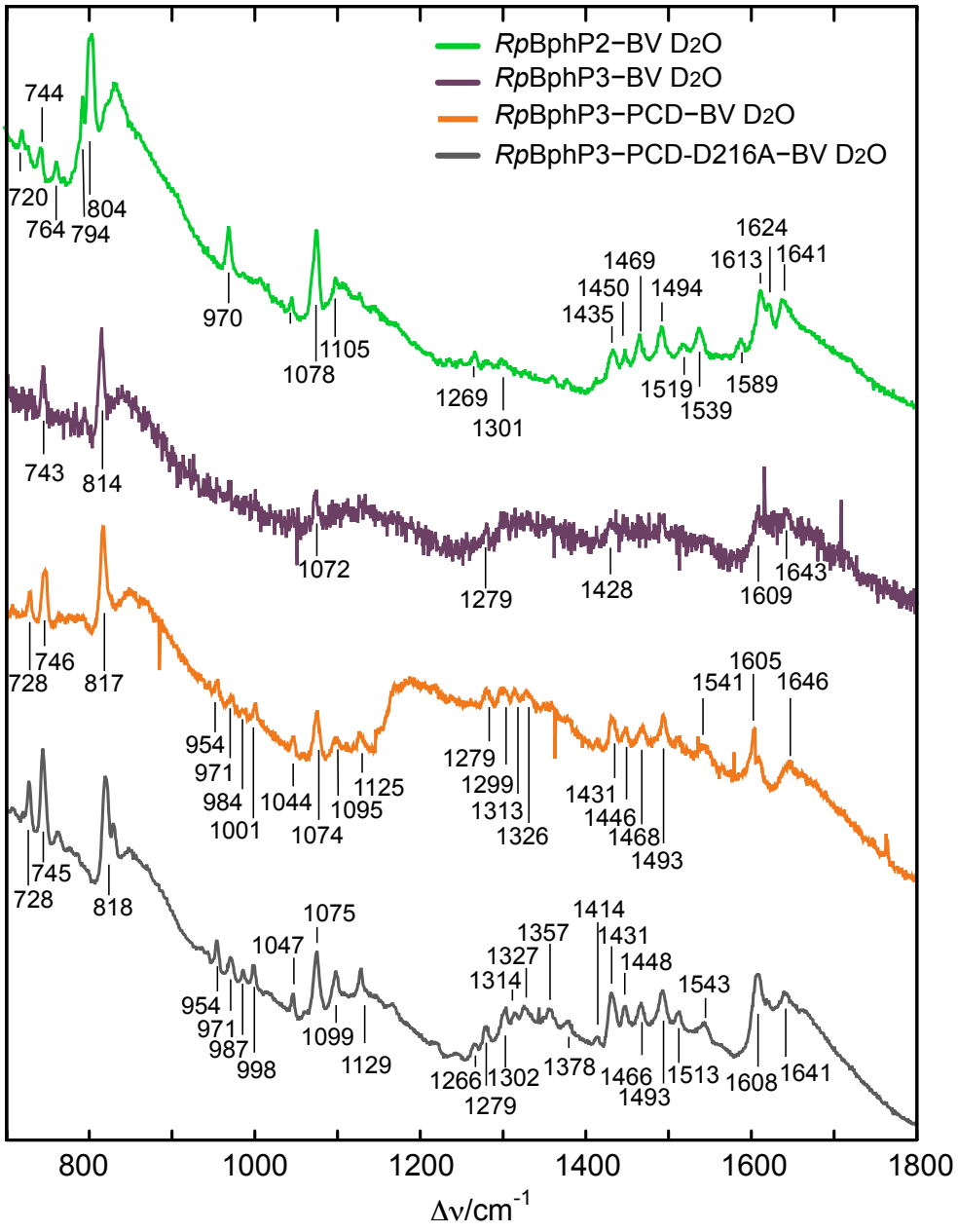

Figure 4.22: FLN spectra in the extended fingerprint region as taken from *Rp*BphP2-BV, *Rp*BphP3-BV as well as from the variants *Rp*BphP3-PCD-BV and *Rp*BphP3-PCD-D216A-BV in deuterated buffer solutions at 6 K.The further experimental parameters can be found in Table 3.1. The peak positions are given in wavenumbers with an estimated error of $\pm$ 6 cm^{-1}.

with two peaks located at 840 cm^{-1} and 852 cm^{-1} is resolved. Additionally two further resolved peaks are observed at the high energy side to the peak located at 750 cm^{-1} with maximum position at 763 cm^{-1} and 780 cm^{-1} as well as on the high energy side to the peak at 962 cm^{-1} with occurrence at 974 cm^{-1} and 993 cm^{-1}. At these positions similarly all other *Rhodopseudomonas palustris* phytochromes show broadened substructures.

FLN spectra were additionally taken in deuterated buffer solutions for the phytochromes from *Rhodopseudomonas palustris*. The respective spectra are shown in Figure 4.22. The overall spectral shape differs from those analyzed in protonated buffer solutions in the ranges 1040 – 1250 cm^{-1} and 1400 – 1570 cm^{-1} where increased broad fluorescence intensity as well as fine structure is present. Upon deuteration specific spectral lines arise and other lines vanish from the spectra. The bands characteristic for protonated samples are found around 1320 cm^{-1} and 1570 cm^{-1} while in deuterium based buffer solution bands arise at $\sim$ 1080 cm^{-1}, 1420 cm^{-1} and 1490 cm^{-1}. This isotope effect indicates that deuteration at exchangeable proton sites occurred. In tetrapyrroles these are the nitrogen sites while the carbon sites are less acidic and show low probability for H/D exchange. The H/D exchange at exchangeable proton sites is associated with a lowering of the frequency of the vibrational modes. A peak which is assumed to stem from the same nitrogen site [121] is located at 1570 cm^{-1} in H_2O and shifts to 1080 cm^{-1} in deuterated buffer. This deuteration effect is clearly observed in all FLN spectra taken on all phytochrome and phytochrome variants from *Rhodopseudomonas palustris*. Upon deuteration of the buffer, it is additionally observed that the number of vZPLs on top of broad fluorescence emission increases significantly. Prominent in the spectra measured in D_2O buffer are features occurring in line multiplets comprising four vZPLs. The positions of these multiplets, as taken from the respective spectrum where these are best resolved are 954/971/987/998 cm^{-1} for *Rp*BphP3-PCD-D216A-BV, at 1047/1075/1099/1129 cm^{-1} for *Rp*BphP3-PCD-D216A-BV, a third at 1279/1299/1313/1326 cm^{-1} for *Rp*BphP3-PCD-BV and a fourth at 1431/1446/1468/1493 cm^{-1} for *Rp*BphP3-PCD-BV.

Discussion

FLN spectroscopy was used to study phytochromes and variants from various species in their P_r ground state, including phytochromes Agp1 from *Agrobacterium tumefaciens*, RpBphP2 and *Rp*BphP3 from *Rhodopseudomonas palustris* and *Dr*BphP-BV from *Deinococcus radiodurans*. First the species-dependent differences as observed by FLN spectroscopy are discussed, before the analysis of the

variants, isotope effects and a qualitative comparison of the FLN results with results from LT-SMS.

Phytochrome species-dependency
The wild-type phytochromes are differently well suited for FLN analysis. Even though all variants were analyzed under similar experimental conditions, line-narrowing occurred to different degrees of magnitude for the phytochromes from different species. For each sample the excitation laser wavelength was tuned over the red edge of the absorption band to obtain line narrowing conditions, however, for Agp1 and *Dr*BphP no line-narrowing in form of vZPL-occurrence in the fluorescence emission spectra was achieved. Only subtle fine structure is present in the strongly broadened fluorescence emission spectra of these phytochromes. In contrast, for both phytochromes from *Rhodopseudomonas palustris*, *Rp*BphP2 and *Rp*BphP3, fluorescence line narrowing was clearly observed. These phytochromes show fine structure with a similar degree of magnitude. Even though these phytochromes have largely different photoreactions at room temperature conditions, with *Rp*BphP2 showing the common $P_r \rightleftarrows P_{fr}$ and *Rp*BphP3 having an unusual $P_r \rightleftarrows P_{nr}$ photocycle, the FLN spectra show high similarity.

Fine structure appearance in FLN spectra is dependent on the spectral diffusion characteristics of the chromophore. From single-molecule analysis on various pigment-protein complexes, including PSI [179] and LH2 complexes [180], it was found that the degree of spectral diffusion of a chromophore is specific for its binding conditions. Thus, the binding conditions in Agp1 and *Dr*BphP share a similarity which is not present in the case of *Rp*BphP2 and *Rp*BphP3. The relevant processes for spectral diffusion were found to include proton dynamics inside the protein [181] (see Section 5.3). Thus, the proton mobility in the first coordination sphere of the pigments of Agp1 and *Dr*BphP in average are supposed to be higher than in *Rp*BphP2 and *Rp*BphP3. The findings on Agp1 corroborate the findings from single-molecule spectroscopy where remarkable line broadenings were observed already on the single molecule level. For several phytochrome molecules the linewidth is similar to the inhomogeneous of an ensemble (see Section 4.2 and Ref.: [182]). In the crystal structures of *Dr*BphP, a highly extended H-bond network was identified in the models at 2.5 Å and 1.45 Å resolution and for Agp1 the resolution of 9 Å is not high enough to determine internal waters. One internal water is found close to the BV pigment in *Dr*BphP, referred to as the pyrrole water, which is in H-bonding distance to the nitrogens from three pyrrole rings, A, B and C as well as towards the highly conserved aspartate (Asp207 in *Dr*BphP) and histidine (His 260 in *Dr*BphP). *Rp*BphP3 crystallized as a heterodimer with respect to the pyrrole water. For the pyrrole water-lacking monomer, the H-bonding network is largely decreased

and mainly includes H-bonding interaction between BV and the conserved aspartate (Asp 216 in *Rp*BphP3). This structural difference in degree of H-bonding is assigned to mainly cause the difference in line-narrowing. For *Rp*BphP2 a high resolution structure is not available. Due to the high similarity in line-narrowing with respect to *Rp*BphP3, it can be supposed, that the H-bonding networks around the pigments in *Rp*BphP2 and *Rp*BphP3 are similar with respect to its ability to facilitate proton dynamics, and thus that the probability to have a pyrrole water near the pigment is small compared to *Dr*BphP and Agp1.

Phytochrome mutants

The tyrosine-to histidine point mutation inside the binding pocket of Agp1 (Agp1-PCD-Y166H-BV) (as visualized in Figure 4.6) has only minor effect on the FLN spectrum compared to the spectrum of the wild type fragment. The tyrosine was found to alter the photoreaction of the cyanobacterial phytochrome Cph1 leading to a fluorescent variant. Though concerning the sensitivity of FLN towards spectral diffusion. The expected alterations concerning proton mobility are inspected. The tyrosine is hydrophobic and the mutant instead is a positively charged histidine. Thus possibly, either the hydrophobic tyrosine rejects protons towards the tetrapyrrole or histidine delivers an extra proton towards the pigment. Thus, the tendency to observe spectral diffusion broadened fluorescence emission is the same or even increased in the case of the mutant. As the FLN spectrum of the wild type is strongly broadened a further broadening cannot be observed.

The point mutant *Dr*BphP-CBD-Y307S-BV which is the variant used for improved crystallization characteristics [107], did not show a difference in FLN compared to the wild-type. Thus, the mutant also showed broadened spectra which do not contain substantial vibrational information. With respect to the remote position of this point mutation from the chromophore site, this result of similar FLN spectra for these samples matches the expectations.

On the other hand for the point mutant *Rp*BphP3-PCD-D216A-BV an effect of the point mutation located in H-bonding distance towards the pigment was observed in FLN. The degree of line narrowing compared to the wild type is increased for this aspartate-to-alanine mutant. The alteration indicates less proton mobility in the first coordination sphere of the pigment. This conclusion is in line with the findings from picosecond time-resolved absorption spectroscopy indicating a less extended H-bonding network for this mutant [122], and with respect to a Pre-Resonance Raman (Pre-RR) spectroscopic study on an analogous mutant from Agp1 (Agp1-D197A-BV), indicating a deprotonated instead of a protonated pigment in the P_r state.

The aspartate-to-alanine mutation in the binding pocket leads to a disturbed photoreaction [121], indicating the need of an extended pyrrole water network

for phytochrome function. By comparison of the FLN spectra from the wild type and from the mutant *Rp*BphP3-PCD-D216A-BV, respectively, aspartate is identified as a part of the chromophore, providing a coordinate along which proton mobility can occur. Thus, most probably aspartate os connected directly to the pigment by an H-bond, which is also suggested based on the structural data for *Rp*BphP3 [94].

The synthesized pigment as chromophore

The phytochrome variant with the synthesized tetrapyrrole pigment, with an additional bond between the Ring C and Ring D of the tetrapyrrole chromophore, and bound to the photosensory core fragment of Agp1 (Agp1-PCD-BV15ZA) has strongly altered spectral characteristics compared to the wild type fragment. This variant shows well resolved fine structure in FLN. For Agp1-PCD-BV15ZA a temperature-dependent measurement series was taken (Figure 4.18). The fine structure shows the expected broadening behavior at increased temperatures, thereby, validating the origin of the narrow line features as vibrational resolved fluorescence emission lines. The differences in fine structure appearance in the FLN spectra taken on Agp1-PCD-BV compared to Agp1-PCD-BV15Za (Figure 4.19) indicate a reduced degree of spectral diffusion for the variant with the synthetically locked chromophore. This might either be to a reduced pigment flexibility or to a less implementation into the hydrogen bond network, as present in the wild type phytochromes. The synthesized pigment senses different protein interactions. Additionally, distinct vibrational peaks are observed for the chromophore with chemically modified pigment structure. By LT-SMS a strongly narrowed fluorescence emission spectrum was detected for a single molecule from the variant with locked chromophore (not shown). The fluorescence emission data obtained from 50 individual phytochromes do not mirror an overall trend to reduced spectral diffusion for this variant compared to the wild type. This might be due to the small number of investigated modules, which possibly do not represent the overall ensemble, and thus, further data allowing for an statistical analysis of the single-emitter profiles with respect to spectral diffusion is needed for an evaluation of data correspondence.

Assignment of vibrational peaks upon isotope effects

For *Rp*BphP2-BV and *Rp*BphP3-BV and its variants FLN spectroscopy was applied on samples with protonated and deuterated buffer solutions. The solvent isotope exchange can be used to identify the vibrational modes containing an exchangeable proton site. For the pigment BV these are the nitrogen sites. A strong isotope effect is observed, affecting the overall fluorescence emission band shape as well as the peak positions of the fine structure. Upon deuteration of the phytochrome samples, the observed oscillator strength in the FLN spectra vanishes remarkably in specific bands (e.g., bands at 1550 – 1570 cm^{-1},

see Figure 4.21 and Figure 4.22), thereby indicating that H/D exchange was efficient. Additionally a large number of additional peaks are found mainly in the intervals 1040 – 1250 cm^{-1} and 1400 – 1570 cm^{-1}. For the analysis of solvent isotope effects in the FLN spectra, all determined vibrational peak positions are collected in Table 4.4, the data for Agp1 and *Dr*BphP variants are additionally included. Strong intensity vZPL contributions are indicated by a superscript 'S'. The wavenumber regions susceptible to deuteration are highlighted in gray. For the phytochrome samples from *Rhodopseudomonas palustris* the proton-associated bands are found at ∼1325 cm^{-1} and ∼1570 cm^{-1}, while the deuterium-associated bands are located at around ∼1080 cm^{-1}, ∼1275, ∼1430 cm^{-1}, 1490 cm^{-1} and ∼1540 cm^{-1}. For the spectra from agrobacterial variants as well as for the phytochrome samples from *Deinococcus radiodurans* analyzed in protonated buffer conditions fine structure at similar positions as in the protonated phytochromes from *Rhodopseudomonas palustris* are observed. For the variant Agp1-PCD-BV15Za however specific bands are found at 903 cm^{-1}, 996 cm^{-1} and 1040 cm^{-1} which are not present in the FLN spectra of all other BV-binding phytochrome variants. Peaks which evolve strongly/or exclusively either in H_2O or in D_2O buffer conditions for the phytochromes and variants from *Rhodopseudomonas palustris* are highlighted by gray boxed in Table 4.4. These are discussed in the following.

In the protonated samples from *Rhodopseudomonas palustris* for all variants an intense peak is found between 1324 cm^{-1} and 1327 cm^{-1} which is at an identical position with respect to the error. DFT calculations indicate at this frequency the N–H in-plane bending of rings A and D [146]. In Pre-RR spectra this mode cannot be assigned unambiguously due to a large number of closely spaced bands in this region stemming also from apoprotein modes. In the FLN spectra from the protonated samples in this region a single peak is found. As the FLN technique is solely chromophore sensitive most probably the peak at 1324 –1327 cm^{-1} is associated with the N-H in-plane bending modes of ring A or D. In deuterated solvents, this peak is either not resolved (*Rp*BphP2, *Rp*BphP3) or is part of a multi-pattern with line spacings of 13–20 cm^{-1} (*Rp*BphP3-PCD-BV and *Rp*BphP3-PCD-D216A-BV). Either a remaining contribution of protonated nitrogen sites is present for these samples or, as this mode is part of a multi-line pattern only observable for samples in deuterated solution, is associated with an in deuterated solvents frequency-downshifted mode. At 1570–1573 cm^{-1} for all variants from *Rhodopseudomonas palustris* a peak is observed in protonated buffer solution which is not observed in samples prepared in deuterated buffer, and thus shows a remarkable isotope effect. This mode is assigned to a N-H vibrational mode. DFT calculations indicate that this frequency is indicative for N–H in-plane bending modes of the two central ring

nitrogen atoms of ring B and C [146]. Pre-RR spectroscopy revealed a shifting of this band in deuterated samples to 1080 cm^{-1}. This shift is clearly observed here also by FLN. A strongly intense peak evolves in the FLN spectra taken in deuterated solvents at a position which in protonated solvents is vZPL silent. High-most intensity is found at 1078 cm^{-1}, 1072 cm^{-1} 1074 cm^{-1} 1075 cm^{-1} for the spectra from *Rp*BphP3-PCD-BV and *Rp*BphP3-PCD-D216A-BV, which show a good signal-to noise ratio, two of the four multiline-patterns are found in this wavenumber region. The high-most intensity peak is part of one multiline pattern with inter-peak distances of $\sim$ 30 cm^{-1}. One peak at lower and two peaks at higher wavenumbers. Based on these observations and the results from DFT calculations [146] we assign the 1570–1573 cm^{-1} mode and the $\sim$ 11072–1078 cm^{-1} mode to the N-H/N-D in plane mode of ring B and C nitrogen atoms, respectively. In the wavenumber region $\sim$ 1419 – 1540 cm^{-1} a further strong isotope effect is observed. A strongly intense four lines comprising pattern contributes to the FLN spectra from *Rp*BphP2-BV, *Rp*BphP3-PCD-BV and *Rp*BphP3-PCD-D216A-BV (while the noise affected spectrum from is not allow for a peak assignment). Again the inter-peak distances are measure between $\sim$ 15 and 30 cm^{-1}. This region similarly can be identified as being related to the exchangeable nitrogen sites of the tetrapyrrole in its deuterated form. Concerning the peak positions found for the phytochrome samples from *Rhodopseudomonas palustris* prepared in protonated buffer with the phytochromes samples from Agp1 and *Dr*BphP similar vibrational substructure is found at $\sim$1320 and $\sim$1570 cm^{-1}. We assume that equivalent sites are responsible for these peaks as the considered phytochromes all bind the same BV pigment, or an alternate BV15ZA tetrapyrrole chromophore modified only between two tetrapyrrole rings. Thus peaks at $\sim$1320 and $\sim$1570 cm^{-1} for all protonated phytochromes are attributed to modes involving N-H vibrations at ring A/D and B/C, respectively.
A mode which does not show an isotope effect but is present for all samples showing an intense peak contribution in the FLN spectra is found at $\sim$ 800 cm^{-1}. DFT calculations predict C-H out-of-plane region in this region of the spectrum [146]. As carbon sites do not harbor exchangeable proton sites at the pH conditions used, no isotope effect is expected for these lines. Thus these lines are in accordance to the unchanged peak positions in FLN attributed to C-H out-of-plane modes. Similar in the range of C=O stretching modes expected at 1580 – 1700 cm^{-1} no major isotope effect is observed. All phytochrome samples show peaks in this region, thereby indicating that the electronic transition couples to the C=O modes.

Proton dynamics and line-narrowing
Apart from the peak-shifts occurring upon deuteration of the solvent, a further

effect is observed. The number of lines and their relative intensity significantly is increased compared to the broad fluorescence emission bands present in all FLN spectra measured for the different phytochromes and phytochrome variants. Thus, the degree of spectral diffusion of the BV chromophore seems to be reduced in the phytochromes from *Rhodopseudomonas palustris* upon deuteration (Figure 4.21). As derived from solvent isotope exchange experiments on PSI, proton dynamics strongly influence the degree of spectral dynamics of protein-bound pigments [64] (see Section 5.3). The increased line-narrowing efficiency upon usage of deuterated solvents corroborates these findings.

Spectra from sub-ensembles and single molecules
With respect to the findings on the fluorescence emission of individual phytochrome molecules, the broadened spectral bands observed for Agp1 by FLN can be understood. Strong line-broadenings due to spectral diffusion are observed for most individual phytochromes. The broadening are in parts as large that the line widths of the fluorescence emission bands from an individual phytochrome molecule approach widths expected for molecular ensembles. By LT-SMS phytochrome molecules selectively can be investigated. As the phytochrome molecules are strongly heterogenous with respect to spectral diffusion. From a sub-ensemble of phytochrome molecules, showing minor spectral diffusion, vibrational information was obtained. For these individual phytochrome the vibrational fine structure was substantially better resolved than achieved by FLN spectroscopy.

Compared to FLN there is a further advantage of the single molecule method. FLN allows for the analysis of maximal one substate with red-most absorption. In contrast, LT-SMS is in principle able to provide informations of the entire contributing substates. The different peak positions between the different phytochrome molecules and in comparison with the FLN spectrum are not well understood yet. For example the mode found for all phytochrome species in FLN at ~ 1575 cm^{-1} only is observed with minor occurrence on the single-molecule level. A way to a more comparative analysis would be to measure single phytochrome molecules under similar excitation conditions to obtain spectra from a large number of molecules with identical site energies as excited by the FLN excitation laser. The recorded LT-SMS spectra stem from phytochrome molecules with their purely electronic 0-0 transitions between 680 and 702 nm while the excitation wavelength used for FLN measurements was located to longer wavelength at 714 nm for Agp1. Therefore, a sub-ensemble of molecules with lower electronic excitation energies was analyzed. For a future study using LT-SMS in combination with FLN, the following measurement conditions seem promising to obtain spectra from a similar subset of molecules by LT-SMS and FLN. The excitation should largely be shifted to longer wavelength to 714 nm minus the

width of the cut off filter not to cut parts of the spectra. Then high probability for detecting fluorescence emission from individual molecules with their 0-0 transition at 714 nm is expected.

A_1 - H2O	A_2 - H2O	A_3 - H2O	D_1 - H2O	D_2 - H2O	R2_1 - H2O	R3_1 - H2O	R3_2 - H2O	R3_3 - H2O	R2_1 - D2O	R3_1 - D2O	R3_2 - D2O	R3_3 - D2O
		720			723		729	729	720		728	S 728
	744	S 744	738	740	730 747	747	747	S 750	744	743	S 746	S 745
			787	790	S 792			763	764			
793	791							780	S 794			
808	807	S 824	803	806	S 805	S 816	S 820	S 823	S 804	S 814	S 817	S 818
832	832							S 840				
								852				
		879										
		S 903										
						960	960	S 962			954	S 954
					973			974	S 970		971	S 971
								993			984	S 987
		S 996									1001	S 998
		S 1040									1044	S 1047
									S 1078	1072	S 1074	S 1075
											1095	S 1099
									1105			
		1132									1125	S 1129
		1196										
								1232				1266
								1244				
		1288							1269	1279	1279	1279
		S 1299				S 1296	1299	S 1299	1301		1299	1302
		S 1315	1319	1319							1313	1314
1329	1326	1330			S 1324	S 1326	S 1327	S 1324			1326	1327
1356		1343	1341		1357			1341				1357
		1408										1378
									S 1435	1428	S 1431	S 1414 S 1431
								1445	S 1450		S 1446	1448
		1475			1474		1470	1469	S 1469		S 1468	S 1466
									S 1494		S 1493	S 1493
									1519			1513
									S 1539		1541	1543
1575	1572	S 1572	1570	1572	S 1573	1570	1571	1572				
									1589			
1602	1597	S 1608	1598			S 1615	1619	S 1619	S 1613	1609	S 1605	S 1608
1627	1623		1625	1625	S 1625				S 1624			
1654	1651		1652	1650				1642	S 1641	1643	1646	1641
			1675									

Table 4.4: Peak positions in the extended fingerprint region from 800 –18000 cm^{-1} as determined from the 6 K FLN spectra taken on the various phytochrome variants (A_1: Agp1-PCD-BV, A_2: Agp1-PCD-Y166H-BV, A_3: Agp1-PCD-BV15Za, D_1: *Dr*BphP-BV, D_2: *Dr*BphP-CBD-Y307S-BVR2_1 *Rp*BphP2-BV, R3_1: *Rp*BphP3-BV, R3_2: *Rp*BphP3-PCD-BV, R3_3: *Rp*BphP3-PCD-D216A-BV). On the left peak positions for the protonated samples and on the right for deuterated samples as measured for the phytochromes from *Rhodopseudomonas palustris* are given in wavenumbers with an error of $\pm$ 6 cm^{-1}. The peak positions with a clear kinetic isotope effect are highlighted in bold font and by the symbols (circle for protonated bands and stars for deuterated bands). Strong peaks intensities are indicated by a superscript 'S'.

5

SINGLE-MOLECULE SPECTROSCOPY ON PHOTOSYSTEM I

The functionality of PSI is in analogy to a solar cell. The light activated charge separation inside the protein can be compared to the light induced promotion of an electron into the conduction band of the semiconductor material. The largest difference between these two systems is the length scale of charge separation which is in the order of micrometers for the solid state device, while it is on the scale of nanometers in the protein. The function of PSI, its spectroscopic characteristics as well as its molecular structure are introduced in this section. Additionally, open questions concerning the role of specific low energy chlorophyll states are sketched out.

5.1 Photosystem I: A Key Protein in Oxygenic Photosynthesis

The first systematic experiments on photosynthesis were already performed in the early 18^{th} century. A review on the main achievements in the understanding of the photosynthetic reaction during the last three centuries is given in Ref.: [183]. A list with the vast number of Nobel prizes which were awarded in the research field of photosynthesis is given in Ref.: [184]. The history of photosynthesis research shows that for an ultimate understanding of the photosynthetic reactions, expertise from all natural sciences, including biology, chemistry, biochemistry and physics is needed.

The Photosynthetic Reaction

The photosynthetic reaction describes the energy conversion from light energy into chemical energy as used by plants and other photosynthetic active organisms like cyanobacteria. The net reaction of photosynthesis is:

$$CO_2 + H_2O \xrightarrow[Chl]{h\nu} C(H_2O) + O_2, \tag{5.1}$$

summarizing that light activation leads to the formation of carbohydrates (biomass) and oxygen, from carbon dioxide and water. For this reaction, protein-bound chlorophylls (Chl) are the catalyst as first identified by Willstätter and Stoll who performed detailed chemical investigations on Chl. For his research on plant pigments, Willstätter was awarded a Nobel Prize in Chemistry in 1915. A cooperative network of proteins partly bound to a membrane was identified as the functional building blocks of the photosynthetic reaction. The membrane to which these complexes are bound is referred to as the thylakoid or photosynthetic membrane and comprises four transmembrane protein complexes which are the Chl containing pigment-protein complexes PSII and PSI, cytochrome b6f (Cyt b6f), and ATPase. Figure 5.1 shows an illustration of the photosynthetic membrane and its location inside the chloroplasts within the plant cells in the leaves of the plant.

During the cooperative reaction of PSII, Cyt b6f, PSI and ATPase, oxygen is produced by a water splitting reaction at the PSII site, and a light-induced charge gradient created in PSI leads to the formation of the reducing equivalent nicotinamide–adenine dinucleotide phosphate NADPH from $NADP^+$ at the soluble protein site of ferredoxin–NADP reductase (FNR), involving an electron transport via the mobile protein ferredoxin (FD). The photoreaction, furthermore, induces a proton gradient which drives the molecular motor ATPase to rotate. The rotation causes accessibility of the catalytic site driving the reaction from adenosine diphosphate (ADP) to adenosine triphosphate (ATP), the cellular energy currency driving multiple chemical reactions in cells. The photosynthetic dark reaction which is the photosynthetic carbon reduction cycle was discovered in the years from 1948 to 1954 by Calvin, Benson and Bassham [183]. Calvin was awarded the Nobel Prize in Chemistry in 1961. In the dark reaction of photosynthesis, NADPH and ATP are used for the formation of the carbohydrates, or storable sugar.

The light-driven reaction relies on the cooperative work of two reaction centers which are part of the pigment-protein complexes PSII and PSI. Reaction centers are the sites of photochemical action, where, upon excitation, a charge separation takes place. Both complexes bind hundreds of Chl molecules. In 1936

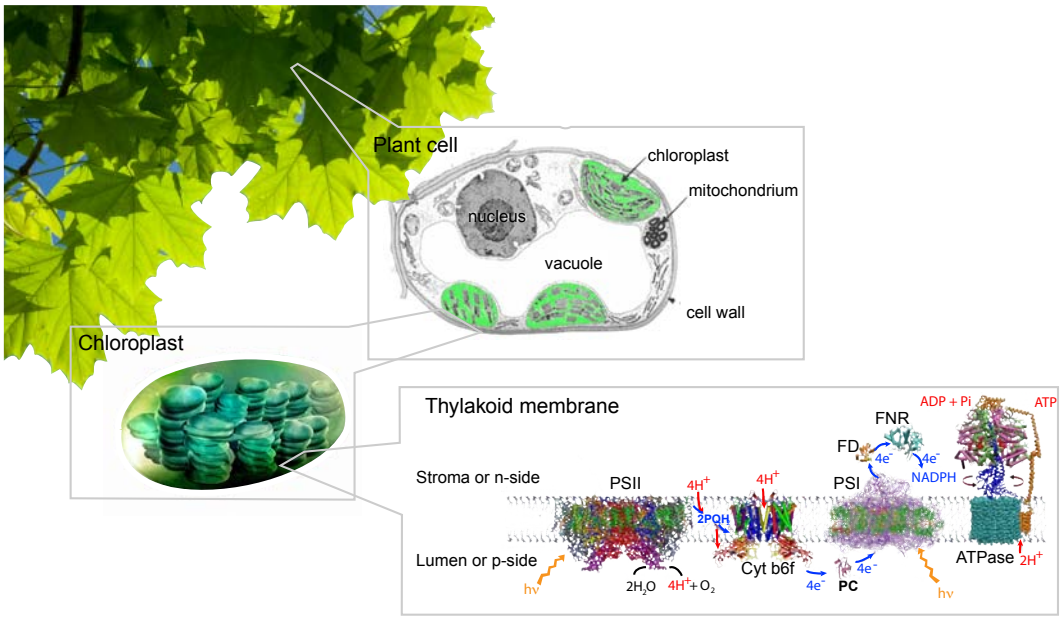

Figure 5.1: Localization of the photosynthetic thylakoid membrane in the chloroplasts in plant cells. During the cooperative reaction of PSII, Cyt b6f, PSI and ATPase, oxygen is produced by a catalyzed water splitting reaction at the PSII site, an light induced charge gradient created in PSI leads to the formation of $NADPH^+$ from NADPH at the soluble protein site of FNR. The photoreaction-induced proton gradient drives the ATPase catalyzing the formation from ADP to ATP. Details of the reaction can be found in the text. The picture of the photosynthetic membrane were taken with modifications from Ref.: [185] and illustration of the chloroplast from Ref.: [186].

Emerson and Arnold found that only one out of several hundreds of cooperating Chl molecules bound to the pigment-protein complexes PSII and PSI are directly involved in photochemistry. Thereby formulating the basis of a photosynthetic unit, which is a Chl antenna system plus a Chl reaction center. The reaction centers each comprise two Chl molecules, called special pairs. The special pair Chl of PSII and PSI are called P680 and P700, referring to their main absorption wavelength, respectively [187]. In both complexes, the special pair releases an electron upon excitation which is funneled via an electron transfer chain from the special pair sites, which are on the lumenal side of the membrane, towards the stromal side of the membrane [188]. The theoretical description of electron transfer reactions was developed by Marcus during 1956 to 1965, and he was awarded the Nobel Prize in chemistry in 1992. Also in the beginning of the 1960s Hill and Bendall introduced the famous 'Z-scheme', summarizing the redox potentials involved in the two light reactions upon excitation of the reaction centers of PSII and PSI [188], illustrated in Figure 5.2.

After excitation of P680 in PSII the released electron is transferred via a pheo-

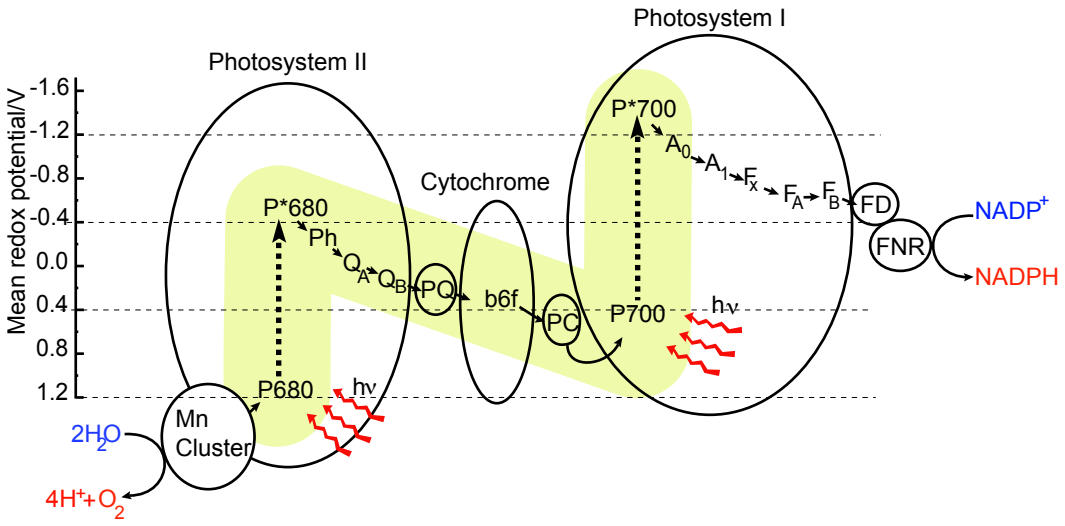

Figure 5.2: The Hill-Bendall or Z-scheme for photosynthesis. The two reaction centers of PSII and PSI work in series to accomplish the reaction of: $2H_2O$ + $2NADP^+ \rightarrow O_2$ +2NADPH + $2H^+$. During the light reaction in the cooperative work of PSII, Cyt b6f and PSI additionally a proton gradient is established which drives the formation of ADP to ATP by interaction with ATPase (not shown). The mean redox potentials involved in the two-light reactions of PSII and PSI involving different electron transfer states form a 'Z' in direction of the potential, which is highlighted in yellow.

phytin (Ph) to a tightly bound plastoquinone (Q_A) and a plastoquinone that binds and unbinds from PSII (Q_B) [189]. The released electron from PSII is transferred via a plastoquinone pool (PQH2) to the cytochrome *b6f* complex. On the lumenal side, PS II captures its missing electron from water molecules in a unique water splitting reaction occurring at the manganese cluster sites of PSII. Thereby, free oxygen and protons are generated.

In PSI, the electron released from the primary donor P700 is transferred via a primary acceptor A_0 composed of chlorophyll *a* (Chla) then to the A_1 state which is a vitamin K_1 and then reaches the iron sulfur clusters referred to as F_X, F_A, F_B. EPR analysis on single crystals from a complex of PSI together with the in cells mobile protein FD indicate that the mid redox potential of F_B changes upon FD-binding to PSI, such that its mean redox potential falls below F_A's [190]. FD can deliver the electron to the ferredoxin–NADP reductase (FNR), where the reduction of nicotinamide–adenine dinucleotide phosphate $NADP^+$ into NADPH takes place. Charge neutralization of the reaction center of PSI occurs via electron delivery from the electron carrier plastocyanin (PC), which is the small and mobile protein accepting electrons from cytochrome b6f complex in the PSII cycle. According to its interaction with the mobile proteins PC and FD after light activation, PSI is also referred to as the light-driven plasto-

cyanin:ferredoxin oxidoreductase.

For most analytical methods used today to unravel the molecular mechanisms of the photosynthetic reaction purified protein samples are required. For the membrane-bound PSI and PSII, extraction from the membrane was first achieved by Vernon, Shaw, Ogawa and Raveed in 1971 [191]. This biochemical achievement paved the way for detailed analysis of the individual protein complexes involved in the photosynthetic reaction, and ,thus, is regarded as a milestone in photosynthesis research.

Today, photosynthesis research focuses mainly on the understanding of the photosynthetic reaction occurring at the protein and sub-protein level. Besides enhancing the knowledge of the molecular processes occurring in the natural system, the current photosynthesis research is motivated by the aim of mimicking the mechanisms from nature for developing technical devices for energy conversion, referred to as artificial photosynthesis [192]. Here, an optical spectroscopic method with sensitivity to single PSI complexes is used to obtain information on the mechanisms relevant for the natural system.

Photosystem I

The reaction center of PSI can either be excited directly by a photon or by an exciton delivered by the antenna system of PSI. The antenna system is composed of ~ 90 Chla molecules which are involved in the absorption and excitation energy transfer (EET) process towards P700. Specific pigment-protein interactions as well as pigment-pigment interaction make the Chla molecules act as efficient light-harvesting antennas [193–195]. In the following paragraph, the effect of the protein-specific interactions on the optical properties of Chla is presented by comparing Chla absorption in solution and as cofactor of PSI.

Optical properties of Chla in solution and as cofactors of PSI
Chla is a planar molecule composed of a chlorin ring that coordinates an Mg^{2+} ion and a long phytol side chain (see Figure 5.3a). In addition to four pyrrole rings, a fifth isocyclic ring is present in the Chla structure. In comparison to the linear tetrapyrrole pigment of the bilin family used as the photosensory pigment in phytochromes the cyclic ring conformation of Chla is rather rigid and does not allow for conformational changes as occurring during the photoisomerization of the tetrapyrrole chromophores in phytochromes (see Chapter 4). An absorption spectrum of monomeric Chla in solution is shown in (Figure 5.3b). The absorption of Chla in the red and orange regions of the visible spectrum is primarily due to the $S_0 \rightarrow S_1$ transition, also called the Q_Y transition. The absorption in the green and yellow regions is primarily due to the $S_0 \rightarrow S_2$

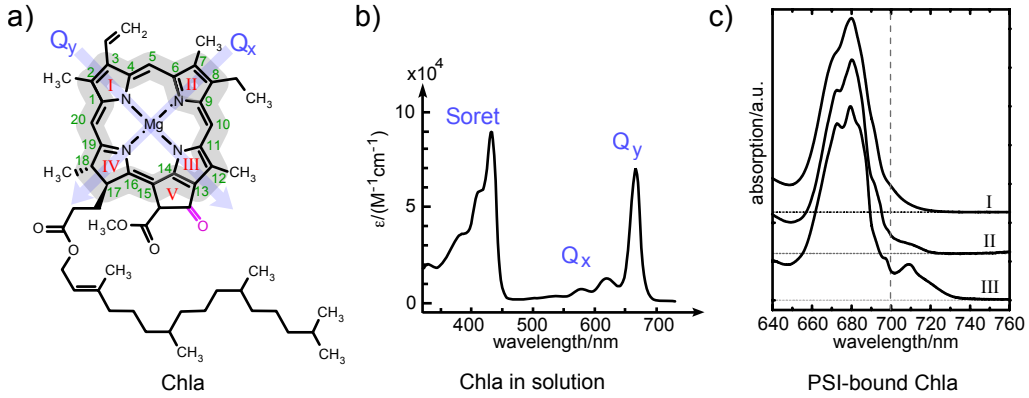

Figure 5.3: a) Chlorophyll *a* (Chla) molecular structure. The common numbering of the pyrrole rings and C-atoms of the π-conjugated system (visualized in gray) as well as the directions of Q_X and Q_Y are given. A keto-group is found at Ring V and highlighted in magenta. b) Absorption spectrum of Chla in solution (toluene) as taken from [196]. The peak assignments to specific transitions between molecular orbitals are indicated. c) Low-temperature absorption spectra of PSI complexes from different species, including a 77 K spectrum from PSI from *Synechococcus* PCC7002 (I) taken from [179], 6 K spectra of PSI from *Synechocystis* (II) and a 6 K spectrum of PSI from *Synechococcus* (III) as taken from [197]. The position of the P700 absorption position is indicated by a dashed line. The absorption of so-called antenna pigments is attributed to the Chla absorbing at the blue side of P700 and the longer wavelength Chlas are referred to as the 'red Chl' states.

transition, also called the Q_X transition [198]. The transition dipole for the Q_Y transition is directed approximately along the N(I)-N(III) axis and the transition dipole for the Q_X transition is directed approximately along the N(II)-N(IV) axis (see Figure 5.3a). Transitions involving higher excited states, $S_0 \rightarrow S_{n>2}$, are located in the blue and higher energy regions of the absorption spectrum and form the so-called B- or Soret bands. The two peaks with highest extinction are found in the blue at $\sim$ 430 nm as part of the Soret band and in the red in the range of the Q_Y transition at wavelengths between $\sim$ 660 nm – 670 nm, dependent on the solvent [198]. Figure 5.3c shows the wavelength region >650 nm of low temperature absorption spectra of PSI complexes from three different cyanobacteria which solely stem from the Q_Y transitions of protein-bound Chla without overlapping absorption from other protein constituents. The PSI absorption spectra show structured bands. In contrast to the Chla spectrum in solution, which shows one inhomogenously broadened band related to the Q_Y transition, for PSI structured bands indicating multiple spectral states are observed. The main absorption peak for the different PSI complexes is found at $\sim$ 680 nm and has a shoulder on the short wavelength side at 672 nm. In the

case of PSI from *T. elongatus* an additional peak at 708 nm is observed. The dashed line in Figure 5.3c indicates the absorption position of the reaction center of PSI at 700 nm, which originates from a Chla/Chla' dimer. Red-shifted to 700 nm, peaks are observed with different oscillator strengths and wavelength positions for the PSI from different species and with inhomogeneous widths as large as 200 to 400 cm $^{-1}$ [199]. These spectral contributions on the low energy side of P700 are called the red pool or the red-most Chls [197]. When the excitation energy is localized within this red pool Chla, the subsequent excitation from P700 to P700* requires additional activation energy, e.g. thermal energy from the phonon bath.

The red Chla absorption contributions for the three cyanobacterial PSI complexes *Synechococcus* PCC7002, PSI from *Synechocystis* PCC6803 and PSI from *T. elongatus* are described in more detail because these are the Chla states analyzed in this work. PSI from *Synechococcus* PCC7002 above 700 nm is one of the PSI complexes with minor red Chla content. The weak featureless red tail extending up to 720 nm in the absorption spectrum is attributed to the absorption of two to three Chla molecules [197]. A decomposition of the absorption into Gaussian bands shows that the intensity above 700 nm can be modeled by a single band with its maximum at 708 nm (C708) [179]. For trimeric PSI from *Synechocystis* PCC6803 a decomposition of the absorption spectrum indicate the presence of four to five Chla molecules being responsible for the broad absorption band at 708 nm (C708) [199, 200]. By hole-burning spectroscopy underlying states with maximum absorption at 706 nm (C706) and 714 nm (C714) were identified [201]. PSI from *T. elongatus* has long wavelength optical properties indicative of four Chla pools formed by 9–11 Chla [202]. The maxima in the low temperature absorption are at 708 nm (C708) and at 719 nm (C719) [202]. It was found by hole burning spectroscopy that an underlying state with absorption maximum at 715 (C715) contributes to the long wavelength absorption [203] and an additional contribution to this band was identified by single-molecule spectroscopy, having its fluorescence emission maximum at 745 nm and being attributed to an absorbing state at 735 nm (C735) [15].

With respect to the absorption spectrum of Chla in solution it is found that different binding situations inside the protein lead to a set of different electronic energies of the Chla molecules, referred to as site-energies. The absorption is mainly red-shifted by $\sim 10 - 30$ nm and partially, dependent on the PSI species, even more red-shifted by 20 – 40 nm. In other PSI systems the absorption of Chla is tuned even further to the long wavelength range by up to ~ 80 nm [204]. Site-energy calculations based on the analysis of the electrostatic interactions in the 2.5 Å structural model (presented below) indicate that the majority of site-energies of Chla are determined by interactions with a large number of

≈20 amino acid residues [205], additionally the dense packing of the pigments in PSI allows for energy level shifts due to strong excitonic coupling.

Molecular structure of PSI

PSI is one of the largest protein complexes in nature. Cyanobacterial PSI occurs as a trimer with a molecular weight of 3 x 356 kDa (1 068 k Dalton). PS I core complexes of all organisms consist of two large subunits, PsaA and PsaB, and at least eight smaller subunits. A high resolution structural model with 2.5 Å resolution is available for PSI from the thermophilic cyanobacterium *T. elongatus* [11]. Comparison with a 3.4 Å structure of PSI from pea shows that Chla organization within PSI from cyanobacteria and higher plants is largely conserved [206]. Thus, the structure for PSI from *T. elongatus* is taken as a model for PSI in general. Beside the $\sim$ 100 Chla, $\sim$ 22 carotenoids and two phylloquinone molecules, as well as three 3 [4Fe4S] clusters and 4 lipids are the cofactors of monomeric PSI from *T. elongatus*. Figure 5.4 visualizes the structure of PSI from *T. elongatus*. As in cyanobacteria PSI occurs as a trimer [207], three monomers were graphically combined for the lumenal top view (Figure 5.4a). The diameter of the trimeric PSI is $\sim$ 20 nm. For the side view given in (Figure 5.4a) a monomer was taken for better visibility of the structural details. The protein backbone is shown in yellow, Chlas in green, only the candidates for the red state Chlas (see below) in red and the special pair Chls in blue. The top view shows that the special pair is located in a central position of a monomer. The antenna Chla are found distributed over the whole complex, while a square lattice like ordering is observable. The red Chl candidates are located at nearest distances from the special pair by about 2.5 nm. So called accessory Chl pigments are found close to the reaction center. The iron sulfur clusters are best seen in the side view. While the special pair is found on the lumenal side, the iron sulfur clusters are found on the stromal side (orange/gray). They are shifted from the membrane plane. The ordering upon increased distance is F_X, F_A, F_B. In the transmembrane direction, the Chla molecules cover the thickness of the membrane, which measures $\sim$ 5 nm. The Chla have high concentrations on the outer lumenal and stromal sides. The organization of the lumenal and stromal Chlas are shown separately in Figure 5.5 (a dashed line added to the side view of PSI in Figure 5.4b indicates the position where the Chlas were divided into lumenal and stromal ones). In the trimeric representation of the lumenal and stromal Chlas shows a well ordered network, which is not obvious in the typical representations of PSI as a monomer or as the full highly complex structure of the trimer.

The red chlorophyll candidates

The dense packing and relative orientation of some Chla molecules in PSI can lead to strong excitonic coupling, and occupation of the lower lying common

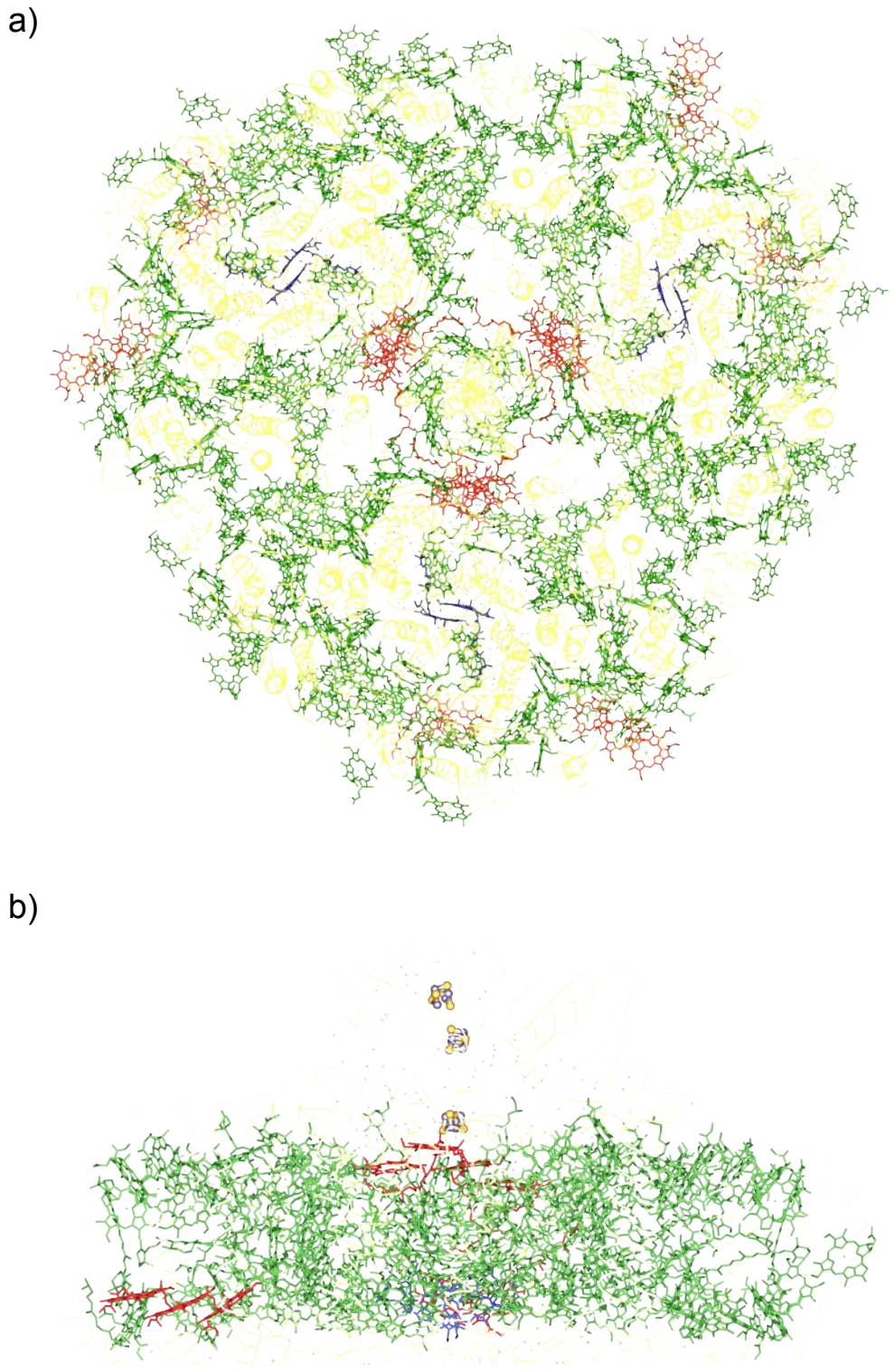

Figure 5.4: Structure of the trimeric PSI (Pdb-entry: 1JB0)[208]). a) Top view and b) side view with respect to the thylakoid membrane plane. The Chlas are shown in green, the red Chla candidates in red and the Chla/Chla' dimer of the reaction center P700 in blue. The protein backbone is shown in yellow, the FeS cluster in orange/gray and oxygens from internal water in blue.

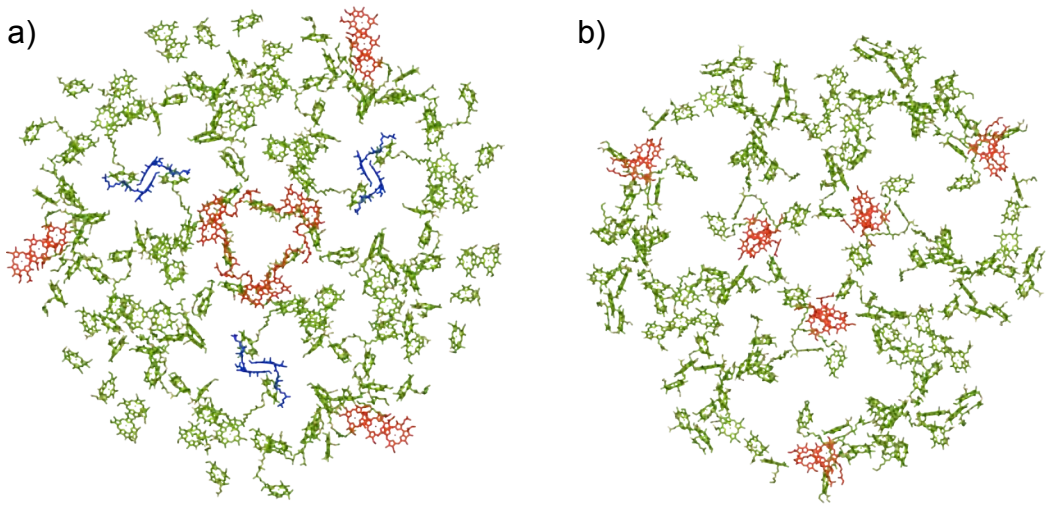

Figure 5.5: a) Lumenal side Chlas and b) stromal side Chlas as well as the FeS clusters of PSI. The division line is shown in Figure 5.4. Chlorophylls are shown in green, the special pair Chla/Chla' in blue and the red Chla candidates in red. FeS clusters in yellow/orange.

ground states of the interacting pigments [11, 208]. And thus, leading to a down shift in the electronic excitation energy. Only a few Chla molecules are found with minor distances so to be considered as being excitonically coupled. Site-energy calculations, based on the structural model, encounter three dimers and one trimer of Chla molecules to be considered as the red Chla candidates [11, 208, 209]. These dimers and the trimer are concentrated near the trimerization axis on both sides of the membrane and on the edge of the complex (see Figure 5.4) and Figure 5.5), two on the lumenal and two on the stromal side of the membrane per monomer. Experimental studies comprising CD-, low temperature absorption-, Stark- and hole burning spectroscopy corroborate excitonically coupled Chla as being responsible for the red-most Chla states of PSI [199, 210–212]. A large permanent dipole change of $\sim$ 2.3 D [212] and large Huang-Rhys factors (S$\sim$2.0) [201] were observed for the red-most Chla states. Although site-energy calculations are now able to reproduce the main features of the ensemble spectroscopic data, the assignment from site energies to Chla states as well as the excitation energy dynamics remain elusive [194, 209]. A red state sensitive experimental method is used in this work to obtain further details on the spectral properties and on the excitation energy transfer in PSI.

Excitation energy transfer in PSI

The structural and spectral characteristics of the protein-bound Chla make them an ideally suited light-harvesting antenna system. Calculation of the Förster critical distance R_0 for spectrally identical Chla with an orientation factor κ^2 of 1 gives distances of R_0 = 8 – 9 nm [28]. Based on the structural model of

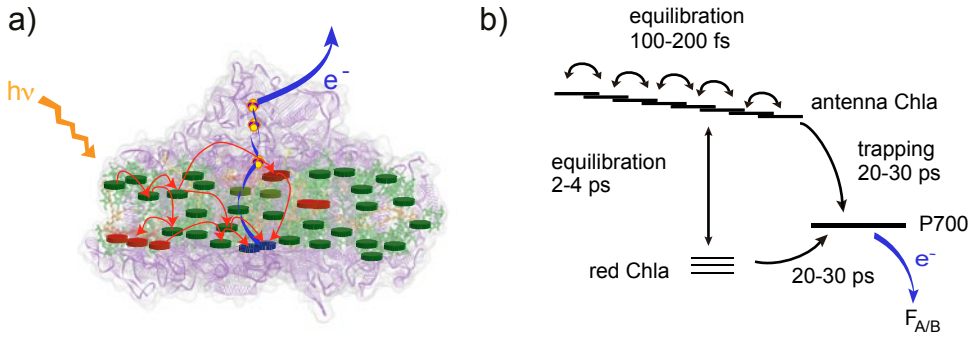

Figure 5.6: Excitation energy transfer in PSI at ambient temperatures. a) Molecular structure of PSI with an overlaid scheme of the EET. b) Energy level scheme and transfer rates. Excitation equilibration times between the antenna states and with the red Chla as well as the time for trapping of excitation by P700 were taken from Ref.: [215] values were measured for PSI from *Synechocystis* PCC6803. The electron transfer towards the proximal iron sulfur centers F_A and F_B after excitation of P700 is indicated.

PSI, the Chla pigments are connected to at least four neighbors with FRET rates > 300 fs^{-1}, forming an approximately two-dimensional square lattice for excitation energy transport [213]. For a minor fraction of Chla molecules in PSI also EET via the Dexter mechanism should be possible. Although the total number of low energy Chlas is species-dependent and small, between 3-10% of the total number of Chlas in the PSI core antenna, they have a pronounced effect on the energy-transfer and trapping dynamics in PSI which is evident from time-resolved and steady-state spectroscopy experiments [197] and model simulations based on X-ray structure models [194, 214]. The equilibration times are reported to vary between 3.4 to 15 ps and the trapping components of excitation energy by P700 between 23 to 50 ps for PSI complexes from different cyanobacterial species [200]. The different dynamics were found to be directly related to the content of red Chla [200]. In Figure 5.6a an illustration of the EET overlaid on the molecular structure of PSI and an energy level scheme is given. At ambient temperatures all Chla, including the red Chl, can funnel the excitation energy towards the reaction center P700. The time constants for equilibration of excitation energy after absorption of a photon between the higher lying antenna states and the red Chla for PSI from *Synechocystis* PCC6803 [215] are included in the scheme Figure 5.6b. Also the trapping time of excitation energy from the antenna by P700 is given [215]. The charge separated state created upon excitation of P700 inside PSI reaches up to the proximal iron sulfur clusters, and is additionally indicated.

At room temperature, the uphill energy migration from the red Chla states towards P700 is efficient. It has been shown that the quantum yield of P700 ox-

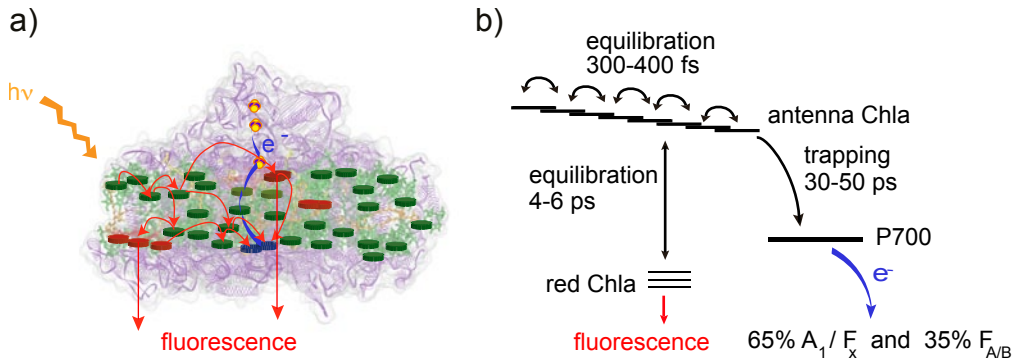

Figure 5.7: Excitation energy transfer in PSI at low temperatures. a) Molecular structure of PSI with an overlaid scheme of the EET at low temperature conditions. The red Chla low temperatures act as deep traps for excitation energy and partially releases excitation energy via fluorescence emission. b) Energy level scheme and transfer rates. The fluorescence emission at LT is indicated. Excitation equilibration times between the antenna states and with the red Chla as well as the time for trapping of excitation by P700 were taken from Ref.: [216] values were measured for PSI from *Synechocystis* PCC6803 at 77 K. The heterogenous electron transfer traps at low temperatures from Ref.: [217] as measured for PSI from *T. elongatus* at 77 K are included.

idation remains independent of the exciting wavelength up to 760 nm [218]. Because of the intriguing consequence that these Chla, can only take part in EET towards the reaction center by the use of extra thermal energy for the energetically upward transition towards P700, their function remains puzzling and is the subject of a wealth of investigations [15, 181, 202, 210, 216, 219, 220]. The question concerning the physiological role of the red pool is still a topic of much debate [197, 221]. They may help to increase the efficiency of the system by concentrating excitations close to P700 [222]. They may have a role in photoprotection [223], or they simply increase the cross section for absorption of red light by the PSI antenna [195]. In shade-light environments they were shown to be important [224]. As the described experiments in this work were performed at low temperature conditions, the excitation energy transfer characteristics at these conditions are described briefly. The equilibration times in the higher lying antenna states as well as the equilibration with the red Chla states remains largely conserved at low temperatures. For *Synechocystis* PCC6803 the antenna state equilibration occurs within At low temperatures Excitation equilibration times between the antenna states and with the red Chla as well as the time for trapping of excitation by P700 were taken from Ref.: [216] values were determined for PSI from *Synechocystis* PCC6803 at 77 K [217]. It was found that the charge separation at low temperatures is heterogenous in the way that a

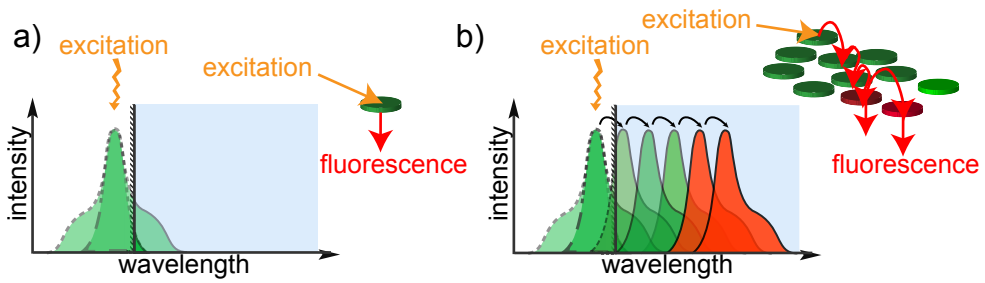

Figure 5.8: Illustration of the advantage of multi-chromophore FRET-coupled systems with respect to fluorescence emission measurements. While the spectrum of a single pigment excited to its main absorption is not fully detectable, due to the fluorescence cut off filter needed in the detection path, the red traps of a multi-chromophore FRET-coupled system are entirely detectable due to their relative red-shift.

fraction of 65% is found in an irreversible charge separation on the iron sulfur centers $P700^+F_A^-$ and $P700^+F_B^-$ while for the other 35% the transfer to the terminal iron sulfur clusters is blocked and dynamic formation and decay occurs between the charge separated states $P700^+A_1^-$ and $P700^+F_X^-$ as determined for PSI from *T. elongatus* at 77 K [217, 225]. Thus, under continuous illumination the reaction center P700 is present in its oxidized $P700^+$ state at low temperature conditions.

One major difference compared to ambient conditions is the strongly increased fluorescence quantum yield of the red Chla states [226]. At low temperature conditions, the red Chla act as deep traps for the excitation energy and they release excitation energy in the form of fluorescence emission. Nevertheless, a part of the fluorescence emission is quenched by $P700^+$, which in the cationic form spectrally overlaps with the red Chla states. An increase of 50% in fluorescence quantum yield was observed for specifically pretreated PSI complexes causing P700 to be trapped in its neutral form. Such pretreatment was not performed in the described experiments and thus in the following only PSI with the oxidized $P700^+$ is considered. Recently, three different to the fluorescence emission contributing states were discerned by their different energy transfer times to $P700^+$ of 6.1 ps , 140 ps, and 360 ps at T = 15 K as measured by spectrally resolved fluorescence lifetimes measurements on PSI from *T. elongatus* and were assigned to red Chls pools C715, C710 (also referred to as C708), and C719, respectively [227]. The fluorescence quantum yield of PSI at low temperatures is sufficient to be detectable on the level of individual PSI complexes [13–15].

The high fluorescence quantum yield of the red states which are fed by excitation energy transfer from the higher lying Chla antenna states makes PSI ex-

traordinarily well suited for LT-SMS. Figure 5.8a illustrates the excitation and fluorescence emission scheme in a one-chromophoric system, where upon excitation into the maximum of absorption, the spectrum is cut-off by the usually needed cut-off filter. Figure 5.8b visualizes excitation and emission in the case of the multi-FRET coupled PSI complex. Excitation into the maximum of absorption is possible without losses of fluorescence emission, as excitation is transferred non radiatively from the higher lying antenna states (green profiles) towards the red Chla states (red profiles) which are energetically largely down-shifted with respect to the excitation laser. It was found that the different spectral contributions of the red state Chla for several PSI complexes can be discerned at temperatures of T = 1.4 K [13–15]. Here, the red Chla emission of PSI from *Synechococcus* PCC7002, PSI from *Synechocystis* PCC6803 and PSI from *T. elongatus* are investigated. In the later parts of this work PSI serves as a model system, as it combines multiple emitters within one protein complex which is well characterized at a resolution of 2.5 Å , details on binding pocket specific interactions as well as on details on the energy transfer can be investigated. In Chapter 6 the plasmonic effects on a multi-FRET-coupled system are investigated by analyzing the effect of coupled metal nanostructures on the fluorescence emission of PSI.

5.2 Characterization of the Red Antenna States of PSI from *Synechococcus* PCC7002

The spectral characteristics of individual PSI complexes from *Synechococcus* PCC7002 are analyzed by low temperature single-molecule spectroscopy. Spectral forms with different spectral diffusion characteristics can be discerned. The spectral region below 710 nm often shows zero-phonon lines (ZPLs), they form a spectral band with a maximum at 698 nm (F698). The region above 710 nm is dominated by broad intensity distributions and the observation of ZPLs is less frequent. The results are discussed with respect to a chlorophyll *a* (Chla) assignment.

The low temperature single-molecule spectroscopic results have been published in *Photosynthesis Research*, (2008) **95**(2-3):155-165 (see publication list on page i). The tentative assignment to chlorophyll species in PSI have been reevaluated here on the basis of recent findings concerning the source for spectral diffusion. These results are presented in Section 5.3 and published in *Journal of the American Chemical Society*, (2008), **130**(51):17487-17493, 2008 (see publication list on page i).

Results

Fluorescence emission spectra of individual PSI complexes

Figure 5.9 shows a selection of five fluorescence emission spectra (denoted I–V) of single PSI complexes from *Synechococcus* PCC7002[1]. The acquisition time for the single complex spectra was between 20 and 30 s. For better comparability, the spectra were scaled to a similar magnitude. Each spectrum exhibits unique features, which will be described briefly. Spectrum (I) consists of a broad emission contribution with a maximum around 712 nm. On the short wavelength side the intensity shows two stepwise increases with narrow peak positions at 690 nm and at 701 nm. These spectral features are attributed to broadened ZPLs. On the long wavelength side the intensity decay is smooth. Spectrum (II) consist of a broad intensity characterized by a steep increase between 690 and 697 nm. A narrow ZPL is found within the steep slope at 697 nm. The broad emission shows two local maxima at 701 nm and 708 nm as well as a long tail to longer wavelengths. Spectrum (III) consists of a broad intensity distribution with a ZPL contribution on top of the broad fluorescence emission band at 710 nm. A smooth intensity decrease is again observed at lower energies.

[1] For details on the sample preparations see Chapter 3, page44.

Spectrum (IV) shows an intense ZPL at 693 nm followed by a slight increase of intensity that passes into a steep increase beginning at 701 nm and ending at the maximum intensity of the spectrum at 703 nm. From there, an almost linear decrease of intensity is observed towards 720 nm. Spectrum (V) consists just of a single broad intensity distribution with its maximum at 712 nm. The majority of fluorescence emission spectra recorded for single PSI complexes of *Synechococcus* PCC7002 show narrow ZPLs together with broad emission bands. In some spectra, ZPLs show up as intense narrow lines and in some spectra they are observed as broadened structures. The number of the ZPLs, their spectral positions and line widths vary from complex to complex. In spectra taken within 20–30 s the line width ranges from $\sim$ 0.2 nm up to some nanometers.

Average spectrum over individual PSI complexes and ensemble spectra
On top of the single complex spectra in Figure 5.9 the average spectrum taken over the fluorescence emission of 36 individual PSI is shown. The average spectrum does not show any ZPL contribution. Thus, the single emitter-specific signals are smeared out already by averaging over a comparably small number of individual PSI complexes. The maximum of the average spectrum is located at 702 nm and shoulders on the short and on the long wavelength side are observed at 699 nm and 711 nm. Figure 5.10 shows ensemble absorption and fluorescence emission spectra of PSI from Synechococcus PCC7002 at 77 K. The absorption spectrum covers the region between 600 and 750 nm. The spectrum shows a strong peak in the region of the Q_Y absorption-band of Chla at 680 nm. Additional shoulders can be seen on the blue side (at 672 nm) and on the red side (at 692 nm) of the maximum. Above 700 nm the spectrum exhibits a featureless red tail extending up to 720 nm. A decomposition of the absorption into Gaussian bands shows that the intensity above 700 nm can be modeled by a single band with its maximum at 708 $\pm$ 4 nm (data not shown). Therefore this band is abbreviated by C708. About 2–3 Chla molecules contribute to the integrated absorption of C708. The fluorescence spectrum given in the range between 655–800 nm shows a broad band with Stokes-shifted maximum at 714 nm. The average spectrum over 36 PSI complexes does not contain any single-emitter specific line shape profiles, nevertheless it does not reconstruct the ensemble fluorescence spectrum, which peaks at 714 nm. For PSI from *T. elongatus* [179] and from *Synechocystis* PCC6803 [181] about one hundred single PSI complexes are found to be sufficient to reconstruct the ensemble spectrum.

Time-dependent fluorescence emission spectra of individual PSI complexes
Time-dependent spectral analysis of individual PSI allows for the analysis of line broadening processes. For each individual complex, time-dependent spectra series were recorded with a time resolution of 1 s. The major fraction of time-dependent spectra taken for single PSI complexes shows dynamic wavelength

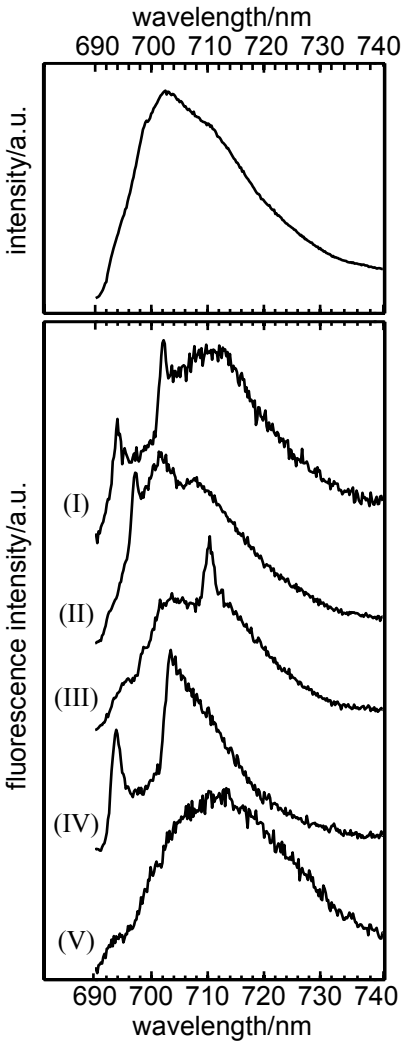

Figure 5.9: Low-temperature fluorescence emission spectra of individual PS I complexes from *Synechococcus* PCC7002 (as published in Ref.: [179]), together with an average spectrum over 36 individual PSO complexes on top of the single complex spectra. The spectra denoted (I) – (V) are described in the text. (λ_{exc} = 680 nm, with P_L = 100 μW, t_{acq} = 20 – 30 s and T = 1.4 K).

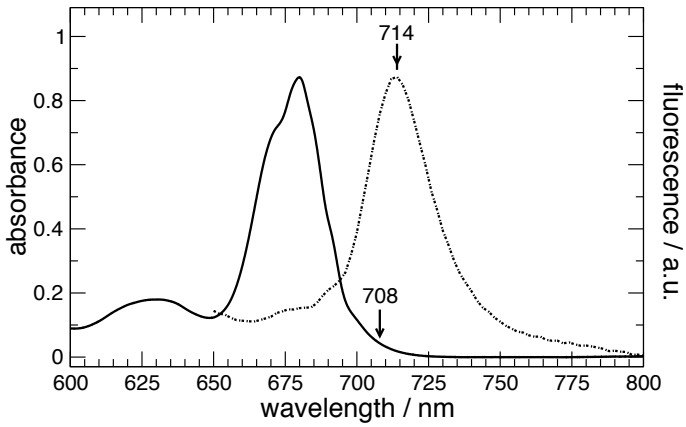

Figure 5.10: 77 K absorption spectrum (line) and 77 K fluorescence emission spectrum (dashed line) of PS I from *Synechococcus* PCC7002. The excitation was at λ_{exc} = 450 nm (as taken from Ref.: [179]).

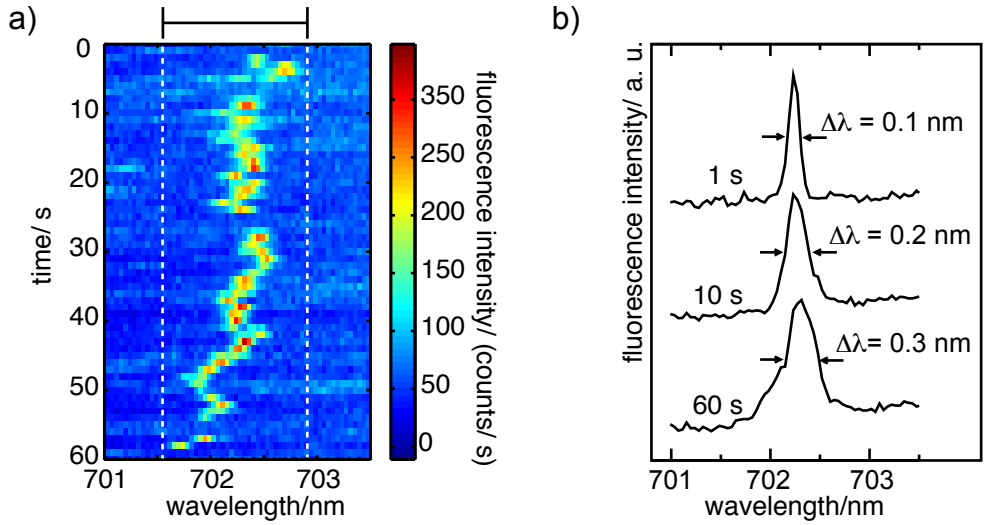

Figure 5.11: a) Time-dependent fluorescence emission spectra of an individual PS I complex. The time resolution is 1 s per spectrum and measurement parameters were λ_{exc} = 680 nm, P_L = 100μW and T = 1.4 K. The horizontal bar on top indicates the range taken for the ZPL statistics shown in Figure 5.12. b) Spectra taken with different accumulation times. The spectra were taken from the time-dependent series shown in a). The 1 s spectrum was directly taken from the spectra series at time position t = 40 s. The 10 s spectrum was calculated by averaging the spectra t = 31 – 41 s and the 60 s spectrum was calculated by taking the mean over the entire data set. The line widths as taken at the FWHW-position are indicated for each spectrum (as published in [179]).

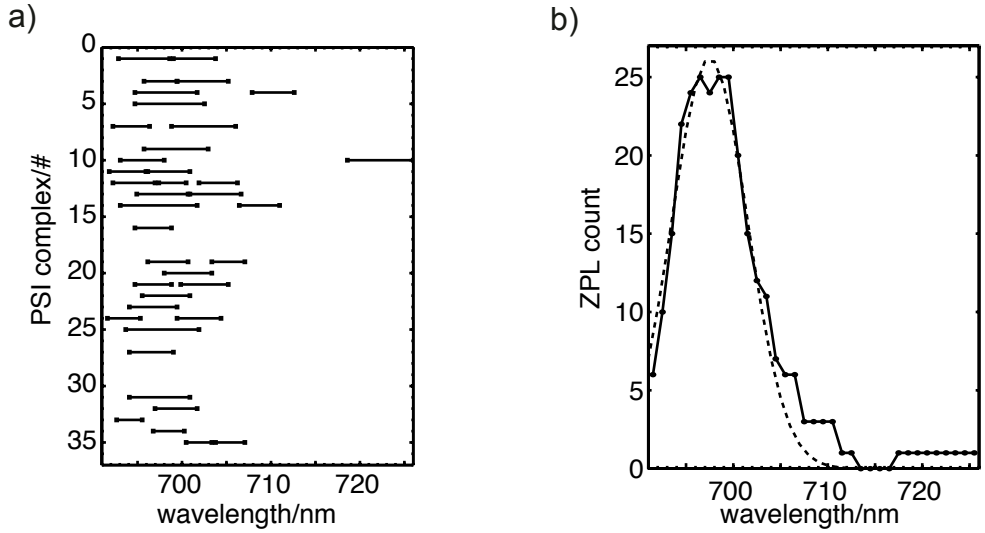

Figure 5.12: Statistical analysis of the distribution of ZPLs. a) The bars represent the individual regions in which ZPLs were observed in the time-dependent spectra of 36 individual PSI complexes. b) Number of molecules showing a ZPL at the given wavelength. The dots represent the number of bars shown in b) at each wavelength using a bin size of 1 nm. Parameters for all measurements were: λ_{exc} = 680 nm, P_L = 100μW and T = 1.4 K (as published in [179]).

changes of ZPLs. One of these time-dependent spectra is given in Figure 5.11a. The intensity of the ZPLs undergo remarkable variation during time. In some spectra, the line is missing completely (e.g., t = 25–26 s). In addition to the intensity variations, the wavelength position of the ZPL also varies with time. These variations show discrete wavelength jumps of the line (e.g., t = 57 s and t = 58 s) as well as a shivering around a mean position (e.g., between 10 and 23 s). These spectral jumps lead to increased line width in spectra taken with longer accumulation times. The ZPL in the spectrum measured at t = 40 s has a line width of Γ_{FWHM} = 0.1 nm. By the summation of ten spectra from the series (31–41 s) the line width of the ZPL contribution increases to Γ_{FWHM} = 0.2 nm. And after summation of the 60 s long spectra series the line width is Γ_{FWHM} = 0.3 nm.

The dynamic behavior of the ZPLs is very heterogeneous for single complexes. But, in general, the ZPLs remain in restricted spectral areas. These ZPL ranges were determined for all PSI complexes by the analysis of the time-dependent spectra series. The spectral range taken as determined for the time-series shown in Figure 5.11a is indicated by added white dashed lines and a horizontal bar on top of the series.

The wavelength range of the ZPL, here, spans from 701.6 to 702.9 nm. The ZPL ranges as determined for 36 individual PSI complexes are summarized in Figure 5.12a. The ZPLs are in some cases well separated and in others they overlap.

If the spectral trails are well separated, the bars represent the dynamic region of one single line. In the case of overlapping ranges, the ranges were combined and are given as one joint bar. As can be seen in Figure 5.12b, the extension and number of the spectral ranges covered by ZPLs vary from complex to complex. The projection of the ZPL ranges on the wavelength axis can be used to calculate the distribution of ZPLs in dependency of the wavelength position. The result of the projection is shown in Figure 5.12b. The ZPL distribution shows one spectral band. The shape of this band can be fitted by a Gaussian (dashed line) with maximum at 698 nm and a half width of 4 nm. Therefore, the band is named F698. In the range > 710 nm, the emission is dominated by broad intensity distributions. At these wavelength only three ZPL contributions were found within 36 analyzed time-dependent spectra series (see Figure 5.12a).

Polarization-dependent spectra of individual PSI complexes

To quantify the number of emitters contributing to the fluorescence emission a polarization analysis can be performed. Figure 5.13 shows fluorescence emission spectra of a single PSI complex taken with a rotating polarizer in front of the spectrograph. The polarizer angle given is defined with respect to an arbitrary laboratory axis and is uncorrelated to the polarization of the excitation light due to the preceding energy transfer steps in the light-harvesting antenna of PSI. In the polarization-dependent spectra series shown in Figure 5.13a three contributions can be distinguished. These are highlighted by white squares. The observed emission is strongly polarized. This is interesting with respect to the broad unstructured emission detected for this individual PSI complex, which is of the type (V) from Figure 5.9 and shows no resolved ZPLs. Three broad spectral intervals can be discerned by their polarization behavior. A 8 nm broad contribution at 691–699 nm (λ_1), a 6 nm broad range at 699–705 nm (λ_1) and a 15 nm broad interval 705–720 nm (λ_3). The integrated fluorescence intensity in these ranges is plotted in Figure 5.13b. A sinusoidal shape with a periodicity of 180° can be seen for all curves. The emission found within the range λ_1 can be assigned to an emitter of F698, the emission within λ_2 can be either assigned to a member of F698 or to a member of C708. The emission within λ_3 is most probable due to an emitting state of C708. Due to the large inhomogeneous broadening of the observed pools, an assignment of emitters of one single complex remains tentative. Similar strong polarization was observed for all PSI complexes investigated in this way. The strong polarization of the emitted light requires either a single emitter as origin of the emission, or a number of emitters with parallel transition dipole moments. Since the PSI complexes in our samples are randomly oriented, it is unlikely that the transition moments of several emitters would appear parallel in all cases.

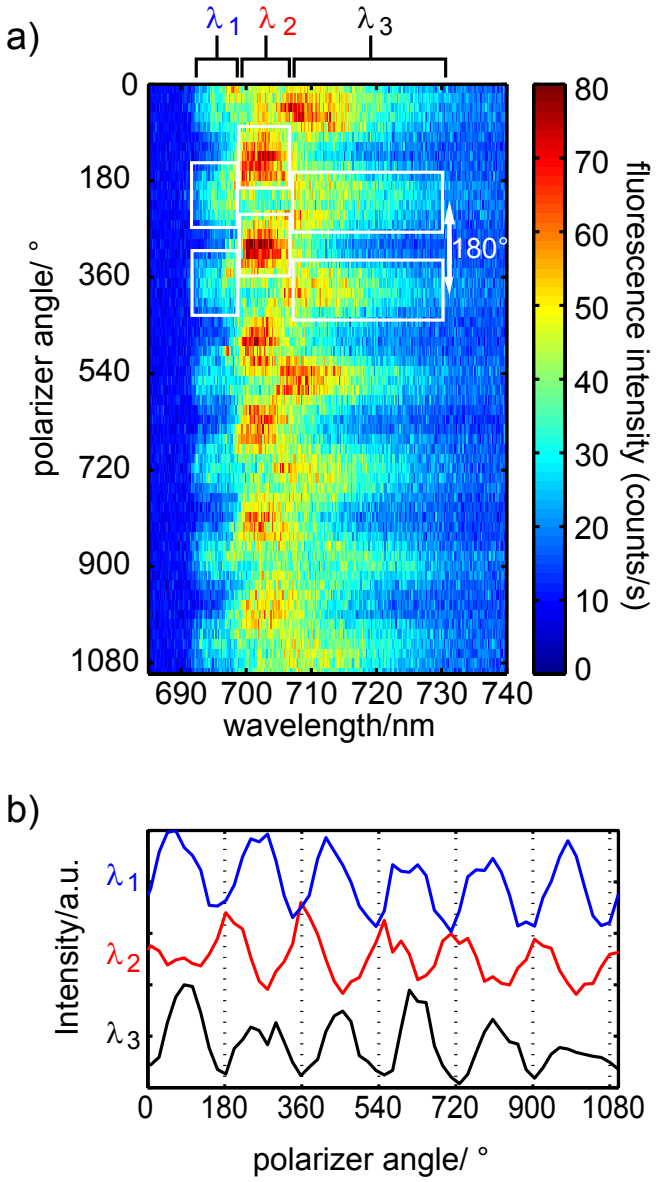

Figure 5.13: a) Sequence of polarization-dependent fluorescence emission spectra of a single PSI complex from *Synechococcus* PCC7002. The white squares highlight the different spectral contributions during the first turn of the polarizer. b) Integrated fluorescence intensities in the intervals indicated in a) as λ_1, λ_2 and λ_3 as a function of the polarizer angle. The acquisition time for a single spectrum was 1 s (as published in [179]).

Discussion

The ensemble spectrum at 77 K absorption (Figure 5.10) shows a high similarity with the absorption spectra from PSI complexes from other cyanobacteria [197]. Interestingly, the most striking similarity is found between *Synechococcus* PCC7002 and the PSI core of maize [197]. The absorption spectrum shows the contribution of 2 – 3 Chla species absorbing at lower energy than P700. The mean absorption of this pool is found at 708 $\pm$4 nm. The wavelength position of C708 is close to an observed pool position in *Synechocystis* PCC6803 (C706) [212] and *T. elongatus* (C708) [226]. However, additional pools were found in PSI from *Synechocystis* PCC6803 as well as from *T. elongatus*. Such additional pools are lacking in *Synechococcus* PCC7002. The total number of red Chla species per monomer is therefore higher for *T. elongatus* (7–9 per monomer) and *Synechocystis* PCC6803 ($\sim$4) [210] than for *Synechococcus* PCC7002. The bulk fluorescence spectrum of *Synechococcus* PCC7002 consists of an unstructured band with maximum at 714 nm. The maximum of the fluorescence emission of *Synechococcus* PCC7002 is remarkably blue-shifted compared to the maximum position determined for PSI from *T. elongatus* and *Synechocystis* PCC6803, where the maxima were found at $\sim$ 730nm [203] and $\sim$ 718.5 nm [199], respectively. Besides the large difference in the wavelength position, the shape of the fluorescence emission shows similarities between these different PSI complexes. The shift between the absorption C708 (*Synechococcus* PCC7002) and the maximum of the fluorescence emission at 714 nm is about 6 nm, that is much larger than expected for monomeric Chla. The value found for *Synechococcus* PCC7002 is between the shifts found for *T. elongatus*, where the maximum fluorescence emission and the absorption C719 are 11 nm apart and the 4.5 nm for C714 in *Synechocystis* PCC6803 [201, 203].

The inhomogeneous broadening of the ensemble spectra was lifted by SMS and the emission of single PSI complexes can be observed (Figure 5.9). Most of the single PSI complex spectra show a broad unresolved intensity distribution with broadened ZPLs superimposed on its blue side. The line width, spectral position and the intensity of the observed ZPLs vary from complex to complex (Figure 5.9). The single-emitter specific spectral components are already averaged out by calculating the mean over a small number of 36 spectra from different single PSI complexes (Figure 5.9 top panel).

Spectral diffusion is the main broadening process for those ZPLs (Figure 5.11). Recording of time-dependent spectra for single complexes (Figure 5.11) shows, that the spectral diffusion process originates from spectral jumps of the ZPLs. The width of those jumps reach into the nm-range. For most of the ZPLs found in the region below 712 nm, the rate of this jump processes is in the range of

our experimental time resolution (1 s). Such frequency jumps can be interpreted as hopping between different conformational substates of the protein [50, 228]. The spectral ranges that are accessible for the emitters in one complex due to hopping between the different substates can be extracted from the time-dependent spectra (Figure 5.11). The shape of the energy landscape formed by the different conformational substates is highly individual for each complex, but general limitations for the hopping process of the ZPLs exist. The collection of all these confined areas (Figure 5.12) form a spectral band. This spectral band has its center at 698 nm (F698). The spectral range covered by F698 represents only a small portion of the overall fluorescence emission of PSI from *Synechoccocus* PCC7002. The F698 Chla's probably belong to the pool giving rise to the shoulder at 692 nm in the 77 K absorption spectrum.

The spectral properties of F698 visible on the single molecule level show similarities with the emission of C708 from *T. elongatus* and F699 from *Synechocystis* PCC6803. The emission of these pools give rise to well resolved ZPLs in the spectra. These ZPLs reside on the blue wing of a broad emission. Comparing the time-dependent effects due spectral diffusion for the ZPLs from F698 and C708 (*T. elongatus*) and F699 from *Synechocystis* PCC6803 shows that the rate as well as the width of the jumps are within the same range. Therefore, it can be assumed, that the chromophores of these pools show structural equivalence.

The dominant portion of the fluorescence intensity is emitted in broad intensity distributions. Such broad distributions are observed in almost all spectra (Figure 5.9). The emission stems from the red-most state C708. Fluorescence emission spectra taken with a rotating polarizer in the front of the spectrograph show that the number of emitters responsible for the broad intensity distribution is small (Figure 5.13). The average spectrum taken over 36 single PSI complexes has a red-shifted maximum peaking at 702 nm. After the analysis of the single complex spectra, the shoulder on the short wavelength of the average spectrum peaking at $\sim$ 699 nm can be attributed to the ZPL contribution, adding up to an inhomogenously broadened band when averaged over multiple PSI complexes, and the shoulder on the long wavelength side at 711 nm can be attributed to the broad spectral component observed for single PSI complexes. The broad emission stems from the red-most state C708.

Fluorescence emission spectra taken with a rotating polarizer in the front of the spectrograph show that the number of emitters responsible for the broad intensity distribution is small (Figure 5.13). In the majority of cases, no indications for ZPLs were observed at wavelengths longer than 710 nm. The shape of F698 suggests that even those ZPLs observed in the region above 708 nm are due to emission from F698. In principle, each single emitter should give rise to a ZPL and a

PW. However no ZPLs are observed for the broad intensity distributions. A similar behavior was observed by SMS for the emission of C719 in PSI complexes from *T. elongatus* [14]. Therefore, it was argued that a large electron-phonon coupling in conjunction with fast spectral diffusion could explain the absence of ZPLs in the spectra. For this explanation, line hopping of the corresponding ZPL must be much faster than the experimental time resolution, and the spectral ranges covered by these fast diffusing ZPLs must be close to the width of the corresponding broad intensity distribution [14]. These properties found for C719 resemble those observed for C708 (*Synechococcus* PCC7002). Therefore, the structural composition of the chromophores of C708 in *Synechococcus* PCC7002 must show an equivalence to the chromophores associated with C719 in *T. elongatus*. Furthermore, this equivalence includes also the red-most pool C714 of *Synechocystis* PCC6803, because a structural similarity between C714 (*Synechocystis* PCC6803) and C719 (*T. elongatus*) was proposed based on hole-burning experiments [203]. In summary, it can be suggested that the red-most Chla in these three different PSI complexes possess a high structural equivalence, and this equivalence of the red-most pools is independent from the difference in red-shifts of these pools.

The observed properties can be interpreted within the picture of an energy landscape as follows: fast spectral diffusion occurs if the barrier between the conformational substates in the energy landscape are crossed with high rate and slow spectral diffusion occurs if the rate is low. The observed spectral width of one emitter corresponds to variations in the site-energy induced by conformation dynamics. In cases where the spectral width of a single emitter is close to the value observed in ensemble experiments, the energy landscapes have low barriers within a wide range of configurations. In cases where the spectral width is remarkably below the width of the ensemble experiments, the energy landscapes have some high barriers that cannot be crossed leading to confined intervals of emission wavelength. The chromophores of C708 show fast spectral diffusion and a large spectral width. This indicates a binding situation of the chromophores that results in higher flexibility than those with lower rates and restricted width.

For PSI from various species the degree of spectral diffusion is specific for the different red pool Chlas. This is interesting with respect to the argument, that photoactivated transitions or local heating due to intense laser irradiation in a confocal setup mainly cause spectral dynamics. The distinct spectral diffusion characteristics of the different red-state emitter of PSI corroborate the finding that protein-bound pigments sense the specific binding situations, and thus, reports on the energy landscape of the respective protein moiety.

spectral diffusion characteristics	PSI from *T. elongatus*	PSI from *Synechocystis* PCC6803	PSI from *Synechococcus* PCC7002
slow	C708	F699	F698
fast	C715	C706	
fast	C719	C715	C708

Table 5.1: Spectral similarities concerning the spectral diffusion characteristics are found for the spectral components of PSI from different cyanobacteria.

Table 5.1 contains the spectral pools observed by low temperature single-molecule fluorescence emission spectroscopy for PSI from *T. elongatus*, *Synechocystis* PCC6803 and *Synechococcus* PCC7002 together with a relative velocity of their spectral diffusion dynamics with respect to the second time-resolution of the measurements.

The spectral properties of F698 visible on the single molecule level show similarities with the emission of C708 from *T. elongatus* and F699 from *Synechocystis* PCC6803. The emission of these pools give rise to well resolved ZPLs in the spectra. These ZPLs reside on the blue wing of a broad emission. Comparing the time-dependent effects due spectral diffusion for the ZPLs from F698 and C708 (*T. elongatus*) and F699 from *Synechocystis* PCC6803 shows that the rate as well as the width of the jumps are within the same range. The broad contribution attributed to C708 corresponds to the spectral pools attributed to C719 in *T. elongatus* and C715 in *Synechocystis* PCC6803, which show similarly fast spectral diffusion behavior and cover similar large wavelength intervals [14, 181]. For PSI from *T. elongatus* and *Synechocystis* PCC6803 additional red pools with fast spectral diffusion dynamics are observed, referred to as C715 and C706, respectively.

Assignment to the red chlorophyll candidates

The similarities of the spectral diffusion characteristics between the different pools of PSI from different species, and the fact that high structure homology is expected between the different cyanobacterial PSI, let us conclude that structurally equivalent Chla molecules are giving rise to the fluorescence emission signals. The structural model of PSI from *T. elongatus* with 2.5 Å resolution is taken as reference for PSI in general. Structure-based calculations indicate that the low energy Chla consist of excitonic coupled Chla dimers and of one trimer [11, 208].

For an assignment of the spectral contributions to the red chlorophyll candidates, the respective local protein surroundings are investigated. Fast spectral

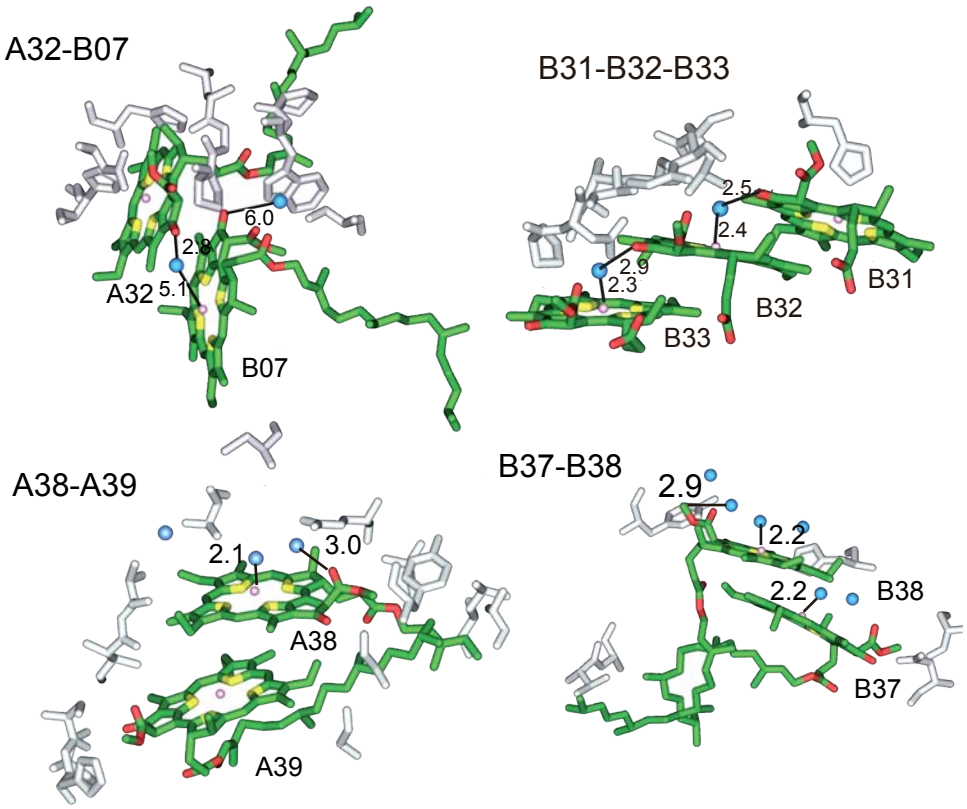

Figure 5.14: The red chlorophyll candidates with their 4 Å surroundings as found in the structural model with PDB entry: 1JB0 [11]. Coloring of the Chla is: C-atoms (green), O (red) and Mg (rose). Amino acid residues are shown in light gray and oxygens from internal ware molecules are shown in blue. The nomenclature of the Chla is according to [208]. Selected distances between Chla and the oxygen of internal waters are included and given in Å .

diffusion and a large spectral width indicates a binding situation of the chromophores associated with higher flexibility than those with lower rates and restricted width [52, 229, 230].

We assumed that a high number of amino acid binding partners inside the pigment binding pockets corresponds to a less flexible binding condition of the chlorophyll pigments. The coordination of the central magnesium ion and the presence of H-bonds at the keto-group site at ring V of the Chla molecule (see Figure 5.3) were inspected. The A32–B07 dimer has coordination partners for both magnesium ions, a histidine and a glutamine [14]. Additionally, two possible partners for a hydrogen bond to the keto-group are found. For the dimers A38–A39 and B37–B38 only one magnesium ion is coordinated by a histidine, respectively [14]. The B31–B32–B33 trimer shows compared to these dimers even less coordination. Only one of the three Chla is ligated at the Mg ion site (B31) by a histidine. For H-bond formation at the keto-group again only

one putative partner is found at B32 [14]. According to these considerations, we concluded that the ordering upon increased structural flexibility of the candidates is: A32–B07 $<$ A38–A39 $\approx$ B37–B38 $<$ B31–B32–B33. And thus the slow spectral diffusing pools (C708/F699/F698) for *T. elongatus*/*Synechocystis* PCC6803/*Synechococcus* PCC7002 were attributed to the dimer A32–B07 and the fast spectral diffusing pools (C715/C706/C708) to A38–A39 or B37–B38, and the trimer B31–B32–B33 located at the outer part of the protein complex and most probably not being part of PSI from *Synechococcus* PCC7002, to C719 and C715 from *T. elongatus* and *Synechocystis* PCC6803, respectively.

Recent results obtained by solvent isotope-dependent analysis of the spectral diffusion dynamics of individual PSI from *Synechocystis* PCC6803 revealed that proton dynamics are a main source for spectral diffusion in pigment-protein complexes (see Section 5.3 and Ref.: [181]). With respect to an evaluation of the respective pigment flexibilities these findings have to be taken into account. H-bonded amino acid residues seem not to have an stabilizing effect associated to decreased spectral diffusion but act as coordinates along which proton dynamics can occur. Thus, H-bonds either with neighboring amino acid residues or internal water molecules are on the contrary supposed to promote strong spectral diffusion dynamics of the protein-bound pigments. H-bond length variations will cause multiple site-energy variations of the pigment in dependence of the distance of the charge and thus probably leads to an interacting 'n-TLS', or 'multi-TLS'.

Strongest site-energy variations are expected, when conformational changes affect the symmetry of the Chla molecule by ligation of the center magnesium ion [231], or when changes occur along the direction of the electric dipole moment associated with the Q_y - transition of Chla [42] occur. The Q_y - transition in Chla points in the direction of the keto-group (see Figure 5.3) which is beside a methyl group the only site of the macrocycle which can form H-bonds.

Thus, internal water molecules or amino acid residues as ligands of the central magnesium ion of Chla or forming H-bonds with the keto-group are expected to tune the electronic site-energy of Chla at maximum. Figure 5.14 shows the red Chla candidates. The visualization contains the oxygens associated with the internal water molecules as present in the structural model of PSI from *T. elongatus* [11]. The highest content of internal water molecules within a 4 Å range is found for B37-B38 where the closest distances are 2.2 Å while in the case of B31–B32–B33 two magnesium ions might be coordinated by nearby internal water molecules which are found closely at distances of 2.3 and 2.4 Å from the magnesium ions and at 2.9 and 2.5 Å to the keto-groups of the adjacent Chla. For A38-A39 a close water molecule is found at 2.1 Å from the magnesium ion

from the A38 Chla. The largest distance between the internal water and closest internal water is found for A32–B07 where the distances between magnesium ion and keto-group are 5.1 Å and 2.8 Å , respectively.

Based on the presence of nearby internal water molecules an ordering with respect to flexibility is similar to the ordering of the flexibility analysis above: A32–B07 is least exposed to protons, followed by A38–A39, B37–B38 and B31–B32–B33. On the other hand, from the inspection of the H-bond partners at the keto-group site, the inverse to the above stated considerations is drawn, such that the ordering in dependency of fast to slow spectral diffusion states is: B31–B32–B33. A38–A39 $\approx$ B37–B38 $<$ A32–B07. As the ordering based on internal water molecule presence and H-bonding partners point in inverse directions an assignment of the spectral states to chlorophyll species in PSI is not achieved.

5.3 Spectral Diffusion Induced by Proton Dynamics in Pigment-Protein Complexes

The fluorescence emission of individual photosystem I complexes from *Synechocystis* PCC6803 shows zero-phonon lines as well as broad intensity distributions. The number and the line width of the zero phonon lines depend strongly on the solvent. An decrease of spectral diffusion for all chlorophyll states responsible for the fluorescence emission of PSI from *Synechocystis* PCC6803 is observed by changing the solvent from H_2O to D_2O. This leads to a substantial increase of well resolved zero-phonon lines (ZPLs). Since the chlorophyll *a* (Chla) chromophores lack exchangeable protons, these observed changes in the spectral diffusion have to be assigned to exchangeable protons at the amino acids and structural water molecules in the chromophore binding pocket. Using $H_2^{18}O$ as solvent does not cause an observable spectral diffusion decrease compared to PSI in H_2O indicating that the role of water molecule motions for spectral diffusion dynamics is minor compared to proton dynamics.

This section contains results published in *Journal of the American Chemical Society*, (2008), **130**(51):17487-17493, 2008 (see publication list on page i). In addition to the analysis of single PSI complexes in H_2O- and D_2O-based solvents presented in the article, here furthermore, the fluorescence emission of individual PSI complexes in $H_2^{18}O$-based buffer solution is studied.

Introduction

The largest influence on the site-energy of protein-bound pigments occurs for conformational variations of the chromophore itself and/or its close surrounding [232]. The observed spectral dynamics in single-molecule experiments often relies on the higher barrier crossing probability between conformational substates in the excited-state of the chromophore than in the ground state [18] (see Chapter 2, 26). These activated barrier crossings enable single chromophores to map the energy landscape even at low temperatures and thus provide a spectroscopic tool to obtain general insights into the characteristics of protein energy landscapes. With single-molecule techniques at low temperature, where large scale motions of the protein are frozen out, these changes of the site-energy can be directly observed. Despite the reduced conformational dynamics at low temperatures, the observed changes in the site-energy reach into the nm-range [232, 233]. An assignment of the origin of the observed changes in the site-energy is still missing, and this study focuses on the physical origin of the site-

energy variations.

The experiments on the single-molecule level were carried out on PSI from *Synechocystis* PCC6803 showing three contributions F699, C706 (also referred to as C708 [212]), and C714 to the fluorescence at low temperature [181, 199, 203]. The abbreviations originate from their first characterization by fluorescence emission with maximum at 699 nm and by abortion at 706 and 714 nm, respectively. Different water isotopes are used as solvent.

Results

Solvent water isotope-dependent PSI spectra
The low temperature fluorescence emission of single PSI complexes from *Synechocystis* PCC6803, (herein, referred to as PSI) is analyzed in dependency of different water isotope based buffer solutions[2]. The water isotopes used were: H_2O, D_2O and $H_2^{18}O$. All samples were studied under identical experimental conditions with λ_{exc} = 680 nm, P_L = 100 μW and T = 1.4 K. In Figure 5.15 a selection of five representative 100 s spectra from different individual PSI scaled to similar magnitude are shown together with the average spectra over a) 100 PSI in H_2O, b) 347 PSI in $H_2^{18}O$ and b) 60 PSI in D_2O.

As similarly observed for PSI from *Synechococcus* PCC7002 (Section 5.2) the spectra of individual PSI complexes are characterized by florescence emission contributions of different line width, relative intensities and wavelength positions. The narrow spectral contributions are indicative for ZPL contributions, which are specific spectroscopic features of low temperature single-emitter profiles (see Chapter 2, page 12). The number of ZPLs, their spectral position, and line width vary from complex to complex. The highest fluorescence emission intensity is found for all complexes in broad fluorescence emission bands, while the ZPL contributions have relatively lower intensities.

For PSI in H_2O, beside broader spectral bands present for all individual PSI complexes, ZPLs are observed in the spectra from individual PSI complexes (see Figure 5.15a). In the spectra taken with 100 s accumulation time the line width of the ZPLs ranges from $\sim$ 0.5 nm to several nanometers. The ZPLs are mainly observed at the blue side of the broader fluorescence emission contributions. Two clearly observable ZPL contributions are present in spectrum (I), and one ZPL contribution in spectrum (III) and (Iv) . The average spectrum over the spectra from 100 individual PSI complexes agrees well with bulk emission spectra except a 4 nm blue shift [199], and does not contain single-emitter spe-

[2]For details on the sample preparations see Chapter 3, page 45.

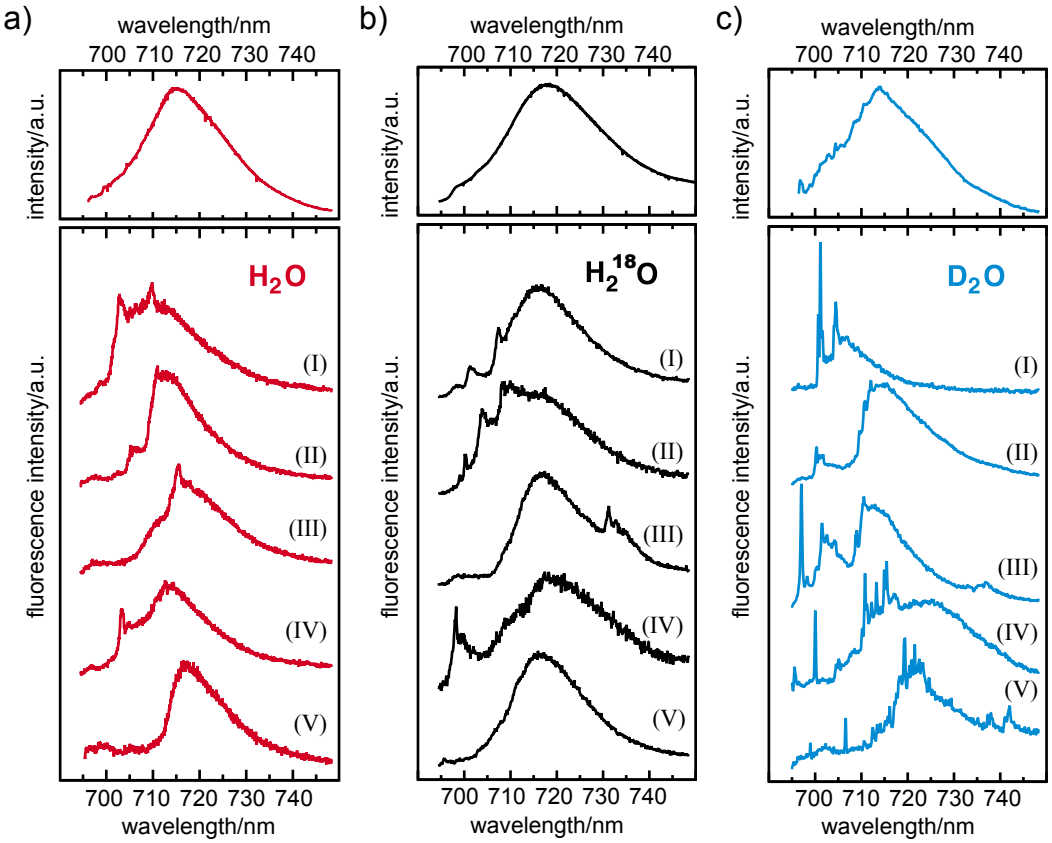

Figure 5.15: Fluorescence emission spectra from individual PSI prepared in a) H_2O -, b) D_2O - and c) $H_2^{18}O$ - based buffer solutions taken with accumulation time of 100 s for each spectrum. The panel tops show average spectra of all studied complexes (100 PSI in H_2O, 60 PSI in D_2O and 347 PSI in $H_2^{18}O$ buffer). Identical experimental conditions were used for all experiments, with λ_{exc} = 680 nm, P_L = 100 μW and T = 1.4 K.

cific narrow line contributions. Instead, a single broadened slightly asymmetric fluorescence emission band is observed.

Figure 5.15b shows fluorescence emission spectra from individual PSI in $H_2{}^{18}18O$. The spectra show high similarity to the spectra obtained from PSI in H_2O. Most ZPL contributions are found at the short wavelength side of the broader fluorescence emission band present for all complexes. In few PSI complexes in $H_2{}^{18}O$ ZPLs are found at longer wavelength positions, as for example in spectrum (III). The average spectrum shown on top shows high similarity to the ensemble spectrum [199]. No indication of single-emitter specific narrow line contributions are observed in the average taken over a large number of 347 spectra from different individual PSI complexes.

For PSI in D_2O, the spectroscopic characteristics change substantially, as can be seen from the spectra shown in Figure 5.15c. The spectra taken in D_2O buffer

show more resolved ZPLs, and their line widths are smaller than in H_2O and $H_2{}^{18}O$ while the same overall shapes of spectra are observed in all cases. Furthermore, the spectra taken in D_2O buffer show ZPLs in the wavelength range larger than 720 nm where almost no lines were observed for PSI in H_2O. The red-most position observed in the spectra depicted is at 743nm in spectrum (V). The average spectrum over the 60 PSI in D_2O still shows residual narrow structures. This difference cannot be attributed to the different numbers of observed complexes but originates from the difference in the number and width of resolved ZPLs in the different solvents.

Determination of ZPL occurrence from the single complex spectra
In pigment-protein complexes, the single-emitter specific ZPL contributions are only observable if the degree of protein dynamics-induced spectral diffusion is comparably low. Typically the site-energy variations for the PSI states occur within wavelength ranges of a few nanometers, thus, spectral diffusion rates similar or smaller as the time resolution of the measurement result in resolved narrow line features, while faster $\gtrsim \mu$s rates cause broadened fluorescence emission lines, without indications for ZPLs (see simulations in Chapter 2, 27). Therefore, the occurrence of ZPLs can be taken as an indicator for the degree of spectral diffusion. A statistic analysis on the occurrence of ZPLs per single complex and wavelength interval is performed on an independently measured set of data, measured in a larger wavelength range from 690 – 780 nm with respect to the data presented in Figure 5.15a and 5.15c covering the wavelength interval from 690 to 747 nm. Fluorescence emission spectra were taken from 109 PSI in H_2O, 78 PSI in D_2O and 347 PSI in $H_2{}^{18}O$. The method used for the ZPL position determination illustrates an alternative method to the ZPL range determination from time-resolved sequences as described in Section 5.2 and Ref.: [64]. This alternate method considers solely comparatively stable ZPLs which contribute to a ZPL feature in a 40 s spectrum. The results shows lower absolute probabilities for ZPL occurrence due to this restriction. As a result ZPLs which were found with minor probabilities of < 6 % per wavelength interval are not present in the ZPL determination analysis presented here. The differences are not considered significant. In Figure 5.16 the method for ZPL determination used here is visualized. ZPLs are identified by the presence of narrow line features, with line width of up to 8 nm (highlighted in light gray) and by steep intensity increases on the edges of broader spectral contributions (highlighted in dark gray). The steep increases are considered based on the analysis of the time-dependent spectral information recorded for each individual PSI complex with a time resolution of 1 s.

Solvent water isotope-dependent ZPL distributions
Figure 5.17 shows the result of the ZPL analysis applied on the 40 s florescence

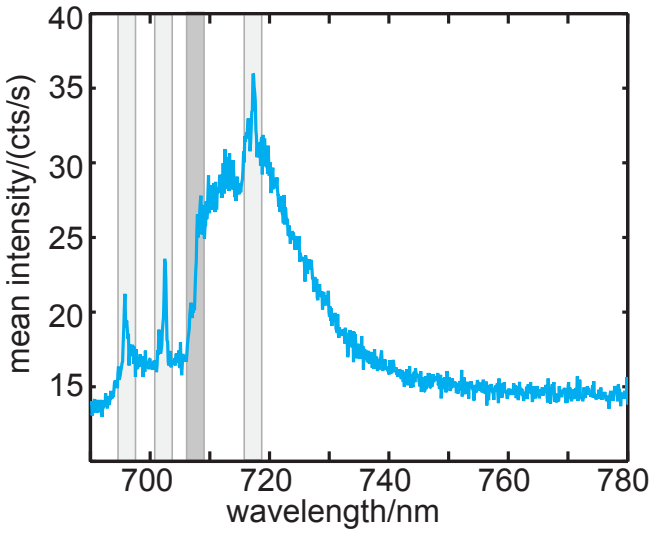

Figure 5.16: The determination of ZPL contributions from 40 s PSI spectra is visualized. ZPLs were determined by the presence of narrow line features with line width of up to 8 nm (highlighted in light gray); additionally steep intensity increases on the edges of broader spectral contributions were identified as ZPLs (highlighted in dark gray). The spectrum shown is from an individual PSI in D_2O taken withλ_{exc} = 680 nm,P_L = 100μW and T = 1.4 K.

emission spectra spectra taken for 109 individual PSI in H_2O (red), 347 PSI in $H_2^{18}O$ (black) and 78 PSI in D_2O (blue). The probability of observing a ZPL contribution in a 40 s spectrum from an individual PSI complex is shown with a binning of 1 nm.

The ZPL distribution for PSI in H_2O (red) shows two local maxima at 699 nm and 714 nm, with ZPL probabilities of, respectively, 32 % and 18 % per complex and 1 nm wavelength interval. Two minor contributions are found at 722 nm with 8 % and at 732 nm with 3 % ZPL probability. The distribution of ZPLs indicates the existence of at least two pools with maxima at 699 and 714 nm. The pool with the maximum at 714 nm is assigned to chlorophylls absorbing around 706 nm (C706), whereas the pool with the maximum at 699 nm (F699) can be assigned to chlorophylls absorbing at 692, 695, or 699 nm. The broad distributions dominating the red side of the spectra are made up of a low number of emitters assigned to the red-most pool C714.

The ZPLs for PSI in $H_2^{18}O$ (black) show similar abundance as observed for PSI in H_2O in the wavelength range covering most ZPL occurrence of PSI in H_2O from 690 to 720 nm, at longer wavelengths an additional contribution is found in a relatively broad band ranging from 740 nm to 770 nm and showing substructures peaking at 746 nm and at 751 nm. The band shows overall minor

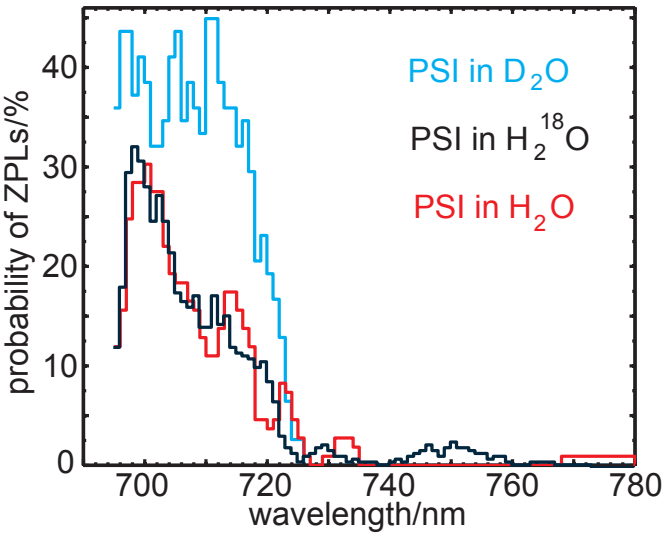

Figure 5.17: Statistics on ZPL occurrence in the spectra from individual PSI complexes in H_2O (red), D_2O (blue) and $H_2^{18}O$ (black).

probability with a maximum of 2.5%. This contribution has not been observed before in the fluorescence emission of PSI and is analyzed in more detail in Section 5.5.

For PSI in D_2O (blue), the probability for ZPL detection in a 40 s spectrum measures between 32 % and up to 45 % in the wavelength interval from 694 to 717 nm, thereby, surpassing the ZPL probability curve for PSI in H_2O and PSI in $H_2^{18}O$ at all wavelength positions within the interval ranging from 694 nm up to 726 nm.

Discussion

The average emission spectra of single PSI complexes from *Synechocystis* PCC6803 in H_2O, D_2O and $H_2{}^{18}O$ buffer are in good agreement with the reported bulk emission spectra [199, 234]. The inhomogeneous broadening dominating the bulk emission can be lifted by single-molecule spectroscopy (SMS), and the fluorescence emission of single complexes can be observed (Figure 5.15). The spectral position and the intensity of the observed features vary from complex to complex. Beside this intercomplex heterogeneity the spectra share general features like narrow line distributions attributed to ZPL and broad intensity distributions. Comparable broad distributions were found for PSI from *T. elongatus* [14] and *Synechococcus* PCC7002 [179] (see Section 5.2) as well as for the light-harvesting complexes LH2 and LH3 [233]. It was argued that these broad intensity distributions are built up by fast diffusing ZPLs

[14, 233].

By using D_2O the spectral diffusion was significantly decreased and this hypothesis is directly confirmed. The number of ZPLs observed in D_2O-based buffer exceeds the number of ZPLs observed in H_2O- and $H_2{}^{18}$-based buffer and the line width of the ZPLs remains smaller. Because of the reduced spectral diffusion in D_2O buffer, the probability for ZPLs increases under identical experimental time resolution. In deuterated solvent conditions, highly resolved single-emitter profiles of all red Cha from PSI from *Synechocystis* PCC6803 were obtained. These can be used to determine the electron-phonon couplings of the red Chla. The Huang-Rhys factor determination from these single-emitter profiles is presented in the following Section 5.4.

All pools contributing to the PSI emission in complexes from *Synechocystis* PCC6803 (F699, C706, and C714) are affected and, therefore, are accessible by the solvent (water) molecules. A direct observation of the diffusing ZPL leading to a broadened band was achieved in a time-dependent spectral measurement with 1 s time resolution (see published data in Ref.: [64]). Indirectly, this is observed from the data shown here, as the average spectrum over the highly ZPL structured PSI complex spectra taken in D_2O forms the same overall shape as average spectrum as in the case of PSI in H_2O- and $H_2{}^{18}$ buffer. Thus the effect of deuterated solvent is a decrease in spectral diffusion rate, but not a decrease in spectral diffusion wavelength range. Thus, the time constants for the underlying conformational dynamics are affected, but not their influence on site-energies.

Sources for spectral diffusion

By changing the solvent from H_2O to D_2O the local surroundings of the protein-bound pigments, responsible for the chromophore site-energies [59], change in two aspects. First, amino acid residues, being part of the binding pocket of the chromophore, may release their exchangeable protons to bind deuterons, and secondly, internal or, in case of solvent-exposed pigments, solvent water molecules, can exchange to deuterated water molecules. The H_2O to D_2O solvent-isotope-exchange experiments do not allow for discrimination between these two local variations. By using $H_2^{18}O$ instead of H_2O, however, the local surrounding of the pigments only changes with respect to the water molecules and the amino acid residues are not affected. Upon introduction of the oxygen isotope ^{18}O instead of ^{16}O, the molecular weight of the water isotope compared to deuterated water is conserved. For the analysis of the degree of spectral diffusion the ZPL abundance was taken as an indicator, as ZPLs only occur in the slow spectral diffusion limit. Although $H_2^{18}O$ and D_2O have the same molecular mass, their effect on the spectral diffusion on the red Chla of PSI is largely dif-

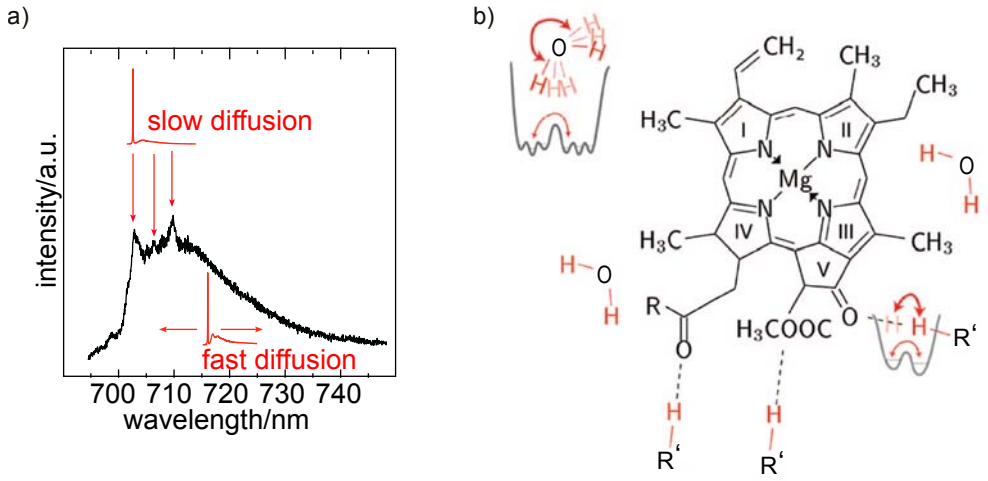

Figure 5.18: The results are visualized. a) While narrow line width contributions stem from slow diffusing single-emitter profiles, broadened bands can be due to fast spectral diffusion. b) Further refined version of the model published in Ref.:[64] with respect to the proton dynamics which are mainly causing spectral diffusion while water molecule motions have minor spectral diffusion effect at T = 1.4 K. Schematic structure of Chla. Chla harbors two sites accessible for hydrogen bonds (the methyl-ester carbonyls and keto-group of ring V). These positions might be involved in hydrogen-bridges with potential partners in their close environment. Possible conformational motion in a TLS and n-TLS is illustrated.

ferent. In D_2O based solvent, the red Chla are subject to substantial decreased spectral diffusion, whereas for $H_2^{18}O$ no spectral diffusion reducing effect is observed. Thus, mobility of water molecules, as an molecular entity of increased molecular mass, are not causing the strong spectral diffusion reducing effect. Instead, D-atoms are responsible for reduced spectral diffusion. D-atoms in "hydrogen" bridges formed by neighboring amino acid residues or by water molecules towards an chlorophyll molecule play the key role in the observed reduction of spectral diffusion of the red pool chlorophylls in PSI.

Exchangeable hydrogens as origin of the observed spectral diffusion

The observed changes of the transition energy in the nm range at cryogenic temperatures are believed to originate from conformational changes in the second tier of the hierarchically ordered anergy landscape of proteins [53] (see Chapter 2, page 26). The site-energy variation of the chromophore are either due to changes in the chromophore itself or its surrounding. The influence of the surrounding decreases strongly with the distance, therefore, only fluctuations in the first coordination sphere of the chromophores must be taken into account [59]. The analysis of the fluorescence emission spectra of individual PSI show the fluctuation rate strongly to be determined by exchangeable hydrogens. The

conformational fluctuation of these hydrogens affects the π-conjugation system of the Chla macrocycle and yields the observed spectral dynamics. Proton mobility in proteins is a prerequisite for function (for review see Ref.: [235]), and they are mobile even at helium temperatures [236]. The Chla molecule harbors no bound hydrogens exchangeable at physiological pH conditions. Therefore interactions, like hydrogen bonds, between the Chla moiety and nearby amino acid residues as well as the hydrogens from internal water molecules have to be taken into account [53, 237]. Chla harbors two sites accessible for hydrogen bonds, these are the methyl-ester carbonyls and keto-group of ring V [238] (see also Figure 5.18). Ring V shows high sensitivity of the site-energy towards changes close to this keto-group [42]. Fluctuations of a hydrogen atom in H-bonds between the keto-groups and nearby amino acid residues or water molecules may induce the largest changes of the site-energy possible at cryogenic temperatures. The large number of wavelength positions accessible for the individual emitters in PSI implies that a simple two-level system (TLS) model, as used for visualization in Figure 5.18 and in Chapter 2, page 26), is not capable of explaining the conformational dynamics of the H-bonds relevant for the spectral dynamics in PSI, a n-TLS (n stands for a larger number) is added to the model to account for these multiple site energy variations.

In summary, the observed spectral dynamics of single PSI complexes is strongly reduced in its rate by the exchange of the solvent from H_2O to D_2O. The same molecular mass water isotope $H_2^{18}O$ compared to the D_2O water isotope does not yield a diffusion rate decrease. All red-pools contributing to the fluorescence emission are affected upon deuterated solvent and therefore are accessible by the solvent. The structural origin of the spectral diffusion is most probable due to fluctuations of hydrogen atoms in the close environment of the π-conjugation system of the macrocycle of the emitting Chlas. The largest changes of the site-energy are suggested to stem from fluctuations of hydrogen atoms in a H-bond from the keto-group of ring V of the Chla to nearby amino acid residues or to structural water.

5.4 Huang-Rhys Factors of the Red Chlorophylls States of PSI from *Synechocystis* PCC6803

Resolved single-emitter profiles obtained by fluorescence emission spectroscopy on individual PSI from *Synechocystis* PCC6803 in D_2O-based solvent at T = 1.4 K allow for the determination of the electron-phonon couplings. For PSI from *Synechocystis* PCC6803 three spectral contributions were found either by low temperature single-molecule spectroscopy or by low temperature absorption, these are F699, C706 and C714 according to the emission maximum at 699 nm and two absorption maxima at 706 and 714 nm, respectively. The single-emitter profiles were resolved over the entire wavelength range covered by fluorescence emission of PSI. Thus, the Huang-Rhys factor determination can be performed for all the red chlorophyll *a* (Chla) states. A shifting procedure on time-dependent spectra series is applied for further resolution-enhancement. Hereby, line-broadening effects caused by slow spectral diffusion dynamics occurring on a second time scale are efficiently removed. As a result, resolution-enhanced single-emitter profiles with increased signal-to-noise ratios were obtained. On these spectra the Huang-Rhys factor determination is performed. A wavelength-dependent analysis of the Huang-Rhys factors reveals three contributions with their center positions at $\sim$ 700 nm with S $\approx$ 0.5 attributed to the F699 pool, a contribution at $\sim$ 713 nm with a larger Huang-Rhys factor of S $\approx$ 2 attributed to the C706 pool as well as a third contribution around 726 nm with a smaller Huang-Rhys factors of S $\sim$ 0.8. Recently, is was supposed that a general correlation exists between site-energy and electron-phonon coupling strength such that lower site energies are connected to higher Huang-Rhys factors. This suggestions does not hold to describe our observations.

This section presents an analysis of the electron-phonon couplings as determined for single PSI complexes in D_2O. The spectroscopic results are published in *Journal of the American Chemical Society*, (2008), **130**(51):17487-17493, 2008 (see publication list on page i).

Results

For all PSI complexes in D_2O buffer solutions[3] spectra series with 1 s time resolution were recorded. By using D_2O instead of H_2O as solvent the spectral diffusion dynamics are substantially decreased (see Section 5.3). However, spectral diffusion occurring on the time scale of seconds is present in the time-

[3]For details on the sample preparations see Chapter 3, page 45.

dependent spectral data. Figure 5.19a shows a time-dependent fluorescence emission spectra series taken from an individual PSI complex in D_2O buffer with a time resolution of 1 s. Second time scale dynamics are observed for two resolved ZPL contributions. One ZPL is present in the wavelength range between 700 – 706 nm and the other in the region between 710 – 715 nm. The ZPL in the region 700 – 706 nm shows only few large frequency jumps (for example in the first 20 s), but otherwise shows emission almost stable at a wavelength of $\sim$ 701 nm. The spectral trail of the ZPL in the range 710 – 715 nm shows more jumps with variable jump widths. This ZPL is accompanied by an intense PW. The spectral shape of the ZPL and its PW remains unchanged during the significant jumps of the ZPL over several nm (as shown for three different wavelength positions in Ref.: [64]). The shape stability of the emission line irrespective of the particular line position allows the extraction of the Huang-Rhys factor for this emitter after appropriate shifting of the line for signal-to-noise enhancement.

Shifting for resolution enhancement and increased signal-to-noise ratio
A shifting procedure is applied on all resolved single-emitter contributions of the 60 measured PSI complexes to remove the dynamics occurring on the second time scale. The shifting procedure relies on the search for the maximum position within a selected wavelength range. In the case of highly resolved single-emitter profiles, the range was selected around the ZPL contribution. Beside a clear narrowing of the spectral contributions of ZPL and PW and increased signal-to-noise ratio is obtained (see Figure 5.19b). This shifting-procedure leads to an 1 pixel sharp artifact due to accumulation of noise at the respective maximum position. Thus, the profile of the ZPL is extended, by a certain degree depending on the number of spectra contributing to the signal. As the ZPL contribution is a sharp feature in all analyzed spectra, the noise accumulated inside the 1 pixel sharp feature does not lead to an overestimation of the integral ZPL intensity. In Figure 5.19c the shifted data set after application of the shifting-procedure on the ZPL contribution found between 700 – 706 nm in the time series given in Figure 5.19a is shown. The spectra with vanishing intensity at the ZPL position were excluded from the data set. Therefore, the ordinate is no more a time axis but indicates number of spectra. The abscissa here is a relative wavelength axis. In Figure 5.19c the on the second ZPL contribution shifted data set is shown. All spectra of the series show a ZPL contribution in that range. Figure 5.19c shows the average spectrum as taken over the unshifted data set shown in Figure 5.19a (panel on top), and over the spectral regions covered by the single-emitter profiles in the shifted sequences shown in Figure 5.19b and Figure 5.19c (lower panel). The single-emitter profiles are plotted against the wavelength axis with the ZPL contribution positioned at the

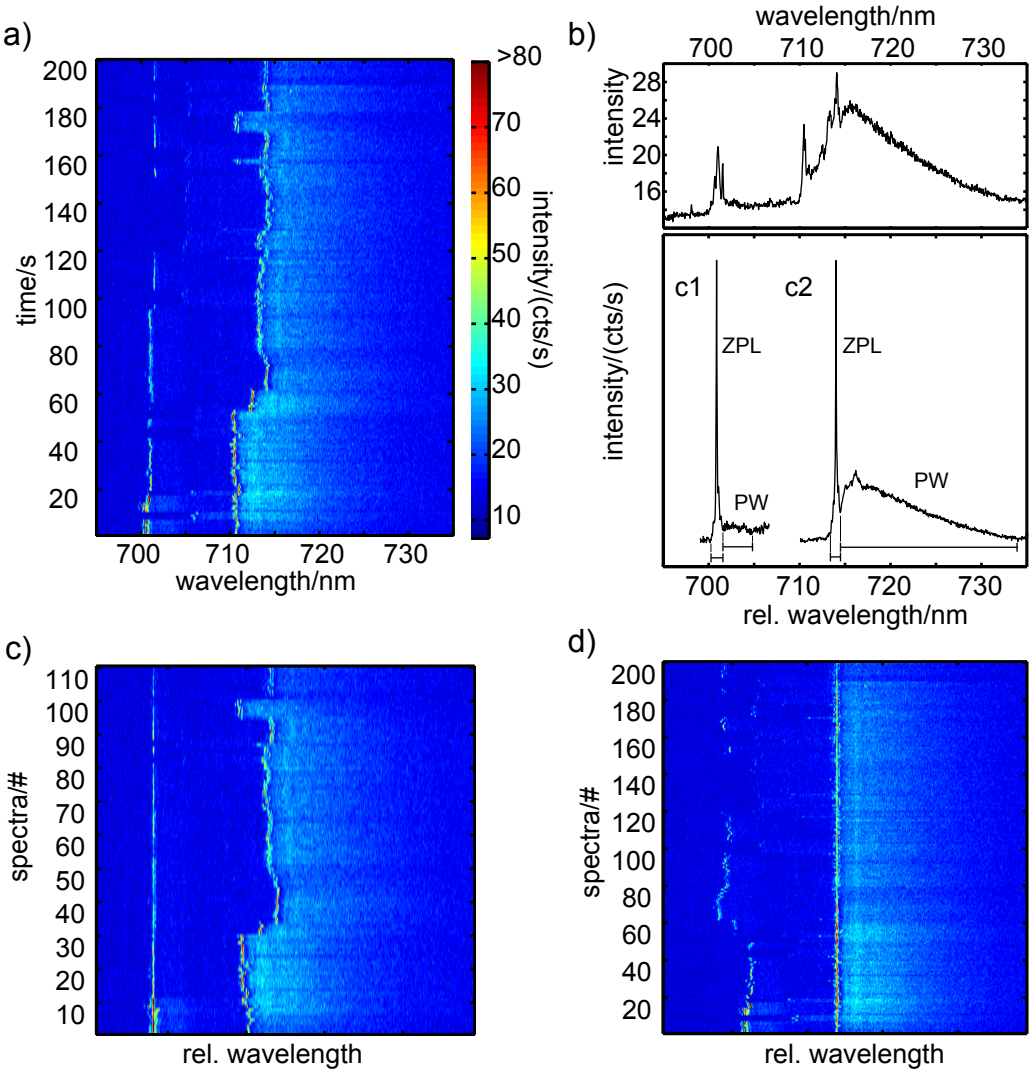

Figure 5.19: a) Time-dependent fluorescence emission spectra of an individual PSI complex with 1 s time resolution. The average spectrum is given on top of the sequence. White dashed lines indicated the regions wherein the ZPLs reside. b) Three single spectra out of the sequence given in a). c) For the determination of the Huang-Rhys factor of the emitter in the range 710 – 715 nm, 16 spectra where the ZPL resides almost on the same position (here 710.4 nm) were summed up (c1), the assumed width of the PW (710.8 – 730 nm) is given by a bar. For the ZPL in the range 700 – 706 nm the spectra between 15 – 17 s were summed up (c2), the assumed width of the PW (from 701.3 – 705.5 nm) is indicated by a bar (as published in [64]).

mean ZPL position occupied during the considered time interval, which is at 700 nm and 714 nm, respectively. The average spectrum of the unshifted time-dependent spectra series contains multiple peaks due to the line hopping on the second time scale and does not allow for a Huang-Rhys factor determination. The shifting leads to well resolved single-emitter profiles with increased signal-to-noise ratios.

Huang-Rhys factor determination

The Huang-Rhys factor determination is based on the numerical integration of the intensity found in the ZPL I_{ZPL} and in the PW contribution I_{PW} following the relation $\exp(-S) = \frac{I_{\mathrm{ZPL}}}{I_{\mathrm{ZPL}}+I_{\mathrm{PW}}}$. The determination of ZPL and PW from the resolution-enhanced single-emitter profiles is visualized by the two examples given in Figure 5.19c in the lower panel. The wavelength regions attributed to ZPL and PW contributions are indicated by bars below the spectra for both single-emitter profiles, respectively. The bar to lower wavelength indicates the spectral region of the ZPL and the bar to longer wavelength indicates the spectral interval attributed to the PW. For all single-emitter profiles a linear background is subtracted from the data to remove intensity due to dark counts of the detector. The Huang-Rhys factors determined for the depicted single-emitter profiles are S = 0.6 $\pm$ 0.1 for the profile with the ZPL mean position at 700 nm and S = 2.4 $\pm$ 0.3 for the ZPL with mean position at 714 nm. The Huang-Rhys factors indicate weak and strong coupling of the chromophores to their environments, respectively [234].

Huang-Rhys factors of the red Chla emitters of PSI

The Huang-Rhys factors were determined for 63 resolved single-emitter profiles present in the spectra from 60 individual PSI in D_2O buffer. The emission spectra of 51 PSI complexes show one to four resolved single-emitter profiles. The Huang-Rhys factor was determined by the method described above. In the case that single-emitter profiles are found on top of a broader spectral contribution a linear background was subtracted. The error was estimated for each line by performing the ZPL and PW interval selection as well as background subtraction several times. For single-emitter profiles indicating large Huang-Rhys factors a larger variance is found. This is due to the larger wavelength ranges to be considered for those single-emitter profiles. For single-emitter profiles with small Huang-Rhys factors of S = 0 – 0.5 the error is $\sim$ 0.2 for values of S = 0.5 – 1.5 the error is $\sim$ 0.1, for S = 1.5 – 2.5 the error is $\pm$ 0.3 and for the larger Huang-Rhys factors determined the error is $\pm$0.5. Figure 5.20 shows the determined Huang-Rhys factors of all resolved and resolution-enhanced single-emitter profiles from PSI in dependence on the wavelength position of the ZPL contribution. The mean wavelength position and the wavelength ranges occupied during the time-dependent measurement interval considered for the anal-

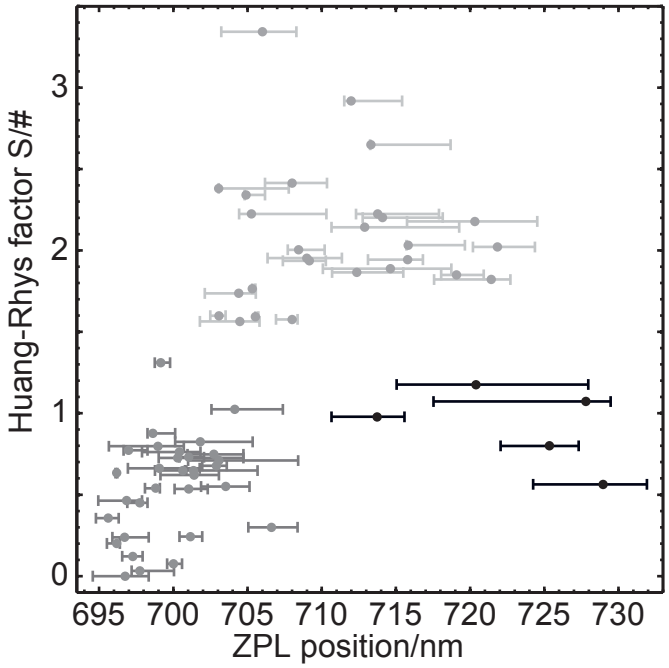

Figure 5.20: The Huang-Rhys factor was determined from single-emitter profiles obtained from PSI in D_2O. When spectral diffusion led to jumping of the spectral emission in the wavelength a shift algorithm was applied to get resolution enhanced spectra. The wavelength ranges indicate the range where the associated ZPL of the single emitter appeared, while the circles indicate the mean wavelength position in the considered detection time interval. The error of the determined S-values are given in the text.

ysis are given by circles and bars, respectively. The Huang-Rhys factors of the single-emitters of PSI differ between S = 0$\pm$0.02 and relatively large values of up to S = 3.3$\pm$0.5.

In the wavelength-dependent representation of the Huang-Rhys factors a point cloud with mean wavelength position at $\sim$ 700 nm and Huang-Rhys factor of S$\sim$ 0.5 spreading from 694 to 708 nm in wavelengths and from S = 0 to S = 1 in Huang-Rhys factors can be identified (highlighted in dark gray). The wavelength ranges occupied by the ZPL contributions have smaller widths compared to the contributions at longer wavelengths. The ZPL ranges of the contributions in this point cloud measure between $<$1 nm and 7.5 nm. This fluorescence emission contribution is attributed to the F699 pool of PSI from *Synechocystis* PCC6803. A further fluorescence emission contribution can be discerned by its wavelength-dependent Huang-Rhys factor (highlighted in light gray). This contribution has a larger spread with respect to both, wavelength and Huang-Rhys factors, and is found between 702 and 724 nm and with Huang-Rhys factors between S = 1.5$\pm$ 0.3 and S = 3.3$\pm$ 0.5, and thus, has a

middle position at $\sim$ 713 nm and S$\approx$2. The wavelength ranges occupied by the ZPL contributions in the respective time intervals varies between 2 nm and up to 9 nm. This contribution is assigned to the C706 pool. An additional probability for single-emitter contributions with small Huang-Rhys factors varying between 0.5 and 1.2 are found at longer wavelength positions at 721 to 731 nm. Though, with a middle position of $\sim$726 nm and S$\sim$0.8 The overall occurrence of single-emitter profiles in this wavelength region is minor, as only 5 of 63 resolved single-emitter profiles show a ZPL contributions in this wavelength range. The wavelength regions occupied by the single-emitters in time are relatively large varying between 5 and 13 nm. According to the wavelength position of these profiles these contributions are assigned to the C714 pool.

Discussion

Single-emitter profiles as resolved by low temperature fluorescence emission spectroscopy on individual PSI complexes from *Synechocystis* PCC6803 in deuterated solvent were analyzed. The single-emitter contributions are composed of a ZPL and a PW. The ZPL contribution was used for shifting the spectra from a time-dependent measurement to obtain resolution-enhanced spectra. The shifting relies on the search of the maximum. The effect of line broadening linked to spectral dynamics occurring on a second time scale were removed. From the resolution-enhanced single-emitter profiles which show substantially increased signal-to noise ratios the Huang-Rhys factors were determined. The single-emitter profiles are found at various wavelength positions and with different Huang-Rhys factors. By plotting the Huang-Rhys factors in a wavelength-dependent manner three different contributions were discerned. One contribution is found at $\sim$ 700 nm with S$\sim$ 0.5 with minor electron-phonon couplings, a second contribution between 702 and 724 nm and with large Huang-Rhys factors of S$\sim$1.5 to 3.3, and a third at longer wavelengths spanning from 721 to 731 nm and with relatively small Huang-Rhys factors between S = 0.5 and 1.2.

At these long wavelengths a contribution with small electron-phonon couplings has not been observed before for PSI, neither by hole-burning or fluorescence line narrowing techniques. In the low temperature fluorescence emission spectra of individual PSI complexes ZPLs are resolved with minor probability. Mainly strongly broadened fluorescence emission bands are found in this wavelength range. Furthermore, the fluorescence emission of the C706 pool with larger Huang-Rhys factors partially overlaps with the emission attributed to the C715 pool. Therefore, most probably this contribution is not accessible

in ensemble or sub-ensemble specific methods, as the C706 contribution most probably predominates the hole-burning spectrum.

Using D_2O instead of H_2O as solvent for low temperature single-molecule spectroscopy the probability for detecting single-emitter profiles in this wavelength region rises. These findings indicate that the C715 pool is surrounded by protons which are mobile in proteins at low temperatures [236]. Probably the chlorophyll molecules contributing to the C715 pool are coordinated by H-bonding partners, either amino acids residues or internal water molecules.

Recently, a direct correlation between site-energy of pigments and the Huang-Rhys factor was proposed based on a δ FLN study on chlorin and Chla [21]. PSI is particularly well suited to test this relation because a number of different Chla species with distinct couplings to their protein surroundings are detectable by their fluorescence emission on the single-molecule level. The herein presented findings indicate that the supposed direct correlation between lower site-energy of a pigment with a higher Huang-Rhys factor [21] does not hold. In contrast to an increase of Huang Rhys factor with wavelength, a Chla species with lower electron-phonon couplings at longer wavelength was observed.

5.5 An Additional Contribution Observed in the Fluorescence Emission of Individual Photosystem I Complexes from *Synechocystis* PCC6803

Time-dependent fluorescence emission spectra were taken for a large number of individual PSI complexes from *Synechocystis* PCC6803 exceeding the statistics yet taken on the single-molecule level for individual PSI. An additional component with a minor integral intensity and minor occurrence in the spectra from individual PSI complexes was identified. This spectral component has its maximum at average at 770 nm and indicates minor electron-phonon coupling of S<1. The oxidized reaction center $P700^+$ is considered as the putative origin of this spectral component.

Results

Emission Spectra of Individual PSI Complexes

For observing solvent-isotope exchange effects on the optical properties of PSI from *Synechocystis* PCC6803 a relatively large number of 347 individual PSI in $H_2^{18}O$-based buffer solution (PSI in PSI in $H_2^{18}O$)[4] is analyzed by time-dependent LT-SMS and compared to the spectral characteristics of PSI in H_2O-based buffer solution (PSI in H_2O) for which 109 PSI complexes were analyzed (Description of the characteristic line shapes of PSI in H_2O are described in Ref.: [181]). All PSI fluorescence emission signals were recorded under identical experimental conditions with an excitation wavelength of λ_{exc} = 680 nm, an excitation power of P_L = 100 μW and at temperatures of T = 1.4 K.

In Figure 5.21, time-dependent sequences of fluorescence emission spectra from individual PSI complexes prepared in $H_2^{18}O$-based buffer solution are shown together with the respective mean spectra taken over the time-dependent spectra series displayed on top. The time resolution was 1 s per spectrum and the spectral sequence display a time windows of 40 s. The average spectra on top correspondingly have an acquisition time of 40 s. Common for the depicted spectra series from individual PSI complexes is the composition of the overall spectrum by a limited number of spectral contributions, which vary in line widths, spectral position and spectral dynamics. The spectral characteristics of individual PSI complexes shown in Figure 5.21 are briefly described:

The mean spectrum of the spectral sequence in Figure 5.21a shows a narrow

[4]For details on the sample preparation see Chapter 3, page 45.

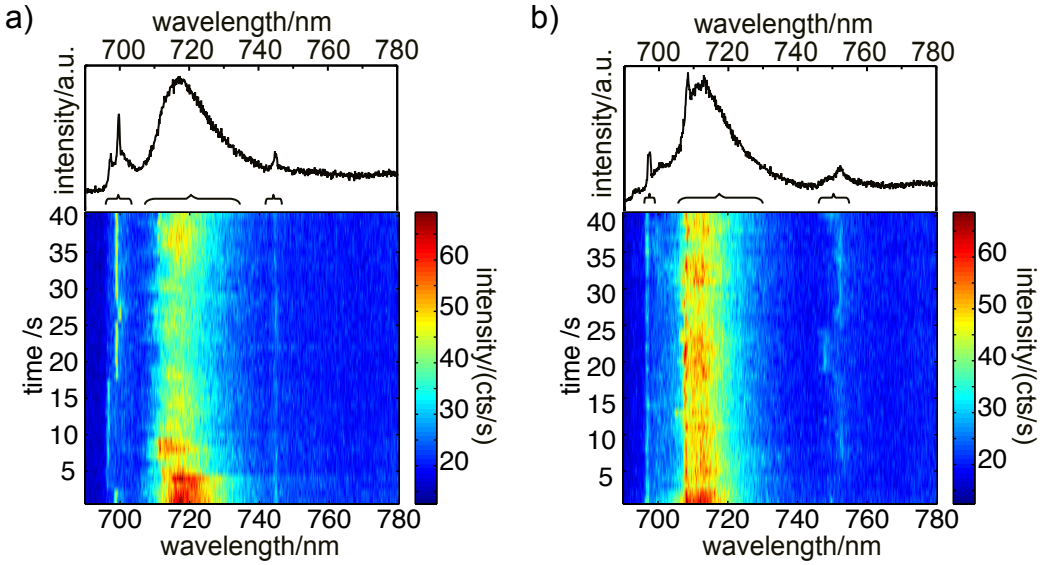

Figure 5.21: Time-dependent fluorescence emission sequences of individual PSI complexes in $H_2^{18}O$ with the associated average spectrum on top. The curly brackets on top of the spectral series indicate the extracted information on spectral range and center position. Experimental conditions for all measurements were λ_{exc} = 680 nm, P_L = 100 μW, t_{res} = 1s and t_{acq} = 40 s.

contribution at 699 nm with a line width $<$ 1 nm. Even though the spectral diffusion-induced line broadening prohibits the detection of lifetime-limited width of ZPLs which are of the order of 1 cm^{-1}, we will refer to these contributions as ZPLs. A less intense narrow line of comparable width is found at 698 nm. Furthermore, a broader intensity distribution with an asymmetric line profile peaking at 716 nm and a FWHM line width of $\sim$ 20 nm is present. This component contributes with highest intensity to the fluorescence emission to the spectrum. A further narrow peak of minor intensity is observed at 745 nm with a spectral width of $\sim$ 1 nm. From the time series it can be observed that the narrow contributions detected at 698 nm and 699 nm in the mean spectrum stem from a single emitter which undergoes spectral dynamics. The dynamics occur on a second time scale and thus are observed as spectral jumps. After 2 s of data acquisition the spectral line observed at 699 nm undergoes a jump towards 698 nm. A jump back to 699 nm occurs after 17 s of the detection time interval. After 26 s the ZPL is detected for a short period of 3 s slightly to the red, before the spectral line is again detected at 699 nm. A broader spectral contribution at 716 nm shows intensity fluctuations. After 4 s of the detection period an abrupt intensity decrease is observed. It seems that two broad contributions overlay while one of these photo-bleaches after 4 s of the detection interval. The ZPL contribution at 745 nm shows minor spectral diffusion but intensity variations. Thus, a single narrow line appears in the mean spectrum.

Figure 5.21b shows spectral information of a different individual PSI complex in $H_2^{18}O$. The mean spectrum is characterized by a narrow contribution which resides on the flank of a broader spectral contribution at 698. Beside a low intensity spectral band peaking at 700 nm covering a spectral range of $\sim$ 3 nm, a steep intensity increase is observed between 707 and 708 nm. At 708 nm a narrow peak is observed. To longer wavelength a broad contribution with FWHM $\sim$15 nm peaking at 713 nm is present. To longer wavelengths a narrow spectral component with minor intensity is found at 751 nm. This narrow peak resides on a broader intensity distribution of $\sim$ 10 nm in width and relatively low intensity. Again the associated time-dependent spectra series is inspected. The ZPL contribution at 698 nm shows minor spectral dynamics but intensity fluctuations. To the red in the interval between the ZPL contribution at 698 nm and the high most spectral line at 708 nm a diffuse intensity distribution near noise level is observed showing uncorrelated intensity changes compared to the ZPL contribution. Thus, these spectral components which resemble a ZPL with associated PW in the mean spectrum are not the ZPL and PW from a single-emitter but stem from different emitters. The broad intensity band peaking at 713 nm and the narrow line contribution on the short wavelength side seem to have the same intensity fluctuations and thus are attributed to a ZPL and its PW. The ratio of ZPL to PW indicates a relatively large electron-phonon coupling. The ZPL contribution at longer wavelength shows spectral diffusion with a time constant of several seconds and intensity fluctuations. In the beginning of the spectral series the intensity drops below noise level in the interval from 2 – 5 s. For the most part of the detection interval the contribution is found at 751 nm but in the time-interval from 19 – 25 s a line jump towards 749 nm and overall spectral diffusion at around these positions are observed. In the average spectrum on top, therefore, the ZPL contribution is on top of a broadened contribution.

Pool-widths and pool center positions

To compare the signals from hundreds of PSI complexes, parameters should be selected which efficiently reduce the comprehensive information contained in hundreds of time-dependent spectral series of PSI complexes without losing the ability of LT-SMS to look behind the ensemble averages. Hence, specific parameters for the single-emitter contributions should be extracted. Analysis of the spectral sequences reveals that each single red pool emitter exhibits a characteristic degree of spectral diffusion which occurs in confined spectral ranges. Thus, the width covered by individual spectral components, in the following referred to as the pool widths (not to be confounded with a FWHM value) is determined as a descriptor of the single-emitter contributions. This parameter is chosen because it is applicable to the various line profiles observed in PSI spectra. Considering the spectral time series in Figure 5.21a the narrow line con-

tribution which shows up at different line positions, for example, can hardly be described by a FWHM value, as the single-emitter profile shows up as two distinct peaks in the 40 s average spectrum. For the broader spectral component in Figure 5.21a one could argue that a fit with an asymmetric line profile could be used to describe this contribution. From measurements on deuterated samples though, it is known that the broadened spectral bands of the C714 state in PSI from *Synechocystis* PCC6803 state are at least partially due to fast spectral diffusing ZPLs, thus, the restricted 40 s interval only gives a snapshot of the positioning of the line profile within the interval of 40s, which could be different when taken at different observation times. More characteristic is the spectral range which is covered by the spectral contribution in time, which seems additionally not change upon deuteration [64]. The spectra of an individual PSI-$H_2^{18}O$ in Figure 5.21b shows a similar broad spectral contribution as the one discussed for the series in Figure 5.21a which in contrast shows up as a single-emitter profile composed of a ZPL and a PW. Thus, again a unified description for the broad spectral components based on an FWHM value is neither applicable to all single-emitter contribution nor is able to represent the single-emitter characteristics. These considerations led to the choice of the pool width together with the mid spectral position, referred to as pool center positions which are deduced from the analysis of the spectral sequences each taken with 40 s of time-dependent spectra series with 1 s time resolution. In Figure 5.21 the extracted information is visualized by horizontal curly brackets on top of the spectral sequences indicating the pool widths by the ends of the brackets and the pool center positions of the different single-emitter contribution by the spike of the bracket in the middle position. Thus it becomes clear that the parameter of the pool center position is not to be confused with a spectral center, which is characterized by high-most intensity. In contrast, theoretically this position can be associated with a position, where a hopping line never is registered.

For the spectra series in Figure 5.21a three different single-emitter contributions were identified. The time-series shown in Figure 5.21b highlights, that time-dependent data is required to estimate the number of contributing single emitters. Whether a narrow line and a broader contribution on the longer wavelength side are due to a single emitter or not can be judged by analyzing the spectral dynamics. Correlated dynamics indicate that most probably one emitter is the source for both contributions, while uncorrelated dynamics indicate that at least two emitters are responsible for the fluorescence contributions, respectively. In this way, the ZPL contribution at 698 nm was identified as a single-emitter profile, while the diffuse background around 701 is neither the PW nor has identifiable spectral range of spectral diffusion due to minor signal-to noise ratio and signal overlap with the broader contribution and thus is not

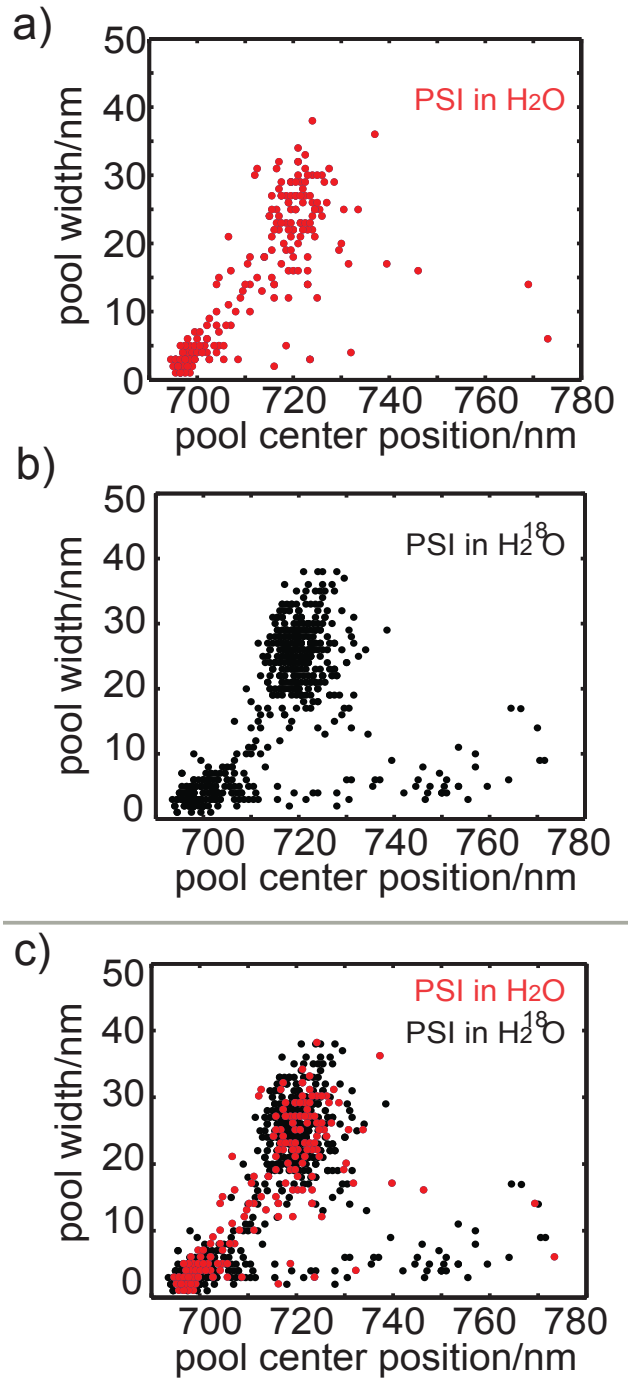

Figure 5.22: Scatter plots summarizing the extracted information on spectral ranges and center positions of the different spectral contributions within the fluorescence emission of individual PSI complexes, as obtained from the analysis of spectral sequences from 109 single PSI in H_2O (a) and from 347 PSI in $H_2^{18}O$ (b), taken at T = 1.4 K with λ_{exc} = 680 nm, P_L = 100 μW, t_{res} = 1s and t_{acq} = 40 s. In (c) the scatter plots of (a) and (b) are combined, the red points represent the data from PSI in H_2O and the black dots data from PSI in $H_2^{18}O$.

considered. Instead the peak at 708 nm and the broad contribution at 713 nm were identified as being associated with a single emitter. The pool width indicated by a curly bracket spans both contributions. A third single-emitter is identified in a 10 nm broad range at 745 to 755 nm.

Statistical analysis of the red chlorophyll emission
The scatter plots in Figure 5.22 summarize the pool width and pool center positions as deduced from the spectral sequences of 109 individual PSI in H_2O and of 347 individual PSI in $H_2^{18}O$. Each clearly identifiable spectral contribution detected within the time-dependent spectral series is represented by its center position and by its pool width covered within 40 s of observation. In Figure 5.22a the parameters given in wavelength obtained on PSI in H_2O are shown. Two point clouds of high density can be identified. The center of the first point cloud is found at a wavelength position of 699 nm and at a pool width of 4 nm. The range of center positions associated with this point cloud span from 695 nm to 705 nm and the pool widths span from 1 nm to 8 nm. A second point cloud is found at a center position of 721 nm and at a pool width of 25 nm. It has a larger spread, ranging from 712 nm to 729 nm in center positions and with pool widths varying from 12 nm to 35 nm. Less density of scatter points are detected in the area connecting the described point clouds. Additionally, single events are detected at wavelengths up to 772 nm.

In Figure 5.22b the extracted information about pool center positions and widths for PSI in $H_2^{18}O$ are collected. One dense point cloud is found with a center position at 700 nm and at a pool width of 5 nm. Spanning from 693 nm to 711 nm in center positions of the spectral contributions and with pool widths spreading from 1 nm to 8 nm. A second point cloud is located at 721 nm and at a pool width of 26 nm with a spread ranging from 711 nm to 731 nm in center position and from 17 nm to 38 nm in pool width. Similarly to the point clouds found for PSI in H_2O these point clouds are connected by a band of less point density. An additional band of points spread over a large center wavelength range spreading from 717 nm up to 772 nm and with minor pool width is present. The band spans from 717 nm where the pool widths range between 1 nm and 5 nm to 772 nm where the pool widths have higher values, ranging from 8 nm to 18 nm.

Figure 5.22c contains both overlaid scatter plots. The data of PSI in H_2O is shown in red and the data of PSI in $H_2^{18}O$ in black. While the point clouds with centers at ($\sim$ 699 nm/4 nm) and at ($\sim$ 721 nm/25 nm) appear in both PSI samples, the band spanned by points observed in 347 PSI in $H_2^{18}O$, being characterized by relatively long wavelengths and minor pool width, ranging from 717 nm to 772 nm and from 1 nm and 18 nm, is, beside single events not

observed for 109 PSI in H_2O. We will refer to this spectral contribution as the far-red contribution. A fraction of 40 complexes which corresponds to 12 % of the analyzed PSI complexes in $H_2^{18}O$ shows a far-red contribution, while for PSI in H_2O only a minor fraction of 6 complexes, which are 6 % of the analyzed PSI complexes, have this spectral feature. Due to the relatively small number of analyzed complexes, these percentage values are subject to large experimental errors.

Analysis of the far-red contribution
The far-red spectral component observed in spectral series from individual PSI complexes appears at wavelength positions between 717 nm and 772 nm and has pool widths ranging from 1 nm to 5 nm on the short wavelength side. The pool widths of this component increase towards longer wavelengths, measuring 8 nm to 18 nm on the long wavelength side. The scatter plot given in Figure 5.23a highlights all spectral contributions belonging to the far-red contribution as dots colored in orange, while all other spectral contributions found for PSI in $H_2^{18}O$ are shown in black.

In Figure 5.23b the average spectrum over the 40 s fluorescence emission spectra from 40 PSI complexes displaying the far-red spectral contribution is given (orange). The number of 40 PSI complexes, here, almost leads to a complete loss of the single-emitter features, including ZPLs and distinct broader spectral contributions with varying line widths (as in Figure 5.21). Beside a minor narrow feature at 764 nm, the spectrum resembles an ensemble spectrum of PSI from *Synechocystis* PCC6803.

The average over all 40 s fluorescence emission spectra from 347 PSI complexes in $H_2^{18}O$ is additionally given in Figure 5.23b (black). In the mean spectrum the single-emitter specific line profiles are averaged out and the ensemble spectrum of PSI *Synechocystis* PCC6803 is reproduced. The difference spectrum between the average spectrum taken over all complexes minus the complexes containing the far-red-spectral contribution is shown (brown). For better visualization a scaled difference spectrum is given (gray). A positive band in the difference spectrum starts at 735 nm spreading towards longer wavelengths, thereby, exceeding the analyzed wavelength range on the long wavelength side at 800 nm. The maximum of this broad band lies at 772 nm. Narrow line features in the difference spectrum peaking at 731 nm, 738 nm, 744 nm and 764 nm are attributed to single-emitter profiles which not have been averaged out. Additionally a peak of $\sim$10 nm in line width is found at 749 nm. As inferred from the density of points at this wavelength position in the scatter plot (Figure 5.23a) multiple single-emitter profiles are present at this wavelength position. These contributions are characterized by relatively small pool widths spreading from 3 nm to

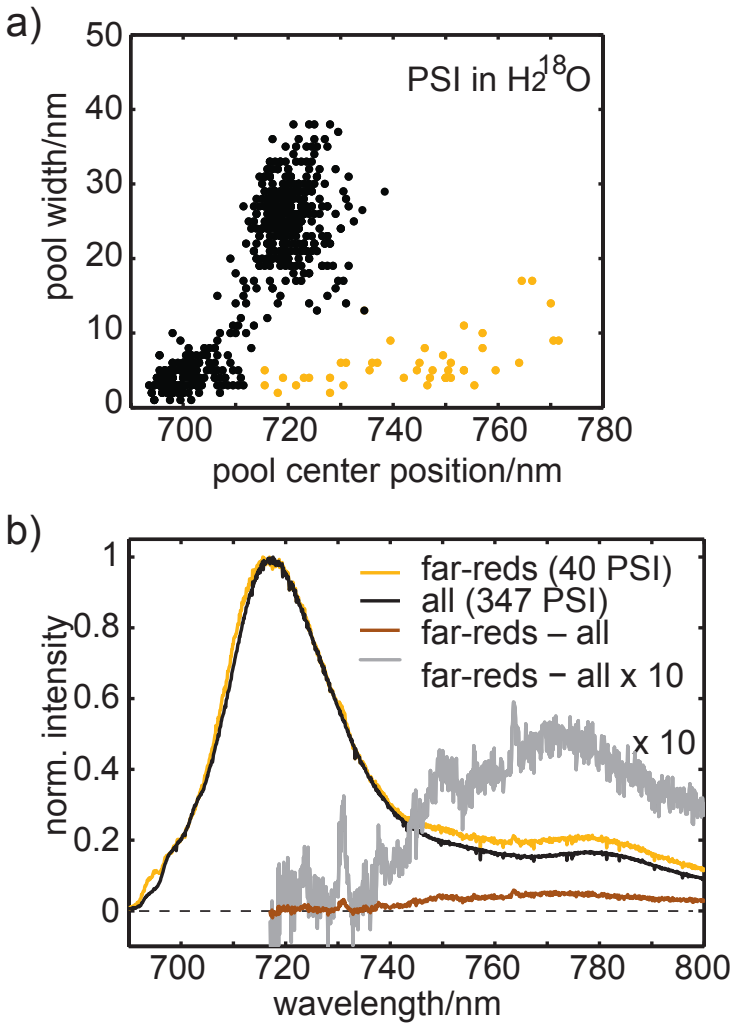

Figure 5.23: Beside the scatter plot for PSI in $H_2^{18}O$, here with the far-red contribution highlighted in orange (a), average spectra (b) of the 40 PSI complexes displaying the far-red contribution as well as the overall average over 347 fluorescence emission spectra obtained from individual PSI in $H_2^{18}O$ are given. The averaged spectra are build-up from the respective fluorescence emission spectra, each taken at T = 1.4 K with λ_{exc} = 680 nm, P_L = 100 μW, and with 40 s acquisition time.

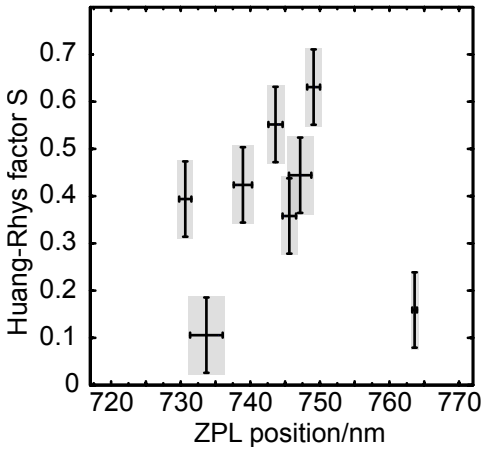

Figure 5.24: The Huang-Rhys factors of the far-red spectral contributions from individual PSI complexes. Huang-Rhys factor determination is based on the fluorescence emission spectra taken at T = 1.4 K with λ_{exc} = 680 nm, P_L = 100 μW. For resolution enhancement a shifting procedure was applied. The horizontal errorbars indicate the ZPL hopping range, which is occupied by the ZPL contribution in the considered time interval. Huang-Rhys factors are given with their errors.

8 nm and thus lead to the substructure in the far-red spectral range.

In Figure 5.24 the determined Huang-Rhys factors for single-emitter profiles resolved in the wavelength range associated with the far-red spectral contribution are shown. The determination of Huang-Rhys factor was performed as described in Section 5.4. The values indicate relatively small electron-phonon couplings of the emitting states as the Huang Rhys values are of S$<$1.

Discussion

An additional spectral contribution was observed in the low temperature fluorescence emission spectra of individual PSI complexes, which has not been reported before. We refer to this spectral contribution as the far-red spectral component.

The far-red spectral component is found at wavelength of up to 772 nm and thus is strongly red-shifted compared to the known red Chla contributions which are found at $\sim$ 699 nm, $\sim$ 712 nm and $\sim$ 715 nm for PSI from *Synechocystis* PCC6803. The red Chla candidates for the known spectral components are excitonic coupled chlorophyll *a* dimers and a trimer [239]. It is improbable that an as large site-energy lowering is possible by excitonic coupling of the Chla of PSI and site-energy calculations based on the structure model of PSI from *T. elongatus* with 2.5 Å resolution do not indicate such large red-shifts [209].

The far-red contribution is of minor occurrence in the spectra of individual PSI complexes. The occurrence of the spectral component is 6% (6/109) and 12% (40/347) for PSI in H_2O-buffer and PSI in $H_2^{18}O$-buffer, respectively. If this variance is due a non-balanced statistic [240] arising because of the small and different numbers of analyzed molecules for the respective sample preparations, or if the variance reflects an isotope effect remains an open question and is beyond the scope of this work. The application of advanced statistical methods such as mixture distribution models, which find application in fields where data series are often limited to similar small number of test ensembles, could be helpful to estimate the significance of this variance [241]. Furthermore, an increased number of measurements allowing for a more balanced statistic is supposed.

The integral intensities of the far-red spectral contributions in comparison to the intensities measured for the other fluorescent states of PSI is low (Figure 5.21b1 and b2) indicating that the fluorescence emission of the state is strongly be quenched. The spectral position of the far-red contribution varies in a broad spectral range and is found between 717 nm to 772 nm for different individual PSI complexes (Figure 5.23a). In the average spectrum taken over all PSI complexes analyzed in $H_2^{18}O$ this contribution does not appear as a distinct spectral peak (Figure 5.23b). This might explain, why this spectral contribution has not been observed before by fluorescence emission spectroscopy on ensembles of PSI molecules. By calculating the difference spectrum of the far-red contribution containing PSI average spectrum minus the fluorescence emission of all analyzed PSI complexes, an quasi bulk fluorescence emission spectrum is achieved of the far-red contribution (Figure 5.23b). Without the discrimination of the signals from individual PSI complexes the far-red spectral component, would not have been identified. This difference spectrum shows high similarity with the ensemble spectrum of chlorophyll a^+ [242]. Furthermore, the $P700^+$-minus-P700 absorption difference spectrum of PSI particles shows an positive contribution from 730 nm to 800 nm [226]. Under the used experimental conditions (low temperatures of 1.4 K, with Na-ascorbate pre-reduced PSI samples and continuous illumination with red light) P700 is expected to be stabilized in its the cationic $P700^+$ state [217]. $P700^+$ fluorescence emission is furthermore known to be strongly quenched and therefore has not been observed by ensemble fluorescence emission spectroscopy.

The Huang-Rhys factors determined from single-emitter profiles indicate rather weak electron-phonon couplings with values of $S<1$ (Figure 5.24) for the far-red spectra contributions. This finding points towards a state which has vanishing charge transfer character associated with minor rearrangements of the pigment's surroundings after excitation. Probably the excitation energy transfer within the pigment species being source of the fluorescence emission of Dexter

type transfer which probably is connected to lower electron-phonon couplings as the electron exchange occurs between overlapping molecular orbitals of the pigments. The interaction radius for Dexter coupling in general is limited to pigment distances of $\sim$ 5 Å. If the Dexter mechanism is be able to explain the observed red-shifts the far-red emission chlorophyll molecules (calculations are lacking) only chlorophyll molecules have to be considered as candidates for the far-red spectral contribution which are found in close vicinity to each other, not exceeding a distance of 5 Å . For the special pair chlorophylls this requirement is fulfilled. Concerning the small Huang-Rhys factors connected to the far-red spectral contribution further considerations are made. The Huang Rhys factors of $S \leq 1$ indicate monomeric Chla being responsible for the fluorescence emission as Chla multimers typically have Huang-Rhys factors of $S \geq 2$ [201]. From electron nuclear double-resonance [243] and electron paramagnetic resonance studies on single crystals [244] a monomeric nature for $P700^+$ is predicted. Based on these consideration, the oxidized special pair state, $P700^+$, is considered as the most probable candidate being responsible for the far-red spectral component detected for individual PSI complexes.

5.6 Protein Dynamics-Induced Variation of Excitation Energy Transfer Pathways

Strong anticorrelation between the fluorescence emission of different emitters is observed by employing single-molecule fluorescence spectroscopy on photosystem I at cryogenic temperatures. This anticorrelation demonstrates a time-dependent interaction between pigments participating in the exciton transfer chain, implying that uniquely defined energy transfer pathways within the complex do not exist. Fluctuations of the chromophores themselves or their immediate protein surroundings induce changes in their site energy, and, as a consequence, these fluctuations change the coupling within the excitation transfer pathways. The time scales of the site energy fluctuations of the individual emitters do not meet the time scales of the observed correlated emission behavior. Therefore, the emitters must be fed individually by energetically higher lying states, causing the observed intensity variations. This phenomenon is shown for photosystem I pigment– protein complexes from three different cyanobacteria (*Thermosynechococcus elongatus*, *Synechocystis* PCC6803 and *Synechococcus* PCC7002) with strongly different spectral properties underlining the general character of the findings. The variability of energy transfer pathways might play a key role in the extreme robustness of light-harvesting systems in general.

This section contains adapted "Results" and "Discussion" parts published in *Proceedings of the National Academy of Sciences of the United States of America*, **106**(29):11857-11861, 2009 (see publication list on page i). In addition to the spectral analysis of PSI from *Thermosynechococcus elongatus* and *Synechocystis* PCC6803 herein also PSI from *Synechococcus* PCC7002 is analyzed.

Results

Time-dependent LT-SMS on PSI from *T. elongatus*

In Figure 5.25A a time-dependent fluorescence emission spectra series as measured on a single PSI complex from *T. elongatus* at T = 1.4 K is shown[5]. The average spectrum is shown on top of the sequence. In the average spectrum, a zero-phonon line(ZPL) of C708 at 712 nm can be identified. In the spectral region of C715/719 ($>$ 712 nm) an unstructured broad distribution with maximum $\sim$ 723 nm is observed. The broad emission band shows no evidence for ZPLs. The emission intensity of the ZPL and the broad emission undergo large and opposite variations. It is important to note that the broad intensity distribu-

[5]For details on the sample preparations see Chapter 3, page 45.

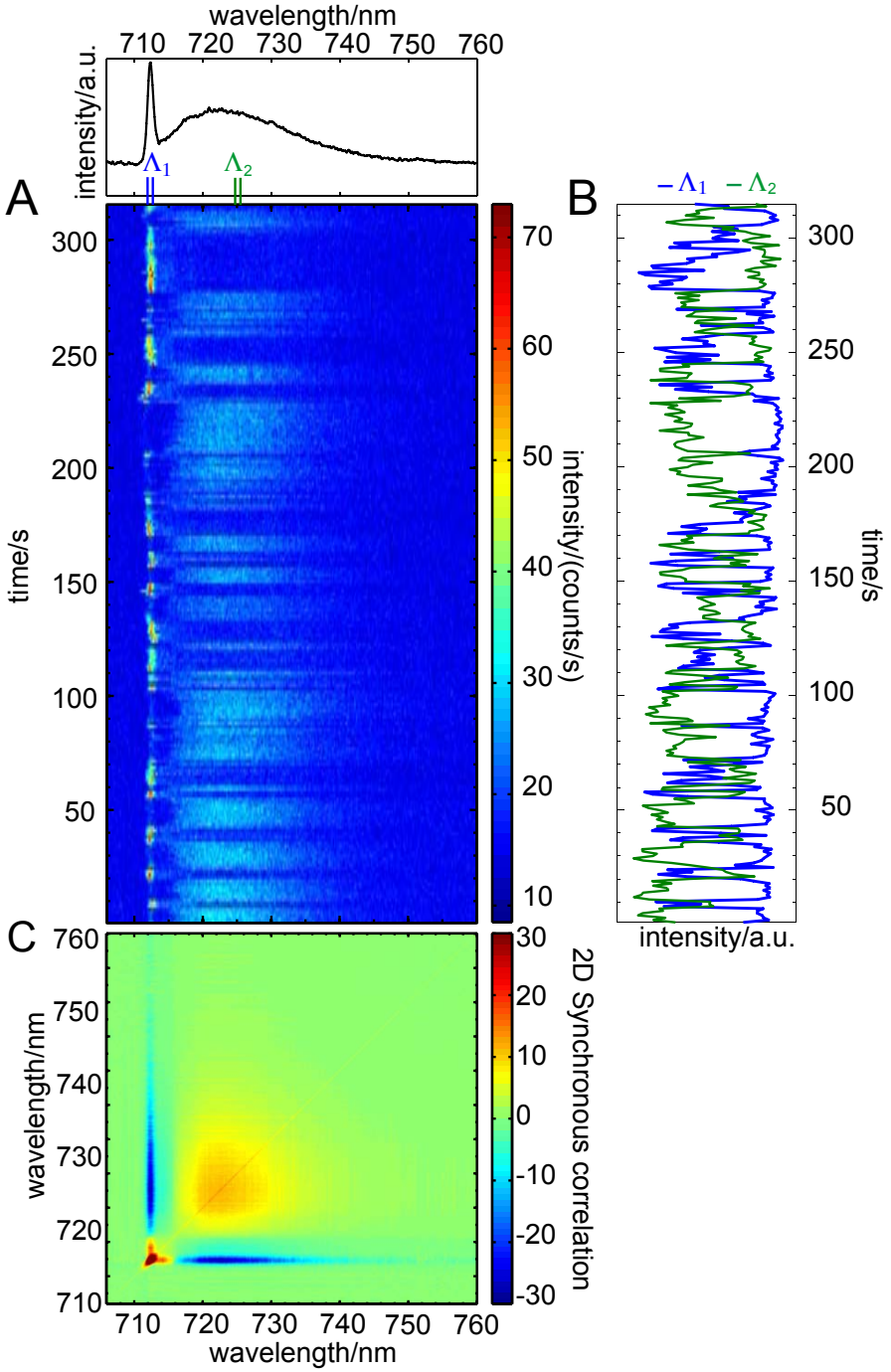

Figure 5.25: Time-dependent fluorescence emission and 2D-synchronous correlation spectrum (2D-SCS) of an individual PSI complex from *T. elongatus*, as published in [45]. A) Time series of spectra; the spectrum on top represents the time average. B) Integrated intensity of the wavelength ranges as indicated on top of the series shown in A and labelled Λ_1 and Λ_2. C) Contour plot of the 2D-SCS for the sequence given in A. The color code is indicated on the right; positive values correspond to positive correlation, and negative values correspond to anticorrelation. (Experimental conditions were λ_{exc} = 680 nm, P_L = 100 μW, t_{acq} = 1 s per spectrum, and T = 1.4 K)

tion varies uniformly. For better visualization of these variations, the integrated fluorescence intensities of the ZPL in the wavelength region Λ_1 (from 711.5 nm to 712.5 nm) and an of an arbitrary interval of the same width for the broad intensity distribution Λ_2 (from 724.5 nm to 725.5 nm) are plotted against time in Figure 5.25B. The intensity variations of the ZPL (Λ_1) and the broad band (Λ_2) are anticorrelated over the whole time of data acquisition. The strong anticorrelation between the two traces in Figure 5.25B is reflected by a correlation coefficient r(Λ_1, Λ_2) = -0.8.

The correlation coefficient r(λ_1, λ_2) between two time-dependent intensities at two wavelengths I(λ_1, t_i) and I(λ_2, t_i) is given by:

$$r_{\lambda_1,\lambda_2} = \frac{\frac{1}{n}\sum_{i=1}^{n}(I(\lambda_1,t_i)-\bar{I}(\lambda_1))\cdot(I(\lambda_2,t_i)-\bar{I}(\lambda_2))}{\sqrt{\frac{1}{n}\sum_{i=1}^{n}(I(\lambda_1,t_i)-\bar{I}(\lambda_1))^2}\cdot\sqrt{\frac{1}{n}\sum_{i=1}^{n}((I(\lambda_2,t_i)-\bar{I}(\lambda_2))^2}} \quad (5.2)$$

with the average spectra $\bar{I}(\lambda_j) = \frac{1}{n}\sum_{i=1}^{n} I(\lambda_j, t_i)$.

Insights into the wavelength dependence of the correlation behavior can be obtained by calculation of the 2D synchronous correlation spectrum (2D-SCS) as shown in Figure 5.25C.

The generalized numerical method used to calculate the correlation coefficients in two dimensional datasets of a two-dimensional data array y(λ_j, t_i), e.g., of wavelength λ and time t, is given by the expression [245]:

$$\Phi(\lambda_1,\lambda_2) = \frac{1}{m-1}\sum_{i=1}^{m}\hat{y}(\lambda_1,t_i)\cdot\hat{y}(\lambda_2,t_i), \quad (5.3)$$

where $\hat{y}(\lambda_j, t_i) = y(\lambda_j, t_i) - \bar{y}(\lambda_j)$ describes the dynamical part of the spectrum, e. g. the variation of the measured intensity (y = I) measured at a time t_i compared to its average value $\bar{y} = \bar{I}$ in the entire detection interval [t_{min},t_{max}]. For sets of spectra taken as a function of time, the 2D-SCS represents correlated changes of intensities measured at wavelengths λ_1 and λ_2 during data collection. The 2D-SCS is symmetric with respect to the diagonal $\lambda_1 = \lambda_2$. Peaks appearing on the diagonal and off-diagonal positions are referred to as autopeaks and cross-peaks, respectively. Autopeaks of a symmetric spectral band possess a circular shape in the 2D-SCS representation. Bands that undergo large intensity variations during the time of data collection show strong autopeaks, whereas bands that undergo no intensity variations show vanishing autopeaks. Cross-peaks represent a correlated change of intensity at two different spectral positions λ_1 and λ_2. The sign of the cross-peak specifies whether the changes are correlated (positive sign) or anticorrelated (negative sign).

The 2D-SCS of the time-dependent spectral series shown in Figure 5.25C is characterized by autocorrelation and cross-correlation peaks. Autopeaks are found

at positions of the ZPL and of the broad intensity distribution. The intense autopeak of the ZPL covers a small area in agreement with its narrow line shape in the average spectrum. Accordingly, an extended autopeak is found in the spectral range of the broad intensity distribution. The intensity of this extended autopeak increases from ~ 716 to 720 nm, followed by a region with almost constant intensity (720 – 728 nm) and a smooth decay for $\lambda > 728$ nm. Cross-peaks indicative for correlation between different spectral components are found between the position of the ZPL and its phonon wing (PW) as well as between the ZPL and the broad intensity distribution. Cross-peaks due to positive correlation of the ZPL with its PW are found in form of two narrow extensions of the ZPL autopeak. A narrow ridge represents the negative cross-peak between the ZPL and the broad intensity distribution. This negative cross-peak covers the whole emission range of the ZPL and the broad intensity distribution. Decreasing strength of correlation toward longer wavelength is associated with a decrease of signal intensity.

The anticorrelated behavior between the spectral contributions referred to as the ZPL contribution and the broad contribution to longer wavelength in the time-dependent spectral data set shown in Figure 5.25 is obvious. The dynamic changes between the spectral distributions occur on the time scale of the time resolution, which was 1 s. Therefore, calculation of the correlation coefficient $r(\Lambda_1, \Lambda_2)$ and the 2D-SCS spectrum reflect the anticorrelation but no substantial additional information was gained by application of 2D-SCS. For other time-dependent spectral data sets of PSI from different species including PSI from *T. elongatus*, PSI from *Synechocystis* PCC6803 and PSI from *Synechococcus* PCC7002 correlated behavior between the different spectral contributions is not obvious as the spectral diffusion dynamics occur on faster time scales as the time resolution of the measurements. For these spectral data sets, calculation of correlation coefficients either in 1D or 2D can yield meaningful information, as will be demonstrated by application of the 2D-SCS method on simulated data sets.

Simulations on the 2D-SCS method

The simulated spectra series are shown in 3D representation in the top row and in 2D contour plot representation in the middle row of Figure 5.26. Three types of time-dependent spectra were simulated; each of them has three contributions at the wavelengths λ_1, λ_2, and λ_3. In Figure 5.26a, these three contributions undergo either a linear decrease (λ_1, λ_3) or a linear increase (λ_2). In Figure 5.26b the time order of the spectra shown in Fig 5.26a was changed randomly; and in Figure 5.26c, noise was added to the spectra shown in 5.26b. In the third row the corresponding 2D-SCS are given. The autopeaks are labeled in the left 2D-SCS as *a1*, *a2*, and *a3* and the three cross-peaks as *c12*, *c23*, and *c13*. The cross-peaks *c13* connect the intensity at position *a1* with the intensity at *a3*. The positive

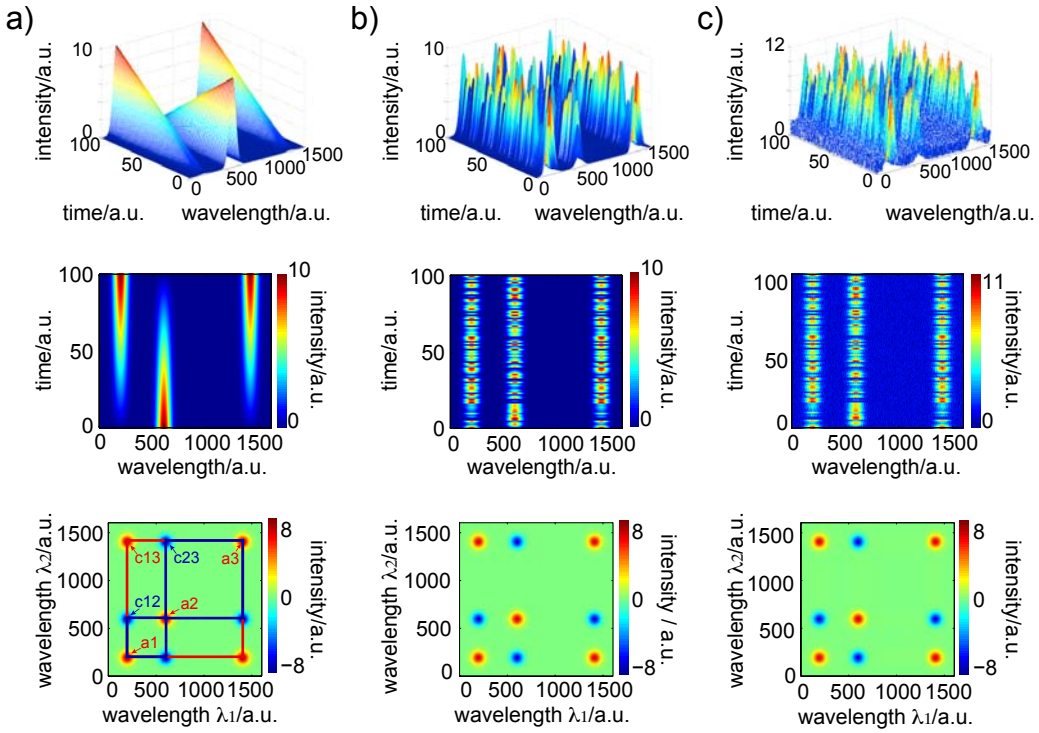

Figure 5.26: Simulated spectra to illustrate the information gained by calculation of the 2D-SCS from series of spectra. Each of the series of spectra given in the top row show three contributions that change in dependence of an external parameter, here the time. a) The contributions undergo a linear increase or decrease in their intensity. b) The same spectra as in a) are shown, but the time order of the spectra was changed stochastically. c) Noise was added to the spectra shown in b). The middle row shows the contour representation of the spectra shown above. The bottom row shows the resulting 2D-SCS spectra of the above spectra.

sign of the cross-peak *c13* reflects the correlated intensity change between the linear decreasing components at λ_1 and λ_3. Negative signs for the cross-peaks are found in the case of *c12* and *c23* as the respective intensity changes at λ_1 and λ_2 as well as between λ_2 and λ_3 are anticorrelated. The 2D-SCS spectra shown for the simulated spectra series in Figure 5.26b and Figure 5.26c show the same features as in Figure 5.26a, irrespective of the random time order of the spectra and the added noise. This result indicates that 2D-SCS can be used to unravel correlated behavior in single-molecule spectra that might be hidden in the time-dependent spectra due to random variations and limited signal-to-noise ratio.

PSI from *Synechocystis* PCC6803 and *Synechococcus* PCC7002

Figure 5.27a-A shows a series of continuously taken fluorescence emission spectra measured on a single PSI complex from *Synechocystis* PCC6803 at T = 1.4 K.

The average spectrum is shown on top of the sequence. The average spectrum shows two broad maxima at $\sim$ 706 and $\sim$ 717 nm. These broad contributions are most likely due to the emitters C706 and C714, respectively. In the time sequence, no evidence for stably emitting ZPLs is found, therefore both contributions are subject to fast spectral diffusion. The time-dependent variations of the emission frequency and intensity suggest a single emitter as the origin of these contributions. For better visualization of the respective intensity variations, the fluorescence intensities in the range of 700 – 710 nm (Λ_1) and 713 – 726 nm (Λ_2) are displayed in Figure 5.27a-B. These time traces show clear anticorrelation with a correlation coefficient r($\Lambda_1$1, Λ_2) = -0.4. The corresponding 2D-SCS of the sequence is given in Figure 5.27a-C. Autopeaks and cross-peaks are found for the emitters centered at 706 nm and 717 nm. The extension of the autopeaks is in agreement with the line shape in the average spectrum. A large negative cross-peak covers almost the whole emission region of the two emitters, indicating strong anticorrelation between the contributions from C706 and C714.

Figure 5.27b-A shows a series of continuously taken fluorescence emission spectra measured on a single PSI complex from *Synechococcus* PCC7002. The average spectrum is again shown on top of the sequence. The average spectrum shows two narrow contributions maxima at $\sim$ 693 nm and $\sim$ 701 nm and a broad contribution peaking at $\sim$ 707 nm. The narrow contributions are most likely associated with the F699 and the broad contribution with the C708 pool found for *Synechococcus* PCC7002. The fluorescence intensities in the range of 700 – 703 nm (Λ_1) and 708 – 718 nm (Λ_2) are displayed in Figure 5.27b-B. These time traces show anticorrelation with a correlation coefficient r($\Lambda_1$1, Λ_2) = -0.4. The corresponding 2D-SCS of the sequence is given in Figure 5.27b-C. Autopeaks and cross-peaks are found for the emitters centered at 701 nm and 707 nm. The fluorescence intensity in the narrow spectral contribution found at 693 nm does not show a significant auto-correlation peak or cross-peaks with the other two components. The slight negative cross-correlation of -1.8 with the ZPL contribution at 701 nm in comparison to values found for the cross-correlations of -20 between the 701 and 707 nm contribution, as well as the slightly positive cross-correlation of +2 with the broad contribution are not regarded as significant. The extension of the autopeaks is in agreement with the line shape in the average spectrum. A sharp negative cross-peak spanning the range of the narrow line contribution from 700 nm to 702 nm covers the entire wavelength interval connected to the broad fluorescence emission with a maximum at 707 nm, indicating strong anticorrelation between the contributions from F699 and C708.

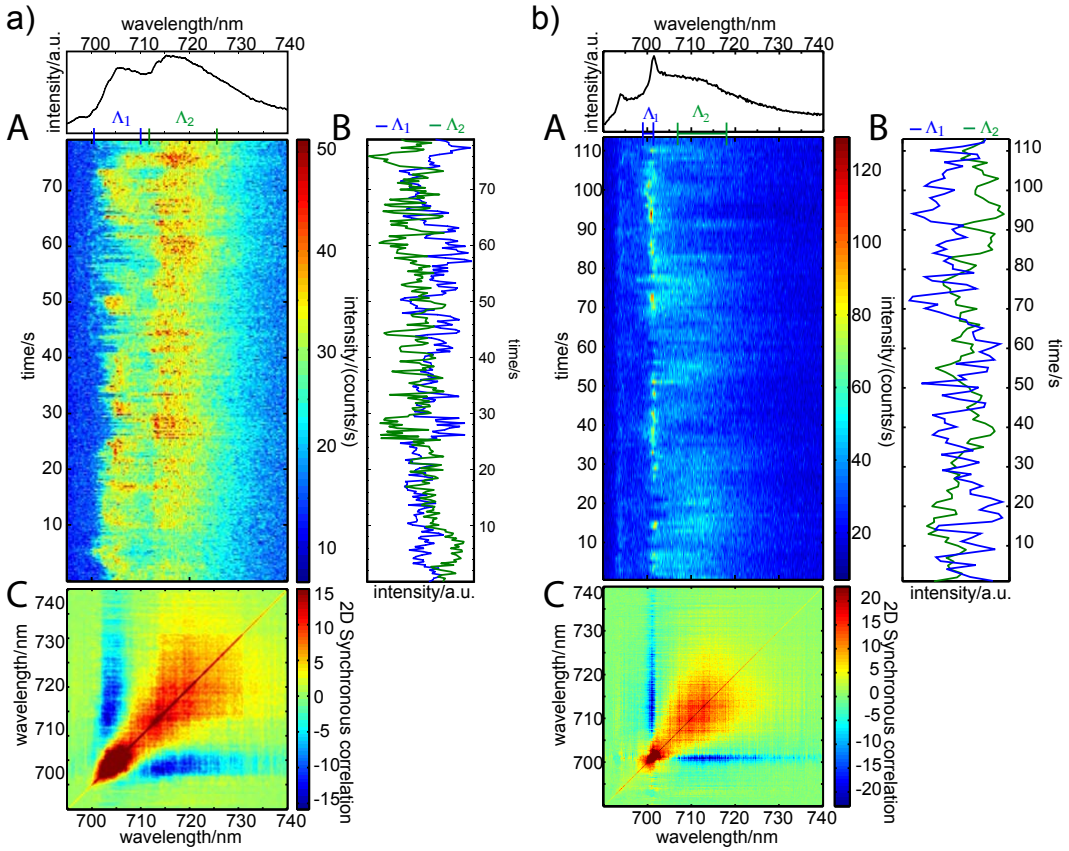

Figure 5.27: Time-dependent fluorescence emission and 2D-SCS of an individual PSI complex from a) from *Synechocystis PCC6803* (as published in Ref.: [45]) and b) from *Synechococcus* PCC7002. (A) Time series of spectra; the spectrum on top represents the time average. (B) Integrated intensity of the wavelength ranges as indicated on top of the series shown in A and labelled Λ_1 and Λ_2. (C) Contour plot of the 2D-SCS for the sequence given in A. (Experimental conditions were λ_{exc} = 680 nm, P_L = 100 μW, t_{acq} = 1 s per spectrum and T = 1.4 K)

Discussion

Two different processes can account for observing anticorrelated signals between two wavelength positions. First, an anticorrelation can be due to spectral hopping of a single emitter between these two wavelength positions, or secondly, the signals at different wavelength positions originate from two different emitters which are exclusively fed with excitons. For PSI the first scenario can be excluded [45]. Otherwise this would imply that large spectral changes of a single emitter are associated with (i) large variations of the electron-phonon coupling, as well as, with (ii) strongly altered polarization characteristics.

This should be explained in more detail: By various spectroscopic as well as computational methods the optical properties of PSI in the wavelength

range$>$ 700 nm were analyzed and attributed to multiple chlorophyll states. The different red chlorophyll states for example were identified by low temperature absorption spectroscopy [199, 202], hole-burning spectroscopy [201, 203, 210, 212, 246, 247] as well as by LT-SMS [14, 15, 179, 181]. By hole burning spectroscopy differences of the electron-phonon couplings were determined for the different red states [210, 212, 248]. Furthermore, polarization-dependent spectroscopy in the long wavelength region of the optical spectrum of PSI, either with ensemble spectroscopy [199, 202] or with LT-SMS [15, 179, 181] show differences in polarization for the different spectral contributions. To account for these experimental findings, the single-emitter scenario can only apply if spectral diffusion is so large that the entire PSI fluorescence emission is covered. And if the site-energy variation goes hand in hand with electron-phonon coupling changes, as well as, with polarization changes.

With respect to (i): Polarization-dependent LT-SMS spectra as shown in Figure 5.13 and as published in Refs.: [179, 181] do not show any indication of spectral diffusion-associated polarization changes. The polarization behavior is the same over the entire wavelength interval attributed to the emission of an individual emitter affected by spectral diffusion. Only between spectral bands attributed to different emissive states a phase shift of the polarization is observed. With respect to (ii): Changed electron-phonon coupling upon spectral wavelength changes are not observed, instead the electron-phonon coupling remains constant after site-energy changes of up to 5 nm (see time-dependent spectral data shown in Figure 5.19).

Hence, both requirements are not fulfilled as evident from time-dependent and polarization-dependent LT-SMS. It is more likely that the anticorrelated spectral components originate from different red pool emitters in the way that either one or the other state is fed by excitons. This implies flexible EET pathways. The EET in PSI is mainly due to FRET interaction between the multiple Chla molecules. As at T = 1.4 K the distances and orientations of the Chla are largely fixed, the only free parameter which strongly affects FRET-efficiency is the spectral overlap between donor and acceptor Chla. That observed spectral dynamics occur even at the low temperature conditions of T = 1.4 K suggest dynamic FRET-efficiencies between the spectrally observed chromophores and the feeding antenna states. Under the assumption of different chromophores as the origin of fluorescence emission from PSI in the different spectral regions, the observed anticorrelated emission (Figure 5.26 and 5.27) can be described by two simple models for the excitation energy transfer. These models are visualized in Figure 5.28.

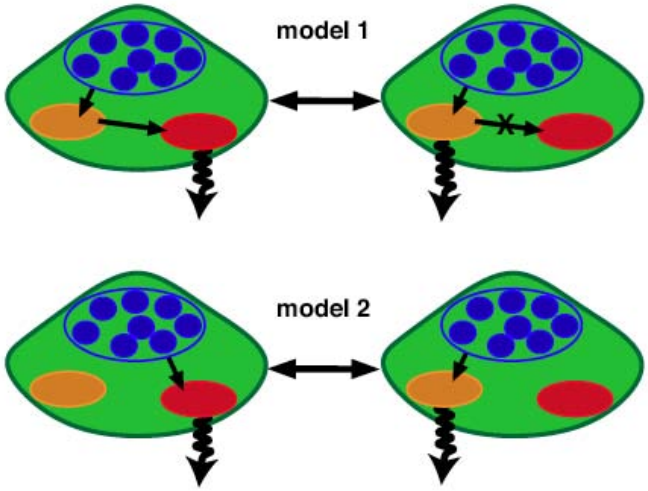

Figure 5.28: Models of excitation energy transfer pathways to the red traps. While the upper models presents energy transfer between the red pools, the lower model implies direct feeding of the different red states by the energetically higher lying antenna states (as published in Ref.: [45]).

Model 1 assumes a linear downhill energy transfer of the excitation energy from the antenna (blue) to the final trap (red). The anticorrelation is induced by changes in the transfer rates between the two red traps (orange, red). Model 2 assumes a parallel feeding of the red traps by energetically higher lying antenna states in the transfer pathway of the exciton. To distinguish between these two models, further analysis is needed. First the dynamic properties of the observed emitters are inspected as the potential origin of the correlated behavior. The anticorrelated intensity variations for the three different PSI complexes (shown in Figure 5.26 and Figure reffig:anicoorcys) occur on a second time scale. In the spectra taken for PSI from *T. elongatus*, the emitter C708 undergoes virtually no change of its emission frequency, whereas the spectral dynamics of C715/ C719 is much faster than the acquired second time scale. Therefore, both pools have to be excluded as source for the observed intensity variations. A similar observation can be made for the time-dependent behavior observed for PSI from *Synechococcus* PCC7002, where the spectral contribution attributed to the F699 state is relatively stable in its wavelength position over the detection time interval and where the spectral contribution attributed to the C708 state undergoes spectral wavelength changes on a sub-second timescale. And the same holds for time-dependent spectral information taken on PSI from *Synechocystis* PCC6803 (Figure 5.27a) where both emitters show spectral dynamics much faster than the second time scale of the intensity anti-correlation.

As a consequence, direct transfer of the exciton energy (model 1) between C708

and C719 in *T. elongatus*, as well as between C706 and C714 in *Synechocystis* PCC6803 and between F699 and C708 in (*Synechococcus* PCC7002 has to be excluded at least for the fraction of the emission intensity of C708/C706/F699 being anticorrelated to the intensity of C719/C714/C708 (model 1, Figure 5.28). Therefore, we conclude, that the anticorrelated intensity is induced by an energetically higher lying state within the antenna system for all PSI (model 2). Spectral dynamics of these antenna states occur on a second time scale. Depending on the actual site energy of the energetically higher lying state the excitation energy is fed into different pathways with individual energetic traps. The variability of the EET pathways was shown for PSI from different cyanobacteria (*T. elongatus* and *Synechocystis* PCC6803 in Ref.: [45]) and additionally here for PSI from *Synechococcus* PCC7002, underlining the general character of the finding.

The variation of the EET at low temperatures has a direct consequence for the discussion of EET in PSI at ambient conditions. Although all calculations for the EET analyzed so far assumed, at best, a static distribution of site energies, it seems much more appropriate to include fluctuations of the site energies for realistic modeling of EET in PSI and similar complexes. At ambient temperatures, the degrees of freedom available for conformational changes of the protein are largely increased compared to the low temperature conditions of T = 1.4 K. Thus, the coupling between protein and cofactors will lead to faster modulations of the cofactor site energies, probably on the sub-nanosecond time scale. This time scale is much shorter than the average time between two photon absorption events in an individual PSI complex under ambient light conditions. Therefore, the changes in site energies between two successive absorption events likely lead to different EET pathways for each exciton. The variability of the EET pathways induced by protein dynamics might play a key role in the high photostability of PSI and might give a hint to the robustness of proteins in general. Furthermore, our finding shows that tiny changes in the 3D structure of the complex are able to vary the excitation transfer pathway in PSI remarkably.

At low temperatures, the observed spectral dynamics is at least partially photoinduced [47, 228, 249]. Under strong illumination at ambient conditions, such photoactivated dynamics can increase the rate of fluctuations in the EET pathway or even alter the preferential EET route away from the reaction center towards protective quenching sites. The finding of protein dynamics-induced alterations of EET pathways points towards an efficient protection mechanism.

6

Single-Molecule Spectroscopy on Hybrid Systems

6.1 Hybrid Systems Composed of Pigment-Protein Complexes and Plasmonic Nanostructures

Plasmonic metal-nanostructures are an emerging tool for manipulating optical properties of fluorophores [250–252]. They are used for enhancing the sensitivity of fluorescence-based assays in drug discovery and high-throughput screenings as well as in immunoassays [35]. Even plasmon-assisted detection of biological reactions in vivo has been suggested [253]. The fast evolving range of applications for plasmonic nanomaterials make a deeper understanding of nanostructure–protein interactions necessary.

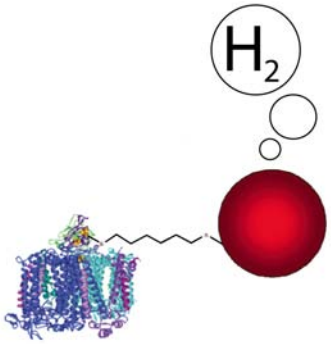

Figure 6.1: Hybrid system of a PSI with a molecular wire to an AuNP, where H_2 production is initiated by PSI photoactivation as experimentally demonstrated by Grimme et al. [254].

6.2 Fluorescence Studies into the Effect of Plasmonic Interactions on Protein Function

Interactions of plasmonic nanostructures with single fluorophores [37, 255, 256] and two-chromophore Förster resonance energy transfer (FRET) coupled systems [257] have been extensively studied, and first studies on biologically relevant systems with single chromophores [255]or with two coupled chromophores were published recently [258]. Studies of plasmonic interaction effects on more complex systems, with multiple chromophores coupled within one molecular assembly, are lacking. Herein, we use a key protein of the photosynthetic apparatus, photosystem I (PSI), as a model for multi-chromophore FRET-coupled systems. To study the affect of plasmonic interaction PSI was prepared in hybrid sample composition with metal nanostructures. These are 100 nm diameter gold spheres (AuNP) and silverisland films (SIF).

This section is basically a reproduction of the work published in *Angewandte Chemie International Edition*, (2010) **49**(52):10217–10220 (see publication list on page i).

Results and Discussion

For PSI, PSI-AuNP and PSI-SIF samples[1], fluorescence intensity scans, taken of the same sized area under identical experimental conditions, are shown in Figure 6.2a–c. An identical color scale ranging from 0 to 100000 counts per second was chosen for comparison of the data. As a consequence the spot sizes increase in the scans of PSI-AuNP and PSI-SIF, where maximum intensities were about 50-times the threshold of 100000 counts per second. The deviation of the spots from circular shapes can be attributed to the low imaging quality of the employed microscope objective at low temperatures. An intensity increase from PSI to PSI-AuNP, and to PSI-SIF is clearly seen. Intensity scans of samples solely composed of AuNP or SIF without PSI also yield fluorescence signals (see Figure 6.3), suggesting intrinsic signals from AuNP and SIF, and/or signals from impurities.

In Figure 6.3a fluorescence intensity scans of of the metal-nanostructures AuNP and SIF are shown.The same intensity scale was used as for the PSI-containing samples (Figure 6.2a–c). The spectra associated with the spots in the fluorescence intensity scans from AuNP and SIF are shown in Figure 6.3b and Fig-

[1]For details on the sample preparation and SIF characterization please consult the Material and Methods in Chapter 3, page 46.

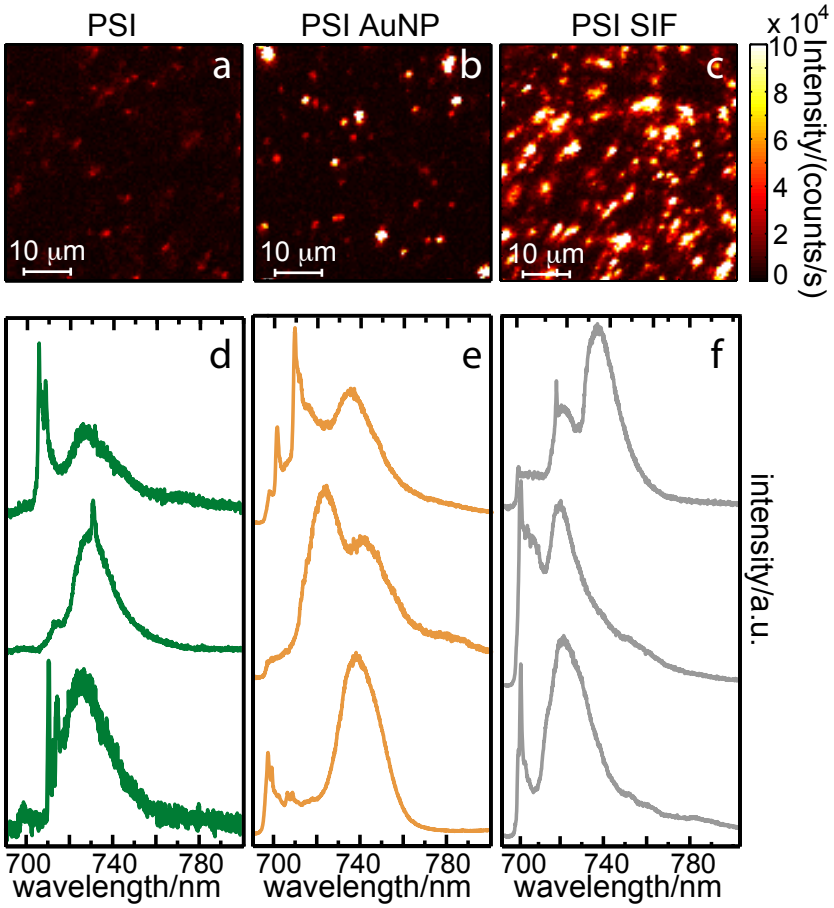

Figure 6.2: a - c) Fluorescence intensity scans of PSI (a), PSI-AuNP (b), and PSI-SIF (c) and three PSI spectra from different individual PSI complexes for each sample type (d–f). The fluorescence intensity scans were acquired with an integration time of 2 ms per pixel. The spectra (d–f) were taken with an acquisition time of 40 s. For all experiments temperature was at T = 1.4 K, λ_{exc} = 680 nm and $P_L = 100\mu W$.

ure 6.3c, respectively. All spectra were measured under the same experimental conditions as the PSI spectra described in the article. The spectra were classified similarity classes. For AuNP three and for SIF five classes of spectra were discerned. Each spectral class is represented by one spectrum. a) For the AuNP sample the majority of the spectra are marked by a characteristic double peak pattern with 30 nm distance between the two peaks (64%) or by very broad intensity distributions relative to the PSI fluorescence (21%). A minor contribution (14%) is marked by multiple narrow line signatures; b) for the SIF sample broad spectral shapes with rather constant intensity over the whole analyzed wavelength range (41%) as well as with an increase to maximum positions > 800 nm (23%) and with the maximum between 700 and 740 nm (22%) are observed. A further contribution (12%) shows Raman-like narrow line structures,

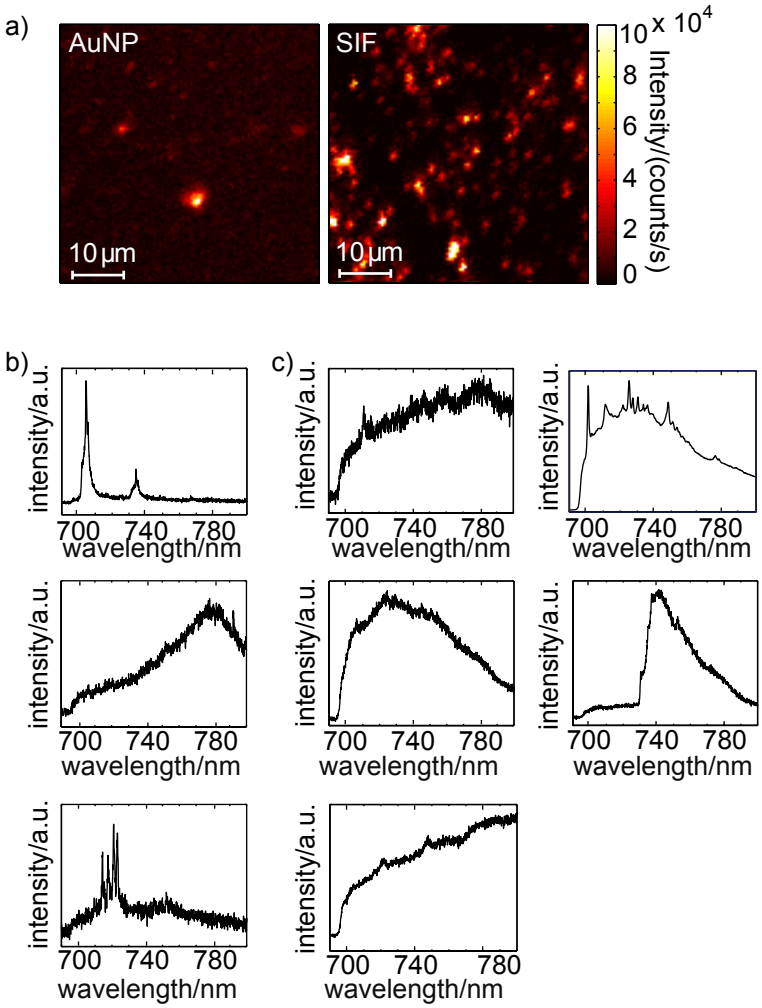

Figure 6.3: a) Fluorescence intensity scans of the metal-nanostructures AuNP and SIF with identical intensity scaling as in Figure 6.2. Together with the typical spectral features observed for the bare nanostructures. In b) the spectra observed from the sample AuNP and in c) from SIF (see text for details).

in some cases on top of broad intensity contributions. Spectra from a minor contribution (3%) are marked by peaks of similar spectral width as PSI fluorescence, but with differing wavelength position or spectral shape, which might be attributed to impurity molecules, which are efficiently enhanced by the SIF.

Therefore, a determination of the fluorescence enhancement factors for the different plasmonic structures is not possible based on intensity information alone. A spectral analysis of the intensity contributions present in the PSI-free samples of AuNP and of SIF shows that their signals are easily distinguishable from the PSI emission fingerprints and makes a separation of signals intrinsic to the nanostructure possible (see Figure 6.3). In total 148 spectra were recorded for PSI in buffer, 158 for PSI-AuNP, and 72 for PSI-SIF. In Figure Figure 6.2d–f, rep-

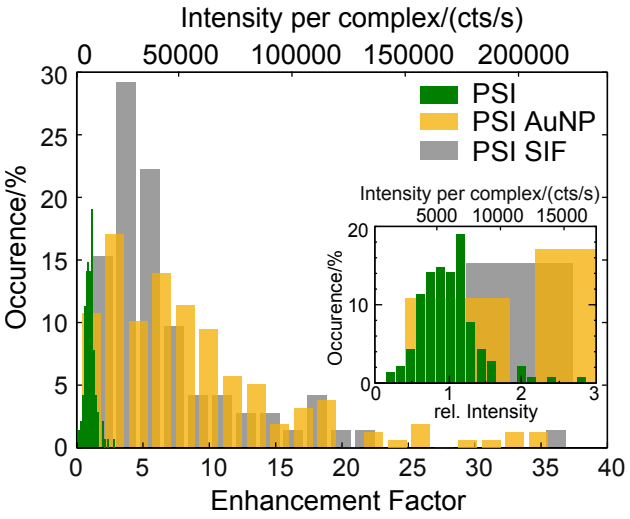

Figure 6.4: Intensity histograms of signals from PSI (green), PSI-AuNP (orange), and PSI-SIF (gray). The intensities for the individual complexes were obtained from spectrally resolved data. The counts detected in the wavelength interval from 690 nm to 800 nm were integrated after subtraction of a constant background to eliminate dark counts and stray light. The intensity ranges for the different samples were each divided into 20 bins. The inset shows a zoom into the PSI intensity statistics around the mean intensity of uncoupled PSI.

resentative PSI spectra for each of the sample types, measured under identical experimental conditions, are shown. The spectra are composed of characteristic contributions, appearing at different wavelength positions in the emission spectrum of PSI. The increased signal-to-noise ratios in the spectra from PSI-AuNP and PSI-SIF samples reflect enhanced fluorescence emission. The line widths of the different red chlorophyll contributions within the spectra of individual PSI remain largely preserved (Figure 6.2); unexpectedly, the increased exciton flux migrating through PSI upon coupling to a plasmonic nanostructure does not significantly increase the probability for fluctuations that would result in line broadening. The integrated fluorescence intensities of all the individual PSI complexes are given as histograms in Figure 6.4. The intensity histogram (green) of uncoupled PSI has a nearly Gaussian shape (see the inset), while the histograms for PSI-AuNP and PSI-SIF steeply increase to a maximum value and decay approximately exponentially to higher intensities.

Enhancement factors Figure 6.4, bottom x-axis) give the relative intensity of individual PSI-AuNP and PSI-SIF with respect to the mean intensity of uncoupled PSI. Maximum observed enhancements are 36 for PSI-SIF and 37 for PSI-AuNP and the average enhancements are 7 and 9, respectively. This significant metal-enhanced fluorescence (MEF) of PSI coupled to AuNP or SIF is of the same order of magnitude as that reported for other fluorophore–metal-nanostructure

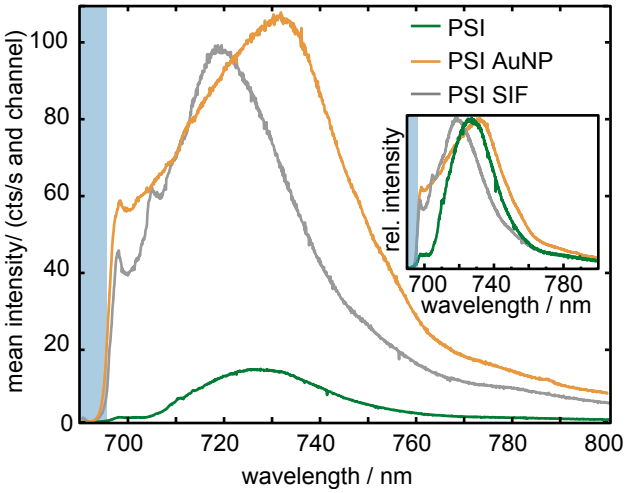

Figure 6.5: Mean spectra of 142 PSI in buffer (green), 158 PSI coupled to AuNP (orange), and 72 PSI on SIF (gray). The wavelength range suppressed by the fluorescence cut-off filter is marked in blue. Inset: Associated average fluorescence emission normalized to the fluorescence peak.

interactions [258–263].

The inset in Figure 6.5 shows the normalized average spectra of all the PSI, PSI-AuNP, and PSI-SIF complexes, respectively. The AuNPs lead to an increased line width of the PSI fluorescence (Γ_{FWHM}(PSI) = 33 nm versus Γ_{FWHM}(PSIAuNP) = 52 nm; FWHM: full width at half maximum); in contrast, the line width of SIF-coupled PSI remains virtually unchanged (Γ_{FWHM}(PSI-SIF) = 37 nm). The peak position of fluorescence emission for PSI-SIF is blue-shifted by 8 nm to 719 nm compared with uncoupled PSI (727 nm), whereas the peak position of the PSI-AuNP (732 nm) is red-shifted relative to uncoupled PSI. Both plasmonic structures lead to strongly increased fluorescence at the short-wavelength side of the fluorescence emission indicating strongly enhanced fluorescence deactivation of the higher energy antenna pigments, which show virtually no fluorescence emission in the absence of plasmonic structures. Relative fluorescence intensities between 698 – 705 nm and the respective fluorescence maximum intensity increase from around 10% for PSI to 40 – 60% and 50 – 60% for PSI-SIF and PSI-AuNP, respectively. The average enhancement factors in this wavelength range are as large as 40 – 60 for both structures and the enhancement reaches maximal values of about 200 for PSI-SIF and about 400 for PSI-AuNP. Thus, the shape of the average spectra of PSI-AuNP and PSI-SIF shows considerable deviations from the average spectrum of uncoupled PSI. This situation is in contrast to single chromophore systems and two-chromophore FRET-coupled systems interacting with similar plasmonic structures, where nearly uniform fluorescence enhancement was observed [258, 264, 265]. Only mi-

nor spectral shifts were observed for albumin in gold-nanoparticle biconjugates, which were explained by conformational changes of the water-soluble protein on the metal surface [266]. The rather uniform fluorescence enhancement of organic chromophores is because the plasmon spectra of the nanostructures used are rather featureless [267, 268] over the fluorescence emission profiles of the chromophores studied. The fluorescence emission of PSI at low temperatures is of comparable width to the systems studied at room temperature to date [258, 264, 265], and larger structural changes are unlikely, since PSI complexes retain their charge-separation capability even in close proximity to nanostructures or metal surfaces [254, 269–272]. Thus, for PSI a rather uniform fluorescence enhancement could be expected. The observed non-uniform enhancement can be understood taking into account the properties of multi-chromophore assemblies.

The FRET efficiency between chromophores depends on their spectral overlap, separation, and orientation [273]. The specific coupling conditions between the chromophores lead to a characteristic set of transition rates (Figure 6.6a). In PSI this is optimized for the efficient excitation of the reaction center. The interaction between pigments and plasmonic structures is also strongly distance- and orientation-dependent [273]. A distance-dependent enhancement curve calculated for a fluorophore coupled to a AuNP of 100 nm diameter shows quenching at distances shorter than approximately 2 nm, maximum enhancement at approximately 13 nm, and an exponential decay to longer distances indicating an absence of interactions at around 80 nm [37]. In contrast to other studies, where PSI was prepared in defined orientation on metal surfaces and metal nanoparticles [254, 269, 270], in our case, PSI is randomly oriented towards the plasmonic structures. This feature is a possible origin of the observed broad distribution of enhancement factors.

The size of a PSI trimer, in which around 300 chlorophyll pigments confined in an approximately cylindrical structure measuring around 20 nm in diameter and approximately 5 nm in height, makes coupling scenarios possible where some chlorophyll molecules are quenched and others are subjected to maximum fluorescence enhancement. As fluorescence enhancement is correlated with a decrease in the fluorescence lifetime [267], the balance between fluorescence and other deactivation channels, such as energy transfer, can be changed. Plasmonic interaction alters Förster interaction distances between chromophores [257]. In one donor–acceptor pair the Förster radius increases from 8.3 to 13 nm as a result of plasmonic interaction [257]. This effect can change the exciton distribution within PSI by involving additional chromophores in excitation energy transfer (Figure 6.6b). In conclusion, our experiments show an altered fluorescence of PSI upon interaction with AuNP and SIF.

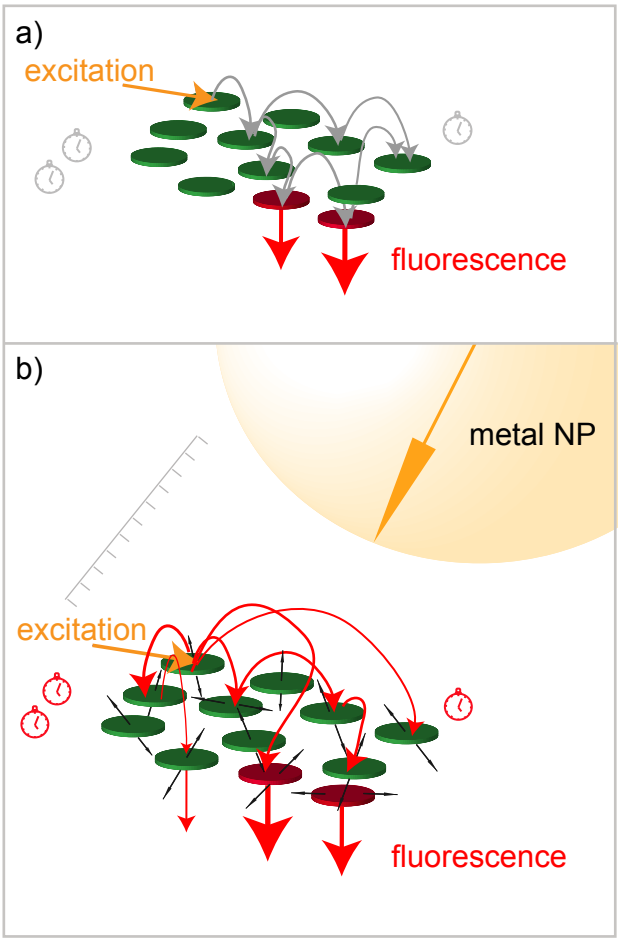

Figure 6.6: Visualization of excitation energy transfer pathways in a multi-chromophore FRET-coupled system. a) Without plasmonic interaction: Specific coupling conditions between the chromophores lead to a characteristic set of transition rates indicated by gray arrows. Clocks indicate the respective excited state lifetimes. b) With plasmonic interaction: The set of transition rates is modified through to plasmonic coupling, which is distance- and orientation-dependent indicated by the ruler and black arrows, respectively. Additional excitation energy transfer pathways (red) illustrate the origin of the modified system response.

Particularly the higher energy chlorophyll molecules with site energies close to that of the reaction center show increased deactivation through fluorescence emission, thereby reducing the efficiency of energy transfer towards the site of charge separation (P700), and thus altering the protein function. We suppose that altered responses can generally be expected for multi-chromophore FRET-coupled systems near plasmonic nanostructures. These findings have to be considered when aiming at nanostructure-assisted bio-applications.

7

SUMMARY AND OUTLOOK

In this work, fluorescence emission signals from individual pigment-protein complexes as well as from hybrid structures composed of pigment-protein complexes and metal nanostructures were analyzed. Single-molecule sensitivity was achieved by highly diluting the protein samples in optical transparent solvents, thereby matching the conditions that statistically less than one pigment-protein complex is found within the detection volume. Spacial selectivity was obtained by using a microscope objective in confocal configuration. For obtaining high-resolution spectra of the protein-embedded pigments low temperature conditions of T = 1.4 K were used.

Dynamic wavelength changes referred to as spectral diffusion were observed in the fluorescence emission signals of both pigment-protein complexes, phytochromes and photosystem I (PSI). These site-energy variations can qualitatively be understood in the energy landscape model of proteins [50]. At the low temperatures used transitions on the lower tiers of the energy landscape remain possible which lead to site energy variations of the protein-embedded pigments. For phytochromes large inter- and intracomplex heterogeneities were observed with respect to the spectral diffusion characteristics (Chapter 4, Section 4.2) while for PSI complexes the different red chlorophyll states show more specific degrees of spectral diffusion (Chapter 5, Section 5.2).

The spectral signatures of the single emitters of phytochrome and the emitters of PSI vary with respect to the spectral information contained in their fluorescence emission spectra. While for the conformational flexible photosensory cofactor of phytochromes vibrational peaks were resolved (Chapter 4, Section 4.3) for the more rigid chlorophyll *a* (Chla) molecule as cofactors of PSI single-emitter profiles composed of a zero-phonon line (ZPL) and a phonon wing (PW) but no vibrational peaks were resolved in the low temperature fluorescence emission spectra. The intensity of a vibrational peak found in fluorescence emission represents the Franck-Condon factor of the vibrational transition associ-

ated with the electronic transition of the chromophore. The Franck-Condon factors associated with the vibrational modes of the phytochrome chromophore are found to be large compared to the Franck-Condon factors connected to the Chla molecules in PSI. This is understandable because the extend of conformational changes occurring after optical excitation of the cofactors in phytochromes largely exceeds structural rearrangements after excitation of the Chla in PSI.

At the low temperature conditions used the one-chromophore binding photoreceptor phytochrome is trapped in its P_r ground state, which subsequently was analyzed by its fluorescence emission. The line widths of the spectral bands of different phytochromes vary between sub nanometer narrow line structures to broad spectral bands covering spectral ranges of tens of nanometers, resembling the line widths typically found for ensembles at ambient temperature conditions. The broad fluorescence emission signals are characterized by two spectral bands with a typical distance of ~ 70 nm, which in the considered wavelength region of $\sim 700 - 770$ nm corresponds to energies of $\sim 1100 - 1700$ cm^{-1}. This energy range is referred to as the fingerprint region of the chromophore, because structural information can be derived from vibrational modes found in that range comprising for example C=C stretching and N–H bending modes [8, 158]. Narrow line features are found over the whole wavelength range of phytochrome fluorescence emission including their occurrence in the vibrational fingerprint region. These spectra are of so far unreached sensitivity as they contain vibrational information of individual chromophores.

The observed vibrational peaks are connected to vibrational modes which are excited in association with the electronic transition of the phytochrome chromophore in its P_r state. In comparison to other vibrational spectroscopic methods like Fourier transform infrared (FT-IR) and Resonance Raman (RR) spectroscopy low temperature single-molecule fluorescence emission spectroscopy has several advantages. It is truly chromophore-sensitive and the fluorescence emission spectrum most probably shows the vibrational modes which are relevant for the first step of photoisomerization as this conformational change in phytochromes is induced by interaction with light. The intensity of the detected vibrational modes represents the coupling strength towards the respective vibrational modes. Further studies on the single-molecule level either on phytochrome mutants or on phytochromes prepared in different states of the photocycle are promising to be helpful for a further understanding of the phytochrome photo-reaction.

By time-dependent fluorescence emission spectroscopy on individual phytochrome molecules it was observed that phytochromes not only are heteroge-

nous with respect to spectra from different individual phytochrome molecules, but the spectral characteristics of single phytochromes vary in time (Chapter 4, Section 4.2). Thus, beside inter-complex heterogeneity single-molecule analysis revealed intra-complex heterogeneity of phytochromes. The dynamic wavelength changes referred to as spectral diffusion are found to mainly cause the broadened spectral lines at T = 1.4 K. The timescale of the observed spectral dynamics spans from a sub-seconds to seconds. Sub-second dynamics were not directly observable and showed up as integral shifts of broadened spectral bands, because the time resolution for single-molecule analysis in the setup used is limited to $\sim$ 0.2 –1 s. For a fraction of phytochrome molecules, however, the spectral dynamics were that slow to be observed as spectral line jumps occurring on the second timescale. The narrow lines detected in the fluorescence emission of phytochromes were found to change their wavelength position synchronically. To obtain resolution enhanced spectra a shifting procedure was applied on the spectra of time-dependent spectra series (Chapter 4, Section 4.3). The developed shifting method was specifically designed with regard to its robustness against noise-affected single-molecule spectra. An PCA-based algorithm turned out to be well suited. The same PCA-based shifting algorithm was in a further step used as a tool for pattern recognition (Chapter 4, Section 4.3). For a subset of phytochrome molecules a similar line pattern in the fluorescence emission was identified. The vibrational peaks resolved for individual chromophores were compared to results from FTIR and RR spectroscopy. A number of modes were assigned due to their appearance at similar energy positions in these spectra. Others appear in energy regions where RR spectra are marked by a large number of closely spaced peaks or where the FTIR difference spectrum is flat. As the selection rules for the transitions probed by the different spectroscopic methods vary a further fluorescence emission technique with vibrational sensitivity was used.

Fluorescence line-narrowing (FLN) spectroscopy was additionally applied for the first time on phytochromes (Chapter 4, Section 4.4). The low temperature site-selective spectroscopic technique as a fluorescence emission technique similarly is purely chromophore sensitive. FLN was used to study phytochromes from various species in their P_r ground state including Agp1 from *Agrobacterium tumefaciens*, RpBphP2 and *Rp*BphP3 from *Rhodopseudomonas palustris* and *Dr*BphP-BV from *Deinococcus radiodurans*. It was found that these phytochromes are differently well suited for FLN analysis. In the case of Agp1 and *Dr*BphP possibly the spectral diffusion characteristics lead to broadening of the spectral lines. A phytochrome variant which contains a less flexible tetrapyrrole pigment shows well resolved line narrowed spectra. The phytochromes *Rp*BphP2 and *Rp*BphP3 from *Rhodopseudomonas palustris* are comparatively well suited

in their natural form. By introduction of a point mutation in the direct vicinity of the chromophore the spectra even get more pronounced fine structure. The point mutant used was *Rp*BphP3-D216A. By solvent isotope exchange from protonated to deuterated buffer bands associated to N-H and N-D vibrational modes were identified. That FLN spectra taken on phytochromes from *Agrobacterium tumefaciens* do not show vibrational line structures corresponds to the findings obtained by low temperature single-molecule spectroscopy. The spectra from individual phytochromes are strongly heterogenous. A superposition of signals from multiple molecules rapidly leads a loss of fine structure. The presented spectroscopic results from both methods reveal that for a heterogenous system like the agrobacterial phytochrome, single-molecule spectroscopy is the method of choice to obtain chromophore-specific vibrational information in fluorescence emission.

Photosystem I (PSI) from different cyanobacteria were spectroscopically characterized by their low temperature fluorescence emission on the single complex level (Chapter 5). PSI from different species have different numbers of fluorescence emitting chlorophyll states, which have overlapping optical properties and hence are difficult to be discerned by standard ensemble spectroscopic methods. For PSI from *Synechococcus* PCC7002 two spectral contributions with different spectral diffusion characteristics were identified by LT-SMS (Chapter 5, Section 5.2). The strongly spectral diffusion affected and therefore broadened spectral contribution was attributed to the C708 state. A further contribution with narrow line width and with spectral diffusion dynamics occurring on a slower time scale was observed on the single-molecule level. At the employed time-resolution of 1s the spectral dynamics for this contribution mainly appear in the form of distinct spectral jumps. The histogram over the wavelength positions of the narrow line in the spectra from all analyzed PSI complexes reveals a single band peaking at 698 nm. This spectral contribution was accordingly called the F698 pool. In analogy to the findings for PSI from different species, where similarly the spectral emitters of PSI were shown to have specific degrees of spectral diffusion, a tentative assignment to the red chlorophyll candidates predominantly discussed in literature is performed. The degree of spectral diffusion is connected to specific binding situations of the pigments.

The multiple emitters with distinct spectral properties as well as the availability of a high resolution structural model make PSI an excellent choice for studies of more general aspects of protein-cofactor interactions. To analyze the source for spectral diffusion solvent water isotope exchange experiments were performed (Chapter 5, Section 5.3). The water isotopes employed as solvent for PSI from *Synechocystis* PCC 6803 were $H_2^{16}O$, D_2O and $H_2^{18}O$. The degree of spectral diffusion for all red chlorophylls states of PSI from *Synechocystis* PCC6803 is de-

creased in D_2O-buffer solution compared to PSI prepared in $H_2^{16}O$ and $H_2^{18}O$. Even though $H_2^{18}O$ and D_2O have the same molecular mass their effect on the spectral diffusion of the red chlorophylls of PSI is different. The comparative experiments indicate that water molecules as molecular entities of increased molecular mass do not cause the strong spectral diffusion reducing effect in the case of D_2O sample preparations but instead proton dynamics influence spectral diffusion in pigment-protein complexes. Exchangeable protons in the first coordination sphere have to be considered when aiming at an assignment of the spectral contributions to specific pigments of the molecular complex. The previous estimation of the chromophore flexibilities, hence, was reevaluated here to account for these recent results (Chapter 5, Section 5.2).

On the basis of well resolved single-emitter profiles as observed in the spectra of individual PSI from *Synechocystis* PCC6803 prepared in D_2O-buffer the Huang-Rhys factors for the red Chla states of PSI were determined (Chapter 5, Section 5.4). Further increased signal-to-noise ratios were achieved by a shifting procedure applied on time-dependent spectra series of individual PSI. Huang-Rhys factors were determined over the entire spectral range of PSI fluorescence emission. Thereby, a unique sensitivity in the long wavelength range was obtained. Unexpectedly a state with minor electron-phonon coupling was found on the long wavelength side of the fluorescence emission of PSI. This finding on the fluorescence emitters of PSI shows that the supposed direct correlation between the electronic energy of a given pigment and electron-phonon coupling [21] does not hold.

By low temperature single-molecule spectroscopy an additional spectral contribution was observed for PSI from *Synechocystis* PCC6803, which has not been reported before (Chapter 5, Section 5.5). This contribution is strongly red-shifted compared to the known red Chla contributions of PSI from *Synechocystis* PCC6803. The far-red contribution is of minor occurrence in the spectra of individual PSI complexes. Its integral intensity compared to the other fluorescent contributions of PSI is low and the associated Huang-Rhys factors indicate low electron-phonon couplings. These spectral characteristics make $P700^+$ a putative source for this spectral contribution in the fluorescence emission of individual PSI complexes.

By application of time-dependent low temperature single-molecule spectroscopy on the multiple-pigments binding PSI complex details on the excitation energy transfer were obtained. In conjunction with a 2D correlation analysis for PSI from three different cyanobacteria including PSI from *T. elongatus*, PSI from *Synechocystis* PCC6803 and from PSI *Synechococcus* PCC7002 anti-correlative behavior of the fluorescence emission of the spectrally contributing

states was determined (Chapter 5, Section 5.6). The observed anticorrelation indicates that protein-induced dynamics modify the optical properties of higher lying antenna states on the second time scale at T = 1.4 K. It can be inferred that at ambient conditions, where conformational dynamics occur with strongly increased rates, the flexibility of excitation energy pathways can be highly increased. Supposedly, this excitation-energy transfer flexibility is one of the protection mechanism developed by nature to secure against photo-damage. It would be of highest interest to observe the multiple pathways at physiological conditions. Ultrafast spectroscopy on the single-molecule level would probably be required to observe this experimentally.

To analyze plasmonic interaction effects on multi-chromophore FRET-coupled systems the fluorescence emission of individual PSI complexes coupled to gold nanoparticles and silverisland films was analyzed (Chapter 6, Section 6.2). Exposed to these nanostructures an altered fluorescence response of the chromophores is observed. The findings indicate affected protein function of PSI near plasmonic nanostructures. An interaction model to understand these plasmonic effects is generally applicable to multi-FRET coupled systems. The analysis of samples with defined geometries between multi-FRET coupled systems and plasmonic nanostructures have a great potential to obtain further detailed insights into the plasmonic interaction effects.

BIBLIOGRAPHY

[1] H.Frauenfelder, F. Parak, and R.D.Young: *Conformational substates in proteins*. Ann. Rev. Biophys. Biophys. Chem. **17**, 451–479 (1988).

[2] W. E. Moerner and L. Kador: *Optical detection and spectroscopy of single molecules in a solid*. Phys. Rev. Lett. **62**, 2535–2538 (1989).

[3] M. Orrit and J. Bernard: *Single Pentacene Molecules Detected by Fluorescence Excitation in A Para-Terphenyl Crystal*. Phys. Rev. Lett. **65**, 2716–2719 (1990).

[4] F. Andel, J. C. Lagarias, and R. A. Mathies: *Resonance Raman Analysis of Chromophore Structure in the Lumi-R Photoproduct of Phytochrome*. Biochemistry **35**, 15997–16008 (1996).

[5] V. A. Sineshchekov: *Photobiophysics and Photobiochemistry of the Heterogeneous Phytochrome System*. Biochimica et Biophysica Acta-Bioenergetics **1228**, 125–164 (1995).

[6] K. Heyne, J. Herbst, D. Stehlik, B. Esteban, T. Lamparter, J. Hughes, and R. Diller: *Ultrafast dynamics of phytochrome from the cyanobacterium Synechocystis, reconstituted with phycocyanobilin and phycoerythrobilin*. Biophys. J. **82**, 1004–1016 (2002).

[7] V. Sineshchekov, L. Koppel, B. Esteban, J. Hughes, and T. Lamparter: *Fluorescence investigation of the recombinant cyanobacterial phytochrome (Cph1) and its C-terminally truncated monomeric species (Cph1 Delta 2): implication for holoprotein assembly, chromophore-apoprotein interaction and photochemistry*. J. Photochem. Photobiol. B-Biol. **67**, 39–50 (2002).

[8] D. von Stetten, M. Günther, P. Scheerer, D. H. Murgida, M. A. Mroginski, N. Krauss, T. Lamparter, J. Zhang, D. N. Anstrom, R. V. Vierstra, K. T. Forest, and P. Hildebrandt: *Chromophore Heterogeneity and Photoconversion in Phytochrome Crystals and Solution Studied by Resonance Raman Spectroscopy*. Angew. Chem. Int. Ed. **47**, 4753-4755 (2008).

[9] J. J. van Thor, M. Mackeen, I. Kuprov, A. Raymond, and M. R. Wormaldy: *Chromophore Structure in the Photocycle of the Cyanobacterial Phytochrome Cph1*. Biophys. J. **91**, (2006).

[10] X. Yang, J. Kuk, and K. Moffat: *Crystal structure of Pseudomonas aeruginosa bacteriophytochrome: Photoconversion and signal transduction*. Proc. Natl. Acad. Sci. USA **105**, 14715–14720 (2008).

[11] P. Fromme, P. Jordan, and N. Krauss: *Structure of photosystem I*. Biochim. Biophys. Acta, Bioenerg. **1507**, 5–31 (2001).

[12] Accelrys Software Inc.: *Discovery Studio Visualizer*. Release 2.5, San Diego (2007).

[13] F. Jelezko, C. Tietz, U. Gerken, J. Wrachtrup, and R. Bittl: *Single-molecule spectroscopy on photosystem I pigment-protein complexes*. J. Phys. Chem. B **104**, 8093–8096 (2000).

[14] M. Brecht, H. Studier, A. F. Elli, F. Jelezko, and R. Bittl: *Assignment of red antenna states in photosystem I from* Thermosynechoccocus elongatus *by single-molecule spectroscopy*. Biochemistry **46**, 799–806 (2007).

[15] A. F. Elli, F. Jelezko, C. Tietz, H. Studier, M. Brecht, R. Bittl, and J. Wrachtrup: *Red pool chlorophylls of photosystem I of the cyanobacterium Thermosynechococcus elongatus: A single-molecule study*. Biochemistry **45**, 1454–1458 (2006).

[16] M. Kasha: *Characterization of Electronic Transitions in Complex Molecules*. Discuss. Faraday Soc., 14–19 (1950).

[17] P. W. Atkins: *Physical Chemistry*. Oxford University Press (1978).

[18] R. Jankowiak, J. M. Hayes, and G. J. Small: *Spectral Hole-Burning Spectroscopy in Amorphous Molecular-Solids and Proteins*. Chem. Rev. **93**, 1471–1502 (1993).

[19] L. A. Rebane, A. A. Gorokhovskii, and J. V. Kikas: *Low-temperature spectroscopy of organic molecules in solids by photochemical hole burning*. Appl. Phys. B **29**, 235-250 (1982).

[20] T. Pullerits, R. Monshouwer, F. van Mourik, and R. van Grondelle: *Temperature-Dependence of Electron-Vibronic Spectra of Photosynthetic Systems - Computer-Simulations and Comparison with Experiment*. Chem. Phys. **194**, 395–407 (1995).

[21] M. Rätsep, M. Pajusalu, and A. Freiberg: *Wavelength-dependent electron-phonon coupling in impurity glasses*. Chem. Phys. Lett. **479**, 140–143 (2009).

[22] F. Neese: *Prediction of molecular properties and molecular spectroscopy with density functional theory: From fundamental theory to exchange-coupling*. Coord. Chem. Rev. **253**, 526–563 (2009).

[23] M. A. Mroginski, D. von Stetten, F. V. Escobar, and S. Kaminski H. M. Strauss, P. Scheerer, M. Gunther, D. H. Murgida, P. Schmieder, C. Bongards, W. Gärtner, J. Mailliet, J. Hughes, L. O. Essen, and P. Hildebrandt: *Chromophore Structure of Cyanobacterial Phytochrome Cph1 in the Pr State: Reconciling Structural and Spectroscopic Data by QM/MM Calculations*. Biophys. J. **96**, 4153–4163 (2009).

[24] T. Förster: *Energiewanderung und Fluoreszenz*. Naturwissenschaften **33**, 166–175 (1946).

[25] D. L. Dexter: *A Theory Of Sensitized Luminescence In Solids*. J. Chem. Phys. **21**, 836–850 (1953).

[26] T. Förster: *Zwischenmolekulare Energiewanderung Und Fluoreszenz*. Annalen Der Physik **2**, 55–75 (1948).

[27] W. Parson and V. Nagarajan: *Light-Harvesting Antennas in Photosynthesis*. Vol. 13, Kluwer Academic Publishers Dodrecht/Boston/London (2003).

[28] R. van Grondelle: *Excitation-Energy Transfer, Trapping and Annihilation in Photosynthetic Systems*. Biochimica et Biophysica Acta **811**, 147–195 (1985).

[29] K. L. Kelly, E. Coronado, L. L. Zhao, and G. C. Schatz: *The optical properties of metal nanoparticles: The influence of size, shape, and dielectric environment*. J. Phys. Chem. B **107**, 668–677 (2003).

[30] M. H. Chowdhury, K. Ray, K. Aslan, J. R. Lakowicz, and C. D. Geddes: *Metal-Enhanced Fluorescence of Phycobiliproteins from Heterogeneous Plasmonic Nanostructures*. J. Phys. Chem. C **111**, 18856–18863 (2007).

[31] B. K. Juluri, J. Huang, and L. Jensen, Extinction, Scattering and Absorption efficiencies of single and multilayer nanoparticles, Doi:10254/nanohub-r8228.2.

[32] K. H. Drexhage: *Influence of a Dielectric Interface on Fluorescence Decay Time*. J. Lumin. **1**, 693 – 701 (1970).

[33] C. D. Geddes and J. R. Lakowicz: *Metal-enhanced fluorescence*. J. Fluoresc. **12**, 121–129 (2002).

[34] K. Aslan, Z. Leonenko, J. R. Lakowicz, and C. D. Geddes: *Annealed silver-island films for applications in metal-enhanced fluorescence: Interpretation in terms of radiating plasmons*. J. Fluoresc. **15**, 643–654 (2005).

[35] K. Aslan, I. Gryczynski, J. Malicka, E. Matveeva, J. R. Lakowicz, and C. D. Geddes: *Metal-enhanced fluorescence an emerging tool in biotechnology*. Curr. Opin. Biotechnol. **16**, 55–62 (2005).

[36] S. Mackowski: *Hybrid nanostructures for efficient light harvesting*. J. Phys.: Condens. Matter **22**, (2010).

[37] P. Anger, P. Bharadwaj, and L. Novotny: *Enhancement and Quenching of Single-Molecule Fluorescence*. Phys. Rev. Lett. **96**, 113002 (2006).

[38] S. M. Nie and S. R. Emery: *Probing single molecules and single nanoparticles by surface-enhanced Raman scattering*. Science **275**, 1102–1106 (1997).

[39] E. Le Ru and P. Etchegoin: *Principles of surface-enhanced Raman spectroscopy and related plasmonic effects*. Elsevier, Amsterdam (2009).

[40] B. Pettinger: *Single-molecule surface- and tip-enhanced raman spectroscopy*. Mol. Phys. **108**, 2039–2059 (2010).

[41] N. C. Rockwell, Y.-S. Su, and J. C. Lagarias: *Phytochrome Structure and Signaling Mechanisms*. Annu. Rev. Plant Biol. **57**, 837–858 (2006).

[42] J. Eccles and B. Honig: *Charged amino-acids as spectroscopic determinants for chlorophyll in vivo*. Proc. Natl. Acad. Sci. U. S. A.-Biol. Sci. **80**, 4959–4962 (1983).

[43] J. Baier, M. F. Richter, R. J. Cogdell, S. Oellerich, and J. R. Köhler: *Determination of the spectral diffusion kernel of a protein by single-molecule spectroscopy*. Phys. Rev. Lett. **1**, 018108 (2008).

[44] Y. Berlin, A. Burin, J. Friedrich, and J. Kohler: *Low temperature spectroscopy of proteins. Part II: Experiments with single protein complexes*. Physics of Life Reviews **4**, 64–89 (2007).

[45] M. Brecht, V. Radics, J. B. Nieder, and R. Bittl: *Protein dynamics-induced variation of excitation energy transfer pathways*. Proc. Natl. Acad. Sci. U. S. A. **106**, 11857–11861 (2009).

[46] H. Janovjak, K. T. Sapra, A. Kedrov, and D. J. Muller: *From valleys to ridges: Exploring the dynamic energy landscape of single membrane proteins*. Chemphyschem **9**, 954–966 (2008).

[47] M. Ketelaars, J. M. Segura, S. Oellerich, W. P. F. de Ruijter, G. Magis, T. J. Aartsma, M. Matsushita, J. Schmidt, R. J. Cogdell, and J. Kohler: *Probing the electronic structure and conformational flexibility of individual light-harvesting 3 complexes by optical single-molecule spectroscopy*. J. Phys. Chem. B **110**, 18710–18717 (2006).

[48] C. Tietz, F. Jelezko, U. Gerken, S. Schuler, A. Schubert, H. Rogl, and J. Wrachtrup: *Single molecule spectroscopy on the light-harvesting complex II of higher plants*. Biophys. J. **81**, 556–562 (2001).

[49] S. Wörmke, S. Mackowski, T. H. P. Brotosudarmo, C. Jung, A. Zumbusch, M. Ehrl, H. Scheer, E. HofMann, R. G. Hiller, and C. Bräuchle: *Monitoring fluorescence of individual chromophores in peridininchlorophyll-protein complex using single molecule spectroscopy*. Biochim. Biophys. Acta, Bioenerg. **1767**, 956–964 (2007).

[50] H. Frauenfelder, S. G. Sliar, and P. G. Wolynes: *The Energy Landscapes and Motions of Proteins*. Science **254**, 1598–1603 (1991).

[51] H. Frauenfelder, P. W. Fenimore, and R. D. Young: *Protein dynamics and function: Insights from the energy landscape and solvent slaving*. IUBMB Life **59**, 506–512 (2007).

[52] D. T. Leeson, D. A. Wiersma, K. Fritsch, and J. Friedrich: *The energy landscape of myoglobin: An optical study*. J. Phys. Chem. B **101**, 6331–6340 (1997).

[53] C. Hofmann, T. J. Aartsma, H. Michel, and J. Köhler: *Direct observation of tiers in the energy landscape of a chromoprotein: A single-molecule study*. Proceedings of the National Academy of Sciences of the United States of America **100**, 15534–15538 (2003).

[54] K. A. Dill, S. B. Ozkan, M. S. Shell, and T. R. Weikl: *The protein folding problem*. Annu. Rev. Biophys. **37**, 289–316 (2008).

[55] H. Frauenfelder, G. Chen, J. Berendzen, P. W. Fenimore, H. Jansson, B. H. McMahon, I. R. Stroe, J. Swenson, and R. D. Young: *A unified model of protein dynamics*. Proc. Natl. Acad. Sci. USA **106**, 5129–5134 (2009).

[56] A. Ansari, J. Berendzen, S. F. Bowne, H. Frauenfelder, I. E. T. Iben, T. B. Sauke, E. Shyamsunder, and R. D. Young: *Protein States And Protein Quakes*. Proc. Natl. Acad. Sci. U. S. A. **82**, 5000–5004 (1985).

[57] G. U. Nienhaus: *Physik der Proteine*. Physik Journal **3**, 37–43 (2004).

[58] P. V. Burra, Y. Zhang, A. Godzik, and B. Stec: *Global distribution of conformational states derived from redundant models in the PDB points to non-uniqueness of the protein structure*. Proc. Natl. Acad. Sci. USA **106**, 10505–10510 (2009).

[59] H. Lesch, J. Schlichter, J. Friedrich, and J. M. Vanderkooi: *Molecular Probes What Is the Range of Their Interaction with the Environment?*. Biophys. J. **86**, 467–472 (2004).

[60] Y. G. Vainer, A. V. Naumov, and L. Kador: *Local vibrations in disordered solids studied via single-molecule spectroscopy: Comparison with neutron, nuclear, Raman scattering, and photon echo data*. Phys. Rev. B **77**, 224202 (2008).

[61] D. Grozdanov, N. Herascu, T. Reinot, R. Jankowiak, and V. Zazubovich: *Low-Temperature Protein Dynamics of the B800 Molecules in the LH2 Light-Harvesting Complex: Spectral Hole Burning Study and Comparison with Single Photosynthetic Complex Spectroscopy*. J. Phys. Chem. B **114**, 3426-3438 (2010).

[62] R. Hildner, L. Winterling, U. Lemmer, U. Scherf, and J Köhler: *Single-Molecule Spectroscopy on a Ladder-Type Conjugated Polymer: Electron-Phonon Coupling and Spectral Diffusion*. Chem. Phys. Chem. **10**, 2524–2534 (2009).

[63] J. Pieper, J. Voigt, G. Renger, and G. J. Small: *Analysis of phonon structure in line-narrowed optical spectra*. Chem. Phys. Lett. **310**, 296–302 (1999).

[64] M. Brecht, H. Studier, V. Radics, J. B. Nieder, and R. Bittl: *Spectral Diffusion Induced by Proton Dynamics in Pigment–Protein Complexes*. J. Am. Chem. Soc. **130 (51)**, 17487 – 17493 (2008).

[65] R. I. Personov, E. I. Al'shits, and L. A. Bykovskaya: *The Effect Of Fine Structure Appearance In Laser-Excited Fluorescence Spectra Of Organic Compounds In Solid Solutions*. Optics Communications **6**, 169 – 173 (1972).

[66] A. A. Gorokhovskii, R. K. Kaarli, and L. A. Rebane: *Hole burning in contour of a pure electronic line in a shpolskii system*. JETP Lett. **20**, 216–218 (1974).

[67] B. M. Kharlamov, R. I. Personov, and L. A. Bykovskaya: *Stable 'gap' in absorption spectra of solid solutions of organic molecules by laser irradiation*. Optics Communications **12**, 191 - 193 (1974).

[68] J. M. Hayes and G. J. Small: *Non-Photochemical Hole Burning and Impurity Site Relaxation Processes in Organic Glasses*. Chemical Physics **27**, 151–157 (1978).

[69] J. Friedrich: *Hole-Burning Spectroscopy And Physics of Proteins*. Methods Enzymol. **246**, 226–259 (1995).

[70] R. Purchase, S. Bonsma, S. Jezowski, J. Gallus, F. Konz, and S. Völker: *The power of line-narrowing techniques: Applications to photosynthetic chromoprotein complexes and autofluorescent proteins*. Opt. Spectrosc. **98**, 699–711 (2005).

[71] M. Rätsep and A. Freiberg: *Electron-phonon and vibronic couplings in the FMO bacteriochlorophyll a antenna complex studied by difference fluorescence line narrowing*. J. Lumin. **127**, 251–259 (2007).

[72] M. T. A. Alexandre, R. van Grondelle, K. J. Hellingwerf, B. Robert, and J. T. M. Kennis: *Perturbation of the ground-state electronic structure of FMN by the conserved cysteine in phototropin LOV2 domains*. Phys. Chem. Chem. Phys. **10**, 6693–6702 (2008).

[73] J. Schlichter and J. Friedrich: *Glasses and proteins Similarities and differences in their spectral diffusion dynamics*. J. Chem. Phys. **114**, 8718-8721 (2001).

[74] J. M. Hayes, P. A. Lyle, and G. J. Small: *A Theory For The Temperature-Dependence Of Hole-Burned Spectra*. J. Phys. Chem. **98**, 7337–7341 (1994).

[75] M. Orrit, J. Bernard, and R. I. Personov: *High-resolution spectroscopy of organic molecules in solids: from fluorescence line narrowing and hole burning to single molecule spectroscopy*. J. Phys. Chem. **97**, 10256-10268 (1993).

[76] A. Kiraz, M. Ehrl, C. Hellriegel, C. Bräuchle, and A. Zumbusch: *Vibronic excitation of single molecules: A new technique for studing low-temperature dynamics*. Chem. Phys. Chem. **6**, 919–925 (2005).

[77] A. Drechsler, M. A. Lieb, C. Debus, A. J. Meixner, and G. Tarrach: *Confocal microscopy with a high numerical aperture parabolic mirror*. Optics Express **9**, 637–644 (2001).

[78] W. P. Ambrose and W. E. Moerner: *Fluorescence Spectroscopy and Spectral Diffusion of Single Impurity Molecules in a Crystal*. Nature **349**, 225–227 (1991).

[79] S. M. Nie, D. T. Chiu, and R. N. Zare: *Probing Individual Molecules with Confocal Fluorescence Microscopy*. Science **266**, 1018–1021 (1994).

[80] H. Heinzelmann and D. W. Pohl: *Scanning near-field optical microscopy*. Appl. Phys. A-Mater. **59**, 89–101 (1994).

[81] G. Donnert, J. Keller, R. Medda, M. A. Andrei, S. O. Rizzoli, R. Lurmann, R. Jahn, C. Eggeling, and S. W. Hell: *Macromolecular-scale resolution in biological fluorescence microscopy*. Proc. Natl. Acad. Sci. USA **103**, 11440–11445 (2006).

[82] J. Michaelis, C. Hettich, J. Mlynek, and V. Sandoghdar: *Optical microscopy using a single-molecule light source*. Nature **405**, 325–328 (2000).

[83] R. M. Stockle, Y. D. Suh, V. Deckert, and R. Zenobi: *Nanoscale Chemical Analysis by Tip-Enhanced Raman Spectroscopy*. Chem. Phys. Lett. **318**, 131–136 (2000).

[84] D. Brinks, F. D. Stefani, F. Kulzer, R. Hildner, T. H. Taminiau, Y. Avlasevich, K. Mullen, and N. F. Van Hulst: *Visualizing and controlling vibrational wave packets of single molecules*. Nature **465**, 905–U5 (2010).

[85] P. Kukura, M. Celebrano, A. Renn, and V. Sandoghdar: *Single-Molecule Sensitivity in Optical Absorption at Room Temperature*. J. Phys. Chem. Lett. **1**, 3323–3327 (2010).

[86] A. Gaiduk, M. Yorulmaz, P. V. Ruijgrok, and M. Orrit: *Room-Temperature Detection of a Single Molecule's Absorption by Photothermal Contrast*. Science **330**, 353–356 (2010).

[87] S. S. Chong, W. Min, and X. S. Xie: *Ground-State Depletion Microscopy: Detection Sensitivity of Single-Molecule Optical Absorption at Room Temperature*. J. Phys. Chem. Lett. **1**, 3316–3322 (2010).

[88] R. H. Webb: *Confocal optical microscopy*. Rep. Prog. Phys **59**, 427-471 (1996).

[89] W. E. Moerner and D. P. Fromm: *Methods of single-molecule fluorescence spectroscopy and microscopy*. Rev. Sci. Instrum. **74**, 3597–3619 (2003).

[90] Hauke Studier: *Einzelmolekül-Spektroskopie am Photosystem I*. Ph. D. thesis, Freie Universität Berlin, (2007).

[91] T. Lamparter, N. Michael, F. Mittmann, and B. Esteban: *Phytochrome from Agrobacterium tumefaciens has unusual spectral properties and reveals an N-terminal chromophore attachment site*. Proc. Natl. Acad. Sci. USA **99**, 11628–11633 (2002).

[92] K. Inomata, M. A. S. Hammam, H. Kinoshita, Y. Murata, H. Khawn, S. Noack, N. Michael, and T. Lamparter: *Sterically Locked Synthetic Bilin Derivatives and Phytochrome Agp1 from Agrobacterium tumefaciens Form Photoinsensitive Pr- and Pfr-like Adducts*. J. Biol. Chem. **280**, 24491–24497 (2005).

[93] E. Giraud, S. Zappa, L. V., J-M. Adriano, L. Hannibal, J. Fardoux, C Berthomieu, P Bouyer, D. Pignol, and A. Verméglio: *A New Type of Bacteriophytochrome Acts in Tandem with a Classical Bacteriophytochrome to Control the Antennae Synthesis in Rhodopseudomonas palustris*. J. Biol. Chem. **280**, (2005).

[94] X. Yang, E. Stojkovic, J. Kuk, and K. Moffat: *Crystal structure of the chromophore binding domain of an unusual bacteriophytochrome, RpBphP3, reveals residues that modulate photoconversion*. Proc. Natl. Acad. Sci. USA **104**, 12571-12576 (2007).

[95] J. R. Wagner, J. S. Brunzelle, K. T. Forest, and R. D. Vierstra: *A light-sensing knot revealed by the structure of the chromophore-binding domain of phytochrome*. Nature **438**, 325–331 (2005).

[96] P. Fromme and H. T. Witt: *Improved isolation and crystallization of Photosystem I for structural analysis*. Biochim. Biophys. Acta, Bioenerg. **1365**, 175–184 (1998).

[97] J. A. Bautista, F. Rappaport, M. Guergova-Kuras, R. O. Cohen, J. H. Golbeck, J. Y. Wang, D. Beal, and B. A. Diner: *Biochemical and biophysical characterization of photosystem I from phytoene desaturase and ξ-carotene desaturase deletion mutants of Synechocystis sp PCC 6803*. J. Biol. Chem. **280**, 20030–20041 (2005).

[98] G. Z. Shen, J. D. Zhao, S. K. Reimer, M. L. Antonkine, Q. Cai, S. M. Weiland, J. H. Golbeck, and D. A. Bryant: *Assembly of photosystem II. Inactivation of the rubA gene encoding a membrane-associated rubredoxin in the cyanobacterium Synechococcus sp PCC 7002 causes a loss of photosystem I activity*. J. Biol. Chem. **277**, 20343–20354 (2002).

[99] H. Otto, T. Lamparter, B. Borucki, J. Hughes, and M. P. Heyn: *Dimerization and Inter-Chromophore Distance of Cph1 Phytochrome from Synechocystis, as Monitored by Fluorescence Homo and Hetero Energy Transfer*. Biochemistry **42**, 5885-5895 (2003).

[100] F. Müh and A. Zouni: *Extinction coefficients and critical solubilisation concentrations of photosystems I and II from Thermosynechococcus elongatus*. Biochim. Biophys. Acta, Bioenerg. **1708**, 219–228 (2005).

[101] K. Ray, R. Badugu, and J. R. Lakowicz: *Polyelectrolyte layer-by-layer assembly to control the distance between fluorophores and plasmonic nanostructures*. Chem. Mater. **19**, 5902–5909 (2007).

[102] W. L. Butler, K. H. Norris, H. W. Siegelman, and S. B. Hendricks: *Detection, assay, and preliminary purification of the pigment controlling photoresponsive development of plants*. Proc. Natl. Acad. Sci. U. S. A. **45**, 1703–1708 (1959).

[103] J. Hughes, T. Lamparter, F. Mittmann, E. Hartmann, W. Gärtner, A. Wilde, and T. Börner: *A prokaryotic phytochrome*. Nature **386**, 663–663 (1997).

[104] S. J. Davis, A. V. Vener, and R. D. Vierstra: *Bacteriophytochromes: Phytochrome-like photoreceptors from nonphotosynthetic eubacteria*. Science **286**, 2517–2520 (1999).

[105] E. Giraud, L. Fardoux, N. Fourrier, L. Hannibal, B. Genty, P. Bouyer, B. Dreyfus, and A. Vermeglio: *Bacteriophytochrome controls photosystem synthesis in anoxygenic bacteria*. Nature **417**, 202–205 (2002).

[106] K. A. Franklin and P. H. Quail: *Phytochrome functions in Arabidopsis development*. J. Exp. Bot. **61**, 11–24 (2010).

[107] J. R. Wagner, J. R. Zhang, J. S. Brunzelle, R. D. Vierstra, and K. T. Forest: *High resolution structure of Deinococcus bacteriophytochrome yields new insights into phytochrome architecture and evolution*. J. Biol. Chem. **282**, 12298-12309 (2007).

[108] G. P. Moss: *Nomenclature Of Tetrapyrroles*. Pure & Appl. Chem. **59**, 779–832 (1987).

[109] E. Giraud and A. Verméglio: *Bacteriophytochromes in anoxygenic photosynthetic bacteria*. Photosynth. Res. **97**, 141–153 (2008).

[110] R. Tasler, T. Moises, and N. Frankenberg-Dinkel: *Biochemical and spectroscopic characterization of the bacterial phytochrome of Pseudomonas aeruginosa*. FEBS J. **272**, 1927–1936 (2005).

[111] X. J. Yang, J. Kuk, and K. Moffat: *Conformational differences between the Pfr and Pr states in Pseudomonas aeruginosa bacteriophytochrome*. Proc. Natl. Acad. Sci. USA **106**, 15639–15644 (2009).

[112] S. Noack, N. Michael, R. Rosen, and T. Lamparter: *Protein Conformational Changes of Agrobacterium Phytochrome Agp1 during Chromophore Assembly and Photoconversion*. Biochemistry **46**, 4164-4176 (2007).

[113] F. Nagy and E. Schäfer: *Phytochromes control photomorphogenesis by differentially regulated, interacting signaling pathways in higher plants*. Annu. Rev. Plant Biol. **53**, 329–355 (2002).

[114] G. Böse, P. Schwille, and T. Lamparter: *The mobility of phytochrome within protonemal tip cells of the moss Ceratodon purpureus, monitored by fluorescence correlation spectroscopy*. Biophys. J. **87**, 2013–2021 (2004).

[115] G. Bae and G. Choi: *Decoding of light signals by plant phytochromes and their interacting proteins*. ANNUAL REVIEW OF PLANT BIOLOGY **59**, 281–311 (2008).

[116] P. H. Quail: *Phytochromes*. Curr. Biol. **20**, R504–R507 (2010).

[117] P. Eilfeld and W. Rüdiger: *Absorption-spectra of phytochrome intermediates*. Zeitschrift für Naturforschung C-A J. OF BIOSCIENCES **40**, 109–114 (1985).

[118] C. Bongards and W. Gärtner: *The Role of the Chromophore in the Biological Photoreceptor Phytochrome: An Approach Using Chemically Synthesized Tetrapyrroles*. Acc. Chem. Res. **43**, 485–495 (2010).

[119] F. Andel, K.C. Hasson, and F. Gai: *Femtosecond time-resolved spectroscopy of the primary photochemistry of phytochrome*. Biospec. **3**, 421–433 (1997).

[120] W. Rüdiger, F. Thümmler, E. Cmiel, and S. Schneider: *Chromophore structure of the physiologically active form (Pfr) of phytochrome*. Proc. Natl. Acad. Sci. USA **80**, 6244-6248 (1983).

[121] B. Borucki, D. von Stetten, S. Seibeck, T. Lamparter, N. Michael, M. A. Mroginski, H. Otto, D. H. Murgida, M. P. Heyn, and P. Hildebrandt: *Light-induced Proton Release of Phytochrome Is Coupled to the Transient Deprotonation of the Tetrapyrrole Chromophore*. J. Biol. Chem. **280**, 34358–34364 (2005).

[122] K. C. Toh, E. A. Stojkovic, I. H. M. van Stokkum, K. Moffat, and J. T. M. Kennis: *Proton-transfer and hydrogen-bond interactions determine fluorescence quantum yield*

and photochemical efficiency of bacteriophytochrome. Proc. Natl. Acad. Sci. USA **107**, 9170–9175 (2010).

[123] A. T. Ulijasz, G. Cornilescu, C. C. Cornilescu, J. R. Zhang, M. Rivera, J. L. Markley, and R. D. Vierstra: *Structural basis for the photoconversion of a phytochrome to the activated Pfr form*. Nature **463**, 250–U143 (2010).

[124] T. Rohmer, C. Lang, J. Hughes, L.-O. Essen, W. Gärtner, and J. Matysik: *Light-induced chromophore activity and signal transduction in phytochromes observed by 13C and 15N magic-angle spinning NMR*. Proc. Natl. Acad. Sci. U. S. A. **105**, 15229–15234 (2008).

[125] A. J. Fischer and J. C. Lagarias: *Harnessing phytochrome's glowing potential*. Proceedings of the National Academy of Sciences of the United States of America **101**, 17334–17339 (2004).

[126] J. T. Murphy and J. C. Lagarias: *The phytofluors: a new class of fluorescent protein probes*. Current Biology **7**, 870–876 (1997).

[127] X. K. Shu, A. Royant, M. Z. Lin, T. A. Aguilera, V. Lev-Ram, P. A. Steinbach, and R. Y. Tsien: *Mammalian Expression of Infrared Fluorescent Proteins Engineered from a Bacterial Phytochrome*. Science **324**, 804–807 (2009).

[128] L. Shang, N. C. Rockwell, S. S. Martin, and J. C. Lagarias: *Biliverdin Amides Reveal Roles for Propionate Side Chains in Bilin Reductase Recognition and in Holophytochrome Assembly and Photoconversion*. Biochemistry **49**, 6070-6082 (2010).

[129] A. E. Miller, A. J. Fischer, T. Laurence, C. W. Hollars, R. J. Saykally, J. C. Lagarias, and T. Huser: *Single-molecule dynamics of phytochrome-bound fluorophores probed by fluorescence correlation spectroscopy*. Proc. Natl. Acad. Sci. U. S. A. **103**, 11136–11141 (2006).

[130] K. Inomata, S. Noack, M. A. S. Hammam, H. Khawn, H. Kinoshita, Y. Murata, N. Michael, P. Scheerer, N. Krauss, and T. Lamparter: *Assembly of synthetic locked chromophores with Agrobacterium phytochromes AGP1 and AGP2*. J. Biol. Chem. **281**, 28162–28173 (2006).

[131] A. Levskaya, O. D. Weiner, W. A. Lim, and C. A. Voigt: *Spatiotemporal control of cell signalling using a light-switchable protein interaction*. Nature **461**, 997–1001 (2009).

[132] T. Lamparter, N. Michael, O. Caspani, T. Miyata, K. Shirai, and K. Inomata: *Biliverdin Binds Covalently to Agrobacterium Phytochrome Agp1 via Its Ring A Vinyl Side Chain*. J. Biol. Chem. **278**, 33786–33792 (2003).

[133] W. Rüdiger and F. Thümmler: *Phytochrome, the Visual Pigment of Plants*. Angew. Chem. Int. Ed. **30**, 1216-1228 (1991).

[134] T. Lamparter: *Evolution of cyanobacterial and plant phytochromes*. FEBS Lett. **573**, 1–5 (2004).

[135] K. Evans, J. G. Grossmann, A. P. Fordham-Skelton, and M. Z. Papiz: *Small-angle X-ray scattering reveals the solution structure of a bacteriophytochrome in the catalytically active Pr state*. J. Mol. Biol. **364**, 655–666 (2006).

[136] H. Li, J. R. Zhang, R. D. Vierstra, and H. L. Li: *Quaternary organization of a phytochrome dimer as revealed by cryoelectron microscopy*. Proc. Natl. Acad. Sci. USA **107**, 10872–10877 (2010).

[137] L. O. Essen, J. Mailliet, and J. Hughes: *The structure of a complete phytochrome sensory module in the Pr ground state*. Proc. Natl. Acad. Sci. USA **105**, 14709–14714 (2008).

[138] P. Scheerer, N. Michael, J. H. Park, S. Nagano, H. W. Choe, K. Inomata, B. Borucki, N. Krauss, and T. Lamparter: *Light-Induced Conformational Changes of the Chromophore and the Protein in Phytochromes: Bacterial Phytochromes as Model Systems*. Chem. Phys. Chem. **11**, 1090–1105 (2010).

[139] T. Bornschlögl, D.M. Anstrom, E. Mey, J. Dzubiella, M. Rief, and K. T. Forest: *Tightening the Knot in Phytochrome by Single-Molecule Atomic Force Microscopy*. Biophys. J. **96**, 1508–1514 (2009).

[140] A. D. McNaught and A. Wilkinson: *Compendium of Chemical Terminology, 2nd ed.*. IUPAC (1997).

[141] A. Möglich, X. J. Yang, R. A. Ayers, and K. Moffat: *Structure and Function of Plant Photoreceptors*. Annu. Rev. Plant Biol. **61**, 21–47 (2010).

[142] M. Bischoff, G. Hermann, S. Rentsch, and D. Strehlow: *First Steps in the Phytochrome Phototransformation: A Comparative Femtosecond Study on the Forward (Pr →Pfr) and Back Reaction (Pfr →Pr)*. Biochemistry **40**, 181-186 (2001).

[143] Jasper J. van Thor, Nicholas Fisher, and Peter R. Rich: *Assignments of the Pfr - Pr FTIR Difference Spectrum of Cyanobacterial Phytochrome Cph1 Using N15 and C13 Isotopically Labeled Phycocyanobilin Chromophore*. J. Phys. Chem. **109**, 20597–20604 (2005).

[144] D. H. Murgida, D. von Stetten, P. Hildebrandt, P. Schwinte, F. Siebert, S. Sharda, W. Gartner, and M. A. Mroginski: *The chromophore structures of the Pr states in plant and bacterial phytochromes*. Biophysical Journal **93**, 2410–2417 (2007).

[145] P. Piwowarski, E. Ritter, K. P. Hofmann, P. Hildebrandt, D. von Stetten, P. Scheerer, N. Michael, T. Lamparter, and F. Bartl: *Light-Induced Activation of Bacterial Phytochrome Agp1 Monitored by Static and Time-Resolved FTIR Spectroscopy*. Chem. Phys. Chem. **11**, 1207–1214 (2010).

[146] D. von Stetten, S. Seibeck, N. Michael, P. Scheerer, M. A. Mroginski, D. H. Murgida, N. Krauss, M. P. Heyn, P. Hildebrandt, B. Borucki, and T. Lamparter: *Highly conserved residues Asp-197 and His-250 in Agp1 phytochrome control the proton affinity of the chromophore and Pfr formation*. J. Biol. Chem. **282**, 2116–2123 (2007).

[147] S. Seibeck, D. von Stetten, N. Michael, P. Scheerer, M. A. Mroginski, D. H. Murgida, N. Krauss, M. P. Heyn, P. Hildebrandt, B. Borucki, and T. Lamparter: *Mutation of D197 and H250 to alanine in the chromophore binding pocket of Agp1 phytochrome lowers the chromophore pKa and prevents the formation of the Pfr form*. Biophys. J., 315A–315A (2007).

[148] J. R. Wagner, J. R. Zhang, D. von Stetten, M. Guenther, D. H. Murgida, M. A. Mroginski, J. M. Walker, K. T. Forest, P. Hildebrandt, and R. D. Vierstra: *Mutational analysis of Deinococcus radiodurans bacteriophytochrome reveals key amino acids necessary for the photochromicity and proton exchange cycle of phytochromes*. J. Biol. Chem. **283**, 12212–12226 (2008).

[149] H. M. Strauss, J. Hughes, and P. Schmieder: *Heteronuclear Solution-State NMR Studies of the Chromophore in Cyanobacterial Phytochrome Cph1*. Biochemistry **44**, 8244-8250 (2005).

[150] A. R. Holzwarth, E. Venuti, S. E. Braslavsky, and K. Schaffner: *The phototransformation process in phytochrome. I. Ultrafast fluorescence component and kinetic models for the initial Pr → Pfr transformation steps in native phytochrome*. Biochem. Biophys. Acta **1140**, 59–68 (1992).

[151] M. G. Müller, I. Lindner, I. Martin, W. Gärtner, and A. R. Holzwarth: *Femtosecond kinetics of photoconversion of the higher plant photoreceptor phytochrome carrying native and modified chromophores*. Biophys. J. **94**, 4370–4382 (2008).

[152] C. Schumann, R. Groß, M. M. N. Wolf, R. Diller, N. Michael, and T. Lamparter: *Sub-Picosecond Mid-Infrared Spectroscopy of the Pfr Reaction of Phytochrome Agp1 from Agrobacterium tumefaciens*. Biophys. J. **94**, 3189-3197 (2008).

[153] J. J. van Thor, K. L. Ronayne, and M. Towrie: *Formation of the Early Photoproduct Lumi-R of Cyanobacterial Phytochrome Cph1 Observed by Ultrafast Mid-Infrared Spectroscopy*. J. Am. Chem. Soc. **129**, 126–132 (2007).

[154] G. Cornilescu, A. T. Ulijasz, C. C. Cornilescu, J. L. Markley, and R. D. Vierstra: *Solution Structure of a Cyanobacterial Phytochrome GAF Domain in the Red-Light-Absorbing Ground State*. J. Mol. Biol. **383**, 403–413 (2008).

[155] J. Hahn, H. M. Strauss, and P. Schmieder: *Heteronuclear NMR investigation on the structure and dynamics of the chromophore binding pocket of the cyanobacterial phytochrome Cph1*. J. Am. Chem. Soc. **130**, 11170–11178 (2008).

[156] P. Schmidt, T. Gensch, A. Remberg, W. Gärtner, and S. E. Braslavskyand K. Schaffner: *The complexity of the Pr to Pfr phototransformation kinetics is an intrinsic property of native phytochrome*. Photochem. Photobiol. **68**, 754–761 (1998).

[157] S. Kaminski, G. Daminelli, and M. A. Mroginski: *Molecular Dynamics Simulations of the Chromophore Binding Site of Deinococcus radiodurans Bacteriophytochrome Using*

New Force Field Parameters for the Phytochromobilin Chromophore. J. Phy. Chem. B **113**, 945–958 (2009).

[158] H. Foerstendorf, C. Benda, W. Gärtner, M. Storf, H. Scheer, and F. Siebert: *FTIR studies of phytochrome photoreactions reveal the C=O bands of the chromophore consequences for its protonation states, conformation, and protein interaction.*. Biochemistry **40**, 14952–14959 (2001).

[159] S. Heun, R. F. Mahrt, A. Greiner, U. Lemmer, H. Bässler D. A. Halliday, D. D. C. Bradley, P. L. Burn, and A. B. Holmes: *Conformational effects in poly(p-phenylene viny1ene)s revealed by low-temperature site-selective fluorescence*. J. Phys. Condens. Matter **5**, 247–260 (1993).

[160] M. Lippitz, C. G. Hubner, and T. Christ: *Coherent electronic coupling versus localization in individual molecular dimers*. Phys. Rev. Lett. **92**, 103001 (2004).

[161] F. Schindler, J. M. Lupton, J. Feldmann, and U. Scherf: *A universal picture of chromophores in pi-conjugated polymers derived from single-molecule spectroscopy*. Proc. Natl. Acad. Sci. USA **101**, 14695-14700 (2004).

[162] H. Bässler and B. Schweitzer: *Site-Selective Fluorescence Spectroscopy of Conjugated Polymers and Oligomers*. Acc. Chem. Res. **32**, 173–182 (1999).

[163] K. Becker, J. M. Lupton, J. Feldmann, S. Setayesh, A. C. Grimsdale, and K. Müllen: *Efficient Intramolecular Energy Transfer in Single Endcapped Conjugated Polymer Molecules in the Absence of Appreciable Spectral Overlap*. J. Am. Chem. Soc. **128**, 680–681 (2006).

[164] J. G. Müller, M. Anni, U. Scherf, J. M. Lupton, and J. Feldmann: *Vibrational fluorescence spectroscopy of single conjugated polymer molecules*. Phys. Rev. B **70**, 035205 (2004).

[165] R. Métivier, F. Nolde, K. Müllen, and T. Basché: *Electronic excitation energy transfer between two single molecules embedded in a polymer host*. Phys. Rev. Lett. **98**, 047802 (2007).

[166] R. Métivier, T. Christ, F. Kulzer, T. Weil, K. Müllen, and T. Basché: *Single-molecule spectroscopy of molecular aggregates at low temperature*. J. Lumin. **110**, 217–224 (2004).

[167] F. A. Feist, G. Tommaseo, and T. Basché: *Observation of very narrow linewidths in the fluorescence excitation spectra of single conjugated polymer chains at 1.2 K*. Phys. Rev. Lett. **98**, (2007).

[168] I.T. Jolliffe: *Principal Component Analysis*. Springer Verlag (1986).

[169] MATLAB version 7.5 (R2007b), Natick, Massachusetts: The MathWorks Inc., 2007.

[170] J. S. Hyde, A. jesmanowicz, j. J. Ratke, and W. E. Antholine: *Pseudomodulation - A Computer-Based Strategy for Resolution Enhancement*. J. Magn. Reson. **96**, 1–13 (1992).

[171] M. A. Mroginski, D H. Murgida, D. v Stetten, C. Kneip, F.Mark, and P. Hildebrandt: *Determination of the Chromophore Structures in the Photoinduced Reaction Cycle of Phytochrome*. J. Am. Chem. Soc. **126**, 16734–16735 (2004).

[172] J. J. van Thor, N. Fisher, and P. R. Rich: *Assignments of the P_{fr}-P_r FTIR difference spectrum of cyanobacterial phytochrome Cph1 using N-15 and C-13 isotopically labeled phycocyanobilin chromophore*. J. Phys. Chem. B **109**, 20597–20604 (2005).

[173] C. Schumann, R. Groß, N. Michael, T. Lamparter, and R. Diller: *Sub-picosecond mid-infrared spectroscopy of phytochrome Agp1 from Agrobacterium tumefaciens*. Chem. Phys. Chem. **8**, 1657-1663 (2007).

[174] J. Dasgupta, R. R. Frontiera, K. C. Taylor, J. C. Lagarias, and R. A. Mathies: *Ultrafast excited-state isomerization in phytochrome revealed by femtosecond stimulated Raman spectroscopy*. Proc. Natl. Acad. Sci. USA **106**, 1784–1789 (2009).

[175] M. Schmidt, A. Patel, Y. Zhao, and W. Reuter: *Structural basis for the photochemistry of alpha-phycoerythrocyanin*. Biochemistry **46**, 416–423 (2007).

[176] M. A. Mroginski, D. H. Murgida, and P. Hildebrandt: *The chromophore structural changes during the photocycle of phytochrome: A combined resonance raman and quantum chemical approach*. Accounts Of Chemical Research **40**, 258–266 (2007).

[177] B. Borucki, S. Seibeck, M. P. Heyn, and T. Lamparter: *Characterization of the Covalent and Noncovalent Adducts of Agp1 Phytochrome Assembled with Biliverdin and Phycocyanobilin by Circular Dichroism and Flash Photolysis*. Biochemistry **48**, 6305-6317 (2009).

[178] M. A. Mroginski, D. H. Murgida, and P. Hildebrandt: *Calculation of vibrational spectra of linear tetrapyrroles. 4. Methine bridge C-H out-of-plane modes*. J. Phys. Chem. A **110**, 10564–10574 (2006).

[179] M. Brecht, J. B. Nieder, H. Studier, E. Schlodder, and R. Bittl: *Red antenna states of photosystem I from Synechococcus sp. PCC 7002*. Photosynth. Res. **95(2–3)**, 155 – 162 (2008).

[180] C. Hofmann, T. J. Aartsma, H. Michel, and J. Kohler: *Spectral dynamics in the B800 band of LH2 from Rhodospirillum molischianum: a single-molecule study*. New Journal of Physics **6**, 8 (2004).

[181] M. Brecht, V. Radics, J. B. Nieder, H. Studier, and R. Bittl: *Red antenna states of photosystem I from Synechocystis PCC 6803*. Biochemistry **47**, 5536–5543 (2008).

[182] J. B. Nieder, M. Brecht, and R. Bittl: *Dynamic Intracomplex Heterogeneity of Phytochrome*. Journal Of The American Chemical Society **131 (1)**, 69 – 71 (2008).

[183] Govindjee and D. Krogmann: *Discoveries in oxygenic photosynthesis (1727-2003): a perspective*. Photosynth. Res. **80**, 15–+ (2004).

[184] Govindjee and D. W. Krogmann: *A list of personal perspectives with selected quotations, along with lists of tributes, historical notes, Nobel and Kettering awards related to photosynthesis*. Photosynth. Res. **73**, 11–20 (2002).

[185] Savikhin S., http://www.physics.purdue.edu/ sergei/Photosynthesis.html.

[186] Vivetechnologies Inc., http://www.vivetechnologies.com/.

[187] A. J. Hoff and J. Deisenhofer: *Photophysics of photosynthesis. Structure and spectroscopy of reaction centers of purple bacteria*. Phys. Rep. **287**, 2–247 (1997).

[188] K. Brettel and W. Leibl: *Electron transfer in photosystem I*. Biochim. Biophys. Acta, Bioenerg. **1507**, 100–114 (2001).

[189] Govindjee, J. F. Kern, J. Messinger, and J. Whitmarsh: *Photosystem II*. Encyclopedia of life sciences, John Wiley & Sons, Ltd: Chichester. (2010).

[190] P. Fromme, H. Bottin, N. Krauss, and P. Setif: *Crystallization and electron paramagnetic resonance characterization of the complex of photosystem I with its natural electron acceptor ferredoxin*. Biophys. J. **83**, 1760–1773 (2002).

[191] L. P. Vernon, E. R. Shaw, T. Ogawa, and D. Raveed: *Structure of Photosystem I and Photosystem II Of Plant Chloroplasts*. Photochem. Photobiol. **14**, 343–357 (1971).

[192] K. Kalyanasundaram and M. Graetzel: *Artificial photosynthesis: biomimetic approaches to solar energy conversion and storage*. Curr. Opin. Biotechnol. **21**, 298 - 310 (2010).

[193] S. Lin, H. van Amerongen, and W. S. Struve: *Ultrafast Pump-Probe Spectroscopy of the P700–Containing and Fx-Containing Photosystem-I Core Protein from Synechococcus sp pcc-6301 (Anacystis nidulans)*. Biochim. Biophys. Acta **1140**, 6–14 (1992).

[194] M. K. Sener, D. Y. Lu, T. Ritz, S. Park, P. Fromme, and K. Schulten: *Robustness and optimality of light harvesting in cyanobacterial photosystem I*. J. Phys. Chem. B **106**, 7948–7960 (2002).

[195] H. W. Trissl: *Long-Wavelength Absorbing Antenna Pigments and Heterogeneous Absorption-Bands Concentrate Excitons and Increase Absorption Cross-Section*. Photosynth. Res. **35**, 247–263 (1993).

[196] L. Björn, G. C. Papageorgiou, R. E. Blankenship, and Govindjee: *A viewpoint: Why chlorophyll a?*. Photosynth. Res. **99**, 85–98 (2009).

[197] B. Gobets and R. van Grondelle: *Energy transfer and trapping in photosystem I*. Biochim. Biophys. Acta, Bioenerg. **1507**, 80–99 (2001).

[198] L. L. Shipman, T. M. Cotton, J. R. Norris, and J. J. Katz: *An analysis of the visible absorption spectrum of chlorophyll a monomer, dimer, and oligomers in solution*. J. Am. Chem. Soc. **98**, 8222-8230 (1976).

[199] B. Gobets, H. van Amerongen, R. Monshouwer, J. Kruip, M. Rogner, R. van Grondelle, and J. P. Dekker: *Polarized Site-Selected Fluorescence Spectroscopy Of Isolated Photosystem-I Particles*. Biochim. Biophys. Acta, Bioenerg. **1188**, 75–85 (1994).

[200] B. Gobets, I. H. M. van Stokkum, M. Rogner, J. Kruip, E. Schlodder, N. V. Karapetyan, J. P. Dekker, and R. van Grondelle: *Time-resolved fluorescence emission measurements of photosystem I particles of various cyanobacteria: A unified compartmental model*. Biophys. J. **81**, 407–424 (2001).

[201] J. M. Hayes, S. Matsuzaki, M. Ratsep, and G. J. Small: *Red chlorophyll a antenna states of photosystem I of the cyanobacterium Synechocystis sp PCC 6803*. J. Phys. Chem. B **104**, 5625–5633 (2000).

[202] L. O. Palsson, J. P. Dekker, E. Schlodder, R. Monshouwer, and R. van Grondelle: *Polarized site-selective fluorescence spectroscopy of the long-wavelength emitting chlorophylls in isolated Photosystem I particles of Synechococcus elongatus*. Photosynth. Res. **48**, 239–246 (1996).

[203] V. Zazubovich, S. Matsuzaki, T. W. Johnson, J. M. Hayes, P. R. Chitnis, and G. J. Small: *Red antenna states of photosystem I from cyanobacterium Synechococcus elongatus: a spectral hole burning study*. Chem. Phys. **275**, 47–59 (2002).

[204] N. V. Karapetyan, D. Dorra, G. Schweitzer, I. N. Bezsmertnaya, and A. R. Holzwarth: *Fluorescence spectroscopy of the longwave chlorophylls in trimeric and monomeric photosystem I core complexes from the cyanobacterium Spirulina platensis*. Biochemistry **36**, 13830–13837 (1997).

[205] J. Adolphs, F. Muh, M. E. A. Madjet, M. S. A. Busch, and T. Renger: *Structure-Based Calculations of Optical Spectra of Photosystem I Suggest an Asymmetric Light-Harvesting Process*. J. Am. Chem. Soc. **132**, 3331–3343 (2010).

[206] A. Amunts, O. Drory, and N. Nelson: *The structure of a plant photosystem I supercomplex at 3.4 angstrom resolution*. Nature **447**, 58–63 (2007).

[207] E. J. Boekema, J. P. Dekker, M. G. van Heel, M. Rögner, W. Saenger, I. Witt, and H. T. Witt: *Evidence for a trimeric organization of the photosystem I complex from the thermophilic cyanobacterium Synechococcus sp.*. FEBS Lett. **217**, 283–286 (1987).

[208] P. Jordan, P. Fromme, H.T. Witt, O. Klukas, W. Saenger, and N. Krauss: *Three-dimensional structure of cyanobacterial photosystem I at 2.5 angstrom resolution*. Nature **411**, 909–917 (2001).

[209] B. Bruggemann, K. Sznee, V. Novoderezhkin, R. van Grondelle, and V. May: *From structure to dynamics: Modeling exciton dynamics in the photosynthetic antenna PS1*. J. Phys. Chem. B **108**, 13536–13546 (2004).

[210] M. Rätsep, T. W. Johnson, P. R. Chitnis, and G. J. Small: *The red-absorbing chlorophyll* a *antenna states of photosystem I: A hole-burning study of Synechocystis sp PCC 6803 and its mutants*. J. Phys. Chem. B **104**, 836–847 (2000).

[211] M. Byrdin, P. Jordan, N. Krauss, P. Fromme, D. Stehlik, and E. Schlodder: *Light harvesting in photosystem I: Modeling based on the 2.5-Angstrom structure of photosystem I from Synechococcus elongatus*. Biophys. J. **83**, 433–457 (2002).

[212] T. M. Hsin, V. Zazubovich, J. M. Hayes, and G. J. Small: *Red antenna states of PSI of cyanobacteria: Stark effect and interstate energy transfer*. J. Phys. Chem. B **108**, 10515–10521 (2004).

[213] D. Abramavicius and S. Mukamel: *Exciton Delocalization and Transport in Photosystem I of Cyanobacteria Synechococcus elongates: Simulation Study of Coherent Two-Dimensional Optical Signals*. J. Phys. Chem. B **113**, 6097–6108 (2009).

[214] M. Byrdin, I. Rimke, E. Schlodder, D. Stehlik, and T. A. Roelofs: *Decay kinetics and quantum yields of fluorescence in photosystem I from Synechococcus elongatus with P700 in the reduced and oxidized state: Are the kinetics of excited state decay trap-limited or transfer-limited?*. Biophys. J. **79**, 992–1007 (2000).

[215] A. N. Melkozernov, S. Lin, and R. E. Blankenship: *Excitation dynamics and heterogeneity of energy equilibration in the core antenna of photosystem I from the cyanobacterium Synechocystis sp. PCC 6803*. Biochemistry **39**, 1489–1498 (2000).

[216] A. N. Melkozernov, S. Lin, R. E. Blankenship, and L. Valkunas: *Spectral inhomogeneity of photosystem I and its influence on excitation equilibration and trapping in the cyanobacterium Synechocystis sp PCC6803 at 77 K*. Biophys. J. **81**, 1144–1154 (2001).

[217] E. Schlodder, K. Falkenberg, M. Gergeleit, and K. Brettel: *Temperature dependence of forward and reverse electron transfer from A(1)(-), the reduced secondary electron acceptor in photosystem I*. Biochemistry **37**, 9466–9476 (1998).

[218] V. V. Shubin, I. N. Bezsmertnaya, and N. V. Karapetyan: *Efficient Energy-Transfer from the Long-Wavelength Antenna Chlorophylls to P700 In Photosystem-I Complexes from Spirulina-Platensis*. J. Photochem. Photobiol. B-Biol. **30**, 153–160 (1995).

[219] P. E. Jensen, R. Bassi, E. J. Boekema, J. P. Dekker, S. Jansson, D. Leister, C. Robinson, and H. V. Scheller: *Structure, function and regulation of plant photosystem I*. Biochim. Biophys. Acta, Bioenerg. **1767**, 335–352 (2007).

[220] S. Vaitekonis, G. Trinkunas, and L. Valkunas: *Red chlorophylls in the exciton model of photosystem I*. Photosynth. Res. **86**, 185–201 (2005).

[221] B. Gobets, I. H. M. van Stokkum, F. van Mourik, J. P. Dekker, and R. van Grondelle: *Excitation wavelength dependence of the fluorescence kinetics in Photosystem I particles from Synechocystis PCC 6803 and Synechococcus elongatus*. Biophys. J. **85**, 3883–3898 (2003).

[222] A. R. Holzwarth, G. Schatz, H. Brock, and E. Bittersmann: *Energy-Transfer and Charge Separation Kinetics in Photosystem-I .1. Picosecond Transient Absorption and Fluorescence Study of Cyanobacterial Photosystem-I Particles*. Biophys. J. **64**, 1813–1826 (1993).

[223] N. V. Karapetyan, A. R. Holzwarth, and M. Rogner: *The photosystem I trimer of cyanobacteria: molecular organization, excitation dynamics and physiological significance*. FEBS Lett. **460**, 395–400 (1999).

[224] A. Rivadossi, G. Zucchelli, F. M. Garlaschi, and R. C. Jennings: *The importance of PSI chlorophyll red forms in light-harvesting by leaves*. Photosynthesis Research **60**, 209–215 (1999).

[225] E. Schlodder, M. Cetin, M. Byrdin, I. V. Terekhova, and N. V. Karapetyan: *P700(+)- and (3)P700-induced quenching of the fluorescence at 760 nm in trimeric Photosystem I complexes from the cyanobactenium Arthrospira platensis*. Biochim. Biophys. Acta, Bioenerg. **1706**, 53–67 (2005).

[226] L. O. Palsson, C. Flemming, B. Gobets, R. van Grondelle, J. P. Dekker, and E. Schlodder: *Energy transfer and charge separation in photosystem I: P700 oxidation upon selective excitation of the long-wavelength antenna chlorophylls of Synechococcus elongatus*. Biophys. J. **74**, 2611–2622 (1998).

[227] Y. Shibata, A. Yamagishi, S. Kawamoto, T. Noji, and S. Itoh: *Kinetically Distinct Three Red Chlorophylls in Photosystem I of Thermosynechococcus elongatus Revealed by Femtosecond Time-Resolved Fluorescence Spectroscopy at 15 K*. J. Phys. Chem. B **114**, 2954–2963 (2010).

[228] C. Hofmann, M. Ketelaars, M. Matsushita, H. Michel, T. J. Aartsma, and J. Köhler: *Single-molecule study of the electronic couplings in a circular array of molecules: Light-harvesting-2 complex from Rhodospirillum molischianum*. Phys. Rev. Lett. **90**, 013004 (2003).

[229] K. Fritsch, J. Friedrich, F. Parak, and J. L. Skinner: *Spectral diffusion and the energy landscape of a protein*. Biophysics **93**, 15141–15145 (1996).

[230] J. L. Skinner, J. Friedrich, and J. Schlichter: *Spectral Diffusion in Proteins A Simple Phenomenological Model*. J. Phys. Chem. A **103**, 2310-2311 (1999).

[231] J. Heimdal, K. P. Jensen, A. Devarajan, and U. Ryde: *The role of axial ligands for the structure and function of chlorophylls*. J. Biol. Inorg. Chem. **12**, 49–61 (2007).

[232] Clemens Hoffmann: *Pigment-Pigment Interactions and Protein Dynamics in Light-Harvesting Complexes a Single-Molecule Study*. Ph. D. thesis, Universität Bayreuth, (2003).

[233] W. P. F. de Ruijter, J. M. Segura, R. J. Cogdell, A. T. Gardiner, S. Oellerich, and T. J. Aartsma: *Fluorescence-emission spectroscopy of individual LH2 and LH3 complexes*. Chem. Phys. **341**, 320–325 (2007).

[234] M. Rätsep, T. W. Johnson, P. R. Chitnis, and G. J. Small: *The red-absorbing chlorophyll a antenna states of photosystem I: A hole-burning study of Synechocystis sp PCC 6803 and its mutants*. J. Phys. Chem. B **104**, 836–847 (2000).

[235] Z. D. Nagel and J. P. Klinman: *Tunneling and dynamics in enzymatic hydride transfer*. Chemical Reviews **106**, 3095–3118 (2006).

[236] R. Davydov, S. Chemerisov, D. E. Werst, T. Rajh, T. Matsui, M. Ikeda-Saito, and B. M. Hoffman: *Proton transfer at helium temperatures during dioxygen activation by heme monooxygenases*. J. Am. Chem. Soc. **126**, 15960–15961 (2004).

[237] V. Helms: *Protein dynamics tightly connected to the dynamics of surrounding and internal water molecules*. ChemPhysChem **8**, 23–33 (2007).

[238] L. L. Shipman, T. R. Janson, G. J. Ray, and J. J. Katz: *Donor Properties of 3 Carbonyl Groups of Chlorophyll a - Ab-Initio Calculations and C-13 Magnetic-Resonance Studies*. Proceedings of the National Academy of Sciences of the United States of America **72**, 2873–2876 (1975).

[239] J. M. Vanderkooi, J. L. Dashnau, and B. Zelent: *Temperature excursion infrared (TEIR) spectroscopy used to study hydrogen bonding between water and biomolecules*. BBA-Proteins Proteomics **1749**, 214–233 (2005).

[240] D. A. Koster, C. H. Wiggins, and N. H. Dekker: *Multiple events on single molecules: Unbiased estimation in single-molecule biophysics*. Proc. Natl. Acad. Sci. USA **103**, 1750–1755 (2006).

[241] D. S. Courvoisier, M. Eid, and F. W. Nussbeck: *Mixture distribution latent state-trait analysis: Basic ideas and applications*. Psychological Methods **12**, 80–104 (2007).

[242] M. S. Davis, A. Forman, and J. Fajer: *Ligated chlorophyll cation radicals - their function in photosystem-II of plant photosynthesis*. Proc. Natl. Acad. Sci. USA **76**, 4170–4174 (1979).

[243] P. J. O'Malley and G. T. Babcock: *Electron nuclear double-resonance evidence supporting a monomeric nature for P700+ in spinach-chloroplasts*. Proc. Natl. Acad. Sci. U. S. A.-Biol. Sci. **81**, 1098–1101 (1984).

[244] H. Kass, P. Fromme, H. T. Witt, and W. Lubitz: *Orientation and electronic structure of the primary donor radical cation $P700^{+\cdot}$ in photosystem I: A single crystals EPR and ENDOR study*. J. Phys. Chem. B **105**, 1225–1239 (2001).

[245] I. Noda, A. E. Dowrey, C. Marcoli, G. M. Story, and Y. Ozaki: *Generalized Two-Dimensional Correlation Spectroscopy*. Applied Spectroscopy **54**, 236–248 (2000).

[246] J. K. Gillie, J. M. Hayes, G. J.. Small, and J. H. Golbeck: *Hole Burning Spectroscopy Of A Core Antenna Complex*. J. Phys. Chem. **91**, 5524–5527 (1987).

[247] J. A. Ihalainen, M. Rätsep, P. E. Jensen, H. V. Scheller, R. Croce, R. Bassi, J. E. I. Korppi-Tommola, and A. Freiberg: *Red spectral forms of chlorophylls in green plant PSI - a site-selective and high-pressure spectroscopy study*. J. Phys. Chem. B **107**, 9086–9093 (2003).

[248] K. J. Riley, T. Reinot, R. Jankowiak, P. Fromme, and V. Zazubovich: *Red antenna states of photosystem I from cyanobacteria Synechocystis PCC 6803 and Thermosynechococcus elongatus: Single-complex spectroscopy and spectral hole-burning study*. J. Phys. Chem. B **111**, 286–292 (2007).

[249] C. Hofmann, H. Michel, M. van Heel, and J. Kohler: *Multivariate analysis of single-molecule spectra: Surpassing spectral diffusion*. Phys. Rev. Lett. **94**, 195501 (2005).

[250] E. Fort and S. Gresillon: *Surface enhanced fluorescence*. J. Phys. D-Appl. Phys. **41**, 013001–013031 (2008).

[251] J. R. Lakowicz: *Plasmonics in Biology and Plasmon-Controlled Fluorescence*. Plasmonics **1**, 5–33 (2006).

[252] M. Steiner, C. Debus, A. V. Failla, and A. J. Meixner: *Plasmon-Enhanced Emission in Gold Nanoparticle Aggregates*. J. Phys. Chem. C **112**, 3103–3108 (2008).

[253] Y.-E. Koo Lee, R. Smith, and R. Kopelman: *Nanoparticle PEBBLE Sensors in Live Cells and In Vivo*. Annu. Rev. Anal. Chem. **2**, 57–76 (2009).

[254] R. A. Grimme, C. E. Lubner, D. A. Bryant, and J. H. Golbeck: *Photosystem I/molecular wire/metal nanoparticle bioconjugates for the photocatalytic production of H-2*. J. Am. Chem. Soc. **130**, 6308–6311 (2008).

[255] Y. Fu and J. R. Lakowicz: *Modification of single molecule fluorescence near metallic nanostructures*. Laser Photon. Rev. **3**, 221–232 (2009).

[256] J. R. Lakowicz, K. Ray, M. Chowdhury, H. Szmacinski, Y. Fu, J. Zhang, and K. Nowaczyk: *Plasmon-controlled fluorescence: a new paradigm in fluorescence spectroscopy*. Analyst **133**, 1308–1346 (2008).

[257] J. Zhang, Y. Fu, M. H. Chowdhury, and J. R. Lakowicz: *Enhanced Forster Resonance Energy Transfer on Single Metal Particle. 2. Dependence on Donor,áíAcceptor Separation Distance, Particle Size, and Distance from Metal Surface*. J. Phys. Chem. C **111**, 11784–11792 (2007).

[258] S. Mackowski, S. Wörmke, A. J. Maier, T. H. P. Brotosudarmo, H. Harutyunyan, A. Hartschuh, A. O. Govorov, H. Scheer, and C. Bräuchle: *Metal-enhanced fluorescence of chlorophylls in single light-harvesting complexes*. Nano Lett. **8**, 558–564 (2008).

[259] Y. Chen, K. Munechika, and D. S. Ginger: *Dependence of fluorescence intensity on the spectral overlap between fluorophores and plasmon resonant single silver nanoparticles*. Nano Lett. **7**, 690–696 (2007).

[260] S. Kuhn, U. Hakanson, L. Rogobete, and V. Sandoghdar: *Enhancement of single-molecule fluorescence using a gold nanoparticle as an optical nanoantenna*. Phys. Rev. Lett. **97**, 017402 (2006).

[261] P. P. Pompa, L. Martiradonna, A. Della Torre, F. Della Sala, L. Manna, M. De Vit-

torio, F. Calabi, R. Cingolani, and R. Rinaldi: *Metal-enhanced fluorescence of colloidal nanocrystals with nanoscale control*. Nat. Nanotechnol. **1**, 126–130 (2006).

[262] S. Vukovic, S. Corni, and B. Mennucci: *Fluorescence Enhancement of Chromophores Close to Metal Nanoparticles. Optimal Setup Revealed by the Polarizable Continuum Model*. J. Phys. Chem. C **113**, 121–133 (2009).

[263] J. Enderlein: *A theoretical investigation of single-molecule fluorescence detection on thin metallic layers*. Biophys. J. **78**, 2151–2158 (2000).

[264] E. Matveeva, Z. Gryczynski, J. Malicka, I. Gryczynski, and J. R. Lakowicz: *Metal-enhanced fluorescence immunoassays using total internal reflection and silver island-coated surfaces*. Anal. Biochem. **334**, 303–311 (2004).

[265] K. Ray, R. Badugu, and J. R. Lakowicz: *Metal-enhanced fluorescence from CdTe nanocrystals: A single-molecule fluorescence study*. J. Am. Chem. Soc. **128**, 8998–8999 (2006).

[266] L. Shang, Y. Z. Wang, J. G. Jiang, and S. J. Dong: *pH-dependent protein conformational changes in albumin : gold nanoparticle bioconjugates: A spectroscopic study*. Langmuir **23**, 2714–2721 (2007).

[267] J. R. Lakowicz, Y. B. Shen, S. D'Auria, J. Malicka, J. Y. Fang, Z. Gryczynski, and I. Gryczynski: *Radiative decay engineering 2. Effects of silver island films on fluorescence intensity, lifetimes, and resonance energy transfer*. Anal. Biochem. **301**, 261–277 (2002).

[268] J. R. Lakowicz, C. D. Geddes, I. Gryczynski, J. Malicka, Z. Gryczynski, K. Aslan, J. Lukomska, E. Matveeva, J. A. Zhang, R. Badugu, and J. Huang: *Advances in surface-enhanced fluorescence*. J. Fluoresc. **14**, 425–441 (2004).

[269] H. Krassen, A. Schwarze, B. Friedrich, K. Ataka, O. Lenz, and J. Heberle: *Photosynthetic Hydrogen Production by a Hybrid Complex of Photosystem I and [NiFe]-Hydrogenase*. ACS Nano **3**, 4055–4061 (2009).

[270] L. Frolov, O. Wilner, C. Carmeli, and I. Carmeli: *Fabrication of oriented multilayers of photosystem I proteins on solid surfaces by auto-metallization*. Adv. Mater. **20**, 263–+ (2008).

[271] N. Terasaki, N. Yamamoto, T. Hiraga, Y. Yamanoi, T. Yonezawa, H. Nishihara, T. Ohmori, M. Sakai, M. Fujii, A. Tohri, M. Iwai, Y. Inoue, S. Yoneyama, M. Minakata, and I. Enami: *Plugging a Molecular Wire into Photosystem I: Reconstitution of the Photoelectric Conversion System on a Gold Electrode*. Angew. Chem. Int. Ed. **48**, 1585–1587 (2009).

[272] A. O. Govorov and I. Carmeli: *Hybrid structures composed of photosynthetic system and metal nanoparticles Plasmon enhancement effect*. Nano Lett. **7**, 620–625 (2007).

[273] K. Aslan, S. N. Malyn, and C.D.Geddes: *Angular-dependent metal-enhanced fluorescence from silver island films*. Chem. Phys. Lett. **453**, 222–228 (2008).

List of Abbreviations

Agp1/Agp2 phytochromes from *Agrobacterium tumefaciens*

APD Avalanche Photodiode

BphP Bacterio-phytochrome

BV Biliverdin

CBD Chromophore Binding Domain comprising the PAS and GAF domain

PCD Photosensory Core Domain comprising the PAS, GAF and PHY domain

CCD Charge Coupled Device

Cph1 Phytochrome from *Synechocystis* sp. PCC 6803

Chla Chlorophyll a

DFT Density Functional Theory

***Dr*BphP** Phytochrome from *Deinococcus radiodurans*

EET Excitation energy transfer

FPh Fungal Phytochrome

FLN Fluorescence Line Narrowing spectroscopy

FRET Förster-Resonance-Energy Transfer

FT-IR Fourier-Transform Infra-Red spectroscopy

GAF (cGMP phosphodiesterase / adenyl cyclase /FhlA)

GFP Green Fluorescent Protein

HK Histidine Kinase

HKRD Histidine Kinase-Related Domain

LT-SMS Low-Temperature Single-Molecule Spectroscopy

NMR Nuclear Magnetic Resonance

P700 Photosynthetic reaction center of PSI

***Pa*BphP** Phytochrome from *Pseudomonas aeruginosa*

PAS Per/Arndt/Sim protein domain structure

PCA Principal Component Analysis

PCB Phycocyanobilin

PEB Phycoerythrobilin

PhyA–E Phytochrome from plants, A–E denote the different types

PIF Phytochrome Interacting Factor

PΦB Phytochromobilin

P_{fr} Far-red light absorbing phytochrome state

PHY Phytochrome-specific protein domain

P_r Red light absorbing phytochrome state

PSI Photosystem I

PSF Point Spread Function

***Rp*BphP2/3** Phytochromes from *Rhodopseudomonas palustris*

RR spectroscopy Resonance Raman spectroscopy

RR domain Response Regulator domain

SAXS Small Angle X-Ray Scattering

SMS Single-molecule spectroscopy

TD-DFT Time-dependent Density Functional Theory

Curriculum Vitae

Der Lebenslauf ist in der Online-Version aus Gründen des Datenschutzes nicht enthalten.

ACKNOWLEDGMENTS

An erster Stelle möchte ich mich bei Herrn Prof. Robert Bittl dafür bedanken, dass ich in seiner Arbeitsgruppe promovieren durfte. Sie haben mir ermöglicht nach der Diplomarbeit auch die Doktorarbeit auf dem spannenden Gebiet der Einzelmolekül-Spektroskopie durchzuführen. Sie haben immer wieder durch kritischen Fragen die Arbeit vorangetrieben. Durchgängig haben Sie die Neuerungen im Einzelmolekül-Labor unterstützt. Speziell für Ihr Engagement in der letzten Phase meiner Doktorarbeit möchte ich mich bei Ihnen bedanken. Nicht zu vergessen sind die vielen Konferenzen an denen teilzunehmen Sie mir ermöglicht haben und auf denen ich auch für meine wissenschaftliche Zukunft wichtige Kontakte knüpfen konnte.

Bei Prof. Karsten Heyne bedanke ich mich dafür, dass er sich bereit erklärt hat, das Zweitgutachten der Doktorarbeit zu übernehmen. Für die hilfreiche Diskussion im Anschluss an meinen Vortrag, den ich im Januar in Ihrem Seminar gehalten habe, möchte ich mich bedanken.

Bei Dr. Marc Brecht, unserem Einzelmolekül-Gruppenleiter, bedanke ich mich für die vielen lehreichen Diskussionen und die wunderbare Zusammenarbeit während unserer gemeinsamen Zeit an der FU Berlin. Du hast die Arbeit entscheidend vorangetrieben und hattest immer wieder neue Ideen, die es wert waren, umgesetzt zu werden.

Ohne die Kooperationen zur Pflanzenphysiologie und Biochemie wäre eine biophysikalische Arbeit dieser Art nicht möglich gewesen. Für die agrobakteriellen Phytochrome und deren Varianten möchte ich mich bei Tilman Lamparter (U Karlsruhe) und Norbert Michael (TU Berlin) bedanken. André Verméglio (IRD, Montpellier France), merci pour les échantillons des phytochromes de *Rhodopseudmonas palustris*, and thank you John Kennis (VU Amsterdam)/Keith Moffat (U Chicago) for giving the me opportunity to analyze the mutants from *Rhodopseudomonas palustris* by FLN, and Katrina T. Forest (U Wisconsin-Madison) for kindly providing me phytochrome samples from *Deinococcus radiodurans*.

Bei PD Dr. Eberhard Schlodder (TU Berlin) möchte ich mich zum einen für die PSI-Proben bedanken, und zum anderen für die Kooperation im Rahmen der PSI-Spektroskopie. Vielen Dank für die Zurverfügungstellung der Ensembledaten und die netten Laborbesuche bei uns 'Einzelmolekülern'. Über Dich haben wir auch die Proben von B. A. Diner erhalten. Prof. Dr. John Golbeck (U Penn State) thank you

for all the PSI samples that you gave us and for the inspiring discussions we had during your multiple stays at the FU Berlin. Thanks to Rebecca Grimme, your Ph.D. student at that time.

Meinem Vorgänger im Einzelmolekül-Labor, Dr. Hauke Studier, ist ein Großteil des experimentellen Aufbaus zu verdanken. Auch wenn viele Komponenten innerhalb der letzten Jahre ausgetauscht wurden, so ist das Herzstück von Dir, eine ganz grosse Leistung, von der wir nachfolgenden Einzelmoleküler stark profitiert haben!

Meinen Mit-Doktoranden im Einzelmolekül-Umfeld möchte ich besonders danken. Gemeinsam haben wir das Spektrometer zusammen am Laufen gehalten, verbessert und umbebaut und immer einen Austausch über unsere Projekte gepflegt. Dies waren Volker Radics, der wunderbare Einzelmolekül-Daten am PSI aufgenommen hat, sowie den Grundstein für unser 'SMS-Tool', einer Matlab-basierten Visualisierung- und Auswertesoftware gelegt hat, und Martin Hussels, Ansprechpartner für alle weiteren Computerfragen sowie Partner in der Verbesserung der Messsoftware und Aufbau des TCSPC-Setups, woran auch unser Diplomand Axel Luchterhand entscheidend mitgewirkt hat. Gut vernetzt habe ich über Dich Pascal Blümmel aus der AG Prof. Stefanie Reich kennengelernt, der netter Weise für uns die AFM-Charakterisierung der Silberinselfilme durchgeführt hat.

Tim Heinemann ist als Bachelor-Student zu uns gestoßen. Dein Engagement in der PCA-Analyse von Phytochrom-Daten war unübertrefflich und führte zu interessanten Ergebnissen! Die Zusammenarbeit hat sehr viel Freude gemacht! Wendelin Böhmer (TU Berlin) sei gedankt für die hilfreichen Gespräche über Mustererkennungs-Methoden.

Jährlich im Sommer gab es einen gern gesehenen mehrwöchigen Besuch von Studenten der IIT Delhi. Die Betreuung der Projekte von Sushim Gupta, Yatin Tyagi und Aditya Malik haben sehr viel Freude gemacht. Weitere Laborgäste waren Christoph Oelmüller und Kati Hübener aus der AG Prof. Wolfgang Harneit. Christoph, danke für deine Verbesserungen an der Messsoftware!

Die gesamte AG Bittl hat zu einer freundlichen Arbeitsatmosphäre beigetragen, die durch gegenseitige Hilfsbereitschaft, sowie durch viele gemeinsame Kuchenkränzchen geprägt war. (Ich weiß, dass ich Euch noch einen Blaubeerkuchen schuldig bin... und werde das bei der nächsten Gelegenheit nachholen). Dr. Christian Teutloff, vielen Dank für die durchgängige Unterstützung und Deine Hilfsbereitschaft zur Lösung verschiedenster fachlicher und persönlicher Fragen. Bezüglich einer wunderbaren Arbeitsatmosphäre sei meinem Bürokollegen Christoph Meier besonders gedankt. Vielen Dank, dass ich von Deinem Organisationstalent und Deiner Hilfsbereitschaft in der letzten Phase der Arbeit profitieren durfte! Sven Keßen, vielen Dank für Deinen wundersamen Humor, Du bist ein echter Freund geworden. Roswitha Brunn, vielen Dank für Deinen Zuspruch und Deine Hilfe im Chemielabor. Der Teamgeist in der AG Bittl hat sich besonders deutlich in der überaus zahlreichen Teilnahme an der Marathonstaffel gezeigt! Dieses Ereignis hat mir sehr viel Freude gemacht. Keinerlei

Überredungskünste waren gefragt, um den sportlichen Eifer in den darauffolgenden Wochen beim Eiskunstlauf zusammen mit Susanne Pudollek weiterzuführen.

Bedanken möchte ich mich bei den Freunden und Kollegen, die Teile der Arbeit zur Korrektur gelesen haben: Sven Keßen, Christoph Meier, Dr. Ben Johnson, Dr. Jan Behrends, Richard Brosi, Henryk Kalbe und Christopher Engelhard.

Die Berliner Phytochromforschung ist fantastisch vernetzt. Mein Dank bezüglich des wissenschaftlichen Austauschs geht an Prof. Peter Hildebrandt, Dr. David von Stetten, Patrick Piwowarski (vielen Dank für die Zurverfügungstellung von RR- und FT-IR-Spektren), Steve Kaminski, Dr. Patrick Scheerer, Dr. Berthold Borucki, Prof. Maarten P. Heyn etc. und neu hinzugekommen Prof. Andreas Möglich. Dir vielen Dank für das Gegenlesen der Phytochrom-Einleitung und die lehrreichen Gespräche!

Gern möchte ich mich bei den Theoretikern Prof. Thomas Renger und Dr. Ben Brüggemann bedanken, die großes Interesse an unseren Einzelmoleküldaten gezeigt haben und im wissenschaftlichen Austausch zum Verständnis der roten Zustände im PSI beigetragen haben. Bei Prof. Michael Eid, der bereits erste Rechnungen mit Mischverteilungsmodellen an Lösungsmittel-abhängigen Einzelmolekül-Daten durchgeführt hat, möchte ich mich für sein Engagement bedanken und würde mich über eine weitere Zusammenarbeit freuen.

I had the chance to work for a couple of weeks in the inspiring group of Prof. Rienk van Grondelle at the Vrije Universiteit Amsterdam. Thank you, PD John Kennis, for encouraging me to take part in the LaserLab Europe Program. It was a pleasure to be your guest. Die Arbeitsatmosphaere aan de Vrije Universiteit van Amsterdam was prachtig. Voor hulp bij de voorbereiding van het FLN experimenten wil ik Jos Thieme bedanken. PD Jan Dekker, thank you for your support. You made it possible that I could attend the kick-off meeting of the european Marie Curie research program on light-harvesting systems two months after my stay in Amsterdam. Thereby I got the chance to present my work in an inspiring community and to see some of the colleagues from Amsterdam again. Andreas Stahl and Bart van Oort, we had a nice trip to Helsinki, thank you.

Die Doktorarbeitszeit wäre nur halb so schön gewesen, wenn ihr nicht da gewesen wäret: meine Freunde und ehemaligen Kommilitonen Frauke Eimer, Peter Kupser, Philip Schambach, Frauke Bierau, Volker Radics, Thomas Sieben, Fabian Weise und Björn Lewitz.

Und an letzter Stelle sei herzlichst meiner Familie gedankt. Meinen lieben Eltern Renate und Thomas und meinem lieben Bruder Piet. Ihr wart immer für mich da und habt mich überaus vertrauensvoll unterstützt. Vielen Dank!